Radio Observations of the Gum Nebula Region

THESIS
Submitted in fulfilment of the
requirements for the Degree of
DOCTOR OF PHILOSOPHY
of Rhodes University

by

BEATE WOERMANN

June 1997

Abstract

This thesis describes the results of an investigation of the physical properties of the Gum Nebula. For this investigation a radio continuum map of the region was made at 2326 MHz and resolution $\frac{1}{3}^{\circ}$ with the HartRAO antenna. This map was used to generate spectral index images and an infrared to radio flux density ratio (IRR) image. The latter image shows that the IRR of the nebula is in the range 20 to 250, identifying it as an old SNR.

Several spectral index images of this region were generated using two different methods, one based on the isolation of the nebula from its background radiation, the other based on TT-plots (Turtle et al., 1962). The two methods yield similar results, which show that the nebula has a thermal shell with a non-thermal region in its interior. Below the galactic plane the thermal region dominates and above the plane the non-thermal region. These results suggest a model of an old SNR with an H II region shell.

Spectral line observations of hydrogen recombination lines and hydroxyl (OH) were made with the HartRAO and the Mopra telescopes.

The detection of hydrogen recombination lines at four positions in the thermal regions of the nebula give electron temperatures and emission measures in the ranges 4000 to 6000 K and 220 to 460 pc.cm^{-6} respectively. The turbulent velocities are of the order of 20 km/s.

A search for shocked OH lines at 1667 MHz and 1720 MHz in the Gum Nebula gave results that were negative, but numerous unshocked 1667 MHz OH lines were detected. The latter were used in a test for an expansion of the nebula. The most plausible fit to the data gives an expansion centre at $\ell = 260.5°$, $b = -2.5°$ and at a distance of 0.7 kpc from us. The front face angular radius and expansion velocity are 10.5° and 16 km/s respectively. The back face angular radius and expansion velocity are 8.5° and 7 km/s respectively.

Declaration

I declare the contents of this thesis to be my own unaided work. This thesis is being submitted for the degree of Doctor of Philosophy at Rhodes University, Grahamstown. It has not been submitted before for any degree or examination at any other university.

BWoermann

B. Woermann

27th June 1997

Acknowledgements

The very faint emission of the Gum Nebula meant that numerous blind alleys were searched for methods that would yield creditable results before this work came to fruition. Many people, my parents, friends and colleagues, encouraged me to persevere. Often those that advised me to pursue other things in life seemed wiser (and may well be so). I thank all of them, both the protagonists and antagonists, for their well-meant input.

The observations, which are the backbone of this work, were made with the Hartebeesthoek Radio Astronomical Observatory antenna (South Africa) and the Mopra antenna, part of the Australian Telescope. The research and support staff at both institutions gave excellent service, for which I am most grateful.

In particular, I would like to thank the following people:

George Nicholson, the director of HartRAO, for the use of the facilities at HartRAO and seeing to the smooth running of the antenna during all my observations.

Mike Gaylard for his expert advice on the spectral line work and many hours spent in discussion, guiding me to better scientific reasoning, reading of the first draft of the spectral line chapters and his unflagging encouragement.

Rubina Otrupcek for introducing the Mopra observing system to me, giving me a chance to catch up on sleep by babysitting the antenna during observations on my behalf, cooking scrumptious meals and keeping me company at the then two women station (Rubina and myself).

The CSIRO for free lodging at Mopra. Also particular thanks to Graham Baines and others at Narrabri for dealing promptly with technical problems at Mopra.

Euan Troupe and John Whiteoak for sorting out problems with the spectral line observing program at Mopra.

Lister Stavely-Smith for helping set up SLAP (Spectral Line Analysis Program) on my home computer and good advice on spectral line observing at Mopra.

Chris Koen at SAAO for leading me to the Theil method of straight line regression.

The staff at SAAO during my 8 month stay there using their facilities.

I wish to thank my supervisors, Professor Eddie Baart and Mr Justin Jonas, for the support, advice and help they have given me; Justin for the use of numerous service programs for the routine manipulation of astronomical images; Eddie for the painstaking reading of the manuscript and encouraging me to attend two inspiring overseas converences and to accept the opportunity of observing at the newly commissioned Mopra antenna.

This work was supported by grants from the Rhodes University Joint Research Council and the CSIR.

Contents

List of Figures

List of Tables

Chapter 1

Introduction

When I joined the Rhodes University Radio Astronomy group, two regions of the Rhodes/HartRAO 2326 MHz Survey had already been observed. My contribution to the survey was to observe the area from 05h00 RA to 18h00 RA between declinations $-63°$ and $-24°$. This area contains the Gum Nebula, which is the focus of this work.

The Gum Nebula is one of the most extended Hα emission regions in our Galaxy. On Sivan's 1974 Hα survey of the southern sky (see Fig. [1-1]) it has a radius of 18° and its centre is approximately at G258 − 2 (Chanot & Sivan, 1983). It has been modelled as an H II region, a Fossil Strömgren Sphere (FSS), an old SNR, an interstellar bubble and an old SNR combined with an outer H II shell. Thus a conclusive classification of it has not yet been made. It has also been suggested that this is not a single nebula, but a chance superposition on the sky of several different objects. A detailed motivation for such an interpretation was made by Srinivasan Sahu (1992), who traces out a separate object, the IRAS-Vela ring, on the Infrared Astronomical Satellite (IRAS) data (Beichmann et al., 1988; Wheelock et al., 1994).

A summary of the literature on this nebula is presented in Chapter 2. A detailed examination of the literature revealed that several aspects of the nebula had not been investigated previously.

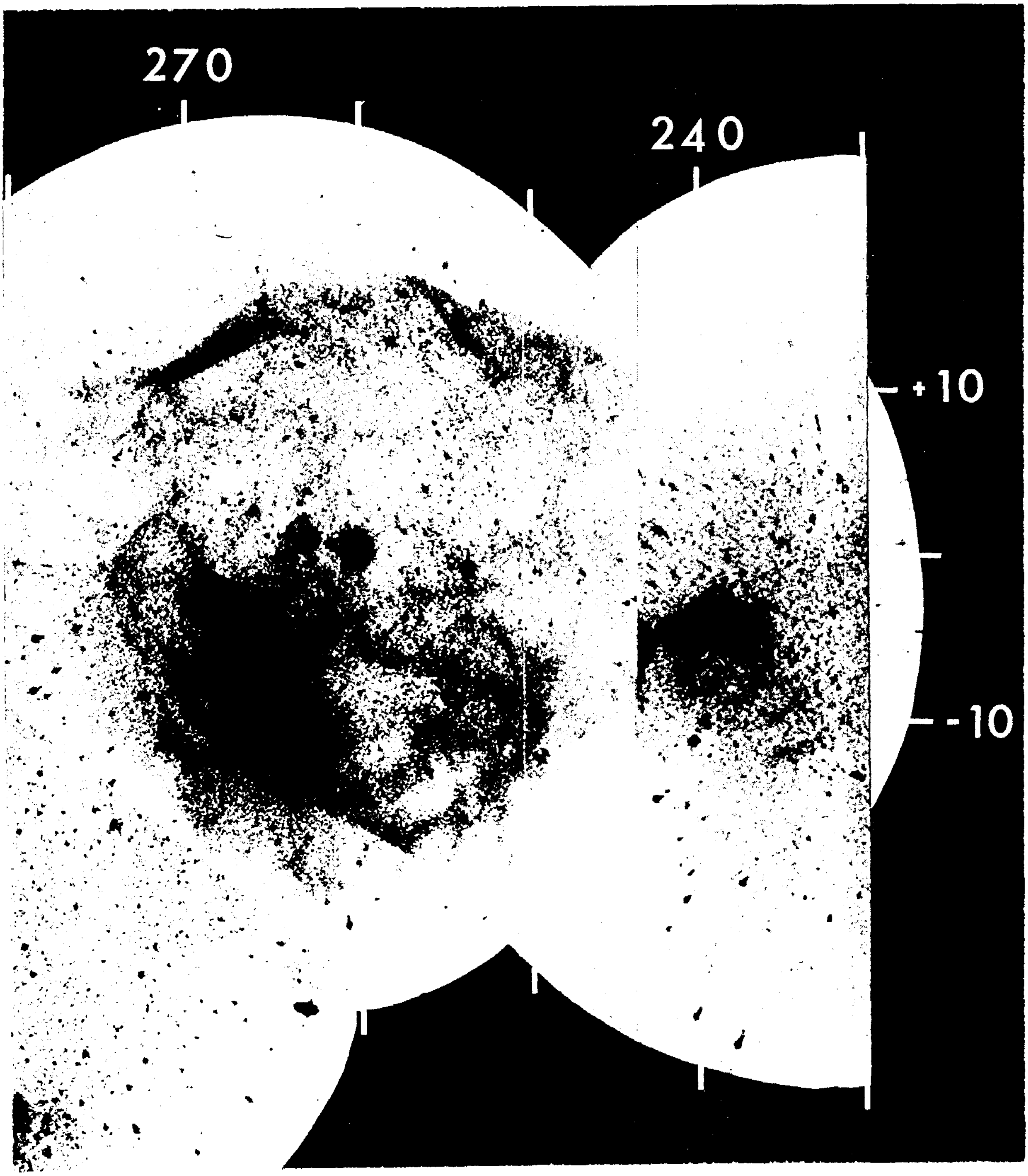

Figure [1-1]: An Hα photograph of the Gum Nebula from Sivan's very-wide-field photographic Hα survey of the whole Milky Way (Sivan, 1974).

Although recent reports are biased towards an SNR interpretation, these do not explain the observational evidence for H II region characteristics. Thus one aim of this work was to determine if there are both thermal parts (i.e. with H II region characteristics) and nonthermal parts (i.e. with SNR characteristics) to this nebula and their distribution across the nebula. Such an investigation would allow one to assess the validity of Reynolds' model (Reynolds, 1976b), the old SNR combined with an outer H II shell model, as well as that of the IRAS-Vela shell (Srinivasan Sahu, 1992). The determination of a spectral index[1] image of the nebula is essential to such an investigation. This requires a minimum of 2 radio surveys at moderately high frequencies, sufficiently separated in frequency to minimise the uncertainty in the result.

As this region of sky had already been observed at 408 MHz by Haslam et al. (1982), only one additional radio continuum map was required for the spectral index determination. I thus observed this region of sky at 2.3 GHz with the Hartebeesthoek Radio Astronomy Observatory (HartRAO) antenna. Sufficient background information on the observations made at 2.3 GHz is given in chapter 3. The resultant

[1]The flux density spectral index, α, of a source, is defined in the equation

$$F_\nu = K\nu^{-\alpha}$$

where F_ν is the flux density of the radio source, K is a proportionality constant and ν is the frequency. The brightness temperature spectral index, β, is defined in the equation

$$T_b(\nu) = M\nu^{-\beta} = M\nu^{-\alpha-2}$$

where $T_b(\nu)$ is the brightness temperature of the radio source at frequency ν and M is a proportionality constant. The brightness temperature spectral index is thus related to the flux density spectral index quite simply as:

$$\beta = \alpha + 2$$

A thermal source can appear optically thick at low frequencies, where it radiates as a thermal black body having $\alpha = -2$ and thus $\beta = 0$. The same source may be optically thin at higher frequencies, resulting in $\alpha = 0.1$ and $\beta = 2.1$.

The spectral index for synchrotoron radiation depends on the energy distribution of the relativistic electrons spiralling in the magnetic field. The most frequently determined spectral indices of SNRs, i.e galactic synchrotron sources, are in the range 0.3 to 0.7 for α, equivalent to a β ranging from 2.3 to 2.7.

A more detailed definition of the spectral index is given at the beginning of chapter 4.

continuum map is presented as a false colour image. The morphology of the Gum Nebula at this frequency is also discussed and compared to that at other radio frequencies, and the Hα image.

The determination of a spectral index image is a non-trivial matter; especially for an object as faint and extended as the Gum Nebula, which also straddles the galactic plane. No directly applicable method was found in the literature. Thus two different methods were investigated and adjusted to suit the purposes of this work. These methods are described in chapters 4 and 5. The method presented in chapter 4 relies on the isolation of the Gum Nebula from its background radiation. Chapter 5 reports on an investigation of the suitability of the TT-plot method (Turtle et al., 1962) for determining a spectral index image of a faint, extended source like the Gum Nebula. This led to the development of a method using such TT-plots. The spectral index images I obtained from these two methods are also presented and discussed in both these chapters. At the end of chapter 5 a comparison of the results from the two different methods is made.

One observational aspect of the nebula that prompted Srinivasan Sahu (1992) to postulate the existence of the IRAS-Vela ring, was that the part of the Gum Nebula at positive galactic latitudes appears infrared quiet. I show that this is not the case in chapter 6. Furthermore, I obtained an infrared radio flux ratio image of the Gum Nebula region from the 60 μm IRAS data and the 2.3 GHz radio continuum data. The infrared radio flux ratio (IRR) allows one to distinguish between thermal and non-thermal regions, thus providing independent information on the results of the spectral index work.

Four of the models, the ordinary H II region, the FSS model, the interstellar bubble and the combined SNR and outer H II shell (Reynolds' model) predict the existence of ionised gas at a temperature of $\approx$ 10 000 K. If present, one should be able to detect this gas in observations of hydrogen recombination lines at radio frequencies. The line parameters from such radio lines, together with the continuum antenna temperature at the observed position, provide one with enough data to determine the electron temperature, turbulent velocity and emission measure at the observed position. I made radio hydrogen recombination line observations with both the HartRAO and Mopra (part of the Australia Telescope) antennas. The results of these observations are reported in chapter 8.

Chapter 7 reports on the aspects of these two antennas relevant to spectral line observations. Some of the difficulties experienced with the analysis of the spectral line data are presented.

A puzzling aspect of the Gum Nebula is that it is not visible as a shell in observations of the 21cm line of hydrogen. This line is emitted by hydrogen gas at cold temperatures (10 K$< T <$1000 K), at which molecules are also able to exist. If such gas is associated with this nebula, it is expected to exist within a cold shell furthest from the centre. Furthermore, if the nebula is still expanding it may interact with the molecular material in the shell and cause a shock wave to propagate into it. Evidence for such an interaction can be seen in anomalously excited ground state hydroxyl (OH) lines with asymmetric line shapes. I made a search for OH lines with these characteristics. The results of this search are presented in chapter 9.

As there is no consensus on the expansion velocity of the Gum Nebula in the literature, another investigation of the expansion of the nebula was warranted. Sufficient data points for such an investigation were available from the observations of the 1667 MHz hydroxyl lines reported in chapter 9 and other molecular line data from the literature. It was assumed that the nebula is an expanding spherical shell. Three such models of increasing complexity are presented in chapter 10. Least-squares fitting of these models to the molecular line data shows that the nebula is still expanding.

The results of the investigations presented in this work are summarised in chapter 11.

Throughout this work galactic coordinates are used, unless otherwise indicated.

Chapter 2

The Gum Nebula: a summary of the literature

2.1 Introduction

The Gum Nebula was discovered by Gum in 1952 on Hα photographs of the southern Milky Way. In the vicinity of its centre are two bright O stars. One of these, the O9I star, is a member of the spectroscopic binary γ^2 Velorum (G262.8 − 7.7). Its twin is a wolf-rayet star (WC8). The other one is the O4f (Bohannan et al., 1990) star ζ Puppis (G256 − 4.7). Gum considered these two O stars as obvious energy sources for the nebula, thus classifying it as an H II region. In 1952 γ^2 Velorum was thought to be at a distance of 170 pc, which implied a diameter of 60 pc for the nebula (Maran, 1971). This is not unusually large for an H II region.

As techniques improved, Hα surveys became more sensitive to faint emission. This led to the discovery of numerous faint nebulosities in the vicinity of the Gum Nebula. In the absence of obvious energy sources for these, it was logical to consider them as part of the Gum Nebula. Gum himself had raised his estimate of the extent of the nebula to $60° \times 30°$ by 1956. Such large angular dimensions, together with a revised distance estimate of 0.5 kpc, implied physical dimensions bigger than those of any known H II region at that time.

Estimates of the energy input required to form and maintain such an enormous ionized region were made from its physical volume, the ionization energy of hydrogen and its electron density. The latter was determined from an assumed path length through the nebula and its emission measure, which was estimated to be 3000 cm^{-6} pc at its most intense regions (Brandt et al., 1971; Brandt, 1973). Such a high emission measure together with the large dimensions lead to estimates of the energy requirements for forming and maintaining this nebula of the order of 10^{51} erg. This was considered much larger than the energy output from the Lyman continuum photon flux of the two central O stars. Thus astronomers were no longer satisfied with the simple H II region model for the nebula.

As supernova explosions were known to release energies of this magnitude and deposit them over thousands of years in the surrounding interstellar matter, a classification as a supernova remnant should have been inevitable. However some of the then available observational evidence did not agree with such a classification. For example, the absorption depression in very low frequency ($<$ 150 MHz) radio surveys, at the position of the Gum Nebula is characteristic of thermal radiation (Alexander et al., 1971, 1973; Ellis, 1972; Cane, 1973; Beuermann, 1973). Also, although being wispy and having a hollow shell appearance in Hα, the nebula lacks the distinct and sharp filamentary structure seen in e.g. the Crab nebula and Vela XYZ supernova remnants.

Instead it was proposed that the nebula is a new kind of object, a Fossil Strömgren Sphere (e.g. NASA Symposium, 1973). This is an ionized region created almost instantaneously by a large impulse of radiation and now visible due to the long recombination time in its low-density medium. This impulse of ionizing radiation was attributed to the supernova event that created Vela XYZ, the supernova remnant that appears to be close to the centre of the nebula on the celestial sphere. Thus one may argue that Vela XYZ and its associated Vela pulsar (PSR 0833-45 (1950)), are similarly positioned along the line-of-sight, i.e. near the middle of the nebula as required by the FSS model.

Supporting evidence that Vela XYZ and its pulsar are approximately at the nebula's centre, comes from other pulsars situated in this region of sky, namely PSR 0736-40 (1950), PSR 0835-41 (1950) and PSR 0940-55 (1950). The dispersion measure determined from the pulses of these three pulsars is approximately twice that for the PSR 0833-45 (1950) (Maran, 1971). As the Gum Nebula is the only large extended ionized region in this part of sky, this could only be explained if we see the pulses from these three pulsars through twice the path length traversed by those from the Vela pulsar. Hence the Vela pulsar and thus the Vela SNR must be at the nebula's centre and the three pulsars must lie on or beyond the far edge of the nebula.

Four different ways in which the supernova event responsible for the Vela XYZ SNR could produce an energetic enough impulse of radiation to instantaneously ionize the Gum Nebula are presented in Brandt et al (1971), Alexander et al (1971), Morrison & Sartori (1969) and Kafatos & Morrison (1971). These and other models for the creation and maintenance of the Gum Nebula were discussed at a symposium entitled "The Gum Nebula and Related Problems" held at the NASA Goddard Space Flight Center in 1971 (NASA Symposium, 1973).

The different FSS models are not considered any further in this work, as subsequent, properly calibrated and improved observations have shown the nebula to be of more moderate size and much lower emission measure, reducing the energy estimate to a value just within the ionizing powers of the central stars (Chanot & Sivan, 1983). The main supporting evidence for the FSS models had been the excessively large physical dimensions and energy requirements.

2.1.1 Angular Dimensions

To date the angular size determinations of the Gum Nebula have been made using the following methods: from Hα photographs of the nebula, derived from a particular model of the nebula, derived from the measured near edge distance of the nebula and an assumed spherical geometry, or determined from the size of the low radio

Angular Size	Method	Near Edge /[pc]	Centre /[pc]	Radius /[pc]	Reference
20° diam.	Hα outline		170		Gum, 1952
40° × 30°	Hα outline				Gum, 1955
60° × 30°	Hα outline				Gum, 1956
90° diam.	line-of-sight path length	100	460	360	Brandt, 1971 Alexander et al., 1971 Maran et al., 1971 Brandt, 1973
35° diam.	Hα outline				Bok, 1971
36° diam.	derived from model	230	330	100	Gott & Ostriker, 1973
36° diam.	low-freq. radio abs.	210 to 250	310 to 350	100	Beuermann, 1973
75° × 40°	large diam. Hα photographs				Brandt et al., 1976
36° diam.	Sivan's (1974) Hα atlas	200	400±60	250	Reynolds, 1976a
36° diam., 50° diam. halo	10 Å passband Hα photographs				Chanot & Sivan, 1983
36° diam.	near edge distance from star reddening by shell dust	200	290	90	Franco, 1990

Table [2-1]: Size estimates of the Gum Nebula frequency absorption depression caused by the nebula. The results of these methods for the angular size of the nebula are listed in table [2-1].

The 36° diameter for the main body of the Gum Nebula determined by Chanot & Sivan (1983) is now generally accepted. Sivan's (1974) Hα-atlas of the Milky Way, which was used by Chanot & Sivan for their determination, was made with a filter of bandwidth 10 Å, narrower than that used by others. It thus rules out a significant contribution from the continuum emission of unresolved stars to the faint emission on the photographs. Fig. [2-1] shows a photograph showing the whole of the Gum Nebula. To confirm the determination from Sivan's Atlas, Chanot and Sivan (1983) obtained additional plates (also of 10 Å bandwidth) of the Gum nebula region.

Figure [2-1]: 60°-field, f/1 photograph showing the whole of the Gum Nebula taken through a 10 Å Hα filter (Chanot and Sivan, 1983).

Two longer exposure photographs (Fig. [2-2]) show unambiguously that there are faint extensions to the nebula beyond $| \, l \, | = 18°$. They also confirm that the main body of the nebula is a bright 36°-ringlike body, approximately centred on G258 − 2.

The extensions form a fainter, irregularly shaped envelope, that surrounds the main body, and gradually merges with the galactic Hα background. This faint envelope has a diameter of about 50° in galactic latitude.

The strong integrated continuum spectrum of unresolved stars and the diffuse galactic Hα background in the galactic plane make the determination of the longitudinal extent of the nebula difficult. Nevertheless Chanot & Sivan (1983) are confident that diffuse emission beyond $l = 282°$ is not part of the nebula (see Figs. [1-1] and [2-1]), but belongs to emission associated with the inner Sagittarius-Carina arm of the Galaxy. They choose the lower longitude boundary of the Gum Nebula to be at $l = 235°$.

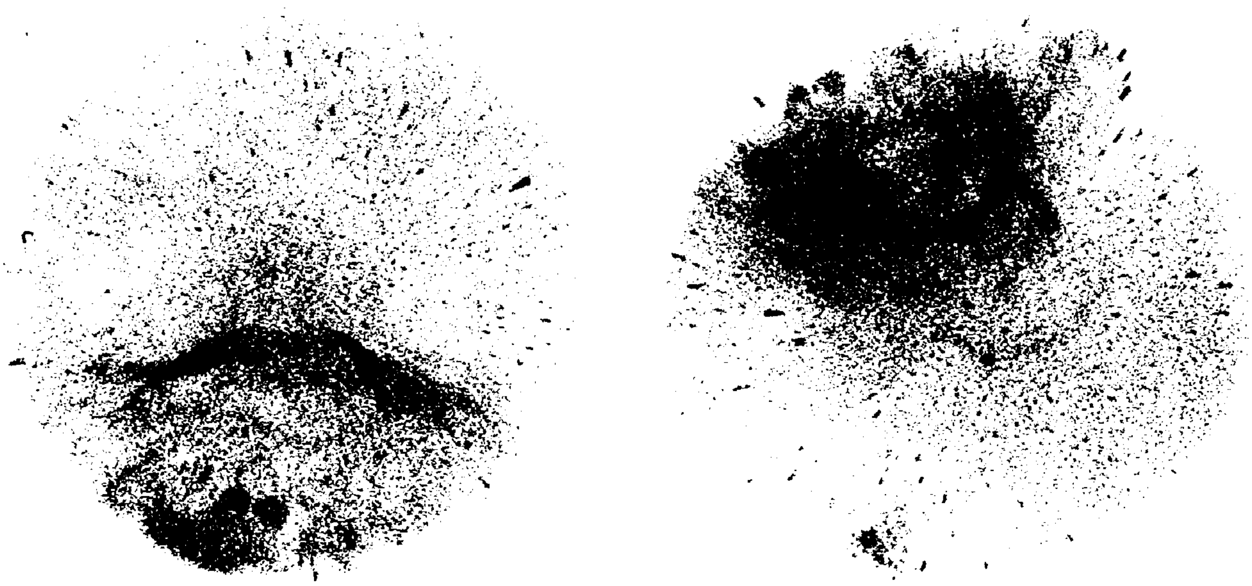

Figure [2-2]: 60°-field, f/1 photograph of the Northern (left) and Southern (right) part of the Gum Nebula taken through a 10 Å Hα filter (Chanot and Sivan, 1983). A comparison with the previous figure shows how these parts are related to the whole Gum Nebula.

The physical size, required for energy estimates, is easily obtained from simple geometric calculations provided that either the distance to the centre or the near edge of the nebula is known. Unfortunately the distance to the Gum Nebula is poorly determined.

2.1.2 Distance

name	position	distance/[kpc]	O B stars	Reference
Pup OB1	$G244.4 + 0.8$	2.51	7 O stars	Sky Catalogue 2000.0, 1985
Vela OB1	$G265.0 - 1.0$	1.4	5 O stars, 11 B stars	Sky Catalogue 2000.0, 1985
		1.9 ± 0.15	18 OB stars, 1 F0 supergiant	Humphreys, 1978
		2.1 ± 0.2		Slawson & Reed, 1988
Vela OB2	$G263.7 - 7.5$	see Tab. [2-5]	$\approx$ 9 B stars, γ^2 Vel	Brandt et al., 1971
Vela OB3	$G275.0 - 1.9$	5 to 6	6 B1 to B3 stars	Miller, 1972
		5.3 ± 0.3	5 O stars, 8 B stars	Slawson & Reed, 1988
Vela OB4	$G268.0 + 0.0$	1.0 ± 0.1	3 O stars, 14 B stars	Slawson & Reed, 1988

Table [2-2]: Distances to the OB associations in the Gum Nebula region.

reference	distance/[pc]
Gum, 1952	170
Gum, 1956	250
Whiteoak, 1961	200
Smith,L.F., 1968	460
Basckek, 1970	310
Hanbury Brown, 1970	350
Abt et al, 1976	480
Franco, 1990	350

Table [2-3]: Distances to γ^2 Velorum.

There is only one report of a direct measurement of the distance to the Gum Nebula. Franco (1990) reports a sharp change after 200 pc in the reddening of stars in two areas covering less than 3% of the Gum Nebula. Franco interprets this as being caused by the interstellar dust associated with the near edge of the Gum Nebula. With the accepted angular radius of 18° for the Gum Nebula this near edge distance predicts, from spherical geometric arguments, a distance of 290 pc $\pm$ 30 pc to its centre and a radius of 90 $\pm$ 10 pc.

The distance to the near edge may also be determined from the local hydrogen density and the hydrogen column density to stars that are positioned within the Gum Nebula. The neutral hydrogen column density along the line of sight to γ^2 Velorum and ζ Puppis as determined from the strength of the Lyman-alpha absorption line is ≈ 25 cm^{-3} pc (Jenkins, 1971). Values quoted for the local neutral hydrogen density range from about 0.1 to 0.4 cm^{-3} (Brandt et al., 1971), giving the range 250 to 60 pc for the near-edge distance. These correspond to distances to the centre of 360 pc and 90 pc respectively, assuming a spherical geometry and an angular radius of 18°.

reference	distance/[pc]
Brandt et al, 1971	450
Upton, 1973	450
Zombeck, 1980	700 to 800
Kudritzki et al., 1983,	450
Kudritzki & Hummer, 1990	450
Srivivasan Sahu (1992)	700
Lamers & Leitherer (1993)	400
Blaauw (1993)	700

Table [2-4]: Distances to ζ Puppis.

reference	distance/[pc]
Brandt et al., 1971	460
Eggen, 1980 & 1982	≈ 450
Slawson & Reed, 1988	650 ± 250
Srivivasan Sahu, 1992	450
Franco, 1990	350 pc

Table [2-5]: Distances to Vela OB2.

All other reported distance estimates are those of stars assumed to be associated with the formation of the nebula in some way. If one favours the old supernova remnant model for the Gum Nebula, the progenitor star is likely to have been a very massive star. Such a star would have been part of an OB association. Hence the distance to the remaining, slower evolving members of the association would be a good estimate of the distance to the nebula. This is also the case for the H II region model and interstellar bubble model, which rely on OB stars as energy sources.

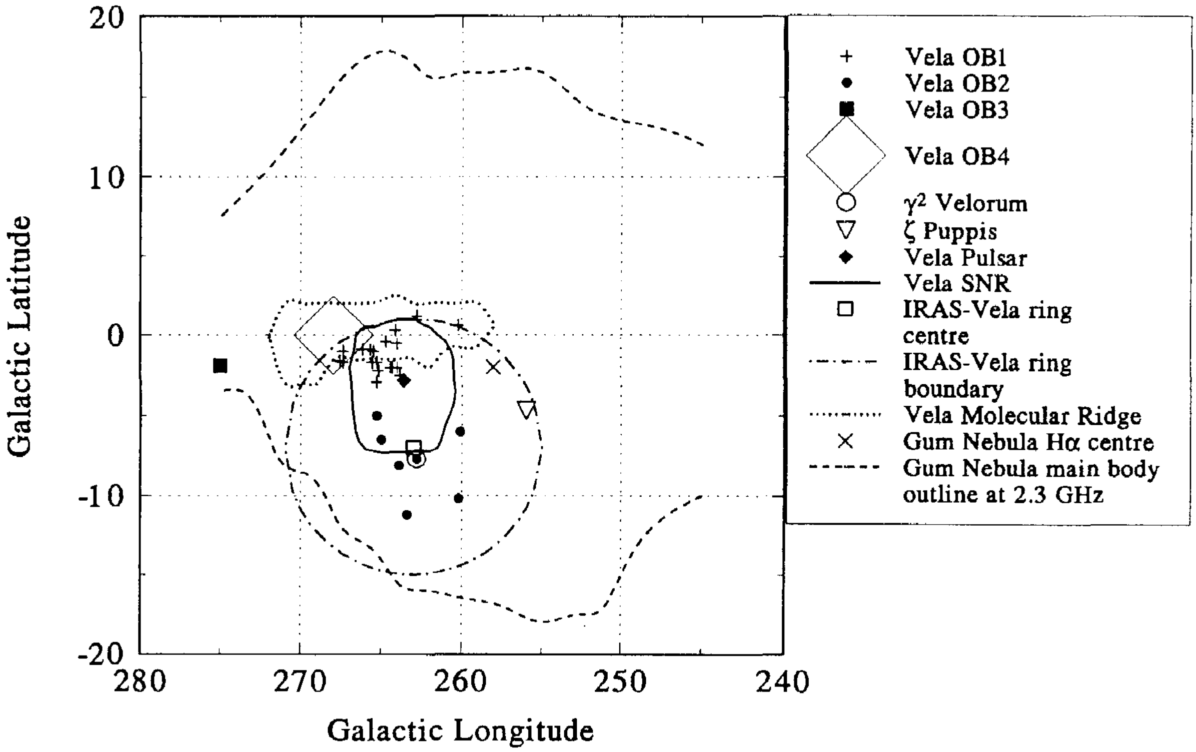

Figure [2-3]: A schematic diagram of the Gum Nebula region, showing the outline of the main body of the nebula at 2.3 GHz. The approximate outlines of the Vela XYZ SNR, Vela molecular ridge and IRAS-Vela shell are indicated. The positions of the four Vela OB associations, the two central O stars and the Vela pulsar can be identified from the legend.

Fig. [2-3] shows the known OB associations in this region of sky and the two central stars in relation to the Gum Nebula. Table [2-2] lists the distances to the known OB associations in Vela. Of these OB associations only Vela OB2 has been considered as a likely ionizing source for the Gum Nebula. Tables [2-3], [2-4] and [2-5] list the distances to γ^2 Velorum, ζ Puppis and the Vela OB2 association respectively.

The distances quoted for this association and the two central stars allow one to infer that the centre of the Gum Nebula could be positioned anywhere between 300 and 800 pc from us, using only post 1970 data and assuming a connection between the stars and the existence of the nebula.

The distance to the Gum Nebula is definitely less than 1 to 2 kpc from us. This is the distance to the Vela Molecular ridge (Murphy & May, 1991), an extensive complex of molecular clouds whose approximate outline is shown in Fig. [2-3]. As there is no obvious region of absorption, mimicking the extent and shape of the Vela Molecular ridge, on Hα photographs of this region, the Gum Nebula must be situated in front of it.

Without any agreement on the distance to the Gum Nebula no good estimate of its physical dimension can be made.

2.1.3 Emission Measure

Even without an improved distance estimate, the energy estimate is significantly reduced by the emission measures determined from calibrated Hα intensities by Reynolds (1976a) and Chanot & Sivan (1983). These are the only ones that have determined calibrated, as opposed to estimated, emission measures for the Gum Nebula. The values they report range from 6 cm^{-6} pc in the faintest regions to 300 cm^{-6} pc in the brightest regions. These are an order of magnitude smaller than those initially used for energy estimates.

2.2 Observational parameters of the models

The reported observable evidence does not rule out classifications of the nebula as an old supernova remnant (SNR), an interstellar bubble produced by the stellar wind from the central stars (Castor et al., 1975; Weaver et al., 1977; Wallerstein et al., 1980; Bruhweiler et al., 1983) or a combination of million year old SNR and

H II region (Reynolds, 1976a,b). Investigations undertaken since the symposium have been directed at eliminating some of the less likely classifications of the Gum Nebula. Several observable physical parameters with their corresponding range of values as for an H II region, an evolved supernova remnant and an interstellar bubble are listed in table [2-6]. If no predicted or observed values are available from the literature, this is indicated by a question mark. In some of these cases an educated guess has been made at a plausible value for this characteristic. Such guesses are followed by a question mark.

	H II region	Evolved Supernova Remnant	Interstellar Bubble
electron temperature	5000 to 10 000 K	$\approx 10^{5.5}$ K	$\approx 10^{5.5}$ K
ionized species	as for photoionized gas	as for strongly shocked gas	as for mildly shocked gas
[SII]/Hα	< 0.1	> 0.7	?
expansion velocity	≈ 0 km/s	≈ 20 km/s	≈ 20 km/s
infrared to radio flux ratio	> 500	40 to 500	as for H II region ?
polarization of radio emission	random	linear	?
brightness temperature spectral index	2.1	≈ 2.3 to ≈ 2.8	2.1 ?
Hydrogen recombination line	yes	no ?	yes ?
X-rays	none	yes	yes

Table [2-6]: Observational parameters of H II regions, supernova remnants and interstellar bubbles.

The observable parameters of the combined old SNR and H II region model of Reynolds are expected to have values that are either those of an H II region or an SNR or weighted averages of both. In order to assess the agreement between observed parameters and those predicted by Reynolds' model, a more detailed description of this model is given below.

As noted by Cleary (1977), it is very difficult to distinguish observationally between bubbles caused by supernovae (i.e. SNRs) and those caused by stellar winds (interstellar bubbles). Thus the similarities and differences between these two bubble types are also presented below. From the morphology of the interstellar bubble given there, it is seen that it has marked similarities to Reynolds' model.

2.2.1 Reynolds' model of the Gum Nebula

Reynolds (1976a) had traced out similar dimensions for the Gum Nebula to those of Chanot & Sivan (1983) on Sivan's 1974 Hα survey. He obtained, from Hα and N[II] spectral line observations, electron temperatures corresponding to those of H II regions, yet an expansion velocity ($\approx$ 20 km/s) corresponding to that of an old SNR. Thus he proposed a model for the Gum Nebula that attempts to marry this contradictory observational evidence.

The model is that of a million year old supernova remnant whose outer shell is being heated and ionized by γ^2 Velorum and ζ Puppis located in the hot, very low-density interior region of the remnant. This outer shell thus has the same properties as the ionized gas in an H II region. The material interior to the shell is predicted to be very hot ($\approx 10^6 K$) and to have a very low density ($\approx$ 0.003 cm^{-3}). A scale diagram of this model is shown in Fig. [2-4].

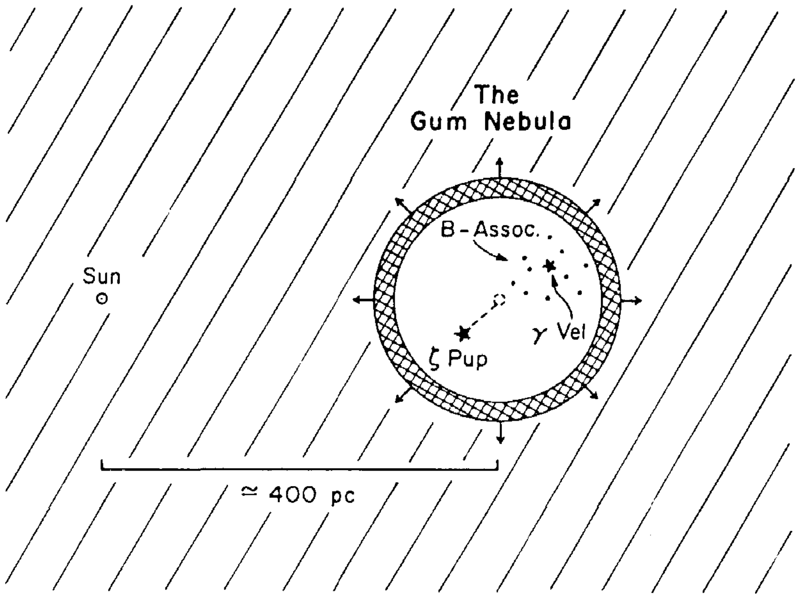

Figure [2-4]: A scale diagram of Reynolds' model (1976b) of one million year old SNR combined with an expanding shell structure. The suggested positions of ζ Puppis, γ^2 Velorum and the Vela OB2 association are also shown.

Others remained sceptical of this model. Those doubting the interpretation of Reynolds suggested that this nebula is an interstellar bubble produced by the stellar wind from the central stars (Wallerstein et al., 1980; Bruhweiler et al., 1983). This model was developed by Castor et al. (1975) and Weaver et al. (1977). They gave the Gum Nebula as a plausible example of such a bubble.

2.2.2 Interstellar bubble model

The evolution of such a wind-driven circumstellar shell shows marked similarities to that of a supernova shell (Castor et al., 1975). Models predict essentially the same four phases that describe the evolution of an SNR. This similarity extends to both SNR and interstellar bubble spending most of their lifetime in the second phase, that of adiabatic expansion. In this phase a bubble has four distinct zones. Closest to the star is the hypersonic wind. Progressing outward from the star there follows a region of shocked stellar wind, then a shell of shocked interstellar gas. Finally surrounding the whole is the ambient interstellar gas (see Fig. [2-5]).

The interior of such a bubble has, typically, a temperature of 10^6K and atomic particle density of 0.01 cm^{-3}. This hot, low-density region, containing the shocked stellar wind, occupies most of the volume of the bubble and should be a soft X-ray source. At the interface of the shocked stellar wind and the shocked interstellar gas there is a transition region at a temperature of about 3×10^5 K. The model predicts a significant amount of O VI in this region. The shocked interstellar gas shell expands as the bubble evolves and may be fully ionized by the central star, or it may have an outer layer of H I and H_2 if the ionization front is trapped in the shell.

Bruhweiler at al. (1983) note that an interstellar bubble interpretation of the Gum Nebula is plausible in terms of the available data. However, as emphasized by Chanot & Sivan (1983), it is impossible to determine whether the shell structure of the Nebula is driven by stellar winds or supernova blasts.

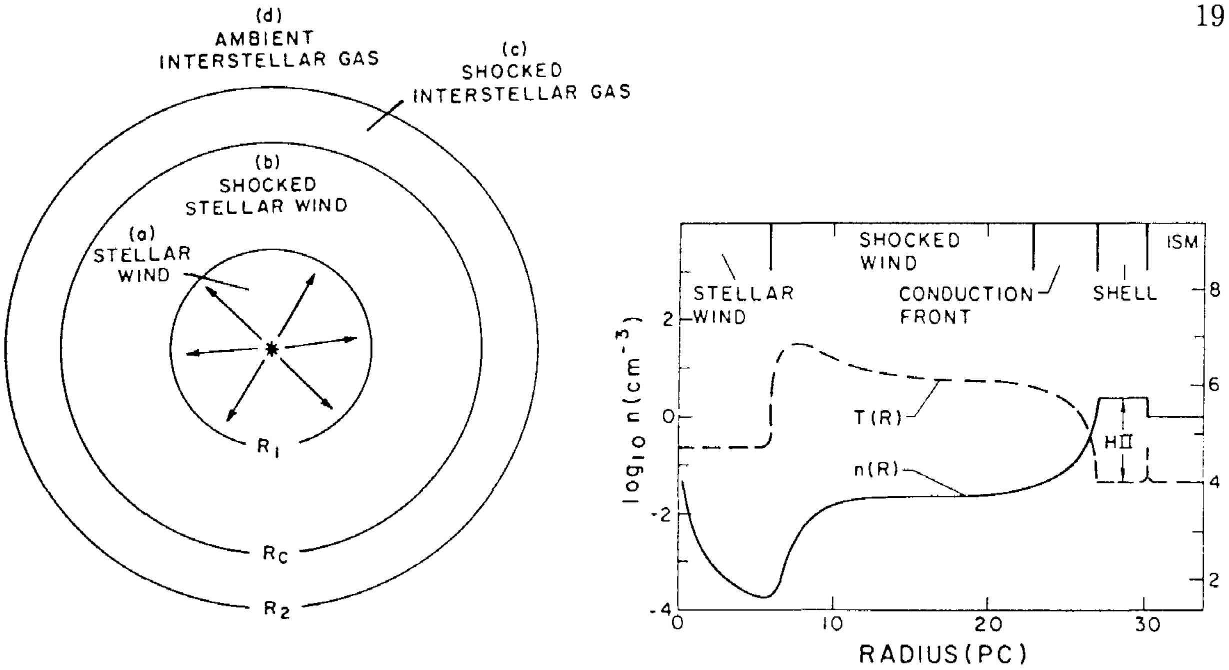

Figure [2-5]: A schematic of the regions in an interstellar bubble is shown on the left. On the right is a radial cross section of temperature and density in such a bubble. (Weaver et al., 1977)

2.3 Observed Physical Parameters

In the following sections the different observed parameters from the literature are presented and their correspondence to the proposed models is discussed.

2.3.1 Lyman continuum photon flux from central stars

Both Reynolds (1976a) and Chanot & Sivan (1983) also determined whether the central stars can account for the Gum Nebula without making use of the poorly determined distance. Their calibrated Hα intensities allow them to estimate the number of recombinations per second in the Gum Nebula. In an H II region model this should match the Lyman continuum photon flux from the star(s) responsible for ionizing the nebula. Even according to the reduced value obtained by Bohannan et al. (1990) of the Lyman photon flux from ζ Puppis, this star alone could almost account for the required flux.

It has been suggested that the Vela OB2 association, which includes γ^2 Velorum as a member star, is responsible for the Gum Nebula. The Lyman photon flux from the O9 star of the γ^2 Velorum binary is only about one tenth that of ζ Puppis (Panagia, 1973). The star of earliest spectral type other than the O9 star of the γ^2 Velorum binary in the Vela OB2 association is a B0 star (Srivivasan Sahu, 1992). The latter produces only about one tenth the Lyman photon flux of the O9 star of the γ^2 Velorum binary (Panagia,1973). The Lyman photon flux from the other B stars of this association (about 9 in total), all of which are of spectral type between B1 and B3 inclusive, is insignificant in comparison to that of the B0 star. Thus the Vela OB2 association cannot be the primary ionization source of the Gum Nebula, as it produces at not even two tenths of the Lyman photon flux from ζ Puppis.

One may conclude that ζ Puppis could possibly account for the nebula on its own, but that it is more likely, in terms of Lyman photon flux requirements, that both γ^2 Velorum and ζ Puppis are responsible. Nevertheless the simple H II region model never totally regained favour, because of the contradictory observational evidence presented below.

2.3.2 Temperature

There are various different methods of determining the temperature of a nebula. As these methods in general sample information from different physical processes they do not necessarily result in temperatures of the same particles in the gas or the same region in the nebula and therefore may quite legitimately be different. Reported temperatures in the literature range from 300 K to 10^5 K (see tables [2-7] and [2-8]). Thus these do not discriminate between the models, but do favour a model that predicts both hot and more intermediate temperatures.

Some of the temperature determinations rely on an assumed electron density. Where this is the case, the electron density has also been tabulated. No further attempt

τ	EM/[$cm^{-6}pc$]	T_e/[K]	Reference
$\leq 3 \pm 1$ (4 MHz)	1300	$\geq 5.7 \pm (1.8, 1.0) \times 10^4$	Alexander et al., 1971
	900	$\geq 4.5 \times 10^4$	
	25	$\geq 4 \times 10^3$	
$\leq 3 \pm 1$ (4 MHz)	$\geq$600	$\geq 4 \pm 1 \times 10^4$	Alexander, 1973
4 ∓ 1 (5 MHz)	600	$3.9 \mp 0.7 \times 10^4$	Ellis, 1972
1.4 (9 MHz)	3000	5.3×10^4	Cane, 1973
	600	2.9×10^4	
≤ 2.5 (10 MHz)	≤ 300	< 8500K (+4500, -3500)	Beuermann, 1973
	≥ 20	> 300	

Table [2-7]: Electron temperature determinations from the emission measure, EM, and optical depth, τ, at low radio frequencies.

was made to compile a list of reported electron densities as these are often entirely dependent on the assumed model in their derivation.

2.3.3 Ionization balance

Different ionization mechanisms give rise to different ionization balances and hence different line intensity ratios. A ratio particularly sensitive to the ionization mechanism is that of [S II] 6717+6731/Hα. The average value of the [S II] 6717+6731 to Hα ratio of 0.35$\pm$ 0.11 obtained by Chanot & Sivan (1983) is consistent with an origin in shock-heated gas. It does not, however, discriminate between shocks due to supersonic winds or supernova explosions (Chanot & Sivan, 1983). They point out that the typical ring structure of the Gum Nebula revealed by their narrow bandwidth Hα photographs together with the moderately high ionization, average [S II]/Hα ratio of 0.35, and possible ionization by γ^2 Velorum and ζ Puppis are all characteristics very similar to those of the largest extragalactic H II regions. These form a category intermediate between classical H II regions and typical supernova remnants.

method	$n_e/[cm^{-3}]$	$T_e/[K]$	Reference
Mg &Fe abs. lines	<2	10^4	Grewing et al., 1973
Mg ion ratios	≈ 0.15	either $7000 < T_e < 10000$ or 300	de Boer at al., 1973
Mg ion ratios/balance		$300 < T_e < 7000$	Burton et al., 1974
fine-structure excitation of CII and NII	$\geq 10^2$	200 in dense cloudlets	Burton et al., 1974
Hα & NII(6584) emission line widths		11800± 5200 11600 ± 4500	Hippelein and Weinberger, 1975
Hα & [NII] line widths		11300	Reynolds, 1976a
optical and radio measurements	0.32 0.26	5940 7260	Vidal,J.-L., 1979
N V and O VI line widths towards γ^2 Vel		$> 10^5$ K	Morton & Bhavsar, 1979
absence of N V and presence of O VI towards ζ Puppis		3.1×10^5 K to 6.5×10^5 K	Morton, 1978
O VI towards γ^2 Vel		2.5×10^5 K $\leq$ T $\leq 6.3 \times 10^5$ K	Bruhweiler et al., 1979
Si IV observable C IV not, towards γ^2 Vel		35000 K < T < 63000 K	Bruhweiler et al., 1979
NII fine-structure excitation in ram-pressure confined supersonically moving clouds		$< 10^4$	Wallerstein et al., 1980
[NII]/Hα emission lines		8000	Chanot & Sivan., 1983

Table [2-8]: Electron temperature and density determinations from optical and ultra-violet line observations.

UV spectra of both ζ Puppis (Morton, 1978) and γ^2 Velorum (Bruhweiler et al., 1979; Morton & Bhavsar,1979; Burton et al., 1974) show interstellar absorption lines of ionized species many of which are consistent with those observed in standard H II regions. However, both ζ Puppis (Morton, 1978) and γ^2 Velorum (Bruhweiler et al., 1979) also have Si IV, C IV and O VI interstellar absorption lines in their UV spectra. These are characteristic of temperatures of the order of 10^5 K. Bruhweiler et al. note that the observed ion species characteristic of an H II region combined with the high temperatures required to explain the presence of O VI in the UV absorption spectra, could be explained by a low-density, high-temperature region interior to a narrow H II region shell. Such a morphology is in agreement with a supernova remnant plus H II region model for the Gum Nebula as proposed by Reynolds (1976b) as well as an interstellar bubble (Castor, McCray and Weaver, 1975).

Only a more subtle difference in the observed versus the predicted parameters for an interstellar bubble by Castor et al. (1975) and Weaver et al. (1977) results in evidence against an interstellar bubble classification. Morton (1978) notes that details of the observed UV spectrum of ζ Puppis do not agree with the predictions of the model of Castor et al. (1975). Similarly for γ^2 Velorum, Bruhweiler et al. (1979) state that the observed Si IV to O VI ratio disagrees with predictions by Weaver et al. (1977).

2.3.4 X-rays

The HEAO-1 satellite surveyed the X-ray emission from the whole sky. From single-temperature, Raymond-Smith model fitting to the observed soft X-ray spectra from the Gum Nebula, Leahy et al. (1992) determined a temperature $\approx 6.0 \times 10^5$ K for this X-ray emitting gas. The extent of this reported X-ray emission is more restricted than that of the Hα emission from the Gum Nebula and does not fit into the morphology of any of the model predictions. It is thus not particularly useful for any model classification of the nebula, other than counting against a simple H II region interpretation.

Better X-ray observations have been made with the ROSAT X-ray telescope, but have not yet been published. In a paper on the X-ray emission of the Vela XYZ SNR, Aschenbach et al. (1995), report the presence of Vela supernova ejecta still visible at X-ray wavelengths outside the boundary of the Vela XYZ SNR. These ejecta have associated Mach cones with low Mach numbers. These low Mach numbers imply that the Vela supernova exploded in a bubble of hot tenuous gas, interpreted to be the interior of the Gum Nebula. From their observations of the Mach cones of the Vela SNR ejecta Aschenbach et al. deduced a temperature, for this interior of the Gum Nebula as high as that expected for old SNRs.

The faint X-ray medium reported by Aschenbach et al. as surrounding the Vela XYZ SNR has a diameter of only 20°, thus not matching the 36° diameter of the Gum Nebula. Aschenbach et al. state that the centre of this 20° diameter region is within the boundary of the Vela SNR, but give no further details.

As most SNRs are limb-brightened at X-ray wavelengths, one may be tempted to interpret this position of the X-ray gas within the nebula as supporting the interstellar bubble model. However, there is a class of SNR that exhibits centrally bright X-ray emission. This unusual morphology is attributed to the effects of the expansion of the SNR into very non-homogeneous interstellar matter (Long et al., 1991; White & Long, 1991; Leahy & Aschenbach, 1995; Leahy & Aschenbach, 1996). Thus no definite conclusion can be drawn on the basis of the position of this X-ray emission within the nebula.

While the reported detection of X-rays in the Gum Nebula point to either an old SNR or interstellar bubble interpretation, the reported temperatures and ionization balance favour a model incorporating an H II region. An interstellar bubble does this as also the combined old SNR and H II region model of Reynolds (1976b). Both of these predict an expansion of the H II shell of ≈ 20 km/s, which Reynolds claims to have observed.

2.3.5 Kinematics of the Gum Nebula

Hippelein and Weinberger(1975) deduce from velocity measurements in Hα at positions of small scale clouds in the Gum Nebula that the evidence for an expansion of the nebula as a whole is poor. Another study of the interstellar gas in the Gum Nebula was made by Wallerstein et al. (1980), who also reports no evidence for expansion. These studies thus contradict the 20 km/s reported by Reynolds.

Some observational evidence that the Gum Nebula certainly underwent significant expansion causing compression of the surrounding interstellar material in the past, comes from the presence of young stars, such as T-Tauri stars (Petterson, 1987), and associated Herbig-Haro objects (Dopita, 1978; Graham, 1986 and others) as well as cometary globules in the Gum Nebula.

2.3.6 Cometary Globules

Cometary globules (CGs) were first discovered in the Gum Nebula in 1976 (Sandqvist, 1976; Hawarden & Brandt, 1976). Reipurth (1983) describes the common features of the CGs in the Gum Nebula as follows. They all have very dense heads that completely obscure the background stars on the available Schmidt plates. On the side pointing towards the center of the Gum Nebula, the heads are well-defined with very sharp edges, exhibiting narrow bright rims. On the opposite side protrudes a slightly luminous tail, in some cases as short as a few arc min, and in one case longer than 1°. In several cases it is seen that the smaller globules are aligned one after the other in a direction away from the center of the Gum Nebula.

There have been numerous attempts at explaining the manner in which these CGs could have formed. Thus Hawarden & Brandt (1976) argue that the non-filamentary appearance of the heads of the CGs counts against an SNR classification of the Gum Nebula as the highly energetic nature of the formation of SNRs leads to more filamentary structures, as generally observed in SNRs. A different view is presented by Brand et al. (1983). They point out a convincing similarity between CGs and late stages of computer simulations of the transformation of an initially spherical cloud hit by a blast-wave (Woodward, 1976 & 1979). Thus Brand et al. conclude that CGs are the late stages of shocked clouds. Hence they derive an age of about 3 M yrs for the Gum Nebula as a cometary globule forming SNR. Srivivasan Sahu and co-workers (Sahu et al., 1988), in a study of the observed properties of CG22, also favour the supernova blast-wave interpretation for the formation of this CG. This was however later retracted by Srivivasan Sahu (1992), who now argues that they were formed by stellar winds and ionization pressure as present in an interstellar bubble. Thus there is no consensus on this matter. The formation of CGs has equally plausible explanations in an SNR and an interstellar bubble scenario.

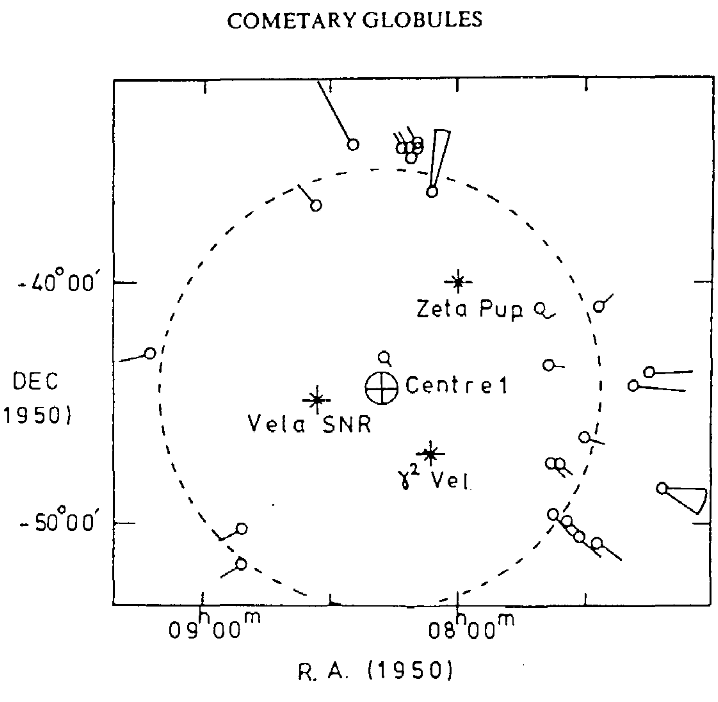

Figure [2-6]: The distribution of CGs, showing their tail orientations in an equatorial coordinate frame, according to Zealey et al. (1983). Centre 1 is the position, determined by Zealey et al., away from which most of the tails point. The dotted circle has a radius of 9° about centre 1.

Although CGs have been observed elsewhere, the large majority of known CGs are in the Gum Nebula. The interesting feature of the Gum Nebula CGs as a group is their orientation and positioning in the nebula. The orientation of the CGs with their heads pointing to the centre of the nebula was already evident with the discovery of the first 10 CGs (Hawarden & Brand, 1976). Later additions to their number (Sandqvist, 1976; Zealey et al., 1983, Reipurth, 1983) confirmed this trend (see Fig. [2-6]). It is thus generally accepted that the CGs are definitely associated with this nebula.

Zealey et al. (1983), Reipurth (1983) and Sridharan (1992) have all determined the centre towards which the CG heads are pointing. Reipurth situates it in the middle of the triangle outlined by ζ Puppis, γ Velorum and the Vela pulsar, also pointing out that the CGs have a preference for the western part of the nebula.

A more precise determination of the centre by Zealey et al. shows that most projected tails pass through his centre 1 at G261.2−5.2 . The remaining six are associated with his centre 2 at $G260.3 - 10.6$. Zealey et al. also fitted a circle of radius $9.5° \pm 1.3°$ to the CG positions, the geometric centre of which is close to centre 1. Sridharan, applying a similar procedure, arrives at a centre at $G260.2 - 4.0$. Although none of these centres agree with the Hα emission centre (Chanot & Sivan, 1983) of the Gum Nebula, $G258 - 2$, the discrepancy is not very significant for most of them, given the large angular size of the nebula. A more serious discrepancy exists for the radius, with the values quoted above being only half the 18° radius of the main body of the Gum Nebula in Hα.

Zealey et al. (1983) have shown that there is no simple correlation between angular tail length and angular distance from the centre. This is contrary to what one would expect from the effects of projection on the observed tail lengths for an assumed spherical shell distribution of constant intrinsic tail length. If one is not prepared to forego the spherical distribution model of the CGs, one must conclude that the intrinsic tail length of the CGs varies.

There is only 1 CG within 6° of the derived centre of the CG distribution (Zealey et al., 1983). As models of a uniform distribution over the shell predict that between 8 and 12 CGs should be projected within 6° of the centre, the lack of observed CGs close to the centre indicates that we are probably seeing a clumpy distribution of CGs.

2.3.7 Kinematics of the CGs

As the CGs are considered part of the Gum Nebula, any evidence for an expansion of the CGs from a common centre would be shared by this nebula.

Zealey et al. (1983) claim that the measured line velocities of formaldehyde absorption lines of the CGs are mostly due to the larger scale effects of the kinematics of the local spiral structure, but that the velocity residuals can only be explained by an expanding shell. The shell would have to be larger than 11° and have an expansion velocity of up to 5 km/s.

Sridharan (1992) detected CO in all but two CGs, giving him far more data points for a kinematical study than used in the other study (Zealey et al., 1983). Sridharan reports agreement of the observed CO velocities with a shell of $\approx 9.5°$ radius expanding at 12 km/s, if it is assumed that the CGs are distributed over a volume within the shell rather than on the surface of a shell.

An expansion velocity of 12 km/s implies an expansion age of about 6 M yrs for the Gum Nebula if one assumes that this nebula shares the expansion velocity of the CGs. The velocity gradients along the tails of the CGs measured by Sridharan (1992) may be interpreted as the cause of the tail stretching and hence of the tails' lengths. This suggests a stretching age of 3 M yr for the tails.

Hence there is no consensus over an expansion of the material, here in the form of CGs, associated with the Gum Nebula. Thus none of the models may be eliminated on the basis of an observed expansion velocity of the nebula.

Other material that should share to some extent any expansion present in the nebula is the neutral ISM which an expanding nebula has to push out of its way. This neutral material may be observed in the 21 cm line of neutral hydrogen which is in the radio regime.

2.3.8 H I bubble

Neither Cleary (1977) nor Kerr et al. (1986) are able to identify an HI bubble corresponding to the Gum Nebula in their respective neutral hydrogen surveys. More recently Dubner et al. (1992) investigated the neutral hydrogen distribution in the Gum Nebula region using 21 cm H I line data from the survey of Strong et al. (1982) in addition to data obtained by themselves. They also do not see evidence for an expanding neutral hydrogen shell coincident with the Gum Nebula.

A possible explanation for the lack of a neutral hydrogen shell corresponding to the Gum Nebula is given by the results of Bohlin et al. (1978). They report that the observed average hydrogen density in the Gum Nebula is more than a factor of 10 lower than the average density found for all objects surveyed, excluding the high density Scorpius-Ophiucus region.

2.3.9 Radio emission and polarization

Of all the proposed models only an SNR is expected to exhibit polarized radio emission.

Duncan et al. (1996) have observed part of the Gum Nebula close to the galactic plane at 2.4 GHz with a resolution of about 10 arcminutes, including polarization measurements. They report that the radio emission from the Gum Nebula contains a significant polarized component. However, the observed total power flux is higher than the polarized component. To account for this they propose that the Gum Nebula contains both thermal and non-thermal radio emission. This points to an old SNR (perhaps with H II shell as in Reynolds' model) classification for this nebula, further supported by the high fractional polarizations and low depolarizations observed. These are considered characteristics of old SNRs.

This is the most convincing argument published to date for a particular classification. Unfortunately these observations only cover a small section of the nebula.

Two discerning observational properties not reported on in the literature are the radio brightness temperature spectral index and the infrared to radio flux density ratio. Both of these require radio continuum observations for their derivation. A minimum of two radio maps at high frequency are required to determine the radio brightness temperature spectral index. The determination of the infrared to radio flux density ratio requires a radio map at high frequency and an infrared continuum map.

One such radio continuum map, the 408 MHz All-sky Continuum Survey (Haslam et al., 1982) with a resolution of 0.85° was in existence when this work was started. The Gum Nebula is clearly identifiable in this survey, as shown by the overlay of a contour map of this 408 MHz radio data on the Hα emission of the Gum Nebula according to Sivan (1974) (see Fig. [2-7]). In the outer regions of the nebula the radio emission structures correlate well with those shown in the optical emission.

During the eighties the infrared data from the IRAS (Beichman et al., 1988; Wheelock et al., 1994) became available. This provided information in a wavelength regime at which little was known about SNRs, while the very infrared bright compact H II regions had already been studied at this wavelength with rocket based instruments. This opened up a different perspective on the Gum Nebula. Inspection of the Gum Nebula region on the IRAS Sky Flux Atlas resulted in the identification of a separate object, the IRAS-Vela ring, by Srinivasan Sahu (1992) and Srinivasan Sahu & Sahu (1993).

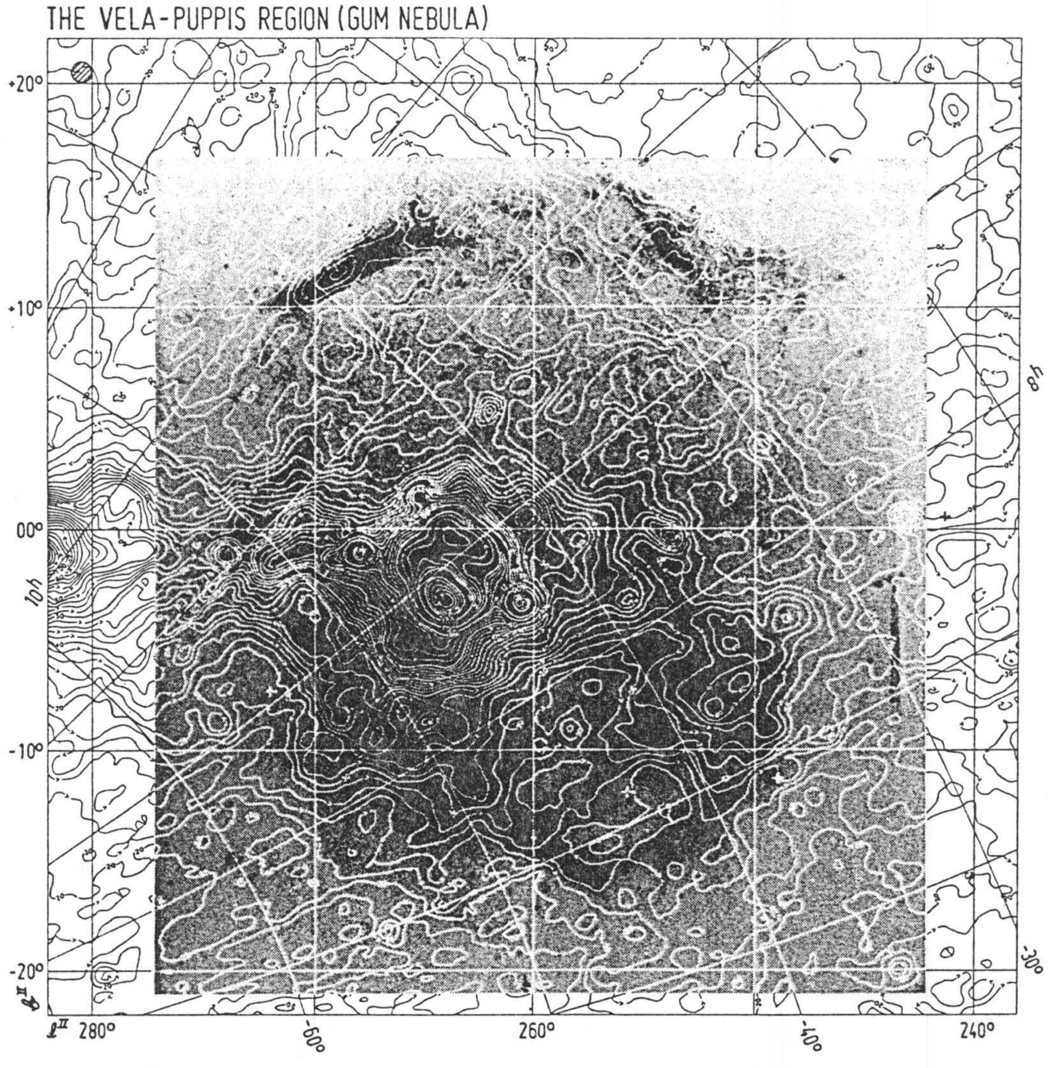

Figure [2-7]: Overlay of the 408 MHz All-sky Continuum Survey of Haslam et al. on Sivan's Hα print of the Gum Nebula (Haslam et al., 1981).

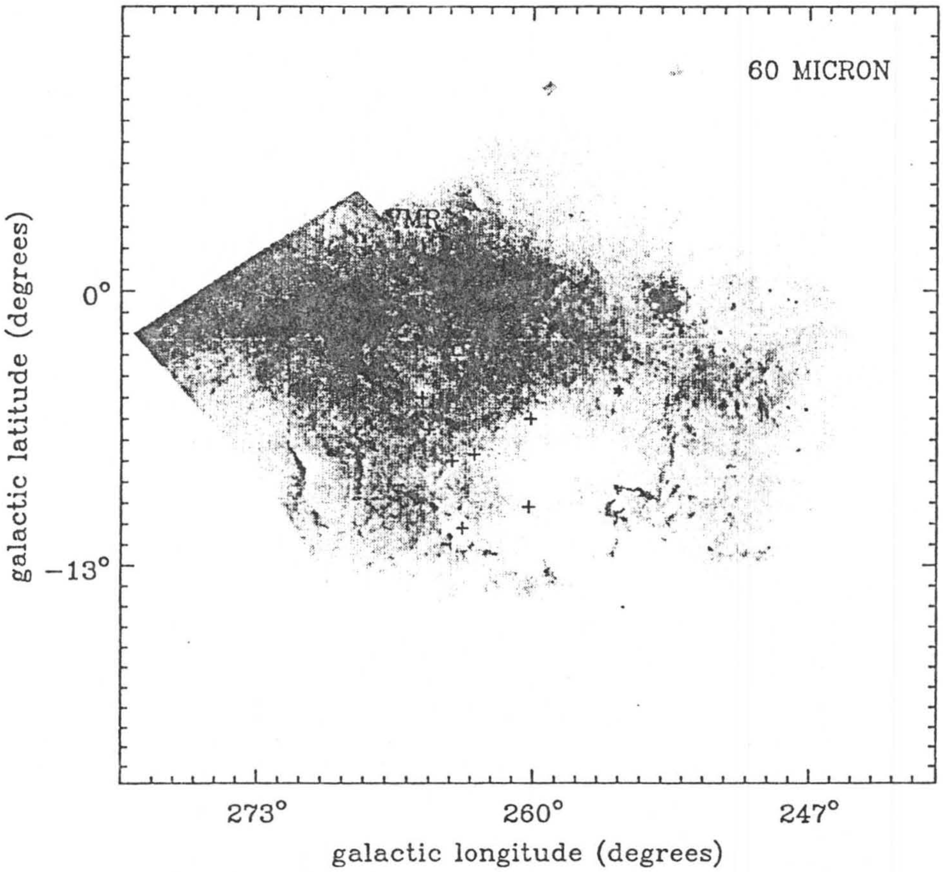

Figure [2-8]: 60 μm IRAS map according to Srinivasan Sahu (1992).

2.4 The IRAS-Vela ring

Srinivasan Sahu & Sahu (1993) interpret the bright region extending from $l = 259°$ to $271°$ and $b = -12°$ to $0°$ on the IRAS Super Sky Flux Atlas images as a source separate from the Gum Nebula. They call this source the IRAS-Vela ring. In the earlier report of Srivivasan Sahu (1992) it is considered to have a radius of about 8° with its centre at $l = 263°$ and $b = -7°$ (see Fig. [2-8] for the 60 μm IRAS map and Fig. [2-3] for a schematic of the region). The latter dimensions do not agree with those given in Srinivasan Sahu & Sahu (1993).

Srivivasan Sahu & Sahu (1993) claim that the IRAS-Vela ring is maintained by the OB association Vela OB2. The latter has also been claimed as energy source for the Gum Nebula, when this nebula is interpreted as an H II region or a mixture of H II region and old SNR.

Srivivasan Sahu & Sahu report that in 18 positions at which Hα λ6563, [NII] λ6548 λ6584 and [OIII] λ5007 emission line spectra were obtained, only positions within the outlined IRAS-Vela shell show double components in [NII]. These double component lines are interpreted as an expansion of the IRAS-Vela ring at 10 ± 2 km/s. They further argue that this corresponds to the expansion velocity determined by Sridharan (1992) for the CGs and that therefore the CGs must be part of the IRAS-Vela ring. This argument needs to be considerably strengthened by further observational evidence, as many of the CGs are positioned far outside the proposed IRAS-Vela ring (see Fig. [2-8]).

Furthermore, Reynolds (1976a) has observed double component spectra of the same species at positions within the Gum Nebula, but not within the area of the proposed IRAS-Vela ring. These positions are shown in Fig. [2-9] together with those at which Srinivasan Sahu made observations. Reynolds observed double components at positions labelled C, D, E, G and H in this diagram. Of these C, D and E are definitely outside the indicated IRAS-Vela shell boundary. Thus, until more evidence to the contrary is provided, one should treat the existence of the IRAS-Vela shell as uncertain.

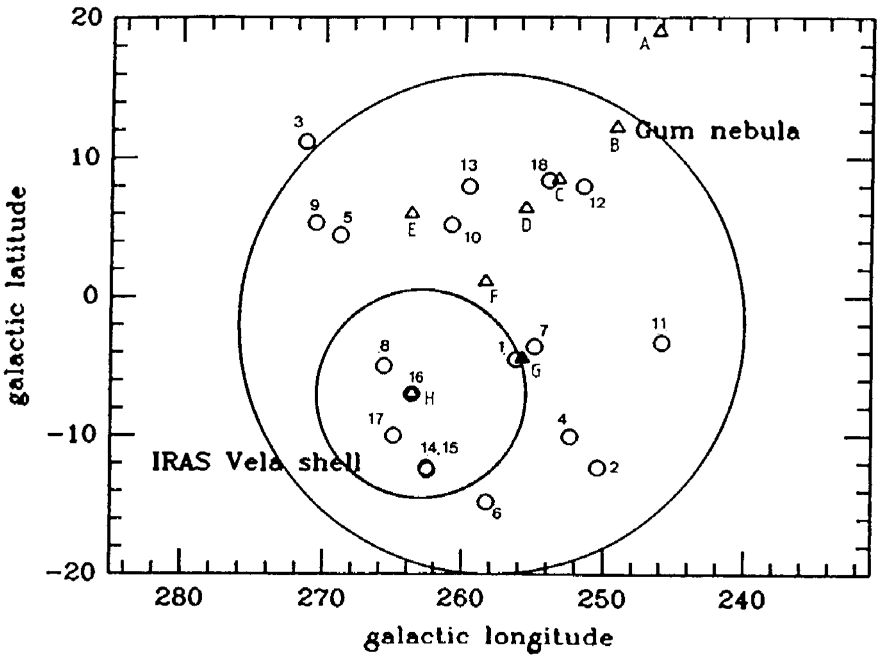

Figure [2-9]: Schematic diagram showing the positions observed by Reynolds (1976a) with an open triangle, labelled A to H. The positions observed by Srinivasan Sahu (1992) are indicated by open enumerated circles (Srinivasan Sahu, 1992).

The greater distance of 700 pc to ζ Puppis (see table [2-4]) suits Srivivasan Sahu's interpretation of events in this region of sky. As she considers the IRAS-Vela ring and the Gum Nebula to be spatially separate entities, this requires the Gum Nebula to be further away and leaves the Gum Nebula without an ionizing source if one insists on an H II region model for it. In a scenario where ζ Puppis at a distance of 700 pc is significantly separated in space from Vela OB2, the proposed ionizing source of the IRAS-Vela ring, ζ Puppis would serve as the ionizing source for the Gum Nebula. Another possibility is that ζ Puppis was the binary companion of the progenitor star of the Gum Nebula and was catapulted into its present runaway-star type trajectory in the SN explosion.

name	position	distance/[pc]
Puppis R3	$252, -1$	1740
Puppis R2	$256, -2$	1000
Puppis R1	$260, -3$	3800
Vela R1	$263, -4$	460
Vela R2	$265, +2$	870
Vela R3	$268, -3$	2190

Table [2-9]: A list of R-associations in the Gum Nebula region (Herbst, 1975).

The interpretation of the Gum Nebula region by Srinivasan Sahu is shown diagrammatically in Fig. [2-10]. She considers the Gum Nebula as a shell structure formed by the R-association Vela R2. ζ Puppis is considered a runaway star from Vela R2, with its displacement to lower longitudes and negative latitudes making up for the significantly off-centre position of the Vela R2 (see table [2-9] for positions and distances to R-associations in the Gum Nebula region). The IRAS-Vela shell is interpreted as the remnant of a giant molecular cloud surrounding the relatively aged Vela OB2 association (Srinivasan Sahu, 1992).

2.5 Conclusion

No conclusive observational evidence for any one of the models has yet been published, although the radio polarization reported by Duncan et al. (1996) can only be explained by an SNR model. Further investigation of the Gum Nebula is thus warranted.

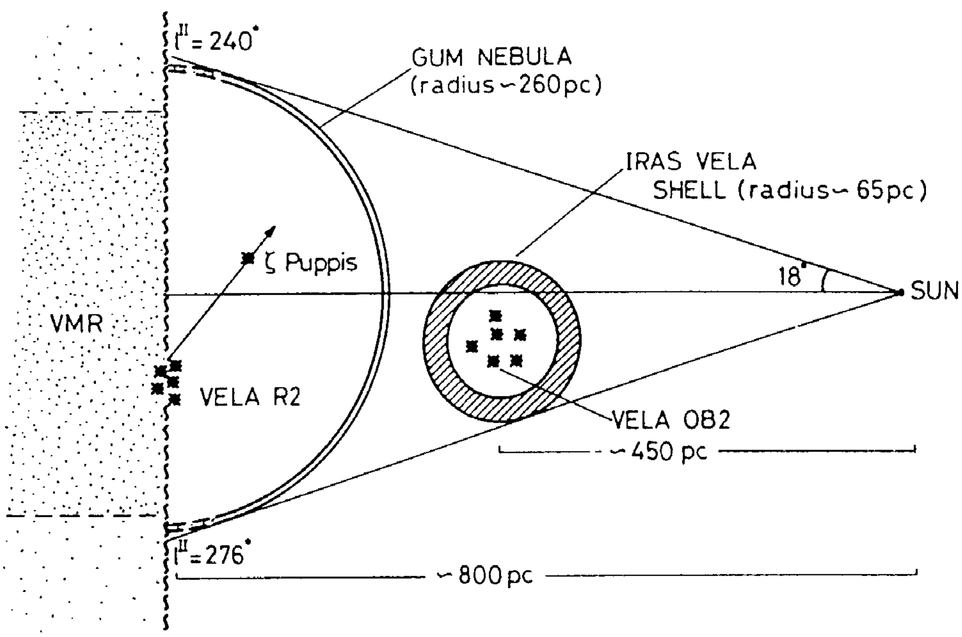

Figure [2-10]: The interpretation of the Gum Nebula region according to Srinivasan Sahu (1992).

2.5.1 Motivation for this work

Two aspects which have not been investigated at all are the radio brightness temperature spectral index and the infrared to radio flux ratio of the Gum Nebula. With the availability of the 408 MHz radio survey and the IRAS data, all the data required for the latter was readily available. By making my own radio continuum observations of the region at 2.3 GHz, I obtained sufficient data for deriving the spectral index of the Gum Nebula. The observations at 2.3 GHz have a resolution of $\frac{1}{3}°$, higher than that of the 408 MHz survey, and are therefore closer to the $\approx 5'$ resolution of the IRAS data. Thus I used the 2.3 GHz data rather than the 408 MHz data for the determination of the ratio of the infrared to radio flux density (IRR).

The value of the spectral index should in principle allow one to decide between the various models. In particular, it should reveal if there is a combination of different events present in the Gum Nebula, as proposed by Reynolds (1976a,b) and

Srinivasan Sahu (1992). If the model of Reynolds is correct one should see a shell of spectral index 2.1 corresponding to the proposed H II shell, surrounding a central non-thermal (spectral index > 2.2) region.

From the information given by Srinivasan Sahu about the IRAS-Vela ring I conclude that it should be thermal, i.e. have a spectral index of 2.1. Thus, if it exists, its circular shape and position should be clearly visible in a spectral index image. It would be identifiable by a thermal spectral index; or a lower spectral index if superimposed on a non-thermal region. The latter would be present if, as proposed by Srinivasan Sahu, the Gum Nebula is a more distant old SNR situated behind the IRAS-Vela shell and of larger angular extent than this shell.

The infrared to radio flux density ratio (IRR) is sensitive to the different mechanisms heating the dust that emits the infrared radiation. As such it allows one to distinguish between H II regions and SNRs. No predictions have been made for this ratio in the model of Weaver et al. (1977) for the interstellar bubble. But as stars with strong enough stellar winds presumably also emit the continuum photons responsible for heating the dust so effectively in H II regions, it is probable that the IRR for these bubbles is the same as for H II regions. Again, a superposition of different events in this region, rather than a single nebula should be evident in an IRR image.

Even if the evidence shows that the nebula is an old SNR, this may still be coupled to a thermal shell as in Reynolds' (1976b) proposed scenario. One way of checking on the existence of thermally emitting gas associated with the Gum Nebula is by observing hydrogen recombination lines at positions in the Gum Nebula. These are indicative of thermally emitting regions with electron temperature somewhere between 5000 K and 10 000 K. If detected they would also allow the determination of the electron temperature, turbulent velocity and emission measure at the observed positions. The low intensity of the Gum Nebula, which requires long integration times for the spectra, makes such a project prohibitive in terms of observing time.

The last project that I embarked upon was an investigation of the kinematics of the nebula. The 1667 MHz main line of hydroxyl (OH) was chosen as tool for investigating the motion of the molecular material associated with the Gum Nebula. These 1667 MHz OH observations, together with 1720 MHz OH satellite-line observations at selected positions, were also investigated for evidence of the interaction of the molecular material with the expanding shell of the nebula.

The line velocities of any detected species can be used for kinematic distance determination with the use of a Galactic Rotation model. The velocities attributed to galactic rotation in the direction of the Gum Nebula vary only very slowly with distance. Thus it was unlikely that such determinations would improve the poorly defined distance to the Gum Nebula. They do however provide a check on other distances quoted in the literature. Thus this aspect of the spectral line data was also investigated in this work.

Chapter 3

Radio continuum observations

The continuum observations were made using the HartRAO 26 m diameter dish antenna. The observing system Skymap was used. Skymap is a procedure for mapping large areas of cosmic radio continuum emission and was developed, tested and implemented by Mountfort (1989) and Jonas (1982) for the HartRAO antenna operating at 13cm. Details of the manner in which these observations are made and the data is reduced are given in Mountfort (1989), Jonas (1982) and Jonas (in preparation). See also Baart et al. (1980), Jonas et al. (1985), Mountfort et al. (1987) and Jonas & Baart (1995).

I made the observations for the region of sky covering the Gum Nebula during the period March to May 1986. I also ran the observed data through a preliminary version of the data reduction process. The final version of the data reduction, incorporating subsequent changes to the reduction process, was made by Jonas (in preparation).

Subsequent to the data reduction of all observed individual regions of the southern sky, all the maps were combined by Jonas to form a composite map. This required further slight adjustments to the data to ensure that the joins of the maps were smooth and consistent. The final product of these observations is a two dimensional

Parameter	HartRAO Radiotelescope at 13 cm
Physical diameter	26 m
Physical aperture, A_p	531 m^2
Receiver	cryogenic cooled GaAsFET (15 K)
Centre frequency	2326 MHz
System Bandwidth, B	40 MHz
Effective aperture, A_e	284 m^2
Aperture efficiency, ϵ_{ap}	0.535
Half-power-beam-width, HPBW	$20'$
Pointing Accuracy	$\approx 1'$ rms
System noise temperature, T_e	≈ 40 K
Calibration noise diode temperature	3.96 K
Antenna beam solid angle, Ω_A	5.95×10^{-5}
Full beam solid angle, Ω_{fb}	$3.94 \pm 0.2 \times 10^{-5}$
Full beam efficiency, $\epsilon_{fb} = \Omega_{fb}/\Omega_A$	0.662
T_A to T_{fb} conversion factor $= 1/\epsilon_{fb}$	1.50 ± 0.08
Polarization	linear E-W
Rms noise level of final map	24 mK

Table [3-1]: Parameters of the HartRAO radiotelescope operating at 2326 MHz at the time (autumn 1986, southern hemisphere) of the continuum observations for the Gum Nebula region.

array of antenna temperature values ordered according to position in the desired coordinate system. The antenna temperature values were converted to full-beam brightness temperature by multiplying by a factor of 1.50 $\pm$ 0.08 (Jonas, private communication).

It is in this final form that the 2.3 GHz map of the Gum Nebula was used in this work. The complete survey is known as the Rhodes/HartRAO 2326 MHz Survey. The parameters of the HartRAO radiotelescope at 2326 MHz are tabulated in table [3-1].

NOTE: As the data reduction method removes any constant contribution to the antenna temperature, both the isotropic microwave background, the isotropic contribution due to unresolved extragalactic sources and the small isotropic (as opposed to non-isotropic) contribution to the Milky Way are not included in the final map.

3.1 2326 MHz continuum map of the Gum Nebula region

The part of the Rhodes/HartRAO 2326 MHz Survey covering the Gum Nebula region, between galactic longitude 285° and 235° and galactic latitude -30° and +30°, is shown in Fig. [3-1] as a false colour image. The positions of the known H II regions and SNRs are indicated in the image by squares and circles respectively. The largest black ink circle shows the approximate extent of the Vela XYZ SNR. The Gum Nebula is the large circular red feature with faint extensions beyond its main circular structure. Immediately apparent is the close correspondence of the Gum Nebula at 2.3 GHz to that in Hα (see Fig. [2-1]). Figs. [3-2] and [3-3] show that this close correspondence also holds for the faint extensions to the nebula in Hα (see Fig. [2-2]).

There is one discrepancy. At positive galactic latitudes the Gum Nebula at 2.3 GHz appears to have a filled body while it is hollow in Hα. This is due to the presence of a faint radio spur at 2.3 GHz, which is not visible in Hα and not considered part of

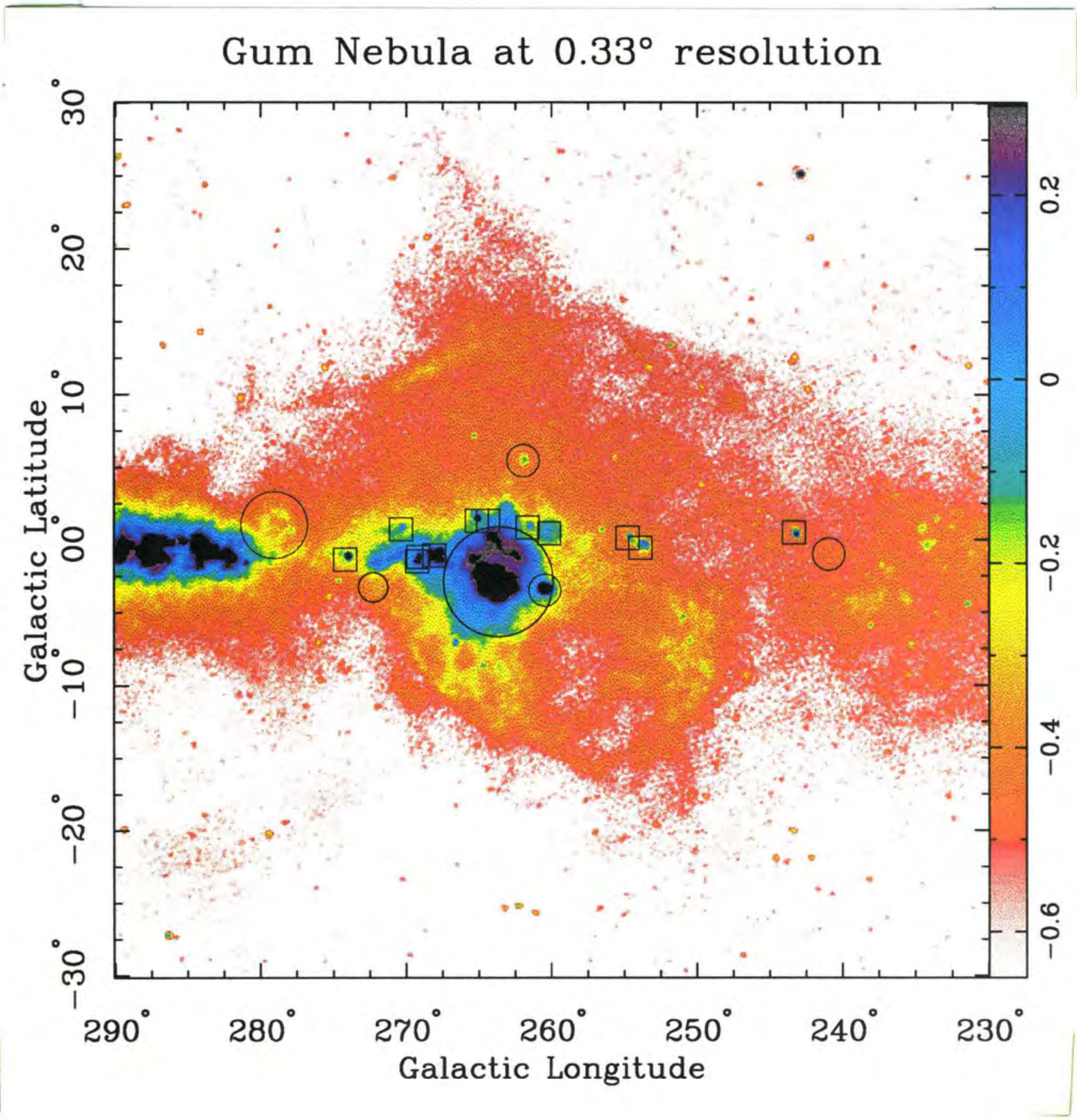

Figure [3-1]: False colour image of the Gum Nebula at 2326 MHz and a resolution of $\frac{1}{3}^{\circ}$. The false colour scale on the right gives the logarithm of the brightness temperature. The positions of the known H II regions and SNRs are indicated by squares and circles respectively.

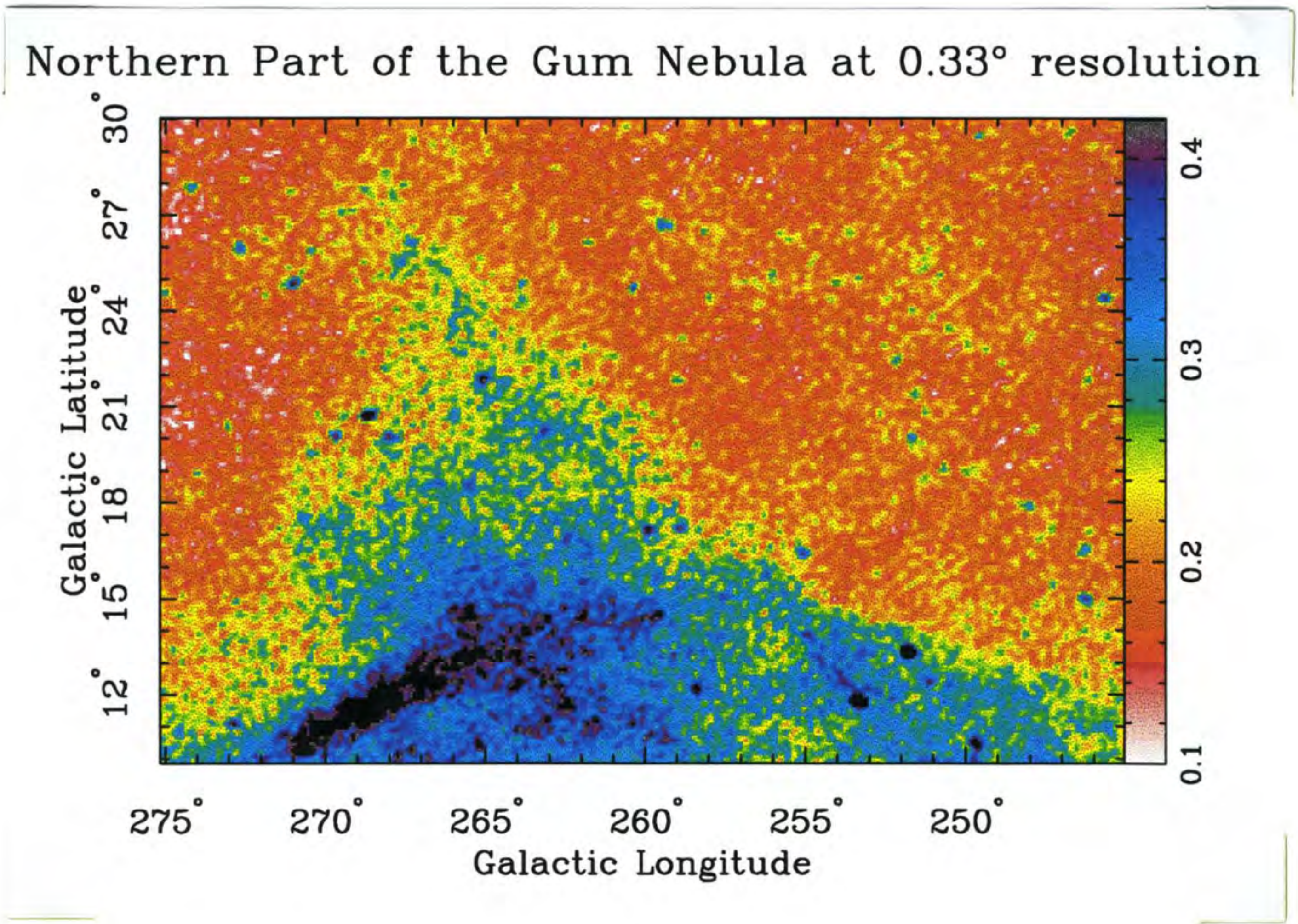

Figure [3-2]: The faint extensions at 2.3 GHz above the main body of the Gum Nebula at positive galactic latitudes. The false colour scale gives the brightness temperature.

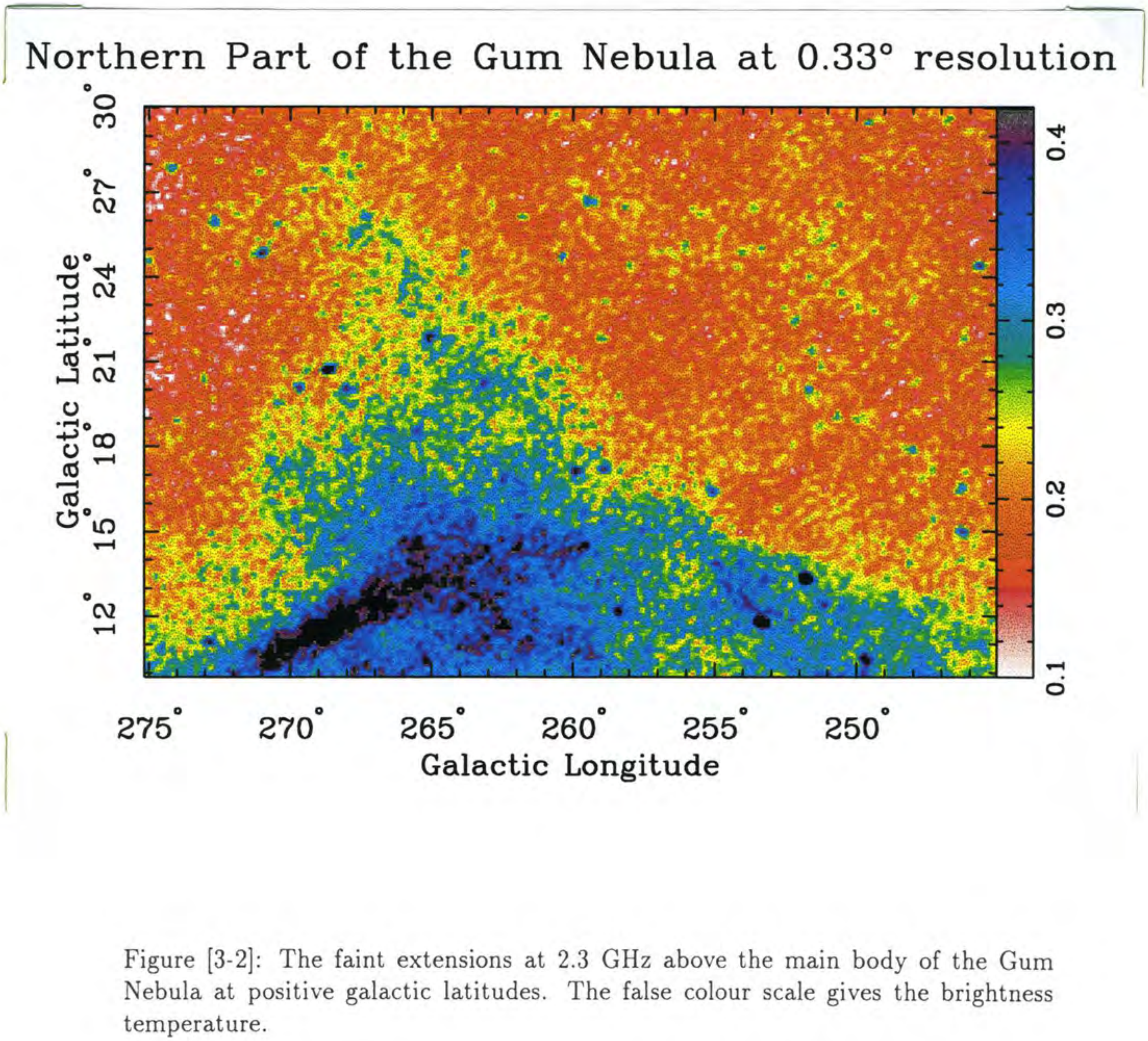

Figure [3-2]: The faint extensions at 2.3 GHz above the main body of the Gum Nebula at positive galactic latitudes. The false colour scale gives the brightness temperature.

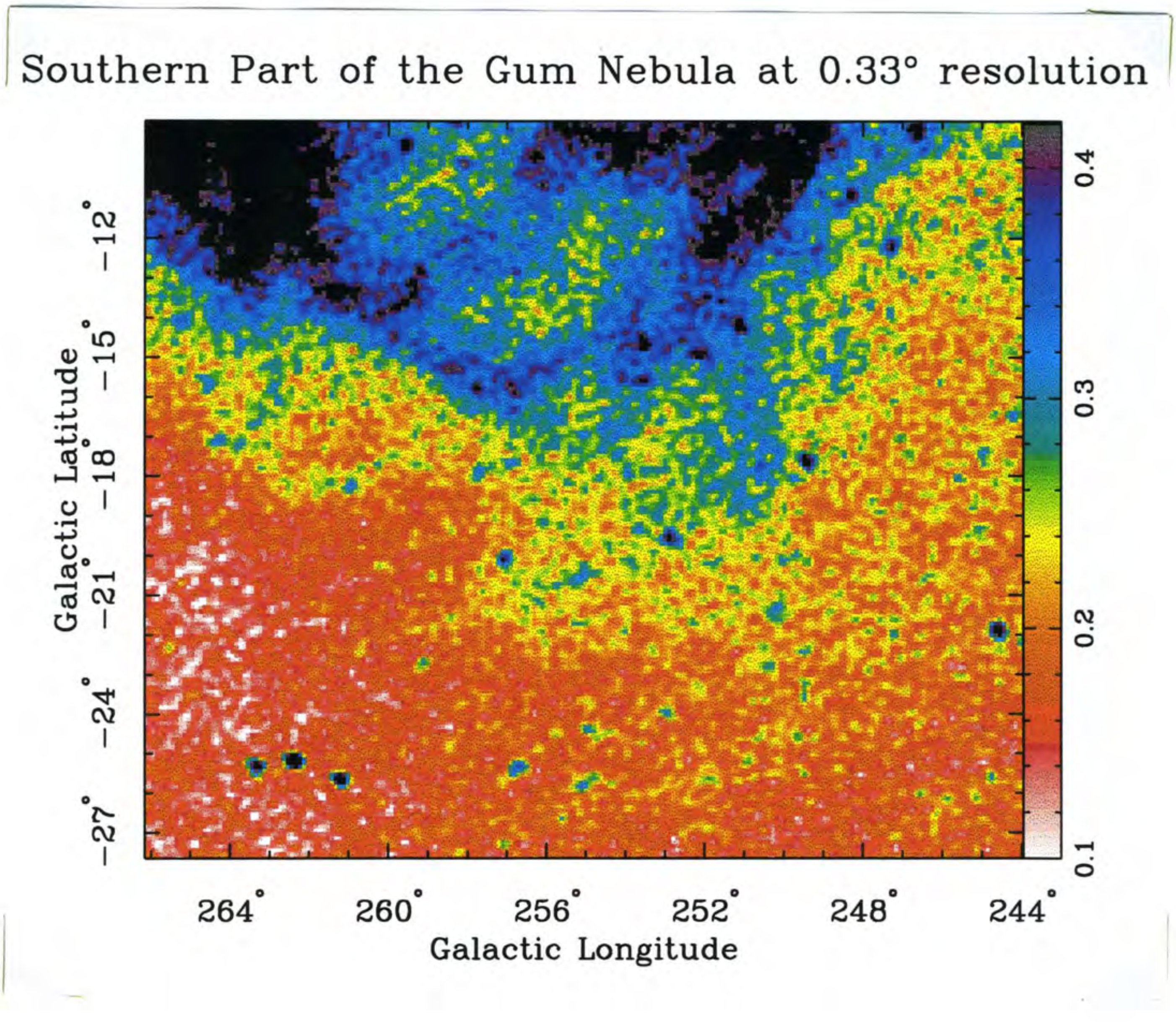

Figure [3-3]: The faint extensions at 2.3 GHz below the main body of the Gum Nebula at negative galactic latitudes. The false colour scale gives the brightness temperature.

the nebula. Although this spur is very faint at 2.3 GHz, it dominates the positive galactic latitudes between longitudes 260° and 268° at very low radio frequencies, as shown in the 34.5 MHz false colour image in Fig. [3-4] (Dwarakanath & Udaya Shankar, 1990).

The 34.5 MHz survey of Dwarakanath & Udaya Shankar covers the declination range $-50°$ to $+70°$ and the complete 24 hours in right ascension (RA). Of this, the region in declination range $-33°$ to $+61°$ is without aliasing. The synthesized beam has a resolution of $26' \times 42' \sec(\delta - 14.1°)$. For the purposes of comparison with the Rhodes/HartRAO 2326 MHz and the Haslam et al. 408 MHz surveys, I convolved the 34.5 MHz survey with appropriate gaussians in declination to give it a uniform resolution in declination. This resolution is, at 1.7°, just lower than the original resolution at the lowest declination. The resolution in right ascension was matched to this by appropriate convolution in RA. The Gum Nebula region was then transformed to galactic coordinates, resulting in the image shown in Fig. [3-4]. Constant brightness temperature contours of the 2.3 GHz image at a resolution of 1.7° are shown superimposed on the 34.5 MHz image, indicating the outline of the Gum Nebula at higher frequencies.

Duncan et al. (1996) identified the 2.4 GHz manifestation of this 34.5 MHz spur as one of the radio counterparts of the Vela XYZ SNR ejecta seen in the ROSAT X-ray image of Aschenbach et al. (1995). At this low frequency it is apparent that this spur is much larger in extent than the Vela SNR and thus unlikely to be associated with it. Its smaller extent at high frequencies, where only the brightest part shows, hints at a very steep spectral index for this spur.

Although this spur, the Vela XYZ SNR and the emission along the plane of the Galaxy, partially hide the shell-like structure of the Gum Nebula at 2326 MHz, stacked constant latitude plots in steps of 0.5° in latitude high-light this structure (see Fig. [3-5]). For these plots the 0.5° resolution background subtracted 2326 MHz image of the Gum Nebula was used (see section 6.2.3).

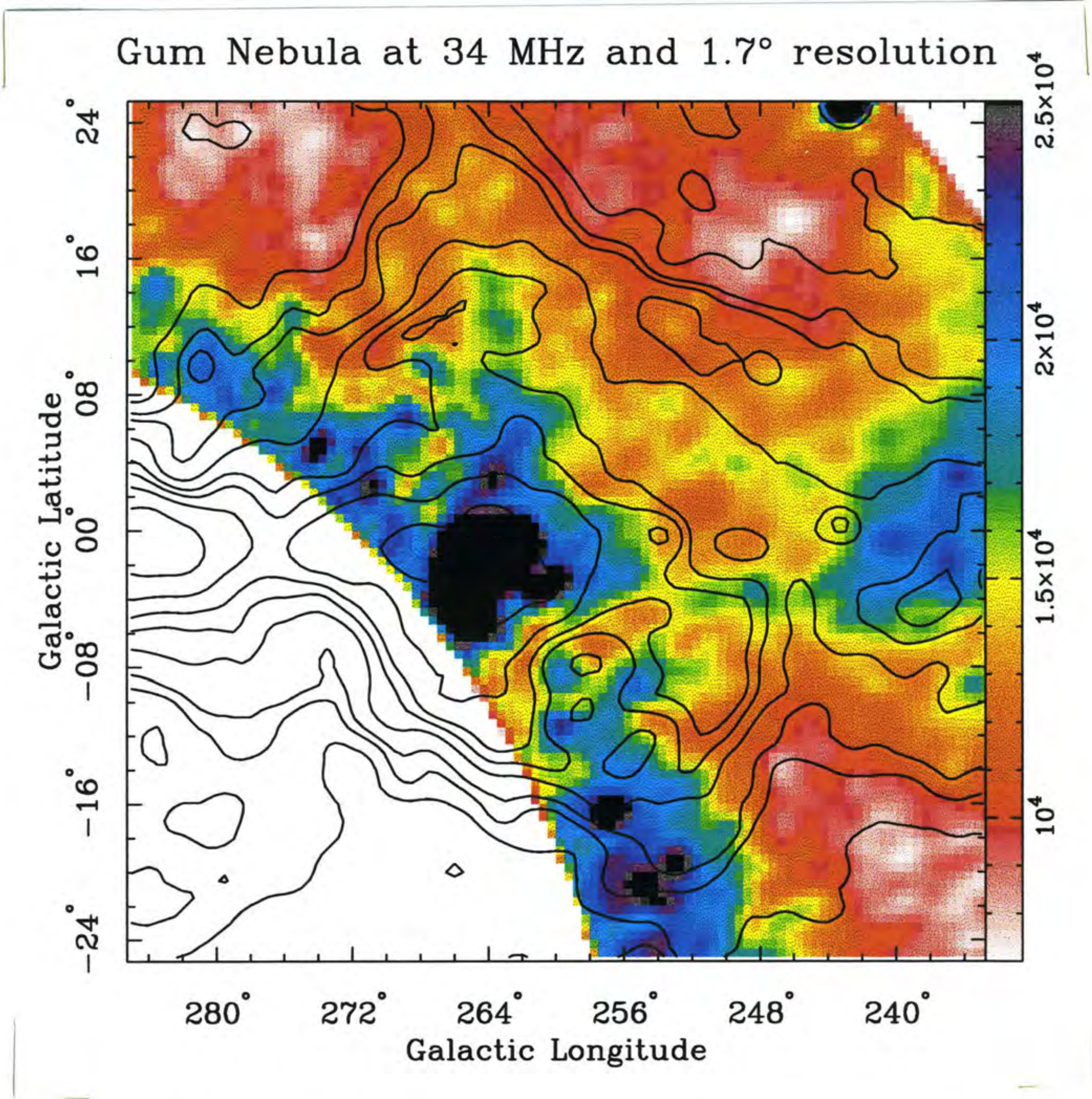

Figure [3-4]: 34.5 MHz false colour image of the Gum Nebula region. Constant brightness temperature contours of the 2.3 GHz image at a resolution of 1.7° are shown superimposed on the 34.5 MHz image. The false colour scale gives the 34.5 MHz brightness temperature.

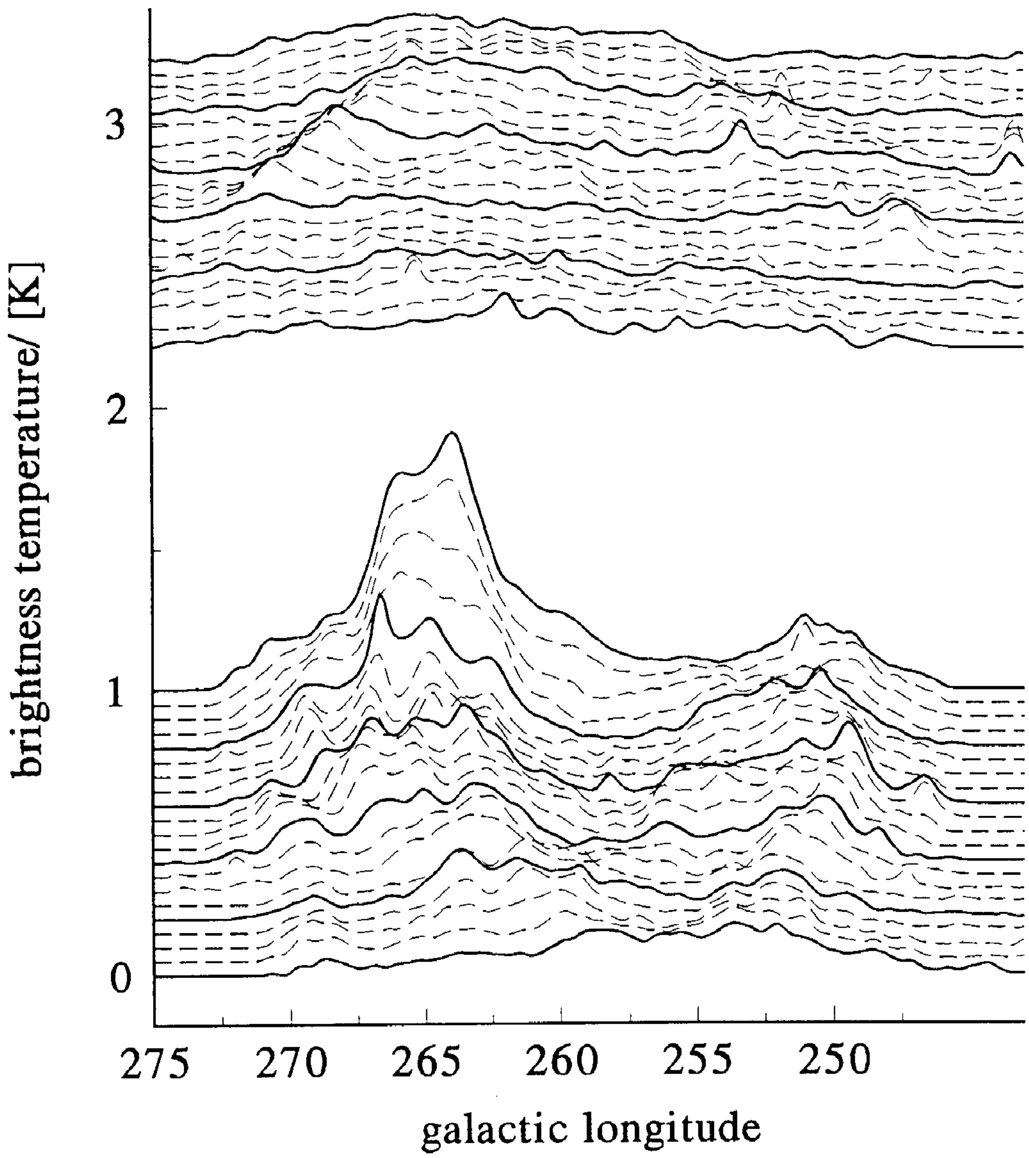

Figure [3-5]: Stacked constant latitude plots of the Gum Nebula at 2326 MHz and a resolution of 0.5°. The constant latitude plots are in the latitude range −15° to −5° at the bottom and +6° to +16° at the top. All plots are in intervals of 0.5°. Solid lines are used at intervals of 2°.

The $\nu^{-\alpha}$ dependence of the intensity of radio emission, where α is the spectral index and a positive number, implies that this emission gets stronger at lower frequencies. However, at such low frequencies free-free absorption processes become significant in thermal emission (brehmsstrahlung), giving rise to self-absorption or absorption by a thermal source in the line-of-sight path. The Gum Nebula is not visible as an emission structure on the 34.5 MHz radio image, but is in some parts mimicked by absorption depressions. Such absorption depressions must be due to thermal regions, or regions with a significant thermal component, within the Gum Nebula.

As shown in Fig. [2-7], the Gum Nebula is visible in the 408 MHz survey of Haslam et al. (1981). Thus their survey together with the 2326 MHz survey provide sufficient data for the construction of a spectral index image of the nebula.

3.1.1 Supernova Remnants in the observed region

The radio survey of this region at 2326 MHz revealed the existence of an SNR at G279.0+1.1. This discovery and the derived parameters of this SNR are documented in Woermann & Jonas (1988).

Other known SNRs in this region are (D.A. Green's catalogue of Galactic SNRs, 1995):

- G240.9 − 0.9: A possible SNR, not identifiable on the 2.3 GHz false colour image. Indeed, recent work by Duncan et al. (1996) supports the theory that this is not an individual SNR, but a feature of the Gum Nebula.

- G260.4−3.4: Puppis A, a shell type SNR of size $60' \times 50'$ and spectral index 2.5. The shell structure is not resolved by the 2.3 GHz survey. The observing run in which a search for OH towards the Gum Nebula region was made, yielded, towards Puppis A, a detection of anomalous OH, with the 1667/5 MHz lines in absorption. The velocity of the absorption lines gives a lower limit of 1.3 kpc for the distance towards Puppis A (Woermann & Gaylard, 1993) using the galactic rotation model of Wouterloot & Brand (1989) .

- $G261.9 + 5.5$: A shell type SNR which, with a size of $40' \times 30'$, is not resolved in the 2.3 GHz survey.
- $G263.9 - 3.3$: Vela XYZ. A composite, i.e shell and plerion, SNR, as identified by the steep spectral index of the large shell and the central component Vela X with its flatter spectrum. There is still some controversy about the details of these spectral indices. The association of this SNR with the Vela pulsar has recently been confirmed (Aschenbach et al., 1995). Rosat X-ray images show that the shell, previously considered irregular with centre significantly off the Vela pulsar position, shows a faint extension in x-rays. Inclusion of this faint extension in the angular extent of the SNR results in a centre very close to the pulsar.
- $G272.2 - 3.2$: An optical SNR that eludes detection in the radio wavelength band. It is not visible in the 2.3 GHz survey.

Chapter 4

The Spectral Index of the Gum Nebula

Two of the models, H II region and SNR, proposed for the Gum Nebula may be distinguished on the basis of their spectral index. The spectral index characterises the variation with frequency of the flux density or brightness temperature of a radio source and its value is directly related to the physical process giving rise to the radiation.

The position of the Gum Nebula, which straddles the galactic plane, as well as its faintness, makes a reasonable determination of its integrated flux density impossible. Thus this work has focussed on determining a brightness temperature spectral index for this nebula rather than a flux density spectral index.

In the following the flux density and brightness temperature spectral indices are defined. Then the theoretically derived values corresponding to an H II region and an SNR are presented. There are several inherent problems with spectral index determination. Thus I made a detailed investigation into the methods for determining the brightness temperature spectral index of a faint extended source, such as the Gum Nebula. On the basis of the conclusions I reached from this investigation I developed an alternative method which I used to determine a brightness temperature spectral index for the Gum Nebula.

4.1 The spectral index of radio sources

Molecular absorption in the atmosphere and ionospheric reflection give rise to the walls of the radio window. The extent of this window ranges in wavelength from a few millimetres to several tens of metres. If ground-based radio observations of a cosmic radio source are made over as much of this wavelength range as possible, a continuum spectrum may be determined for this source.

A radio source subtending a solid angle Ω_s has an integrated flux density, F_ν, at frequency ν given by (Kraus, 1986)

$$F_\nu = I_\nu \Omega_s \tag{4-1}$$

where I_ν is the source brightness assumed constant over the source.

A radio continuum source may be characterised by the slope of the plot of the log of its integrated flux density versus the log of frequency in a particular frequency range. For convenience the flux density spectral index, α, of a source, is defined as the negative value of this slope. Hence

$$F_\nu = K \nu^{-\alpha} \tag{4-2}$$

where K is a proportionality constant.

The variation of the spectral index with position across a region of sky may be determined as well. For this it is convenient to define a brightness temperature spectral index, β.

From the definition of brightness temperature and flux density (Kraus, 1986), assuming a constant brightness over the source, we have

$$T_b = \frac{c^2}{2\nu^2 k} I_\nu \tag{4-3}$$

$$= \frac{c^2}{2\nu^2 k} \frac{F_\nu}{\Omega_s} \tag{4-4}$$

where k is Boltzmann's constant.

Substituting for F_ν from equation (4-2) gives

$$T_b = M\nu^{-\alpha-2} = M\nu^{-(\alpha+2)} = M\nu^{-\beta} \tag{4-5}$$

where M is a constant.

The brightness temperature spectral index, β, is thus related to the flux density spectral index quite simply as:

$$\beta = \alpha + 2 \tag{4-6}$$

With the exception of solid bodies, which none of the sources of interest to this work are, radio continuum emission always comes from free electrons as these have no discrete energy jumps. A free electron only emits radiation when accelerated. There are only two important acceleration mechanisms in astronomy—bremsstrahlung emitted by thermal electrons moving in the electric field of ions, and synchrotron radiation emitted by relativistic electrons gyrating in a magnetic field.

Radio continuum sources can thus be classified as (e.g. Rohlfs, 1986)

- thermal sources which radiate because the medium is hot, giving rise to bremsstrahlung. This radio emission process dominates in H II regions, which are predominantly ionized hydrogen at temperatures in the range 5000 K to 10000 K.

- nonthermal sources in which synchrotron emission dominates—other nonthermal radiation mechanisms being too weak to contribute significantly. This emission process is characteristic of SNRs, in which the interstellar magnetic field has been compressed and is thus stronger and electrons have been accelerated in the shock front to relativistic speeds.

The optical depth, τ, for brehmsstrahlung (thermal radiation) has a strong frequency dependence. Thus a thermal source can appear optically thick at low frequencies, where it radiates as a thermal black body having $\alpha = -2$ and thus $\beta = 0$. The same source may be optically thin at higher frequencies, resulting in $\alpha = 0.1$ and $\beta = 2.1$. Such thermal spectra are characteristic of H II regions.

The spectral index for synchrotoron radiation depends on the energy distribution of the relativistic electrons spiralling in the magnetic field. For a power law electron energy distribution, with index $-p$, the flux density is proportional to $\nu^{-(p-1)/2}$ (e.g. Salter & Brown, 1988). For cosmic rays, which are a sample of the relativistic electrons emitting synchrotron radiation and thus have the same energy distribution, a generally accepted value for p is 2.4 (Kraus, 1986). Hence for such an energy distribution of the electrons, the emitted synchrotron radiation has a spectral index α of 0.7 and β of 2.7.

The frequency dependence of synchrotron radiation is generally derived by assuming that the processes occur in a vacuum. In reality the processes occur in a plasma. The effects of the plasma on the radiation are numerous. For example, Schlickeiser & Fürst (1989) have shown that flat radio spectra ($\alpha < 0.5$, i.e. $\beta < 2.5$) of synchrotron emitting SNRs can be explained by shock wave acceleration of particles in a low-β plasma (Note: the latter β does not refer to a brightness temperature spectral index, but to a property of the radiating plasma.) Also, curved or bent radio synchrotron emission spectra are observed, implying a more complex type of electron energy distribution. Synchrotron self-absorption may occur at very low frequencies.

Fig. [4-1] summarises the spectra theoretically derived for optically thin and thick thermal radiation and nonthermal radiation.

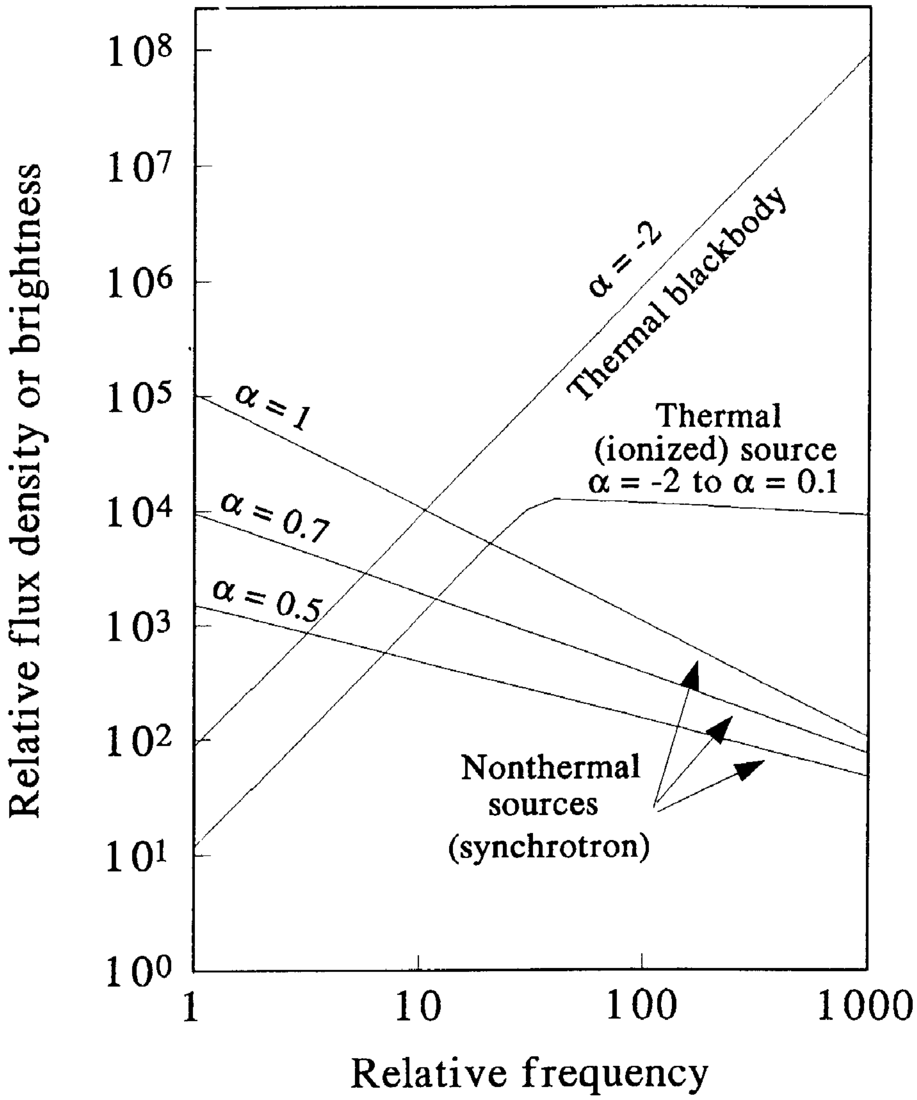

Figure [4-1]: Calculated spectra for optically thin and thick thermal sources and nonthermal sources (Kraus, 1986)

A spectral index α of 0.1 ($\beta = 2.1$) is usually considered as indicative of an optically thin thermal source such as an H II region. However there are a few cases of synchrotron radiation sources (notably that from the Crab Nebula, a special type of SNR, called a plerion) with an α of 0.1. A high percentage polarization of the radiation from such a source or the lack of a recombination line would then support a nonthermal interpretation. It is highly unlikely that the Gum Nebula belongs to this class of object as it does not appear to have an associated pulsar, nor does it have the filled-centre morphology exhibited by plerion type SNRs.

The most frequently determined spectral indices of SNRs, i.e galactic synchrotron sources, are in the range 0.3 to 0.7 for α, equivalent to a β ranging from 2.3 to 2.7.

Combinations of thermal and nonthermal radiation along the same line of sight at a position give rise to composite spectra.

The value of the spectral index of a source thus points to the radio emission mechanisms responsible for the observed emission. The spectral index is thus a diagnostic tool for determining the dominant radio emission process of a source in a particular frequency range.

The determination of the spectral index is nontrivial and methods for doing so are discussed in the following sections.

4.2 Brightness temperature spectral index determination

When determining a brightness temperature spectral index image it is customary to limit the process to two observations of the same source or region at different frequencies, ν_1 and ν_2. In this work, the 2326 MHz Rhodes/HartRAO survey of original resolution 0.33° and the Haslam et al. (1982) 408 MHz survey of original resolution 0.85° were used. No other choice was possible as these were the only surveys available covering the whole Gum Nebula region.

The observing process inherently gives rise to beam dilution of the sky brightness distribution. A reliable spectral index can only be obtained if each observation has been subject to the same amount of beam dilution. i.e. the maps must have the same resolution. Since the resolution of a map depends on the observing frequency and physical size of the dish, the available images rarely have the same resolution. To bring both maps to the same desired common resolution, θ_1, map 2 of higher resolution, θ_2, has to be convolved with a Gaussian function of half-power beam width θ_{smooth} such that

$$\theta_{smooth} = \sqrt{\theta_1^2 - \theta_2^2} \tag{4-7}$$

Where such a process was necessary for this work a convolution program, CTFM, written by Jonas of Rhodes University was used.

The brightness temperatures in a region at frequency ν_1 and ν_2 are then given respectively by (see equation (4-5))

$$T_1(\ell, b) = k(\ell, b)\nu_1^{-\beta} \tag{4-8}$$

$$T_2(\ell, b) = k(\ell, b)\nu_2^{-\beta} \tag{4-9}$$

where $k(\ell, b)$ is a frequency independent constant at each position (ℓ, b) in the region.

Thus at each position (ℓ, b)

$$\frac{T_2}{T_1} = \left(\frac{\nu_2}{\nu_1}\right)^{-\beta} \tag{4-10}$$

and the temperature spectral index is given by (rearranging equation (4-10)):

$$\beta(\ell, b) = -\frac{\log\left(\frac{T_2(\ell,b)}{T_1(\ell,b)}\right)}{\log\left(\frac{\nu_2}{\nu_1}\right)} \tag{4-11}$$

However simple division of the brightness temperatures at the two frequencies is generally not appropriate, as the absolute zero baselevel is generally not known for radio maps due to the manner in which observations are made. One can make subsidiary observations with a small calibrated horn antenna at the same frequency to determine the absolute zero for the observations. In this work the spectral index of a single source, the Gum Nebula, will be determined. Thus one needs to isolate the source from any other radiation not emitted by this source coming from the same region of sky. An absolutely calibrated survey does not aid in such isolation.

When pointing the antenna at a position on a source of interest the radiation received may originate anywhere along the line of sight (assuming optically thin sources); i.e. from the source and from other sources in front of and behind the source. All the radiation not from the source of interest is called the background radiation, even though some of it may originate at positions along the line of sight in front of the source of interest. Both integrated flux density and brightness temperature spectral index determinations of radio sources require the source of interest to be isolated from its background radiation at both frequencies used in the calculation.

The usual manner in which this background removal problem is approached is to obtain an image of the source covering only this source and sufficient adjacent regions to characterise the background. Hence the pixel values along the perimeter of the image are assumed to be representative of the background at the perimeter. For sources of small angular extent on a relatively flat background a reasonable estimate of the background, assumed constant across the image, may be obtained by using the average value of the brightness temperature values on the image perimeter. For sources that sit on a severely slanting or more intricately varying background this method is far from satisfactory. Although I investigated the process of background determination from the pixel values on the perimeter in great detail, no successful method could be developed that works when the angular extent of the source is large. Isolating an extended source such as the Gum Nebula in a "rectangular" image, leaves too much "distance" between the source and the image boundary at high negative and positive galactic latitudes. Thus the perimeter values are not indicative of the background radiation close to the source.

Thus I adjusted the perimeter method to the version described below, which I implemented in the computer program GUMBACK.

4.2.1 Linear background determination at constant latitude

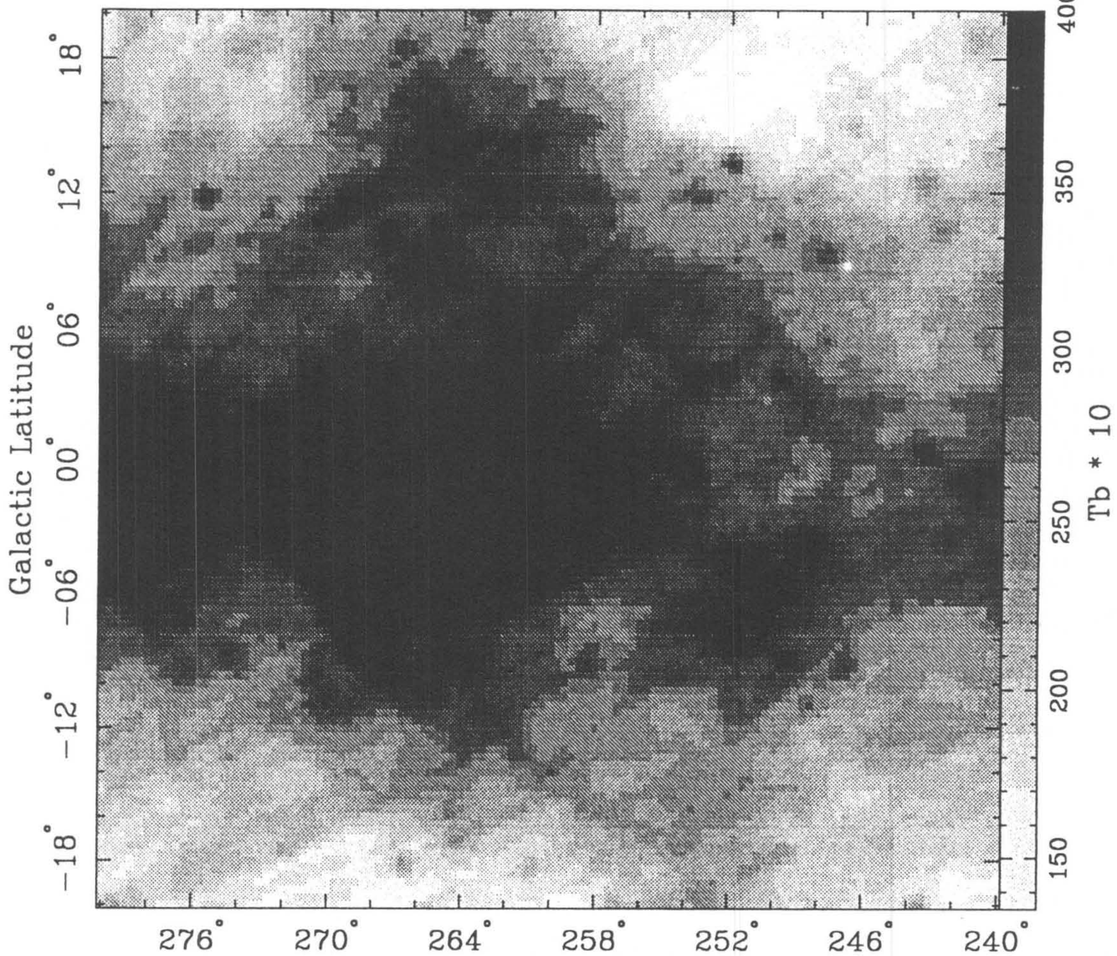

Figure [4-2]: The Gum Nebula region in galactic coordinates at 408 MHz from the survey of Haslam et al. (1982). The striations running approximately from the bottom left to the top right corner are scanning effects.

The program GUMBACK was used to determine a first order approximation to the background of the Gum Nebula at a resolution of 1.2°. This resolution was chosen as the 408 MHz data at the original resolution of 0.85° is severely affected by scanning effects, i.e. striations in the data following the path of the scanning antenna across the sky during the observations (see Fig. [4-2]). These scanning effects make it difficult to identify minima in the data, an important requirement of this method. At a resolution of 1.2° the scanning effects are sufficiently smoothed for an application of the GUMBACK program to be effective.

a)

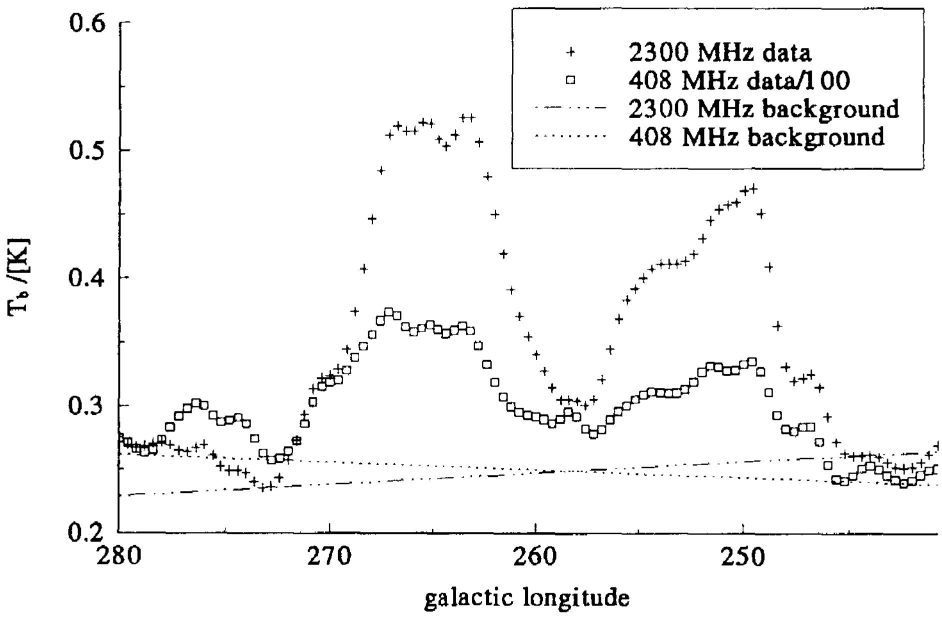

b)

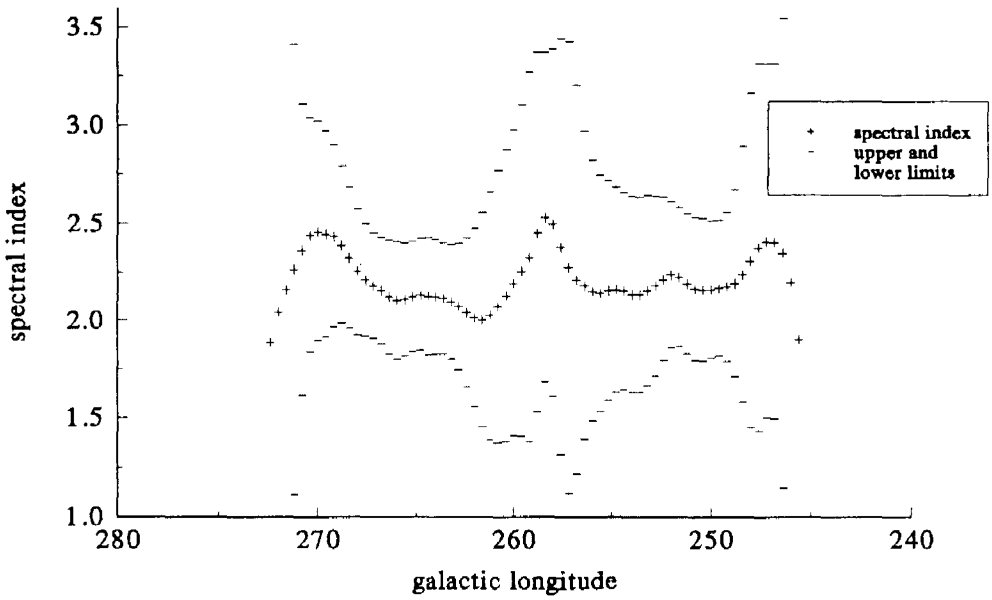

Figure [4-3]: a) An illustration, at constant galactic latitude of $-9.4°$, of the manner in which the program GUMBACK determines a first order estimate of the background of the Gum Nebula at 2326 and 408 MHz with resolution 1.2°. This is an example from the negative galactic latitude part of the Gum Nebula. b) The spectral index and its upper and lower limits determined from the 2326 and 408 MHz background isolated Gum Nebula.

a)

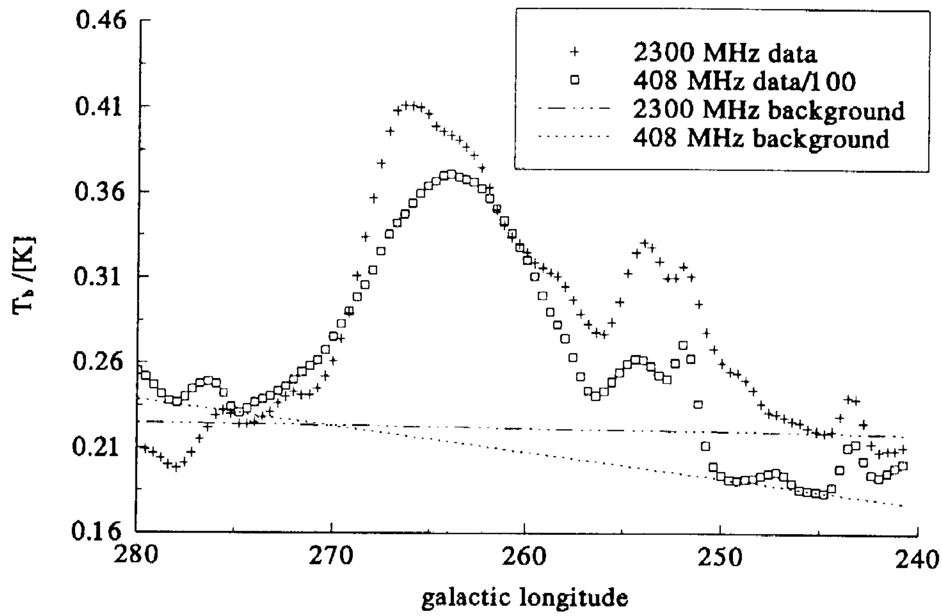

b)

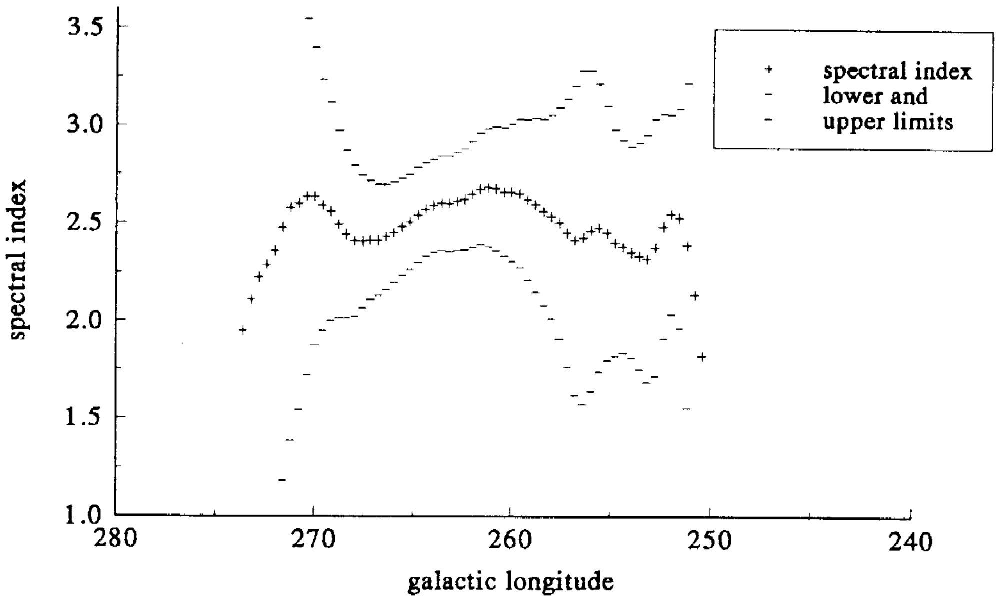

Figure [4-4]: a) A further illustration, at constant galactic latitude of +13.2°, of the manner in which the program GUMBACK determines a first order estimate of the background of the Gum Nebula at 2326 and 408 MHz with resolution 1.2°. This example is from the fainter positive galactic latitude part of the Gum Nebula. b) The spectral index and its upper and lower limits determined from the 2326 and 408 MHz background isolated Gum Nebula.

The manner in which GUMBACK determines this background is summarised in Figs. [4-3] and [4-4]. The top diagram in both figures shows constant latitude scans of the 2326 and 408 MHz data; those in Fig. [4-3] are at $b = -9.4°$ and those in Fig. [4-4] are at $b = +13.2°$. The 408 MHz brightness temperatures were divided by 100 to scale them to the range of the 2326 MHz data.

The program GUMBACK presents such scans to the user for each latitude. The cursor is used to indicate to the program two points on each of the two frequency scans to which to fit a straight line. These points are selected as local high longitude and low longitude minima of the brightness temperatures considered by the user as marking off the extent of the Gum Nebula. The straight line defined by these two points is then taken as representative of the background at that latitude for that frequency (note the straight lines in the figures).

Scans from both maps are displayed on the same plot to make the choice of these two points easier. The selected points should be at positions in whose close vicinity the other frequency image also has a minimum. The minima in the two images are not necessarily coincident, because of the shift in a minimum that occurs at the boundary between different spectral index regions. This is due to the smoothing of the antenna beam, discussed in section 5.2.1.

The linear backgrounds determined at each latitude are stacked into a background image. Such a background image inevitably has slight discontinuities in latitude due to the manner in which it is obtained. As the image is sampled ≈ 3 times per resolution, a running mean over three scans in latitude is applied to the background image. This smoothed background image is subtracted from the original survey image to obtain an isolated source image. As the background determined for the Gum Nebula very soon diverges from a reasonable background outside the nebula, pixels to the higher longitude side of the high-longitude selected point and to the lower longitude side of the low-longitude selected point are set to zero. This is not shown in the figures.

Equation (4-11) was applied to the two final, isolated source images at 2326 and 408 MHz to give a spectral index image. Constant latitude scans through this image are shown in the bottom diagrams of the Figs. [4-3] and [4-4]. The determined spectral index values at the boundaries of the source or towards the middle of the source, where it has very low brightness temperatures, are effectively indeterminate.

A comparison of the 2326 MHz and 408 MHz data in Figs. [4-3] and [4-4]a) from which the spectral index shown in Figs. [4-3] and [4-4]b) is derived, is instructive. Because of the $\nu^{-\beta}$ dependence of radio emission, flatter spectral index regions, which have smaller values of β, will dominate at higher frequencies, but be overshadowed by steeper spectral index regions at lower frequencies. Such flatter spectral index regions are evident between longitudes 268° and 260° and around longitude 250° in Fig. [4-3] a) and b). A similar, but less obvious, trend is seen in Fig. [4-4] at positive galactic latitudes. The flatter spectral index parts are around longitude 267° and between longitudes 255° and 250°.

The two latitudes chosen to illustrate this method indicate that it works satisfactorily. However, a closer inspection of the top diagrams in the two figures shows that other choices of points for the minimum could be equally valid in this context. One criterion for the selection of the points was to avoid obtaining negative brightness temperatures for the isolated image at both frequencies. This frequently constrained the choice; quite often observations at one frequency indicated a different choice than those at the other frequency. It was not always possible to avoid obtaining negative brightness temperatures within the isolated source at both frequencies. That in itself indicates that this method in this context gives at best a first order estimate to the background-isolated Gum Nebula. Within a few degrees of the galactic plane the scenario was too complicated for this method and thus this region was excluded. The false colour images of the isolated source at 2326 and 408 MHz and the resultant spectral index image are shown in Figs. [4-5] and [4-6] for negative and positive galactic latitudes respectively.

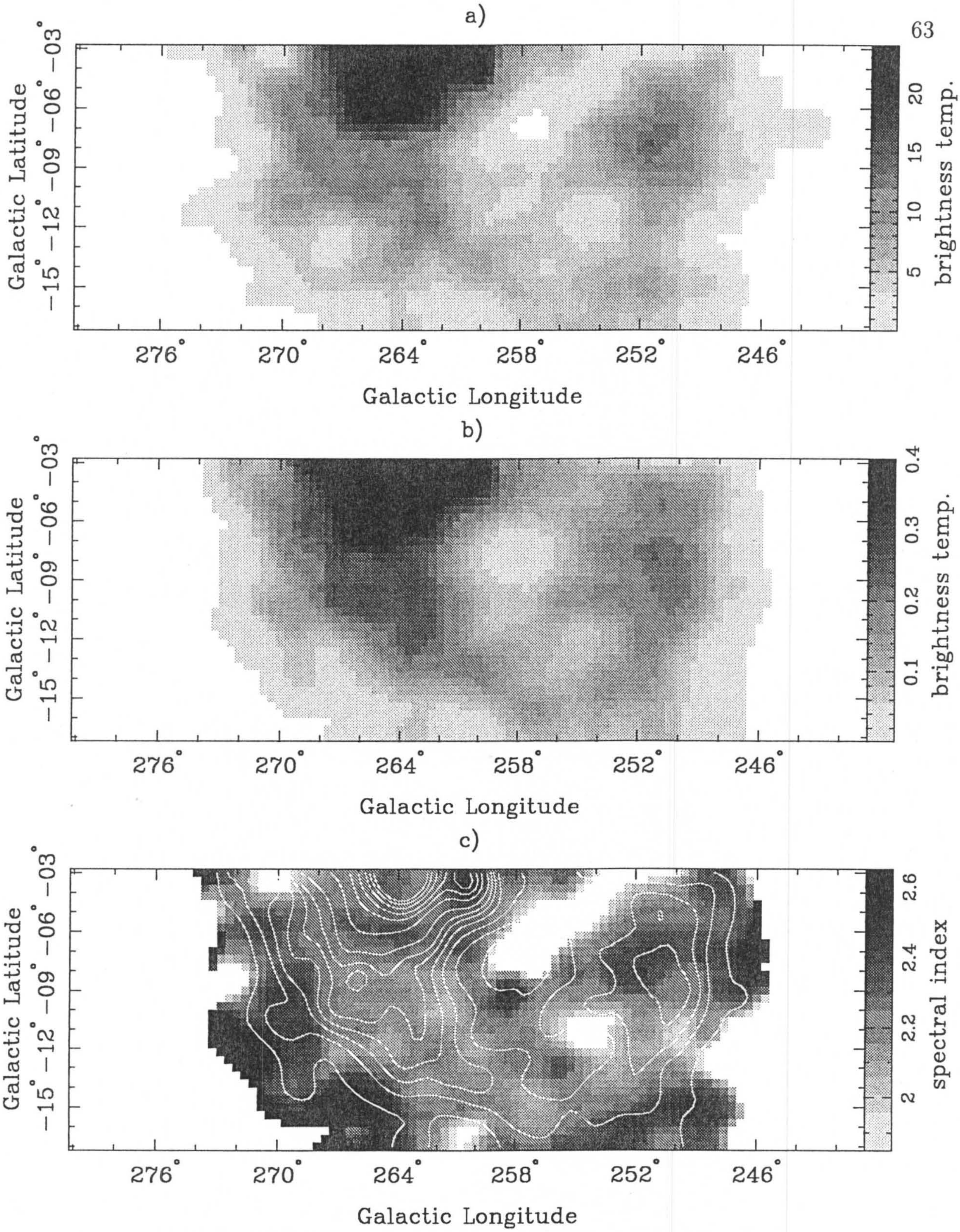

Figure [4-5]: The 408 and 2326 MHz Gum Nebula (1.2° resolution) at negative galactic latitudes, isolated from its background, is shown in a) and b) respectively. The spectral index image derived from the data in a) and b) is shown in c). The superimposed contour levels correspond to the 2326 MHz brightness temperatures from the background subtracted Gum Nebula shown in b).

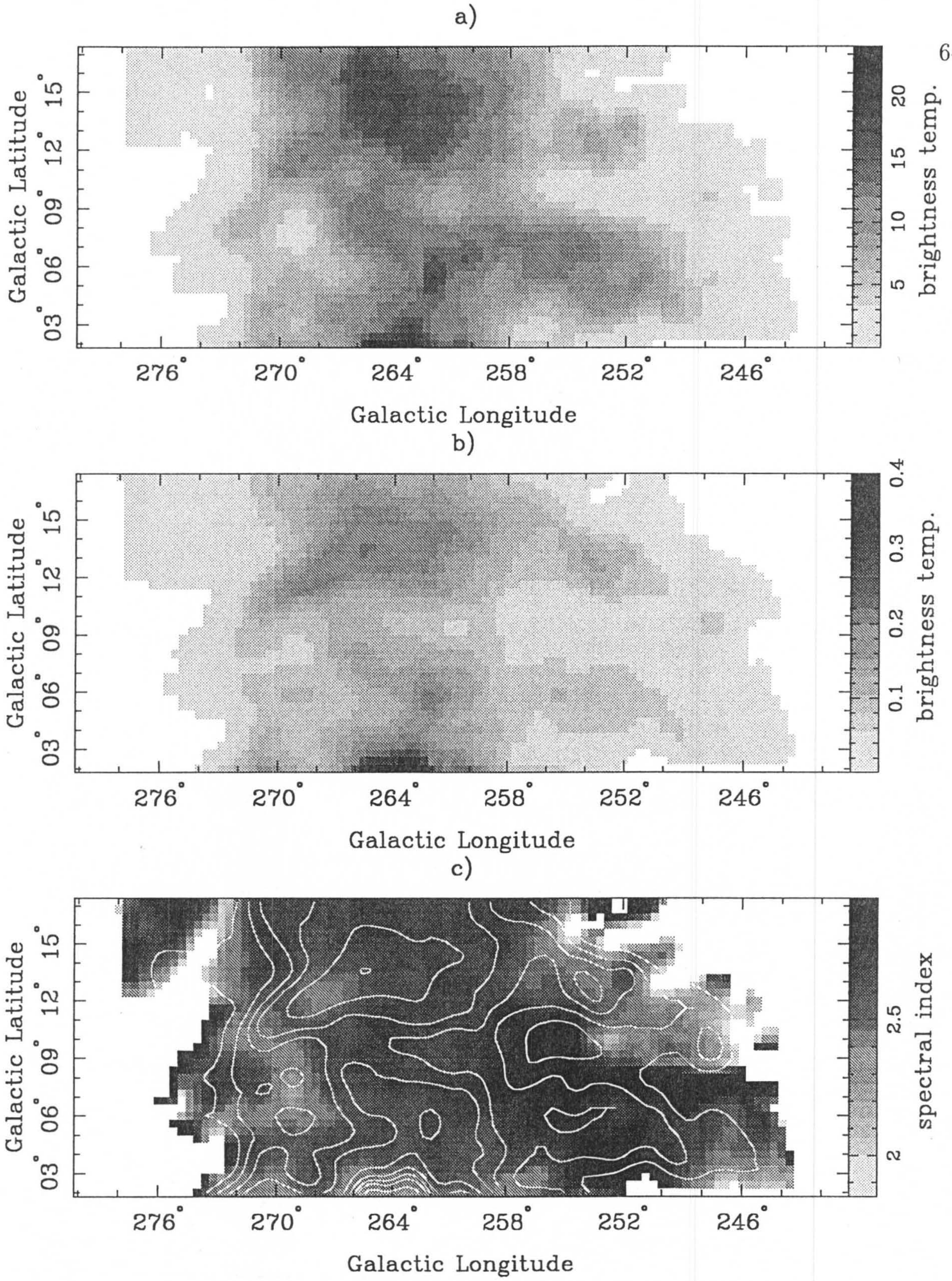

Figure [4-6]: The 408 and 2326 MHz Gum Nebula (1.2° resolution) at positive galactic latitudes, isolated from its background, is shown in a) and b) respectively. The spectral index image derived from the data in a) and b) is shown in c). The superimposed contour levels correspond to the 2326 MHz brightness temperatures from the background subtracted Gum Nebula shown in b).

4.2.2 Discussion of results and spectral index images

The negative galactic latitude spectral index plot (Fig. [4-5], (see also the constant latitude scan at $-9.4°$ in Fig. [4-3] b)), shows that the Gum Nebula has a thin, nonthermal, outer shell, within which there is a somewhat broader, thermal, inner shell and again a nonthermal centre region. Both the thermal and nonthermal shells are incomplete and discontinuous in places. The existence of the thin nonthermal outer shell is in doubt, because edge effects dominate in that region.

The positive galactic region (see Fig. [4-6] and the constant latitude scan at $+13.2°$ in Fig. [4-4] b)) exhibit the same trend, but with the thermal region too weak to override a general nonthermal spectral index.

This positive galactic latitude spectral index image is more difficult to interpret than that at negative galactic latitudes. The 34.5 MHz Vela spur is situated between galactic longitudes 266° and 260° and intrudes into the middle of the Gum Nebula from the galactic plane (seeFig. [4-6] a) and b)). This spur is not part of the Gum Nebula. From the discussion of the 34.5 MHz image (Dwarakanath & Udaya Shankar, 1990) of this region in section 3.1, it is clear that the spectral index of this spur is very steep. As this spur covers much of the low and intermediate positive galactic latitude range of the Gum Nebula, it will increase the value of the spectral index determined for the Gum Nebula in that region.

Note the $\frown$ feature in Fig. [4-6] b) between latitudes 9° and 16° and longitudes 272° and 250°, which essentially mirrors, through the galactic plane, the $\smile$ feature at negative galactic latitudes seen in Fig. [4-5] b) between latitudes $-7°$ and $-15°$ and longitudes 270° and 248°. This upper $\frown$ feature is clearly visible in the Hα image of the Gum Nebula (see Fig. [4-7]) and is thus the radio counterpart of the Gum Nebula.

Beneath this there is another less distinct $\frown$ feature between latitudes 4° and 7° and longitudes 272° and 248°, visible in Fig. [4-6] b) at 2326 MHz. This feature is very

Figure [4-7]: Iso-intensity Hα contours of the Gum Nebula and adjacent regions from a section of Sivan's Hα survey of the Milky Way (1974) as presented in A. Chanot's thesis. (I was provided with this picture by Sivan, but not given further details of the thesis in which it appears. The work published in Chanot & Sivan (1983) is based on this digitised image.) The contours are on a logarithmic scale and give $\log_{10}$ (intensity PDS), with the threshold at 0.45 and steps of size 0.1. The intensity PDS is related to Hα brightness in Rayleigh through figure 5 of Chanot & Sivan (1983). The best straight line fit to the points in that figure is [Intensity (Rayleigh)] = 22.7[Intensity PDS] - 59.1. (Private communication from Sivan) dominant in the 408 MHz image in Fig. [4-6] a), but not evident in the Hα image. This lower $\frown$ feature may be an Hα quiet part of the Gum Nebula, but probably belongs to the galactic plane. It's appearance as a $\frown$ structure may be an artifact of the background removal method.

Also not seen on the Hα image is the 408 MHz 6° diameter circular feature approximately centred on G263° +14° in Fig. [4-6] a). It is superimposed on part of the upper $\frown$ feature. Although still evident in the 2326 MHz image (Fig. [4-6] b)), it is less dominant compared to the $\frown$ feature at this frequency and thus definitely nonthermal emission as seen in Fig. [4-6] c). It is not clear whether this feature is part of the Gum Nebula, or a separate object.

As seen in the Hα image, high intensity Hα from the Gum Nebula extends, between longitudes 270° and 260°, from negative latitudes all the way up to latitude zero. At radio frequencies the pervasive, strong emission along the galactic plane, as well as the strong radio source, the Vela XYZ SNR, totally swamp the Gum Nebula emission and thus make it impossible to determine its spectral index in the region between latitudes $-7°$ and 0° and longitudes 270° and 260°.

4.2.3 Uncertainty in spectral indices

The validity of the interpretation of the results from this determination of a spectral index image depends on the uncertainty of the spectral index values.

An estimate of the uncertainty in the spectral index values was determined as follows. The rms error in equation (4-11) is given by

$$\begin{aligned} \Delta\beta_{rms} &= \sqrt{\left(\frac{\partial\beta}{\partial T_2}\Delta T_2\right)^2 + \left(\frac{\partial\beta}{\partial T_1}\Delta T_1\right)^2} \\ &= \frac{1}{\log(\nu_2/\nu_1)\ln 10}\sqrt{\left(\frac{\Delta T_2}{T_2}\right)^2 + \left(\frac{\Delta T_1}{T_1}\right)^2} \end{aligned} \tag{4-12}$$

Note that the bigger the ratio of the two frequencies at which the two images were observed, the smaller the uncertainty in β. As the only two frequency images available were the ones used in this work, this could not be used as a criterion for the selection of frequency images used. As it is, the two frequencies are about as far apart as one would wish them to be. If the lower frequency image was at a significantly lower frequency than 408 MHz, thermal sources would have reached their turnover frequencies. At much higher frequencies than 2326 MHz all sources become faint because of the $\nu^{-\beta}$ dependence, with nonthermal sources fading sooner.

Although there are several contributions to the uncertainty in the brightness temperature such as the calibration from antenna temperature to brightness temperature and the rms noise in the data, the major contribution in this case would be from the difference between the assumed linear background and the true background. From an inspection of Figs. [4-3] and [4-4] the latter is assumed to be $\approx$ 50 mK and $\approx$ 5 K for the 2326 MHz and the 408 MHz isolated source images respectively.

Figs. [4-8] and [4-9] show the spectral index image in a) and its corresponding uncertainty image in b) for the positive galactic latitude and negative galactic latitude regions respectively. The uncertainty in the spectral index values is generally less than 0.5 for the more intense regions. Only the very faint regions near the edges have an uncertainty greater than 0.5. As the plausible range of spectral index is only between 2 and 3, an uncertainty of the order of 0.5 is on the large side, though not entirely prohibitive. Thus conclusions about the Gum Nebula on the basis of these spectral index images must be treated with caution. Hence one may say that there are regions of different spectral index, but not that the flatter spectral index regions are definitely thermal.

4.3 Spectral index image at 1.7° resolution

I repeated the process at the lower resolution of 1.7°. I chose the two background determining points totally independently of the choices I made for the 1.2° work. At this resolution the background determination at positive galactic latitudes was

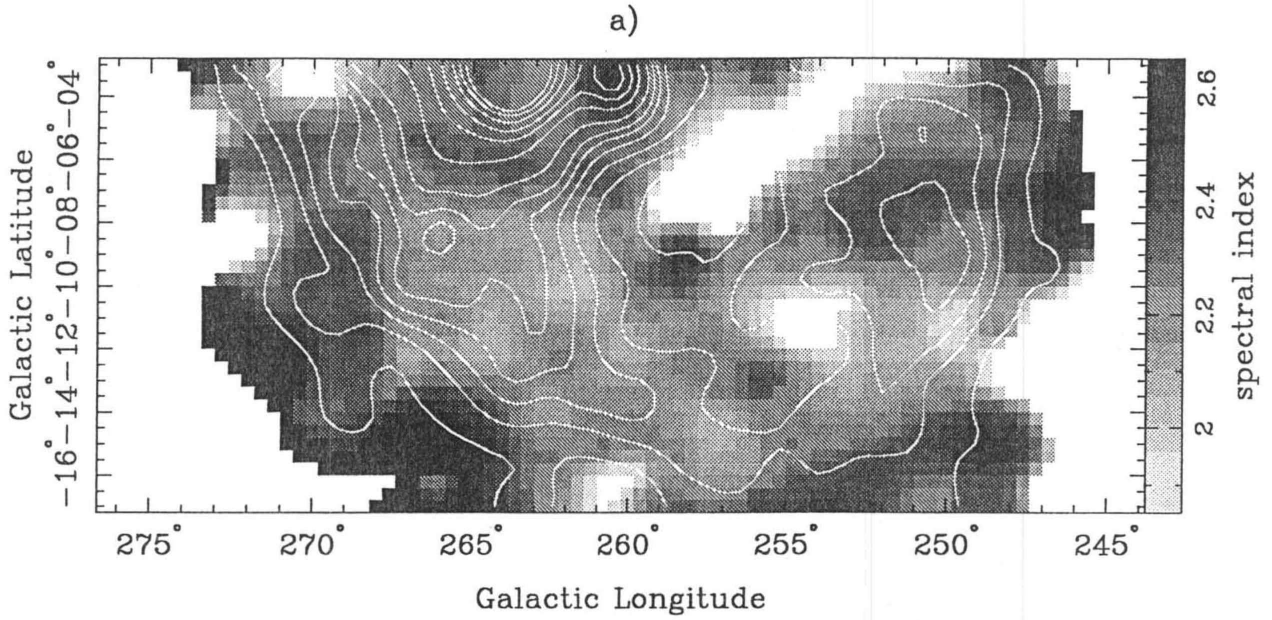

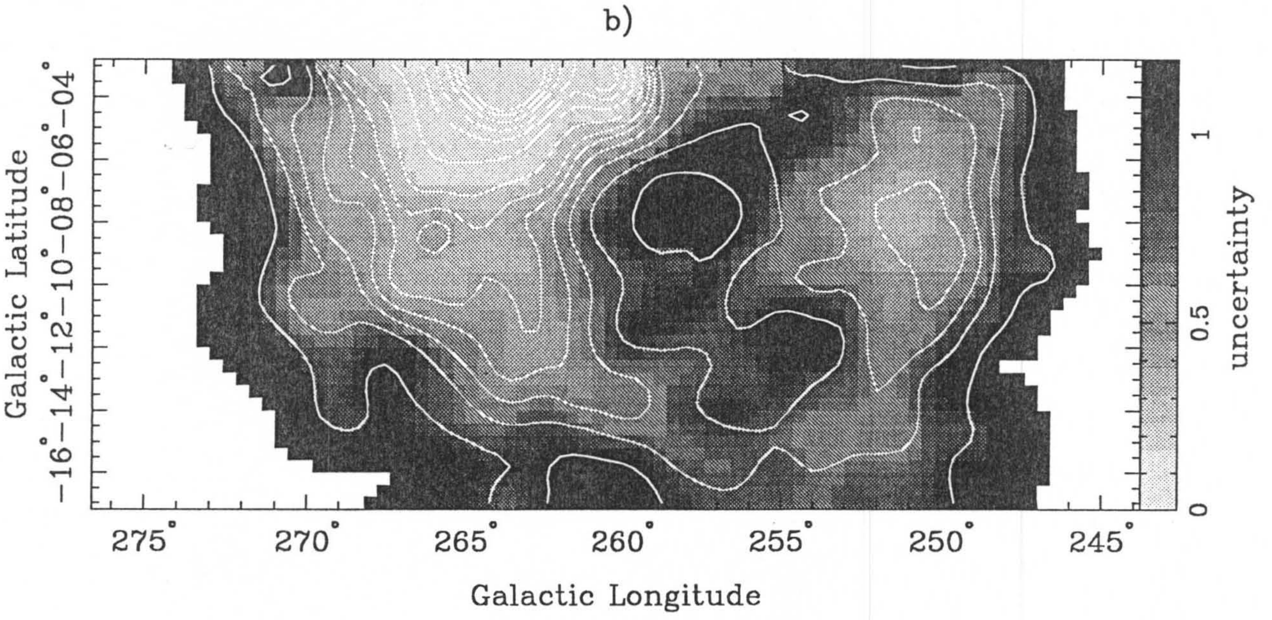

Figure [4-8]: b) shows the spectral index uncertainty image corresponding to a), the 1.2° resolution, negative galactic latitude spectral index image of the Gum Nebula. The superimposed contour levels correspond to the 2326 MHz brightness temperatures from the background subtracted Gum Nebula shown in b) of Fig. [4-5].

a)

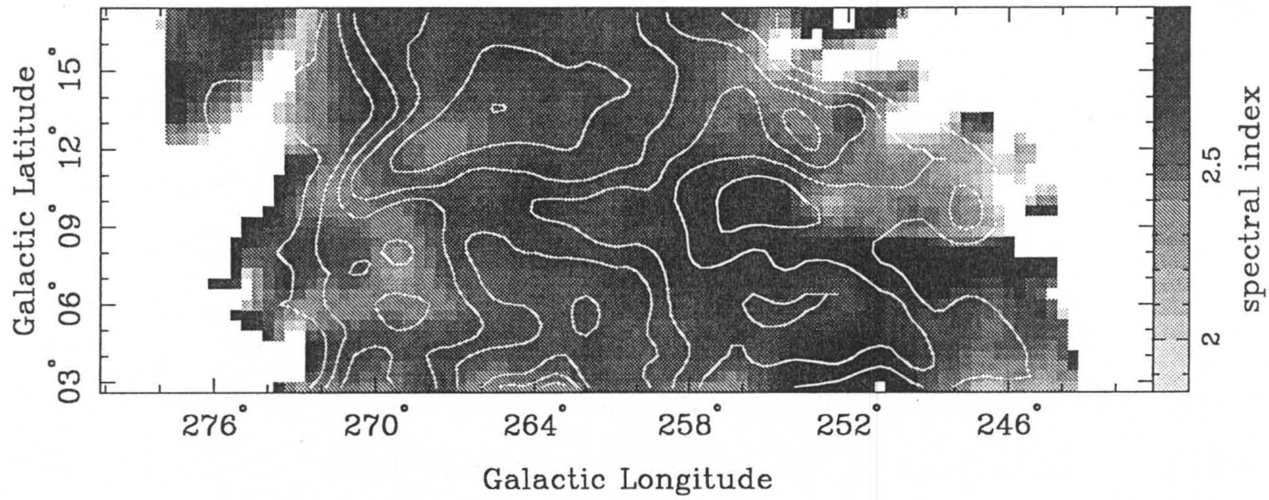

b)

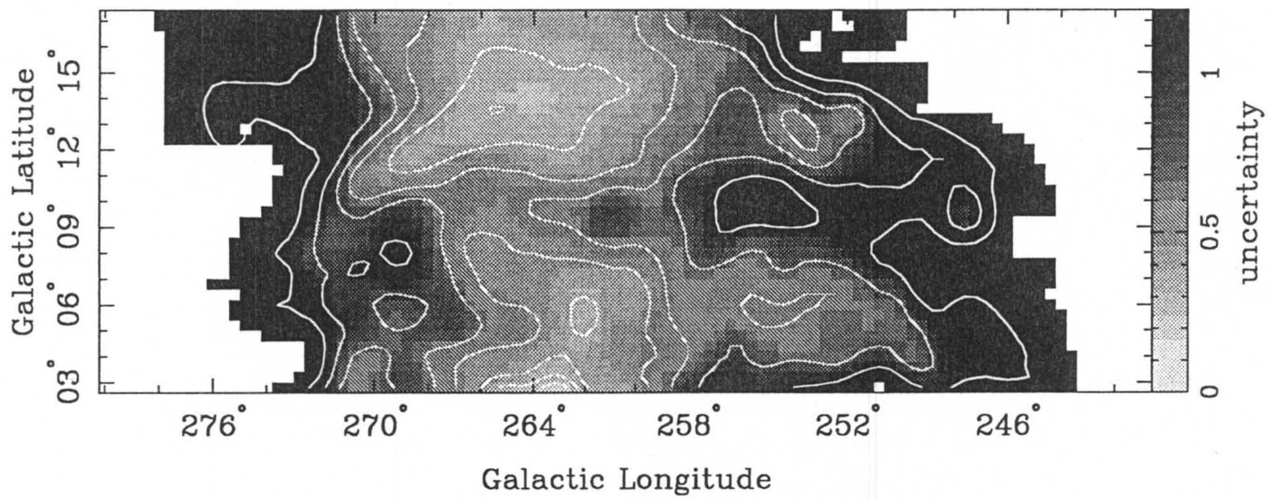

Figure [4-9]: b) shows the spectral index uncertainty image corresponding to a), the 1.2° resolution, positive galactic latitude spectral index image of the Gum Nebula. The superimposed contour levels correspond to the 2326 MHz brightness temperatures from the background subtracted Gum Nebula shown in b) of Fig. [4-6].

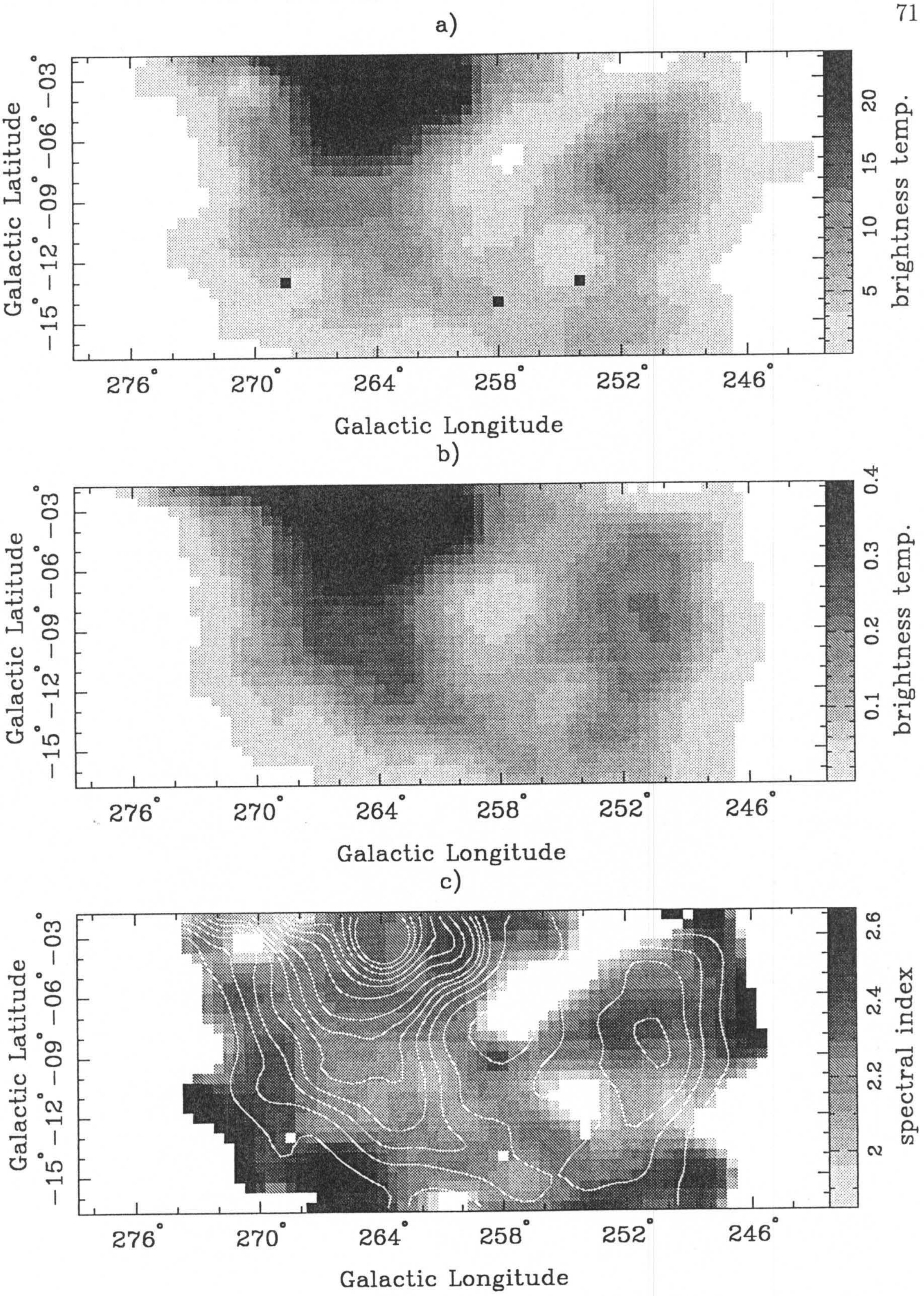

Figure [4-10]: The 408 and 2326 MHz Gum Nebula (1.7° resolution) at negative galactic latitudes, isolated from its background is shown in a) and b) respectively. The spectral index image derived from the data in a) and b) is shown in c). The superimposed contour levels correspond to the 2326 MHz brightness temperatures from the background subtracted Gum Nebula shown in b).

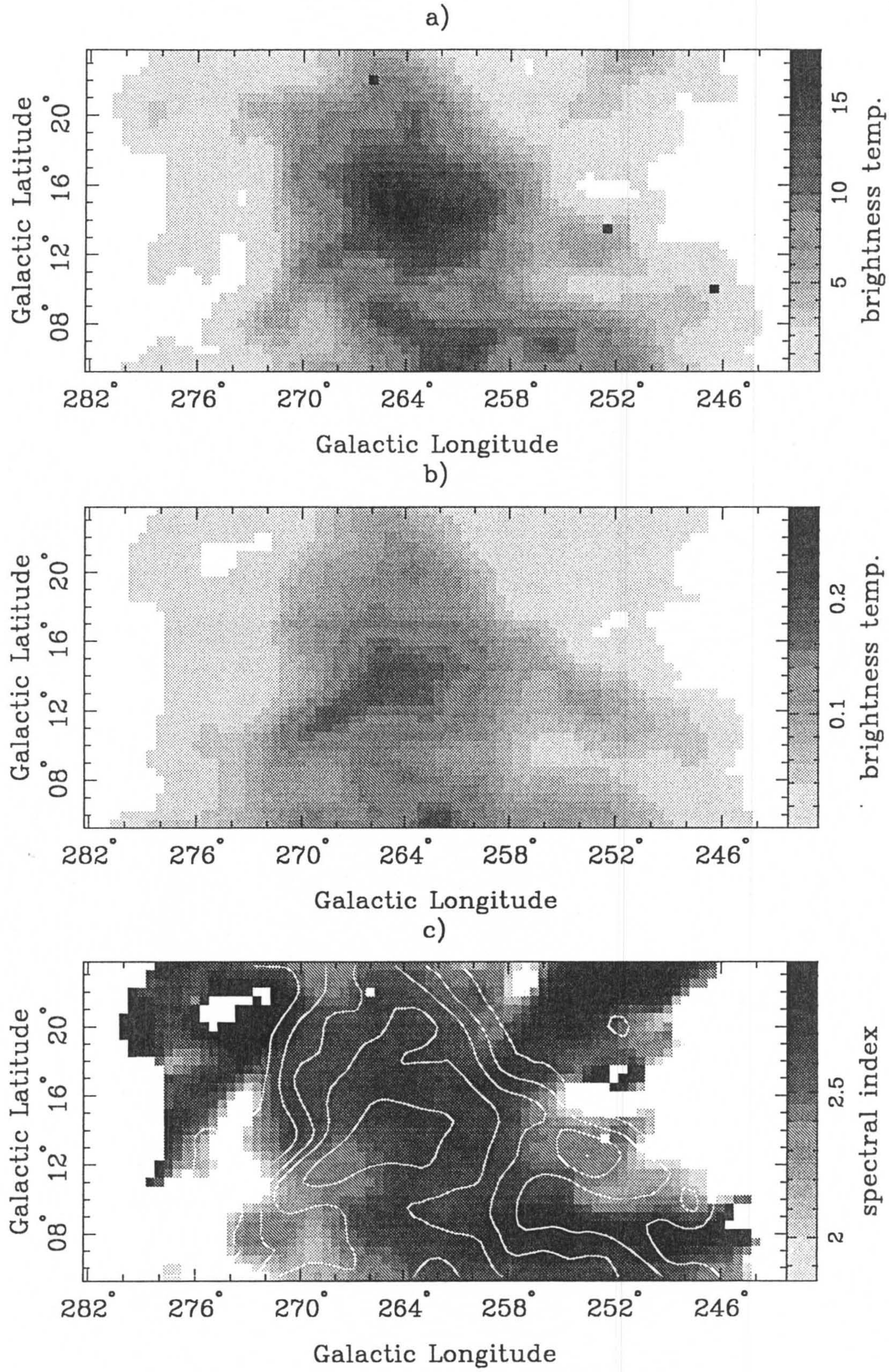

Figure [4-11]: The 408 and 2326 MHz Gum Nebula (1.7° resolution) at positive galactic latitudes, isolated from its background is shown in a) and b) respectively. The spectral index image derived from the data in a) and b) is shown in c). The superimposed contour levels correspond to the 2326 MHz brightness temperatures from the background subtracted Gum Nebula shown in b).

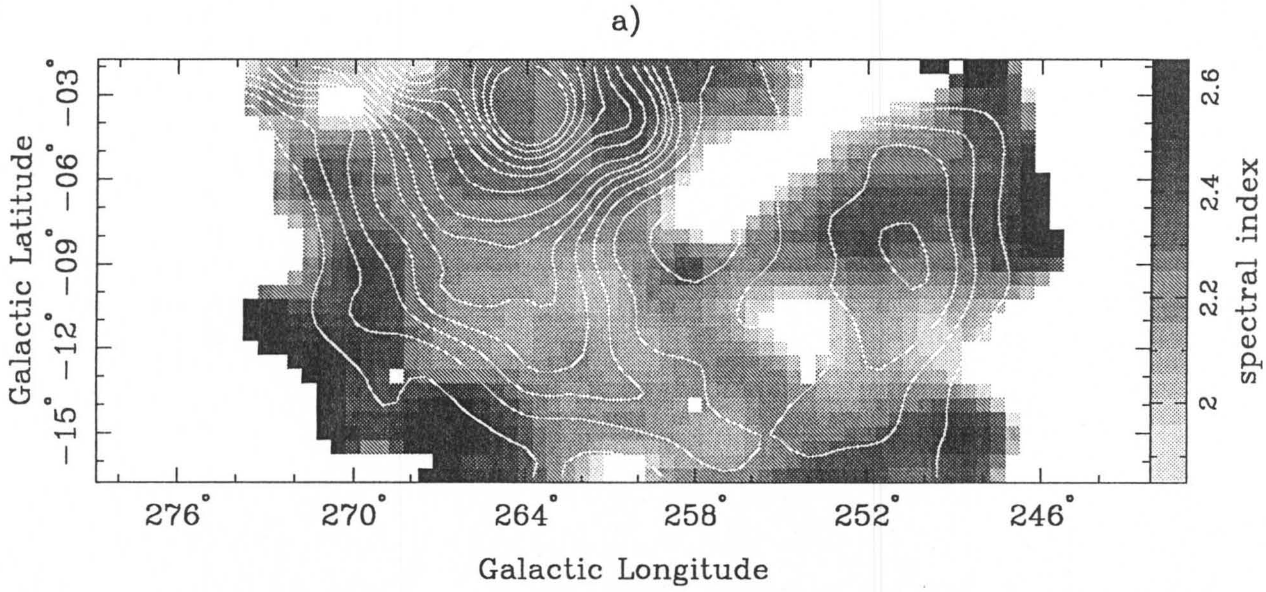

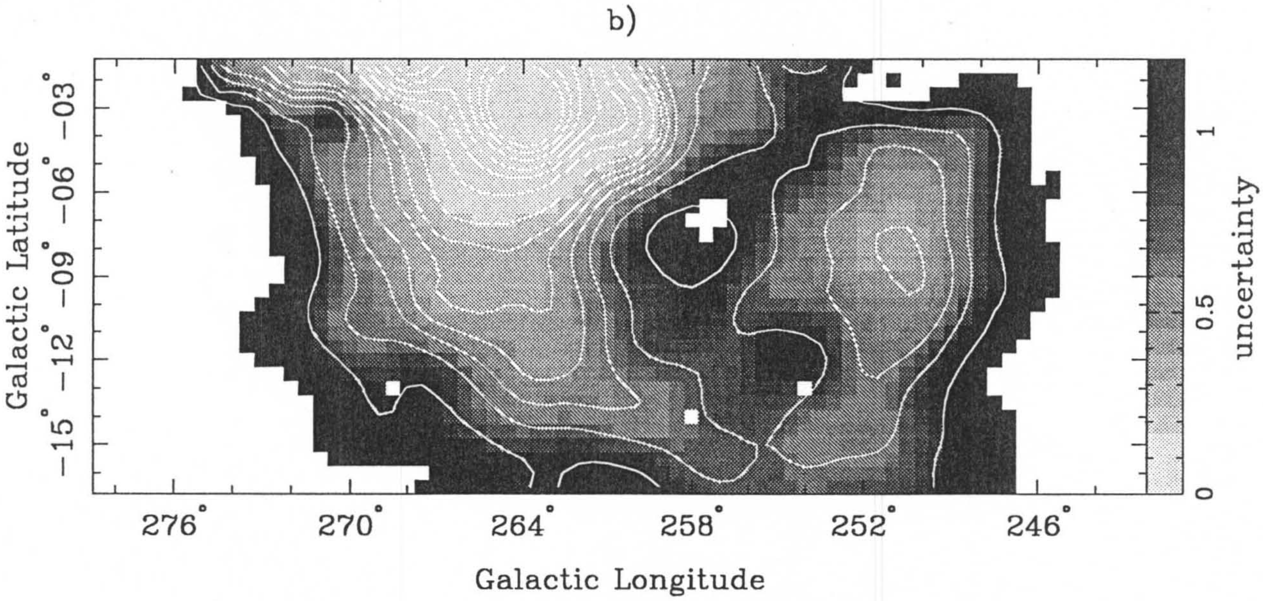

Figure [4-12]: b) shows the spectral index uncertainty image corresponding to a), the 1.7° resolution, negative galactic latitude spectral index image of the Gum Nebula. The superimposed contour levels correspond to the 2326 MHz brightness temperatures from the background subtracted Gum Nebula shown in b) of Fig. [4-10].

a)

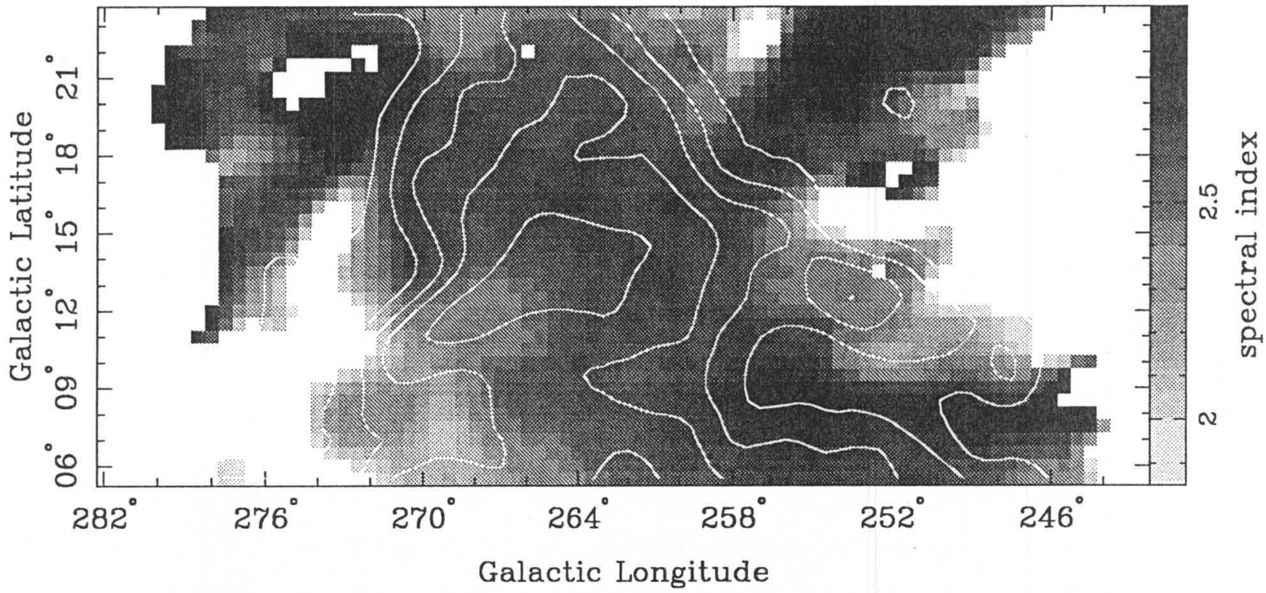

b)

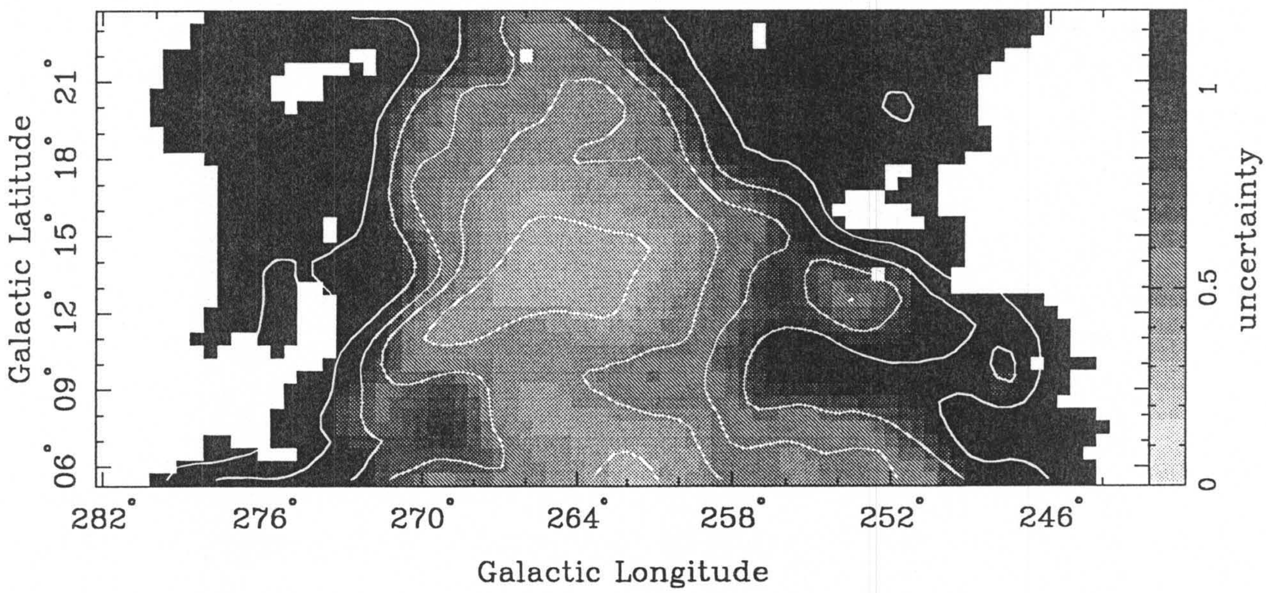

Figure [4-13]: b) shows the spectral index uncertainty image corresponding to a), the 1.7° resolution positive galactic latitude spectral index image of the Gum Nebula. The superimposed contour levels correspond to the 2326 MHz brightness temperatures from the background subtracted Gum Nebula shown in b) of Fig. [4-11].

extended to the region above 17° in order to get a better view of the circular feature at G263 + 14.

It was also investigated whether it was possible to extend the background determination at negative galactic latitudes to include the oblong feature seen in the Hα image (see Fig. [4-7]) around longitude 238° and latitude −4°. It is not clear from the literature whether this feature is considered as part of the Gum Nebula. Insisting that the GUMBACK method of determining a background included this feature was not possible, as this resulted in negative brightness temperatures for the isolated image over a large extent in longitude at both frequencies.

The results of the 1.7° resolution work are shown in figures [4-10], [4-11], [4-12], [4-13]. The 3 isolated black pixels in the negative and positive galactic latitude image at 408 MHz are due to an inappropriate setting of the blank value in the FITS (Flexible Image Transport System, Wells et al., 1981) header of the images and should thus be ignored. This problem was subsequently eliminated.

Note how close the correspondence is between these spectral index results and those for the 1.2° resolution. Thus the interpretation of the 1.7° results is the same as given for the 1.2° results.

The uncertainty in the brightness temperature values used for the calculation of the spectral index uncertainty was taken to be 0.035 K and 3.5 K at 2326 MHz and 408 MHz respectively. These lower values, compared to those at the resolution of 1.2°, are justified as the additional smoothing reduces the temperature variation in the maps, which in turn leads to a flatter background. The resultant uncertainty (see Figs. [4-12] and [4-13]) is thus marginally lower than that of the 1.2° resolution work.

4.4 Conclusion

From the above results, I conclude that the Gum Nebula has a thin, nonthermal, outer shell, within which there is a somewhat broader, thermal, inner shell and again a nonthermal centre region. Both the thermal and nonthermal shells are incomplete and discontinuous in places. The existence of the thin nonthermal outer shell is in doubt, because edge effects dominate in that region. This scenario is in agreement with the model of old SNR with H II shell proposed by Reynolds (1976b).

Neither the 1.2° nor the 1.7° resolution spectral index images show any evidence of a thermal structure of the extent and at the position of the IRAS-Vela ring proposed by Srinivasan Sahu (1992).

The uncertainty in the 1.2° and 1.7° resolution spectral index images is just large enough to cause concern about the reliability of the above conclusions. Thus another determination of the spectral index was made by a completely independent method. This other method for spectral index determination is based on the temperature versus temperature plot i.e. TT- plot. It allows the determination of the spectral index without a knowledge of absolute intensity levels or background radiation (Turtle et al., 1962).

Chapter 5

TT-plot spectral index determination

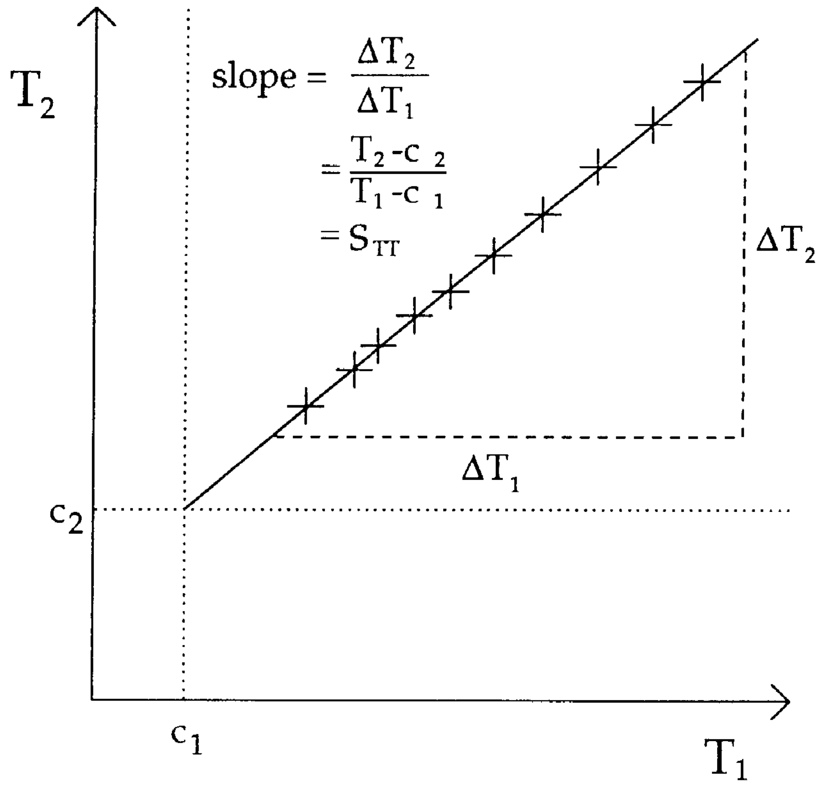

Figure [5-1]: TT-plot for a region of constant spectral index situated on top of a background composed of isotropic components whose total brightness temperature is c_1 at frequency ν_1 and c_2 at frequency ν_2. The slope of the graph gives the ratio $(T_2 - c_2)/(T_1 - c_1)$ for the whole region.

A TT-plot is a plot of the brightness temperatures at one frequency versus the brightness temperatures at another frequency for all the sampled positions in a region of interest—the brightness temperature images at each frequency having the same resolution and sampling positions (Turtle et al., 1962).

Assume that a region of constant spectral index is situated on top of a background composed of isotropic components whose total brightness temperature is c_1 at frequency ν_1 and c_2 at frequency ν_2. A plot of brightness temperature T_2 versus T_1 (see Fig. [5-1]) shows that the ratio, $(T_2 - c_2)/(T_1 - c_1)$, of the isolated source brightness temperatures is identical to any $\Delta T_{b,\nu_2}/\Delta T_{b,\nu_1}$ on the resultant line. Thus the slope, S_{TT}, of this graph may be used to determine the spectral index, β:

$$\beta = -\log\left(\frac{\Delta T_{b,\nu_2}}{\Delta T_{b,\nu_1}}\right) / \log\left(\frac{\nu_2}{\nu_1}\right) \tag{5-1}$$

$$\beta = -\frac{\log S_{TT}}{\log \nu_2/\nu_1} \tag{5-2}$$

Hence the determination of the spectral index from a TT-plot avoids the problem of having to determine the absolute zero of the surveys or the background of the source of interest.

Note that β is thus undefined for a negative slope. This agrees with what the physical radiation processes predict. From equation (4-8)

$$k(\ell, b) = T_1(\ell, b)\nu_1^{\beta} \tag{5-3}$$

Thus, from equation (4-9), substituting for $k(\ell, b)$ from equation (5-3)

$$\begin{aligned} T_2(\ell, b) &= k(\ell, b)\nu_2^{-\beta} && (5\text{-}4) \\ &= T_1(\ell, b)\nu_1^{\beta}\nu_2^{-\beta} && (5\text{-}5) \\ &= T_1(\ell, b)\frac{\nu_1}{\nu_2}^{\beta} && (5\text{-}6) \end{aligned}$$

a)

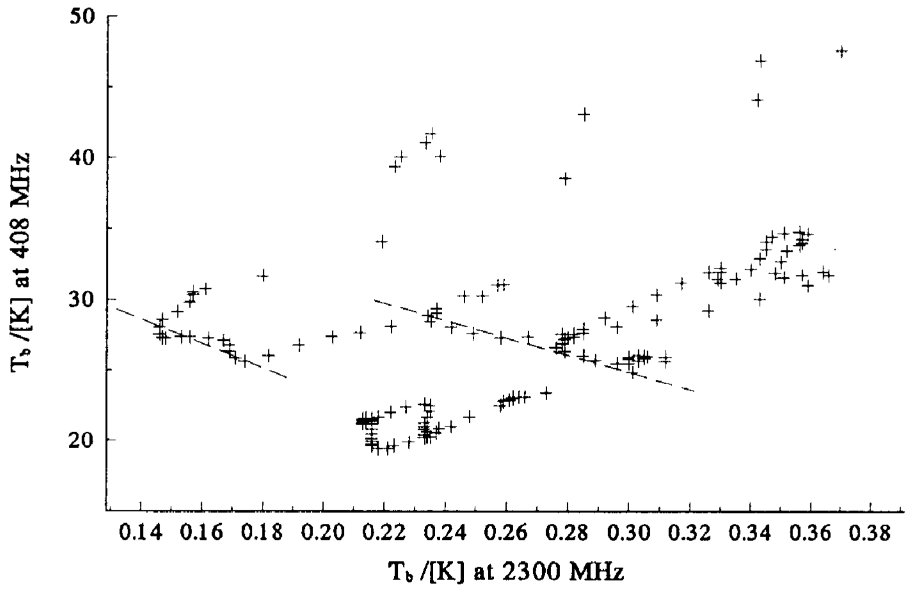

b)

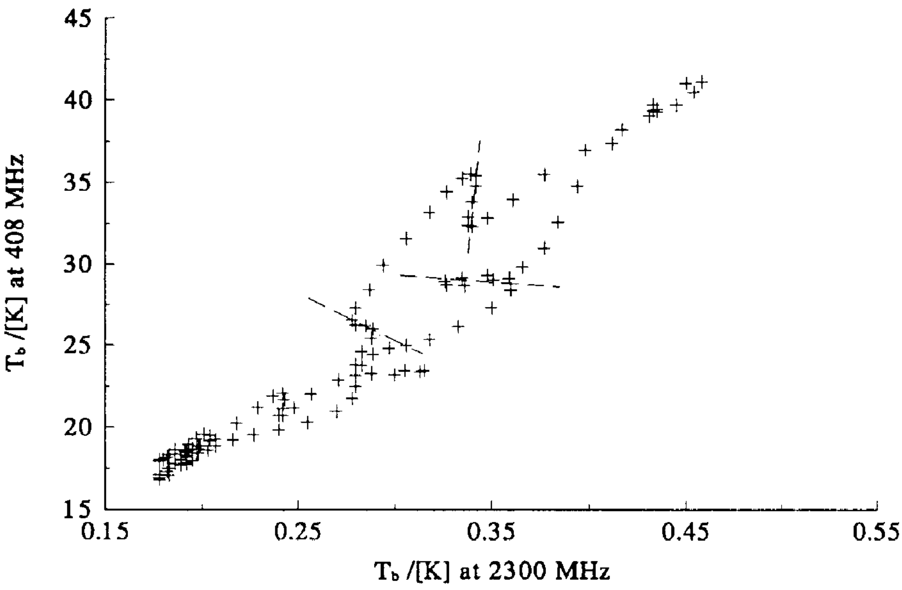

Figure [5-2]: a) Constant latitude TT-plot of the 408 MHz versus 2326 MHz data at 1.7° resolution for galactic longitude 300° to 220° at galactic latitude +10°. The dashed line segments show regions that exhibit negative slopes. b) Constant longitude TT-plot of the 408 MHz versus 2326 MHz data at 1.7° resolution for galactic latitude −30° to +30° at galactic longitude 256°. The dashed line segments show regions that exhibit negative slopes and an unrealistically steep slope.

Since the factor $(\nu_1/\nu_2)^\beta$ is always positive, negative ratios of $\Delta T_{b,\nu_2}/\Delta T_{b,\nu_1}$ are not possible. However, TT-plots of real data (see Fig. [5-2]) do at times exhibit sections where the line has a negative slope. I discovered the cause of this phenomenon and others, such as the very steeply sloped line segment in Fig. [5-2] b), in the investigation of TT-plots of simulated data. This is presented in section 5.2.

It is evident from Fig. [5-2] that the TT-plots of real data are made up of sections with different slopes. This is as expected from a region of sky in which there are sources emitting radiation by different processes and under different conditions. If one wants to identify the different slopes with their source positions on the sky, it is worth obtaining a TT-plot map. For this the region is divided into many equally sized blocks. For the pixel values in each block a TT-plot is made, scaled to fit into the block, and positioned in a coordinate grid as shown in Fig. [5-3]. The best straight line fit is shown in each block and the upper limit, estimate of true value and lower limit of the spectral index are written in the top left corner of each block. A blank space indicates that the corresponding value is undefined. This thus provides a way of regaining some positional information.

It is clear from Fig. [5-3] that real data rarely produces a straight line plot. The cause for this was investigated by modelling on the computer various scenarios at two different frequencies, putting the images through an artificial observing process and finally producing TT-plots of this simulated data. The details of that investigation are given in section 5.2.

I also investigated whether the intercept of an appropriate TT-plot might provide sufficient information to determine the relative zero base levels of the two frequency maps, or the background level on which a source is positioned. This seemed to be a worthwhile approach as some work along these lines had been done by Reich & Reich (1988).

Figure [5-3]: A subblock TT-plot map for 408 MHz data vs 2326 MHz data at resolution of 0.85°. The upper limit, estimate of the true value and the lower limit of the spectral index were determined from the TT-plot in the subblock by using the Theil method (see section 5.4) of fitting a straight line to the data points.

5.1 Theoretical Investigation of TT-plots

The sky radiation at a frequency ν is composed of several anisotropic components (i.e. with brightness temperature gradients) $T_{Ai}(\ell, b)(i = 1 \ldots n)$ and isotropic components (i.e. of constant brightness temperature), $T_{Bj}(j = 1 \ldots m)$. Examples of the latter are the cosmic microwave background and the unresolved extragalactic sources.

Hence the observed brightness temperature at a particular position (ℓ, b) at a frequency $\nu 1$ is:

$$T_{\nu 1}(\ell, b) = \sum_{i=1}^{n} T_{Ai}(\ell, b) + \sum_{j=1}^{m} T_{Bj} \tag{5-7}$$

It is assumed that the continuum spectra of components T_{Ai} and T_{Bj} follow the power law (see equation (4-8)):

$$T_{Ai}(\ell, b) = k_{Ai}(\ell, b)\nu^{-\beta_{Ai}} \tag{5-8}$$

where k_{Ai} is a constant at each position (ℓ, b).

Therefore

$$k_{Ai}(\ell, b) = T_{Ai}(\nu, \ell, b)\nu^{\beta_{Ai}} \tag{5-9}$$

and similarly for the isotropic

$$T_{Bj} = \kappa_{Bj}\nu^{-\beta_{Bj}} \tag{5-10}$$

with

$$\kappa_{Bj} = T_{Bj}(\nu)\nu^{\beta_{Bj}} \tag{5-11}$$

Thus the observed temperature at a particular position (ℓ, b) at frequency $\nu 2$ is (from equations (5-8), (5-9), (5-10) and (5-11)):

$$T_{\nu 2}(\ell, b) = \sum_{i=1}^{n} (\frac{\nu 1}{\nu 2})^{\beta_{Ai}} T_{Ai}(\ell, b) + \sum_{j=1}^{m} (\frac{\nu 1}{\nu 2})^{\beta_{Bj}} T_{Bj} \tag{5-12}$$

As we are interested in determining the slope and the intercept of a TT-plot for the brightness temperatures at these two frequencies (see Fig. [5-1]) we wish to put equation (5-12) in the form:

$$T_{\nu 2}(\ell, b) = \text{“slope”} T_{\nu 1}(\ell, b) + \text{“intercept”} \tag{5-13}$$

This is not possible mathematically, unless we reduce the number of terms in the summations of equation (5-12) significantly.

A simple case of equation (5-12) is one with one isotropic T_A and one non- isotropic component T_B:

$$T_{\nu 1}(\ell, b) = T_A(\ell, b) + T_B \tag{5-14}$$

Thus

$$T_{\nu 2}(\ell, b) = \left(\frac{\nu 1}{\nu 2}\right)^{\beta_A} T_A(\ell, b) + \left(\frac{\nu 1}{\nu 2}\right)^{\beta_B} T_B \tag{5-15}$$

Using equation (5-14) for $T_A(\ell, b)$ in the above equation and rearranging, one obtains

$$T_{\nu 2}(\ell, b) = \left(\frac{\nu 1}{\nu 2}\right)^{\beta_A} T_{\nu 1}(\ell, b) + T_B \left[\left(\frac{\nu 1}{\nu 2}\right)^{\beta_B} - \left(\frac{\nu 1}{\nu 2}\right)^{\beta_A}\right] \tag{5-16}$$

Since T_B is isotropic and thus not a function of position (ℓ, b), we have for a plot of $T_{\nu 2}$ vs $T_{\nu 1}$:

$$\text{“slope”} = \left(\frac{\nu 1}{\nu 2}\right)^{\beta_A} \tag{5-17}$$

$$\text{“intercept”} = T_B \left[\left(\frac{\nu 1}{\nu 2}\right)^{\beta_B} - \left(\frac{\nu 1}{\nu 2}\right)^{\beta_A}\right] \tag{5-18}$$

Note that the intercept is a function of the spectral index of the non- isotropic component as calculated from the slope.

If we increase the number of isotropic and anisotropic radiation components to two or more each, the conversion to the form of equation (5-13) becomes intractable.

Some progress may, however, be made by considering the anisotropic components at frequency $\nu 1$ to have the same brightness temperature distribution, i.e. $T_{A1}(\ell, b) = T_{A2}(\ell, b) = T_{A3}(\ell, b) = Y(\ell, b)$ say. Also, thus far the offset brightness temperature that each map has from absolute zero has been assumed to be zero. As that is not generally the case, such offset brightness temperatures are now included for both maps.

Then for three such isotropic and three anisotropic components:

$$T_{\nu 1}(\ell, b) = 3Y(\ell, b) + T_{B1} + T_{B2} + T_{B3} + T_{off1} \tag{5-19}$$

where T_{off1} is the difference between the absolute zero temperature and the zero relative to which observations at $\nu 1$ were made, assumed here to be independent of position.

As the separate anisotropic and isotropic components are not assumed to have the same spectral index:

$$\begin{aligned} T_{\nu 2}(\ell, b) = \; & \left(\tfrac{\nu 1}{\nu 2}\right)^{\beta_{A1}} Y(\ell, b) + \left(\tfrac{\nu 1}{\nu 2}\right)^{\beta_{A2}} Y(\ell, b) + \left(\tfrac{\nu 1}{\nu 2}\right)^{\beta_{A3}} Y(\ell, b) + \\ & \left(\tfrac{\nu 1}{\nu 2}\right)^{\beta_{B1}} T_{B1} + \left(\tfrac{\nu 1}{\nu 2}\right)^{\beta_{B2}} T_{B2} + \left(\tfrac{\nu 1}{\nu 2}\right)^{\beta_{B3}} T_{B3} + T_{off2} \end{aligned} \tag{5-20}$$

Where T_{off2} is the constant offset of $T_{\nu 2}(\ell, b)$ relative to the absolute zero temperature.

For convenience let $n_{Ai} = \left(\frac{\nu 1}{\nu 2}\right)^{\beta_{Ai}}$ and $n_{Bj} = \left(\frac{\nu 1}{\nu 2}\right)^{\beta_{Bj}}$. Then solving equation (5-19) for $Y(\ell, b)$ and substituting in equation (5-20) gives

$$\begin{aligned} T_{\nu 2}(\ell, b) = & \left(\tfrac{n_{A1}+n_{A2}+n_{A3}}{3}\right) T_{\nu 1}(\ell, b) + T_{B1}\left(n_{B1} - \tfrac{n_{A1}+n_{A2}+n_{A3}}{3}\right) + \\ & T_{B2}\left(n_{B2} - \tfrac{n_{A1}+n_{A2}+n_{A3}}{3}\right) + T_{B3}\left(n_{B3} - \tfrac{n_{A1}+n_{A2}+n_{A3}}{3}\right) + \\ & T_{off2} - T_{off1}\left(\tfrac{n_{A1}+n_{A2}+n_{A3}}{3}\right) \end{aligned} \tag{5-21}$$

Hence

$$\text{“slope”} = \left(\frac{n_{A1} + n_{A2} + n_{A3}}{3}\right) \tag{5-22}$$

$$\begin{aligned} \text{“intercept”} = & T_{B1}\left(n_{B1} - \tfrac{n_{A1}+n_{A2}+n_{A3}}{3}\right) + T_{B2}\left(n_{B2} - \tfrac{n_{A1}+n_{A2}+n_{A3}}{3}\right) + \\ & T_{B3}\left(n_{B3} - \tfrac{n_{A1}+n_{A2}+n_{A3}}{3}\right) + T_{off2} - T_{off1}\left(\tfrac{n_{A1}+n_{A2}+n_{A3}}{3}\right) \end{aligned} \tag{5-23}$$

Hence the slope of a TT-plot for several superimposed anisotropic components will give rise to a weighted average of the spectral indices of the individual components. This is also true in the more general case of arbitrary brightness temperature of individual anisotropic components at $\nu 1$. There is, in fact, no method for distinguishing a genuine spatial variation of spectral index across a source from that caused by the superposition of a smaller relatively strong background source.

5.1.1 Offset determination

If one wishes to use the intercept of the TT-plot for determining the offset relative to zero of the two maps, then, as seen from equation (5-23), one may get closer to the goal by subtracting known isotropic radiation components from each map prior to making the TT-plot. The two components that are relevant here are the cosmic microwave background, which has a temperature of 2.73 $\pm$ 0.05 K (Smoot et al., 1985) and thus by definition the same brightness temperature, and the contribution of the unresolved extragalactic sources given by Bridle (1967) as

$$T_{exgal}(\nu) = 30K(\frac{\nu}{178MHz})^{-2.75} \tag{5-24}$$

Suppose that all these non-instrumental isotropic components have been subtracted from the two images of interest. Then, including just one anisotropic component, we have:

$$T_{\nu 1}(\ell, b) = T_A(\ell, b) + T_{off1} \tag{5-25}$$

and

$$T_{\nu 2}(\ell, b) = \left(\frac{\nu 1}{\nu 2}\right)^{\beta_A} T_A(\ell, b) + T_{off2} \tag{5-26}$$

Substituting from equation (5-25) for $T_A(\ell, b)$ in the above equation one obtains

$$T_{\nu 2}(\ell, b) + \left(\frac{\nu 1}{\nu 2}\right)^{\beta_A} T_{\nu 1}(\ell, b) + T_{off2} - \left(\frac{\nu 1}{\nu 2}\right)^{\beta_A} T_{off1} \tag{5-27}$$

This is Reich & Reich's (1988) equation 2. They go on to assume that T_{off1} is zero, i.e. that the image at frequency $\nu 1$ has been absolutely calibrated. Smoothing both maps to a 15° resolution they choose a relatively empty region of sky for which to perform a TT-plot. The intercept of this TT-plot then gives the offset of the image at frequency $\nu 2$ relative to absolute zero.

As the absolute calibration of a survey is a lengthy process, it is worth investigating whether it is possible to obtain T_{off1} and T_{off2} if neither of the surveys are absolutely calibrated. Hence, in the following, it is assumed that T_{off1} is non-zero in equation (5-27).

If there are two areas, C and D, of different spectral index in the images as shown in (Fig. [5-4], then we have for each area at frequency 2 (see equation (5-27)):

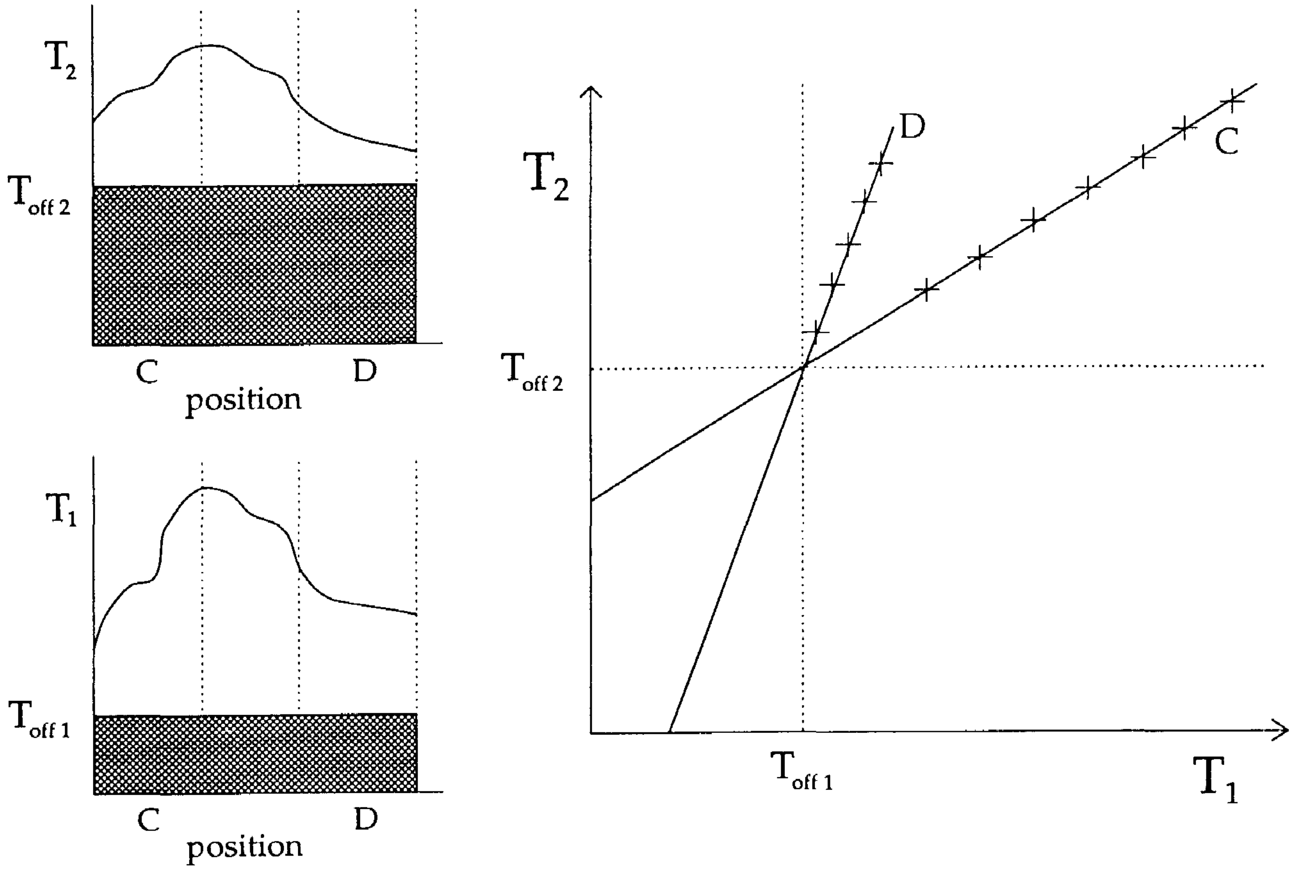

Figure [5-4]: Cross-sections through two regions of different spectral index, C and D. On the right the combined TT-plot for both regions is shown.

$$T_{C2} = n_C T_{C1} + T_{off2} - n_C T_{off1} \tag{5-28}$$

$$T_{D2} = n_D T_{D1} + T_{off2} - n_D T_{off1} \tag{5-29}$$

where 1 and 2 refer to frequencies $\nu 1$ and $\nu 2$ and n_C and n_D are defined as above. A TT-plot of T_{C2} vs T_{C1} gives slope n_C and intercept I_C where

$$I_C = T_{off2} - n_C T_{off1} \tag{5-30}$$

A TT-plot of T_{D2} vs T_{D1} gives slope n_D and interceptI_D where

$$I_D = T_{off2} - n_D T_{off1} \tag{5-31}$$

Equation (5-30) and equation (5-31) are two equations with two unknowns T_{off1} and T_{off2}. Solving for these, we have

$$T_{off1} = \frac{I_D - I_C}{n_C - n_D} \tag{5-32}$$

$$T_{off1} = \frac{n_C I_D - n_D I_C}{n_C - n_D} \tag{5-33}$$

Since all of I_D, I_C, n_C and n_D are known the relative offsets of the two maps may be determined in this manner.

n_C must not be equal to n_D for equations (5-32) and (5-33) to be meaningful. Thus the two regions have to have different spectral indices. Also, as even small uncertainties in the slope will give rise to large uncertainties in the intercept values, the TT-plots for region C and D have to be good i.e. the points have to closely follow a straight line.

In the above it was assumed that the spectral indices of region C and D are pure. As seen earlier, a region with superimposed anisotropic sources gives rise to a weighted spectral index of intermediate value. Such a region cannot be distinguished from a region of pure spectral index of the same value. The effect of such a region of mixed spectral index on the determination of the offsets of the maps in the above manner is investigated below.

Suppose that the anisotropic component in region C at frequency $\nu 1$ is made up of the sum of two anisotropic components $X(\ell, b)$ and $Z(\ell, b)$ which have different spectral indices, β_x and β_z respectively. Thus for this region C, with n_x and n_z defined in the usual way:

$$T_{C1}(\ell, b) = X(\ell, b) + Z(\ell, b) + T_{off1} \tag{5-34}$$

and

$$\begin{aligned} T_{C2}(\ell, b) &= n_x X(\ell, b) + n_z Z(\ell, b) + T_{off2} && (5\text{-}35) \\ &= (n_x + n_z) T_{C1}(\ell, b) - n_x Z(\ell, b) - n_z X(\ell, b) \\ &\quad -(n_x + n_z) T_{off1} + T_{off2} && (5\text{-}36) \end{aligned}$$

It is clear from equation (5-36) that the term, $-n_x Z(\ell, b) - n_z X(\ell, b)$, being a function of position, will affect the slope of the graph in some way and thus change the intercept. Hence if it is assumed that region C has a "pure" spectral index and this region is used in conjunction with another region D to determine the relative offsets of the two maps, one will obtain incorrect results.

In theory the method of using two regions with different pure spectral indices should work well for obtaining the offsets of the two maps. In practice the uncertainties are probably prohibitively large. Furthermore one cannot be certain that the regions used have a pure spectral index.

The above method is valid only for an isotropic background. As the background of the Gum Nebula is the galactic plane, which varies significantly with latitude, the method cannot be used for the background determination of the Gum Nebula—assuming that the nebula has regions of different spectral index. As the brightness temperature of the galactic plane varies only very slowly with longitude, one could perhaps apply this method at constant galactic latitude for each galactic latitude. However, in such a scenario the galactic background contribution would result in an extra unknown isotropic term, T_B, with spectral index β_B. This introduces two extra unknowns, giving a total of four unknowns and only two equations, equations (5-32) and (5-33), to determine them. Thus this method cannot be used for the Gum Nebula.

Thus TT-plots do not provide a method of determining the brightness temperature background offsets of the Gum Nebula at 408 MHz and 2326 MHz. Even with the assumption followed by Reich & Reich (1988), i.e. that the 408 MHz survey is absolutely calibrated, the galactic component at constant latitude introduces two, not just one unknown and hence there are three unknowns, i.e. one to many.

Thus we return to the method of obtaining the brightness temperature spectral index by means of a TT-plot at the sacrifice of positional information. However, based on the experience gained in investigating TT-plots of simulated data, an interactive program was developed that makes use of TT-plots and outputs a spectral index image. The resultant spectral index image does however contain regions in which the spectral index cannot be defined.

5.2 TT-plot simulations

The many inconsistencies in TT-plots of real data with the theoretically expected straight line, as seen in subblock TT-plot maps made of most of the Gum Nebula, were loosely classified. Fig. [5-3] is one of these subblock TT-plot maps and contains at least one example of each of these inconsistencies. The latter, with block coordinates of the example in Fig. [5-3], are listed below.

- negative slopes (e.g. blocks with longitude 245° to 244° and latitude 8° to 9° and 9° to 10°)
- scatter plots (e.g. block with longitude 242° to 241° and latitude 7° to 8°; block with longitude 249° to 248° and latitude 0° to 1° and others)
- Curving lines (good examples are: block with longitude 242° to 241° and latitude 8° to 9°; block with longitude 244° to 243° and latitude 8° to 9°; weak examples are: block with longitude 249° to 248° and latitude 6° to 7°; block with longitude 248° to 247° and latitude 9° to 10°;)
- extremely steep slopes corresponding to $\beta = 3$ and above (e.g. block with longitude 242° to 241° and latitude 0° to 1°; block with longitude 244° to 243° and latitude 6° to 7°)
- flat slopes corresponding to extremely low values of β, ≈ 1.5 to 2.0 (e.g. block with longitude 244° to 243° and latitude 2° to 3°; block with longitude 246° to 245° and latitude 0° to 1°)

The constant longitude and latitude TT-plots of the 2326 MHz and 408 MHz data at 1.7° resolution shown in Fig. [5-2] also show some of these effects. In particular, notice the curvature in some of the sections. Also note the sections with negative slope and extremely steep slope.

To gain some understanding of what gives rise to these peculiarities, I simulated brightness temperature maps. The simulation process has two steps. In the first step images of simple brightness temperature structures at two frequencies with particular spectral indexes for the individual structures are generated with the aid of a program, TTSIMUL, described below. The output of this program gives simple spatial temperature variations of a pristine sky at two chosen frequencies sampled every 0.05°, as it would presumably be seen when not smoothed by a scanning antenna. Thus the images in the first step are generated with relatively high spatial sampling—a tradeoff between approaching a continuous distribution for a pristine sky and a reasonable demand on computer time and space.

The second step simulates the smoothing that is an inevitable result of the finite beam width of the scanning antenna. This is achieved by using the existing convolution program CTFM to convolve these maps with an artificial antenna beam. This artificial antenna beam is assumed to have a gaussian-shaped main beam and no side lobes. The gaussian main beam is a reasonable approximation to a real antenna's main beam. (Baars, 1973)

The half power beam width of the artificial gaussian beam is chosen in accordance with the amount of smoothing required. Here it is assumed, for practical purposes, that the output images of the first stage have infinitely high resolution i.e. corresponding to a gaussian half power beam width of zero. The output images from the convolution program have a spatial sampling frequency chosen to agree with the appropriate sampling intervals for the half power beam width of the gaussian used for the smoothing by convolution (Rohlfs, 1986). Thus inappropriate oversampling is avoided, in case this has an effect on the resultant TT-plot from these simulated data.

The program, TTSIMUL, I wrote to generate the simulated maps at two frequencies chosen by the user, allowed for a superposition of one or more (and repeats of the same) of the following brightness temperature structures:

1. an isotropic offset of different value for each map.

2. a temperature distribution linearly increasing with longitude. Its spectral index and spatial rate of temperature change are chosen by user.

3. a piecewise linear temperature variation with longitude so as to be "V"-shaped in longitude. Each arm of the V may be assigned a different spectral index and rate of increase for frequency one.

4. a piecewise linear temperature variation with longitude resulting in a "VΛ"-shaped structure in longitude. Each branch of the shape may be assigned a different spectral index and rate of increase for frequency one.

5. a very simple Milky Way, modelled as a gaussian function of latitude, independent of longitude, with user chosen HPBW and spectral index always centred on the middle latitude of the image.

6. a simple H II region generated by summing, at positions on a sphere, a user given emission coefficient per pixel along the line of sight through the sphere. The radius of the sphere is chosen by the user. The user also chooses the position of the centre of the H II region in the image.

As all spectral index determinations of real data in this work make use of the 2.3 GHz Rhodes/HartRAO survey and the 408 MHz survey by Haslam et al. (1982), the two frequencies used in the simulations were 2300 MHz and 408 MHz. The resolution chosen for most simulations was 1°, close to the 0.85° resolution of the 408 MHz survey and therefore the minimum possible resolution for any spectral index determinations using these two surveys.

5.2.1 V-shaped temperature distribution with different spectral indices for each branch of the V

The basic clue to the origin of some of the peculiarities in TT-plots of real data is evident when comparing TT-plots of unsmoothed, simulated data with those of the same data smoothed by convolution with a gaussian function representing the antenna beam.

Images at two frequencies (2300 MHz and 408 MHz) were simulated with a piecewise linear temperature variation in longitude so as to be "V"-shaped in longitude at 2300 MHz (see Fig. [5-5] a)). Each arm of the V was assigned a different spectral index, 2.1 and 2.7 respectively, resulting in the mutilated V in the 408 MHz image (see Fig. [5-5] b)). The brightness temperatures of the two images were made constant in latitude. Thus no constant longitude scan is shown.

As this brightness temperature structure was not superimposed on any background temperature, a spectral index image could be formed by applying equation (4-11) to each pixel position in the two images. Fig. [5-5] c) shows a constant latitude scan of the resultant spectral index image with the change in spectral index showing up as a sudden jump, because the data was unsmoothed prior to applying equation (4-11).

That there are two regions with different spectral index is also evident from the TT-plot at constant latitude over the whole longitude range shown in Fig. [5-5] d). This plot shows two straight lines with slopes corresponding to the spectral indices of the two regions, in this case 2.1 and 2.7. Some of the positional information of the spectral index is regained by forming a subblock TT-plot map of the 408 MHz and 2300 MHz images as shown in Fig. [5-5] e). The lack of any variation with latitude is also evident in the latter figure.

The corresponding figures for the same data, convolved with an artificial antenna beam of HPBW 1.5° to simulate the smoothing process that is inherent in the scanning of the sky by an antenna, are shown in Fig. [5-6]. The constant latitude scan (Fig. [5-6] a)) of the 2300 MHz 1.5° resolution image shows the expected smoothing of the bottom cusp of the "V". Comparison of this figure with figure b), the constant latitude scan of the corresponding 408 MHz 1.5° resolution image, shows that the minimum in the latter image is no longer at the same position as that in the 2300 MHz image. This is a consequence of the change in spectral index combined with

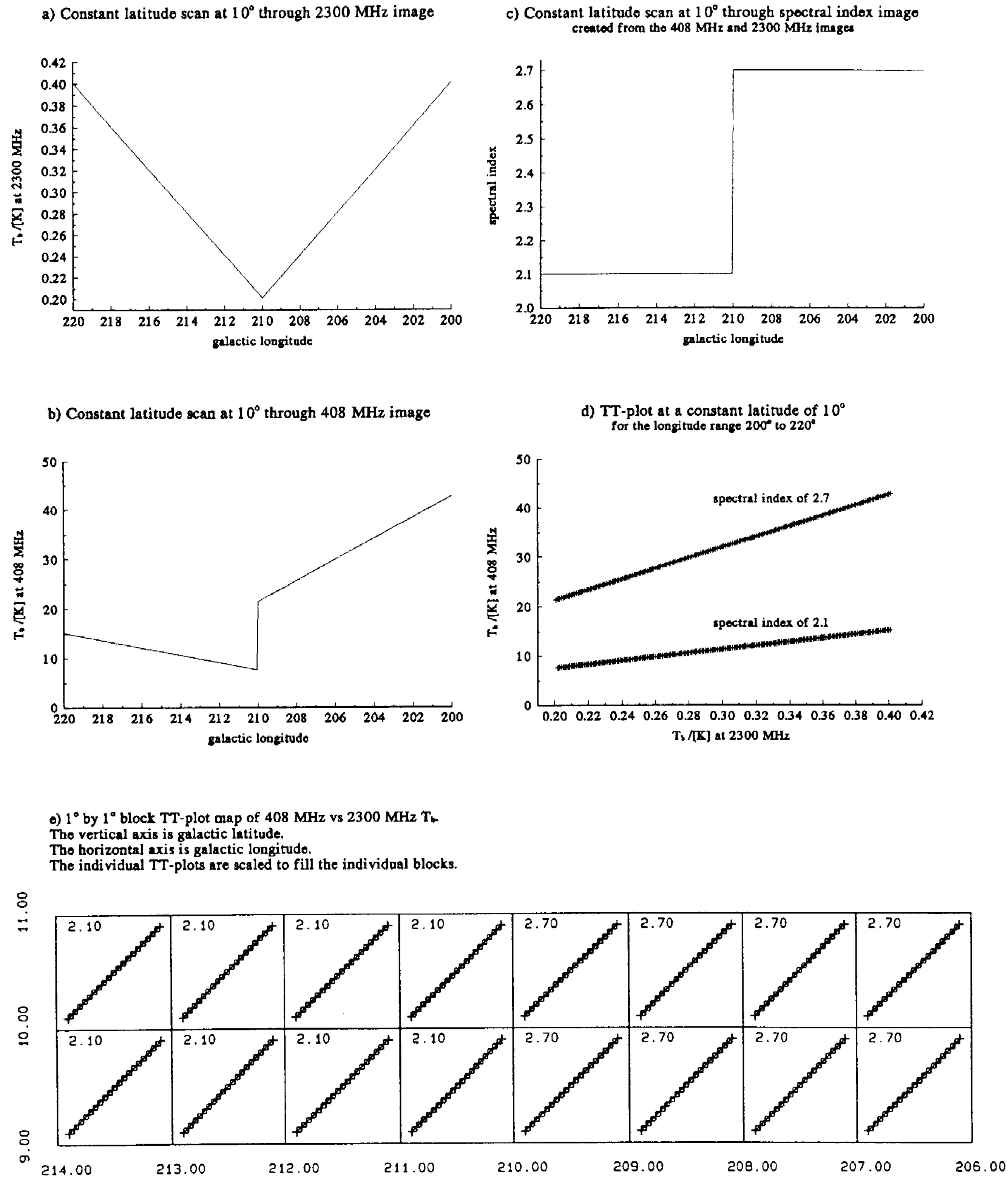

Figure [5-5]: The above figures a) to e) were produced from unsmoothed simulated data. Comparison with the next figure highlights the effects that beam dilution has on spectral index determinations.

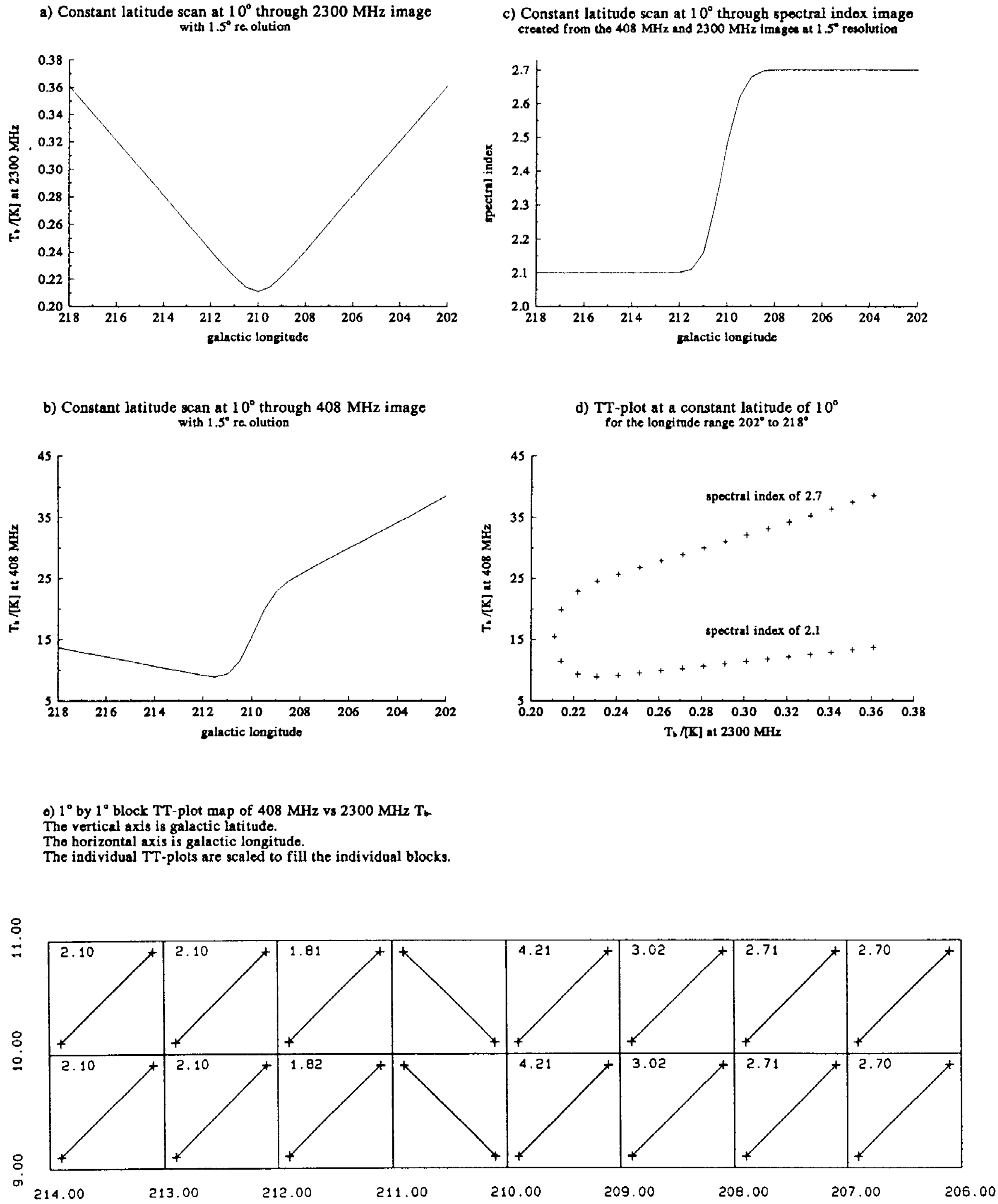

Figure [5-6]: The above figures a) to e) were produced from simulated data smoothed to a resolution of 1.5°.

the smoothing of the data. The effects of this are visible on the scan through the spectral index image (Fig. [5-6] c)) generated from this smoothed data.

More pronounced is the corresponding change in the TT-plot at constant latitude shown in Fig. [5-6] d). Note the smooth turnover join between the two straight lines corresponding to the two different spectral index regions of the data in the TT-plot. This results in the negative slope TT-plots in the corresponding subblock TT-plot map (Fig. [5-6] e)). Also, in several blocks adjacent to this negative slope TT-plot the spectral index derived from the OLS bisector fit (see section 5.3) is either depressed (for the thermal region) or elevated (for the nonthermal region).

The subblocks in Fig. [5-6] e) are too small to contain a reasonable number of independent points in each TT-plot; they were kept at that size for the purposes of comparison with Fig. [5-5] e). A 2° by 2° subblock TT-plot of this same data is shown in Fig. [5-7]. This shows that a cause of the curving line in subblock TT-plots is the smoothing between different spectral index regions.

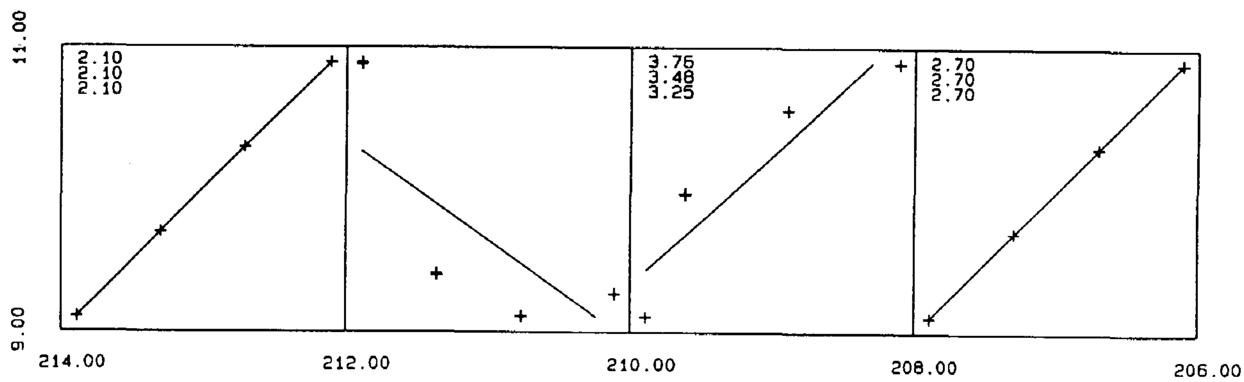

Figure [5-7]: 2° by 2° subblock TT-plot of the smoothed data shown in the previous figure.

Those TT-plot peculiarities that are a direct consequence of the unavoidable smoothing of the sky distribution as a result of the observing process are thus easily picked out by comparison of the unsmoothed data TT-plot with that for the two artificially observed versions of the two simulated data sets.

When the beam of the antenna scans along a section of sky where the beam is filled by an area of sky that contains at least two subregions of different spectral indices, the resultant brightness temperature variation with frequency depends on the proportions in which the different spectral index regions contribute to the total radiation seen by the beam. As these proportions are continuously changing as the scan progresses along the section of sky where the different spectral index regions overlap in the beam, the slope of the TT-plot for that part of the mapped sky is continuously changing. Furthermore the proportions in which the different spectral index regions overlap in the beam are different at different frequencies as a result of the different spectral indices of the brightness temperatures. Thus the minimum brightness temperature occurs at different positions at different frequencies which gives rise to the negative slope sections of the joining curve of the two straight lines of the TT-plot of the smoothed data. At those positions the brightness temperature at one frequency is still dropping to its minimum, while at the other frequency it is already increasing after the minimum.

This effect becomes more pronounced, the lower the resolution of the data, i.e. the larger the area of sky filling the beam as shown in Fig. [5-8]. This figure shows on the same set of axes TT-plots of the identical two frequency maps, but for different resolutions and corresponding different sampling interval. The lower the resolution the greater the extent of the curved region of the TT-plot.

Some other peculiarities that occur in TT-plots of smoothed simulated data are shown in Fig. [5-9]. In this figure a) shows how a step increase in the brightness temperature at 2300 MHz at the same position as a change in spectral index affects the TT-plot. Note the very steep straight line section joining the two slopes corresponding to spectral index 2.7 and 2.1. Thus, if one fits a straight line to this very steep section, one could determine an artificially high, i.e. > 3, spectral index that is only an artifact of the method.

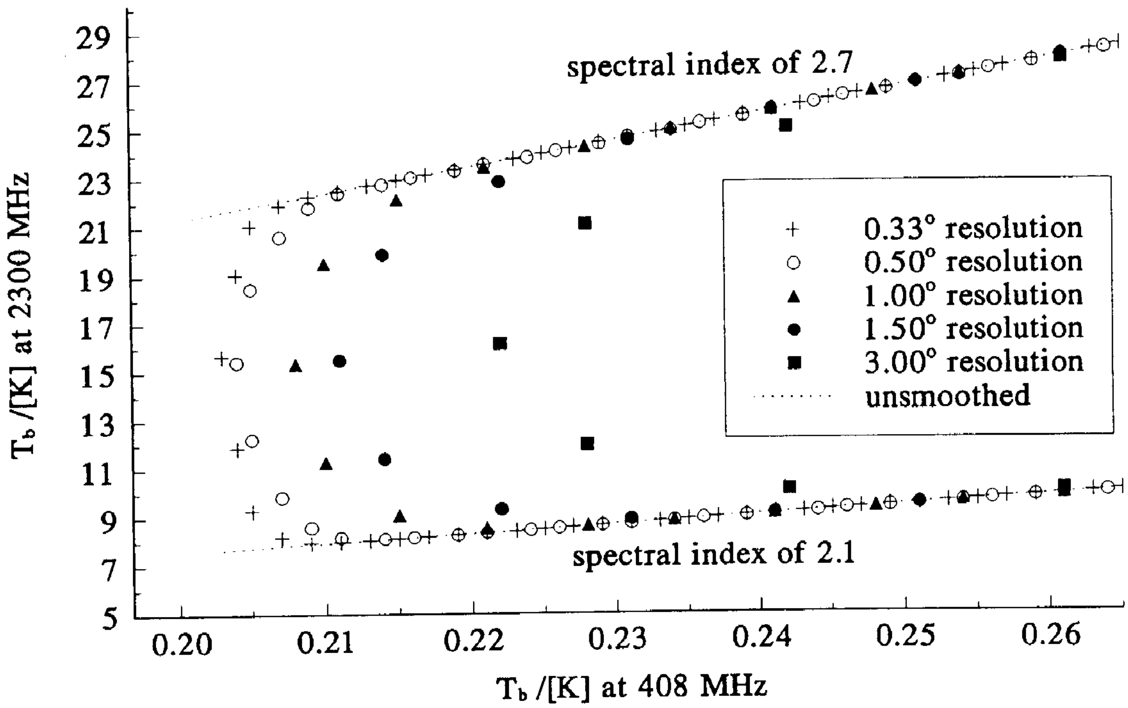

Figure [5-8]: TT-plots of different resolution data showing the effect of beam dilution on the TT-plot.

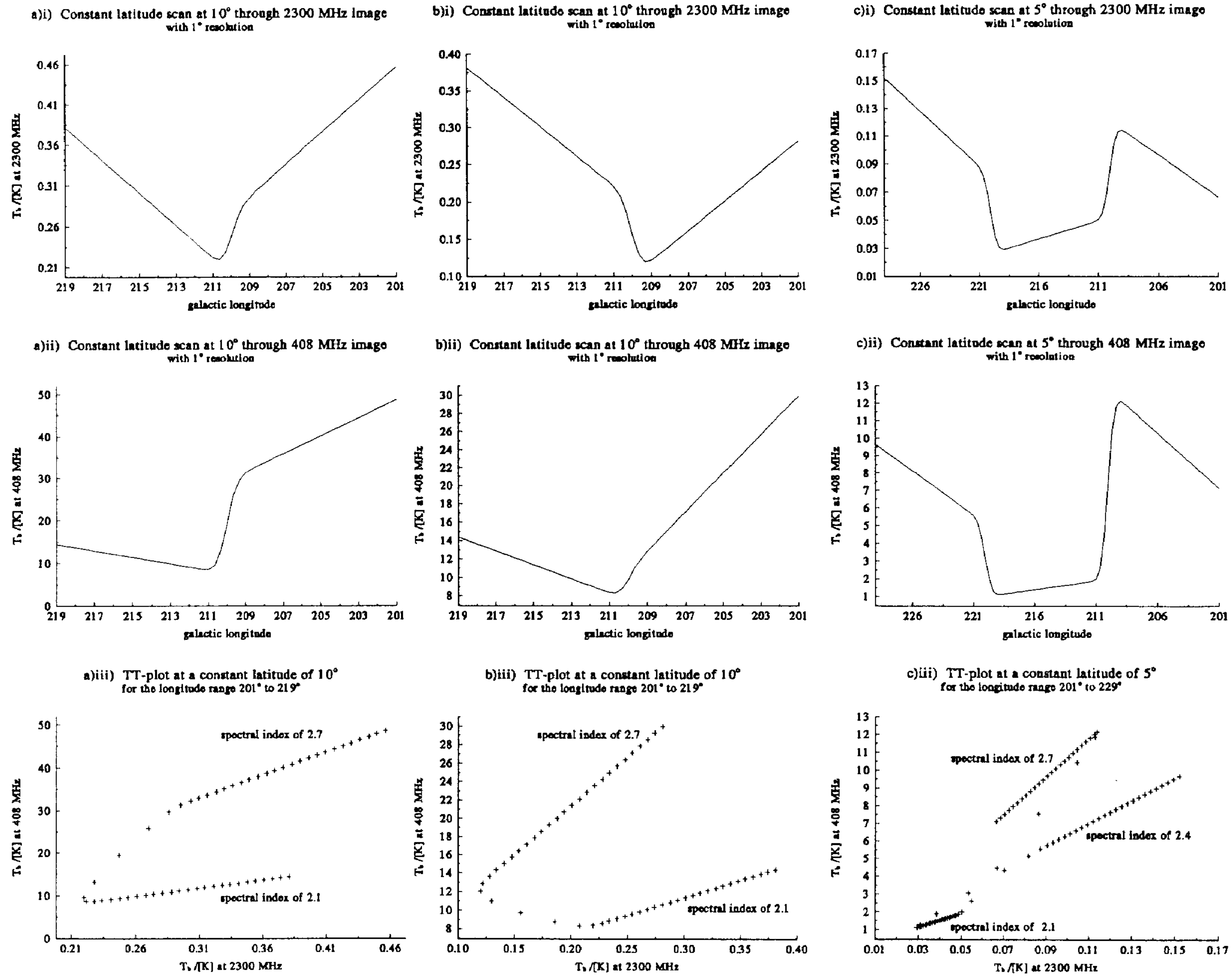

Figure [5-9]: Different deviations from the standard form of the TT-plot shown in three different, a) to c), simulated data sets all smoothed to 1° resolution.

Figure b) shows a step decrease in the brightness temperature at 2300 MHz at the same position as a change in spectral index, resulting in an almost straight line section of negative slope joining the two straight line sections of different spectral index.

Figure c) is a more complicated scenario showing a complex TT-plot. The latter is probably somewhat extreme and unlikely to occur in real data, but does highlight the fact that spectral index determination using TT-plots is not without difficulties.

5.2.2 "\/\"-shaped temperature distribution superimposed on gaussian galactic distribution

The aim of this work was to obtain a spectral index map of the Gum Nebula, a faint, extended, structure straddling the galactic plane. The above discussed simulation lacks an anisotropic background simulating the brightness variation of the Galaxy, whose emission extends far beyond the galactic plane in galactic latitude and is known to have a spectral index in the region of 2.7 to 3. This galactic emission may be modeled to a first order approximation as the sum of a lower, wider Gaussian and a higher, narrower Gaussian centred on zero galactic latitude with the half-power width varying slowly in galactic longitude (Flanagan, 1981).

Hence a gaussian function of latitude, independent of longitude, was added to the simulation under discussion (see Fig. [5-10] b)i) to provide an anisotropic background with spectral index 2.9. A single gaussian turned out to be sufficient for identifying the effect of the anisotropic galactic background on TT-plots of extended structures in our Galaxy. To this were added the structures, whose spectral index I wanted to be able to determine from TT-plots. In this case the 2300 MHz structure was shaped as "\/\" in longitude (see Fig. [5-10] a)i)), and made constant in latitude. The structures \, /, \, have spectral index 2.4, 2.1 and 2.7 respectively. This then allowed the determination of the 408 MHz appearance with longitude of the simulated brightness temperature variation, as shown in Fig. [5-10] a)ii). Its variation in latitude, resulting

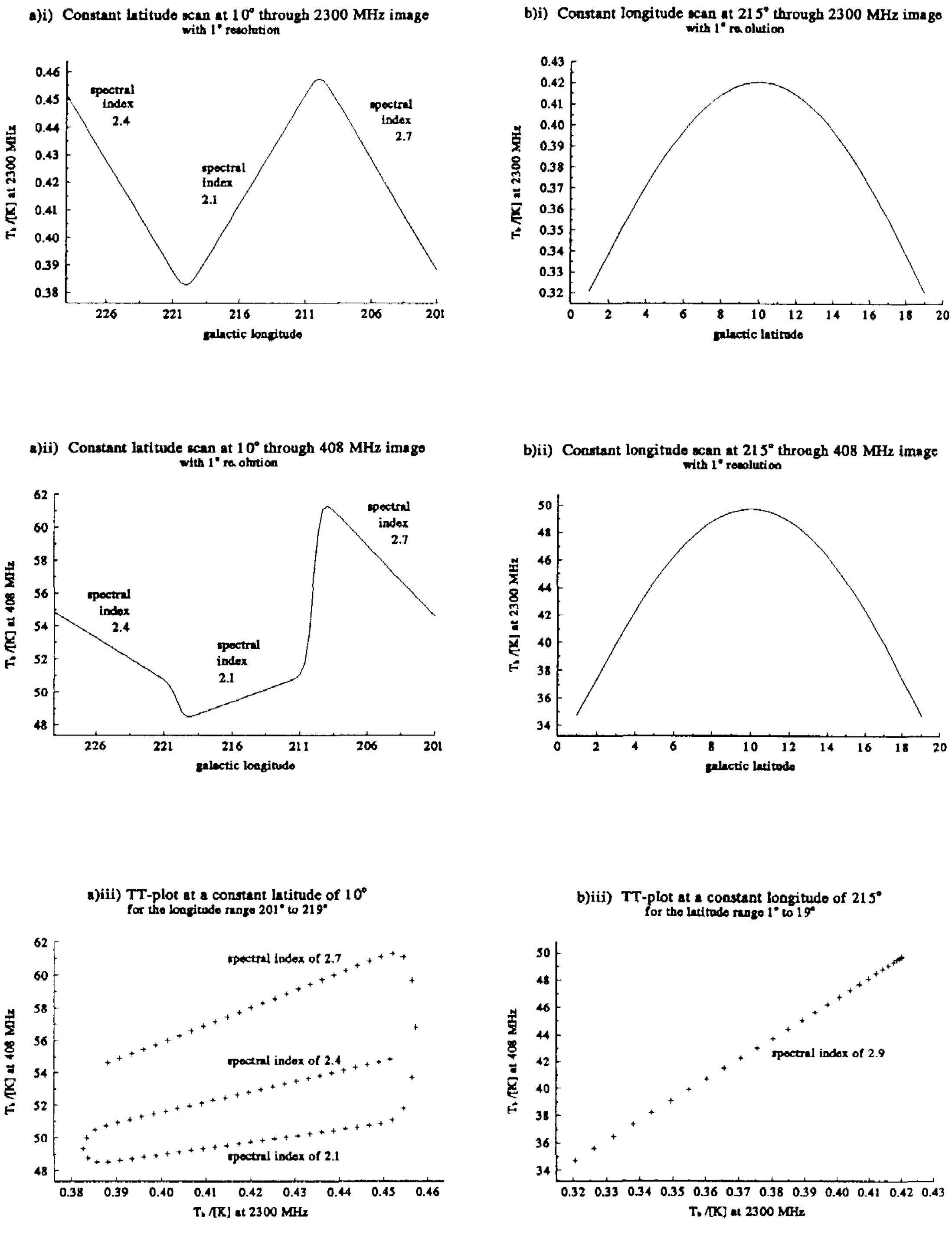

Figure [5-10]: Constant latitude/longitude scans and TT-plots for a "\/\"-shaped temperature distribution superimposed on a gaussian galactic distribution of spectral index 2.9.

from its superposition on an artificial galactic background, is shown in Fig. [5-10] b)ii). Both the 2300 MHz and the 408 MHz simulated images were smoothed to a 1° resolution. Thus the main difference between this simulated data and that discussed in the previous section is the superposition of different spectral index regions with their spatial brightness temperature variations perpendicular to each other; i.e. the one varies with longitude only and the other with latitude only.

Two subblock TT-plot maps of these smoothed simulations are shown in Figs. [5-11] and [5-12]. Fig. [5-11] shows a region asymmetrically straddling the "galactic plane" (which is situated at a latitude of 10° in this simulation) and the adjacent structures of spectral index 2.4 and 2.1. Fig. [5-12] shows the region with the adjacent structures of spectral index 2.1 and 2.7.

These figures clearly show that one cause for the scatter plot TT-plots (see section 5.2 and Fig. [5-3]) in subblock TT-plot maps is certainly the superposition of different spectral index regions with spatial brightness temperature variations in directions at an angle to each other; here at 90°. This effect in combination with the earlier noted curving due to smoothing, at a position where a change in overall spectral index occurs, is able to account for a large number of the peculiarities seen in subblock TT- plots of real data.

From such subblock TT-plots a classification of an object on the basis of a restricted range in spectral index is essentially impossible, as a perusal of the listed upper limit, estimate of true value and lower limit of the spectral index in each subblock indicates. In particular, the spectral index of the middle structure of 2.1 is only estimated reasonably correctly on the peak of the gaussian galactic background, where the latter exhibits a slow variation with latitude relative to the 2.1 spectral index structure's variation in longitude. Yet, even there, almost any interpretation fits into the two sigma limits of the spectral index. Thus the superposition of a structure of flat spectral index (≈ 2.1) on one of much steeper spectral index is vulnerable to misinterpretation in a subblock TT-plot.

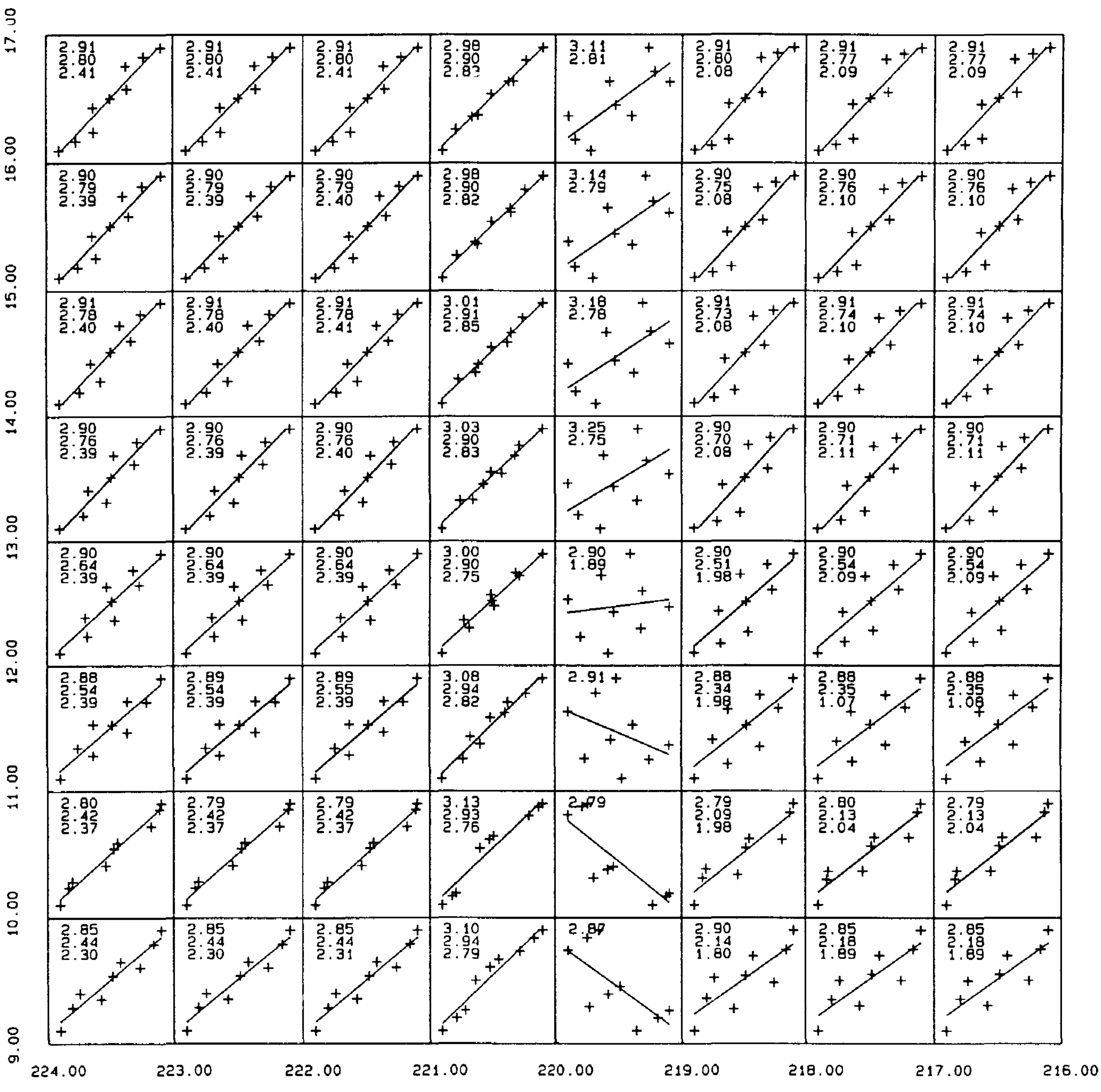

Figure [5-11]: Subblock TT-plots of part of the "⋀⋀"-shaped temperature distribution superimposed on a gaussian galactic distribution

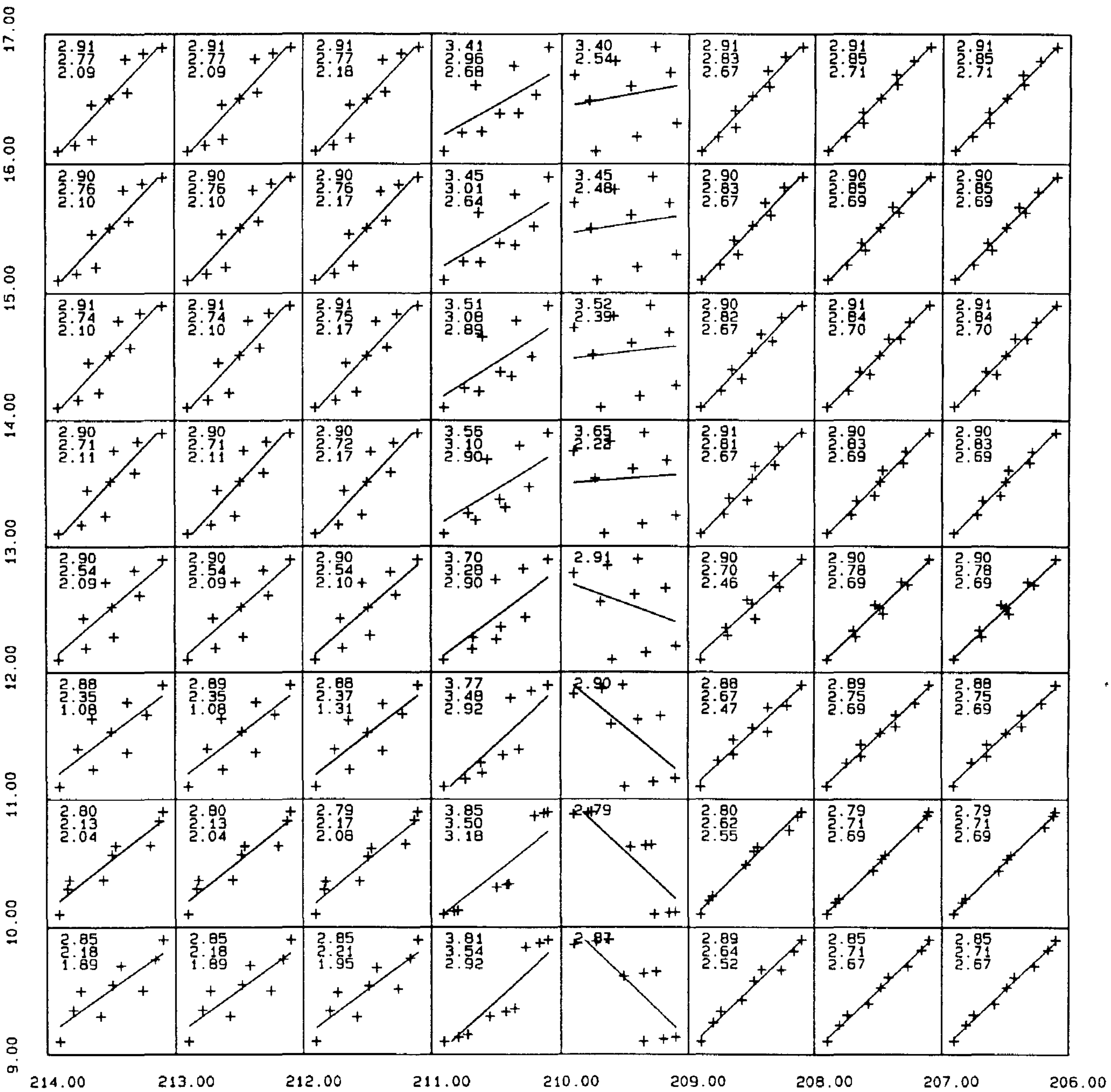

Figure [5-12]: Subblock TT-plots of part of the "V"-shaped temperature distribution superimposed on a gaussian galactic distribution

Further perusal of both Figs. [5-11] and [5-12] shows that the spectral index determination in this manner is also unsuccessful for the 2.4 spectral index as well as the 2.7 spectral index structure. The effect becomes more pronounced at the higher latitudes shown in these figures. There the variation of the galactic background with latitude becomes steeper relative to the structures' longitude variations in the lower frequency (i.e. 408 MHz) image, as seen in Fig. [5-10] a)ii) and b) ii).

As Fig. [5-10] a)iii) shows, the true spectral index value of the structure of interest may be determined from a TT-plot at constant latitude in this ideal case, where the galactic background does not vary with longitude.

This suggests a solution to the problem of loss of positional information. One can overcome this loss at the cost of a lot of hard work, by selecting those longitude ranges of the constant latitude TT-plot that exhibit a constant slope. To each of these selected segments a spectral index may readily be assigned.

The determination, by trial and error, of the longitude ranges for which the TT-plot at constant latitude is free from peculiarities is inefficient and time consuming. Thus I developed a program TVST which works its way through the images starting at the lowest latitude and ending with the highest latitude. At each latitude it works its way sequentially through the data points in longitude as follows.

- The starting point is either the first point in longitude at that latitude or the first point after the most recently fitted line segment of constant slope at that latitude.

- At each latitude a preliminary TT-plot of the first n pixel positions is drawn on screen, where n is chosen by the user.

- The user then indicates to the program at which data point on the preliminary TT-plot the first straight line segment for defining a spectral index starts. This is done by deleting all subsequent data points; starting with the last plotted data point on the preliminary TT-plot and working towards the desired starting data point, thus leaving k data points undeleted on screen.

- The program then sends output to the desired spectral index image, telling it that at the positions corresponding to these k data points no spectral index can be defined. It then presents the next TT-plot at the same constant latitude starting with the desired data point i.e. the k+1 point and plotting a total of n data points. (n may be changed by the user prior to this.)

- As there may be trailing data points on this TT-plot that do not conform to the initial slope, these can be deleted. Again this is done starting with the last plotted data point. Once all the undesired points have been marked the program is told to fit a straight line to the remaining points, resulting in a spectral index at the positions from which these selected data points came.

- These spectral index values are output to corresponding positions in the spectral index image. The next TT-plot at that latitude is started at the last data point deleted from the set plotted on the previous TT-plot.

- This sequence of steps is repeated until the whole longitude range at that latitude has been covered. Then the next higher latitude is tackled.

Thus the TVST program is highly interactive. Preliminary runs of it indicated that it required greater flexibility to be more user friendly; in particular to be able to return to an earlier starting position if a mistake had been made. These adjustments did not change the basic structure and sequence of the program outlined above. The program generates Theil (see section 5.4) upper limit, estimate of true value and lower limit spectral index images, as well as OLS Bisector (see section 5.3) upper limit, estimate of true value and lower limit images for the purposes of comparison.

5.2.3 H II region on inclined plane

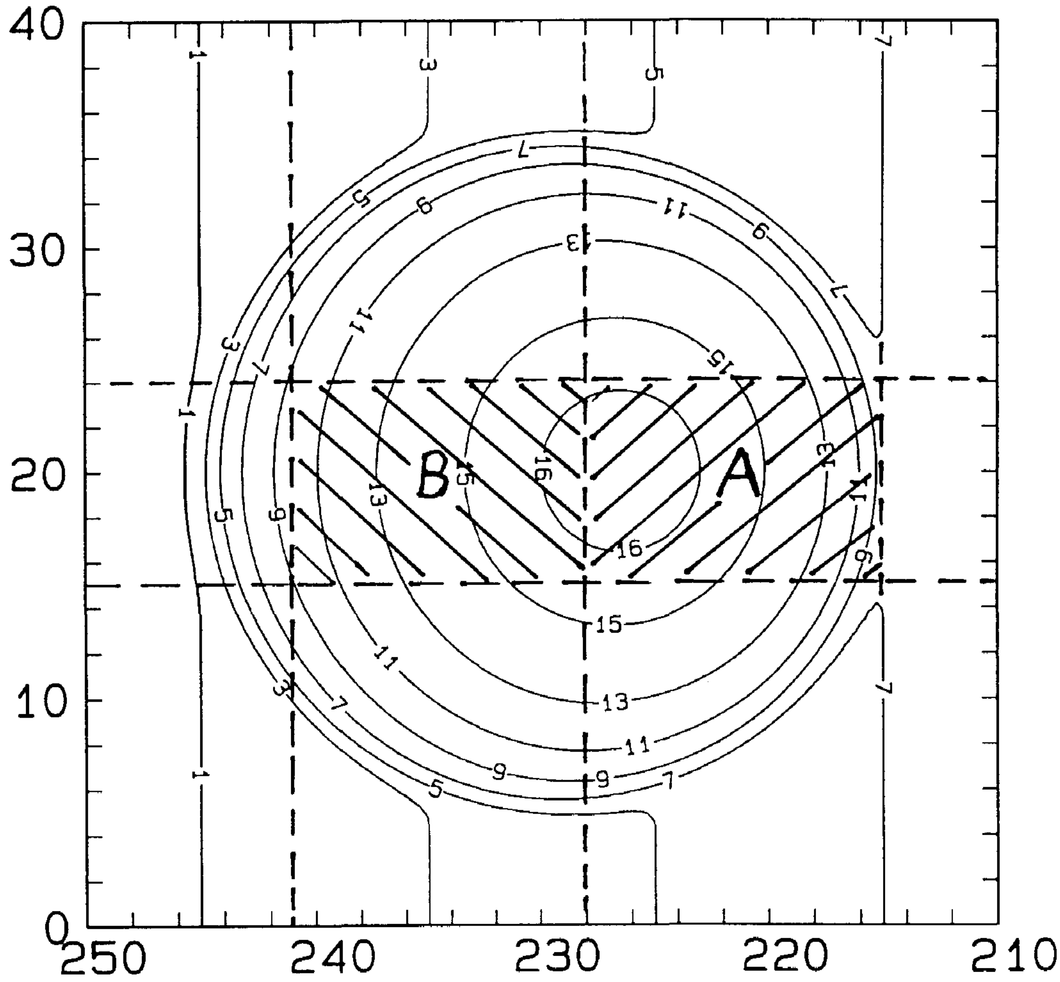

Figure [5-13]: Contour map of the 2300 MHz simulated image, showing an H II region superimposed on a linearly varying background.

In this simulation a large H II region is positioned on an anisotropic background of different spectral index. The background brightness temperature increases linearly with longitude (in contrast to the variation in latitude of the gaussian galactic plane in the previous section) and has a spectral index of 2.7. Both simulated images were smoothed to a 1° resolution. A contour map of the 2300 MHz image is shown in Fig. [5-13].

Subblock TT-plots of this simulated data are shown in Figs. [5-14] and [5-15], covering the regions A and B respectively in the contour map shown in Fig. [5-13].

TT-plots with negative slope are present just to the lower longitude side of the peak of the H II region, between latitudes 18° and 22° in Fig. [5-14]. These arise due to 1) the superposition of the still increasing nonthermal background with decreasing longitude and 2) the decreasing H II region brightness temperature with decreasing longitude. At even lower longitudes, where the spatial rate of decrease in the brightness temperature of the H II region is steeper, this superposition results in line slopes resulting in spectral indices corresponding to optically thick radiation i.e. values significantly less than 2.0. This could lead to an erroneous conclusion that the source is optically thick.

Fig. [5-15] shows the opposite effect for the region where the brightness temperatures of both the background radiation and the H II region are increasing with decreasing longitude i.e. to the higher longitude side of the peak. Here the determined spectral indices are much higher than that of either the background or the H II region.

Also evident in both figures is the scatter plot effect. Closer examination of the trends in those positions, shows that this is due to the superposition of different spectral index regions with spatial brightness temperature variations in directions at an angle to each other—here at a slightly different angle in each block.

The effect of opposing or cumulative spatial brightness temperature changes of superpositioned emission structures is also evident in the TT-plot at constant latitude of this simulation shown in Fig. [5-16] b). Here one sees both the lowered slope (top part of curved semi-loop) resulting in a flattened spectral index, approaching almost zero i.e. a horizontal line at one part—and the increased slope resulting in the

Figure [5-14]: Subblock TT-plots of region A of the simulated H II region on an inclined plane.

Figure [5-15]: Subblock TT-plots of region B of the simulated H II region on an inclined plane.

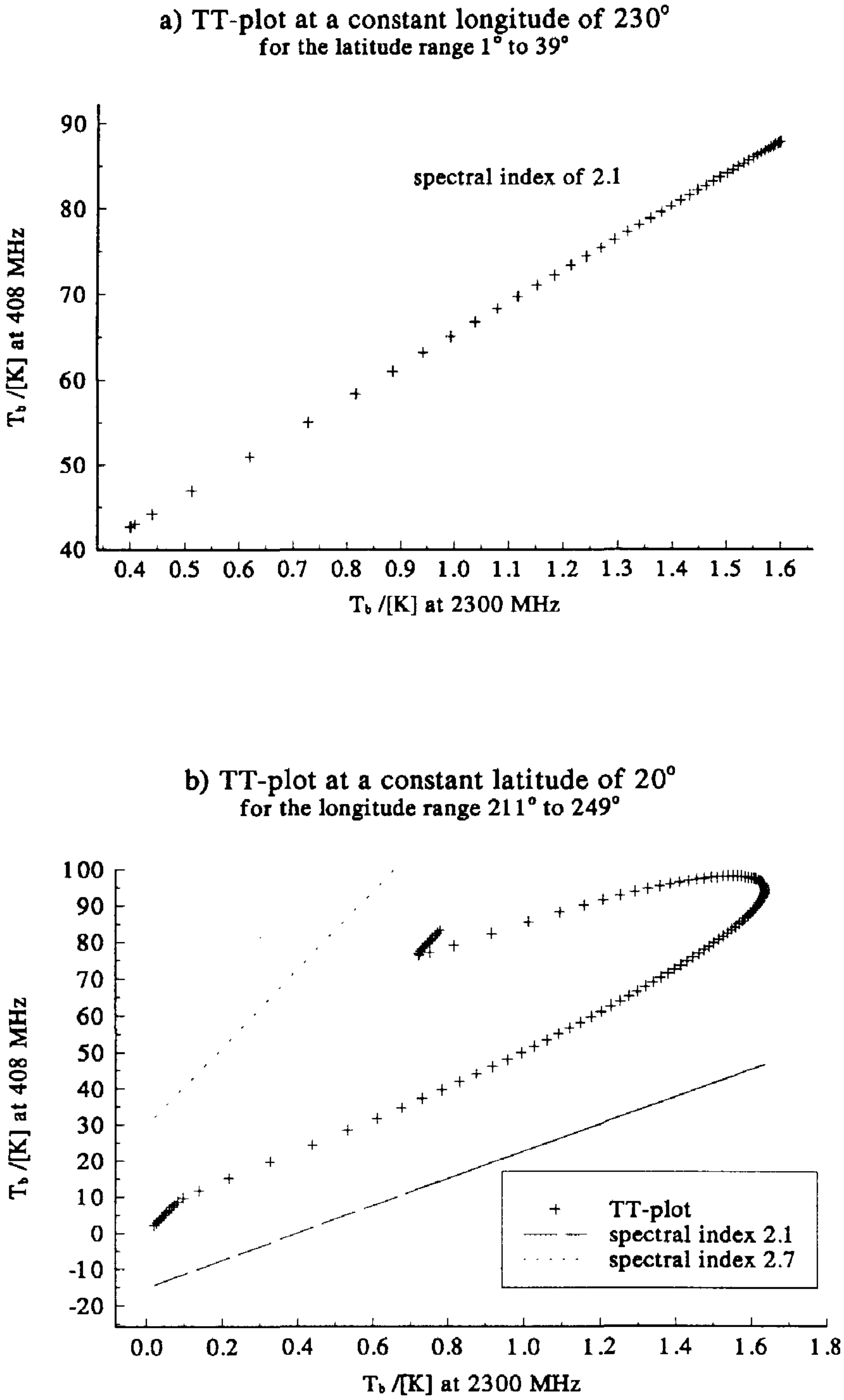

Figure [5-16]: Constant latitude and constant longitude TT-plots for the simulated data of an H II region superimposed on an anisotropic background.

much steeper spectral index (bottom part of curved semi-loop). Also note the general departure of the TT-plot from a straight line. The whole section corresponding to the position of the H II region is a curved line and not straight at all. Note that in comparison Fig. [5-16] a), which shows the constant longitude TT-plot, has no such peculiarities. Note that this constant longitude TT-plot is along the coordinate that does not show any change in the brightness temperature of the background.

From this it is evident that without being able to isolate a source from its background, in this case the sloping nonthermal background, the results from TT-plots can be misleading. Indeed two models of the Gum Nebula, Srinivasan Sahu's (1992), where an H II region, the IRAS-Vela ring, is superimposed on a large distant SNR, and Reynold's (1976b), where an H II region shell surrounds the SNR, would contain the same general aspects as this simulation. Hence the results of applying the TVST program to data images of the Gum Nebula at two different frequencies should be interpreted with care.

5.2.4 Discussion and Conclusion

This investigation does not claim to have exhausted the possible scenarios in which the TT-plots that deviate from the theoretical straight line occur. Obviously more complex situations exist, but those investigated suffice to indicate that many of the TT-plot peculiarities are inherent in the superposition of differently varying emission structures of different spectral index.

Negative slopes of TT-plots can originate from two effects—either due to smoothing of radiation by the beam of the antenna, or too many different things going on in superposition e.g. the part to the right of the peak of the H II region.

Even when the line of the TT-plot looks perfect it may not give you the true spectral index of the source of interest as a result of underlying temperature gradients with other spectral indices, as seen in the theoretical investigation of TT-plots in the previous section.

As shown in section 5.2.2, when the structures of interest are superimposed on the galactic plane, which is assumed to be constant in longitude at each latitude, better results are obtained if TT-plots at constant latitude are used. This method was implemented in the program TVST. One drawback of this method is that it results in regions of undefined spectral index where the TT-plot is not a straight line.

This investigation shows quite clearly that the amount of information available in an image, here the spectral index, is limited by the resolution of the images.

Another aspect of determining β from TT-plots is that the standard well known linear regression methods used for obtaining the slope and its confidence interval are derived assuming a large number of data points (typically greater than 50). From the relationship between the resolution of a map and the critical sampling interval it is evident that this criterion is rarely met. Thus I looked for a method for straight-line fitting that gives valid confidence intervals in the case of a low number of data points.

5.3 Straight line fits to TT-plots

The TT-plot method of determining spectral indices requires fitting a straight line to the points in the TT-plot. For the purpose of defining the symbols used in this discussion, the following definition is given. Straight line linear regression is the fitting of a set of n paired data points (x_i, y_i), $i = 1, 2, \ldots$,n to a straight-line model (Press et al., 1992) (the symbols x and y are used for the variables as a matter of convenience, as it is briefer than T_1 and T_2):

$$y_i = \mathcal{A} + \mathcal{B} x_i \tag{5-37}$$

where $\mathcal{A}$ and $\mathcal{B}$ are the true intercept and slope of the line respectively. However, the results of a straight line linear regression are only estimates a and b of $\mathcal{A}$ and $\mathcal{B}$ respectively.

A good discussion of standard straight line regression methods is given in Isobe et al. (1990) and Feigelson & Babu (1992). These methods, most of which minimize the sum of a particularly defined distance (see later) of the data points from the fitted line, are based on the assumption that the intrinsic scatter of the data dominate over any errors arising from the measurement process. This is not necessarily always true for the brightness temperature values in a TT-plot as scanning effects may in parts dominate over the intrinsic scatter of the brightness temperatures. Also, both variables, i.e. brightness temperatures, have an associated variance, though the one is generally much smaller than the other as one of the maps has been smoothed with a gaussian to bring both maps to the same resolution. This suggests that the standard methods may not be appropriate and that perhaps the use of a weighted regression method would be a better choice.

It is however difficult (if not impossible) to determine the measurement error in the brightness temperatures for the determination of an appropriate weighting factor of the points or even just the variables in the TT-plot. The severity of the scanning effects clearly varies with position in the map, as can be seen in Fig. [4-2] of the 408 MHz survey (Haslam et al., 1982), but cannot be quantified. Also, almost invariably one of the maps has been convolved with a gaussian to achieve the same resolution for both maps, further complicating a quantification of the measurement error in the smoothed map. In fact, if the amount of smoothing applied post-detection to a map has been severe, the brightness temperatures in that map may be considered error free in this context. It is thus unlikely that anything would be gained using a weighted regression method. Also, provided that the brightness temperatures of the map that has undergone the greater amount of post-detection smoothing are used as the independent variable X, the situation is close to that required by the methods discussed in Isobe et al. (1990) and Feigelson & Babu (1992).

The most widely known method of straight line linear regression is that of ordinary least squares regression (OLS($Y|X$)) of the dependent variable Y against the independent variable X. Specifically, the least squares method gives estimates a and b of $\mathcal{A}$ and $\mathcal{B}$ in the equation

$$y_i = \mathcal{A} + \mathcal{B}x_i + \epsilon_i \tag{5-38}$$

where ϵ_i is an unobservable random variable that has a normal distribution with mean zero and variance σ^2, which is independent of x_i. Clearly, it is assumed that the independent variable does not have an associated uncertainty. a and b are chosen so that

$$\sum_i (y_i - a - bx_i)^2$$

is minimized, i.e. the sum of the squares of the vertical distances of the data points from the fitted line is minimized (Sprent, 1989).

In the context of the determination of the spectral index, the brightness temperature at one frequency is no more the independent variable than that at the other frequency, i.e. neither can be described as "cause" or "effect"; roles that the OLS($Y|X$) clearly assumes for the X and Y variables respectively. However, for TT-plots one wants to estimate the underlying functional relation between the two variables, a situation for which Isobe et al. (1990) recommend the use of the OLS bisector, as it is invariant to switching the X and Y variables (i.e. treats them symmetrically) and shows better behaviour in simulation tests than the other symmetric regression methods. The OLS bisector is the line that bisects the OLS($Y|X$) line and its inverse, the OLS($X|Y$) line. The latter minimizes the sum of the squares of the horizontal distances of the data points from the fitted line.

spectral index	b for T_{408} vs T_{2300}	b for T_{2300} vs T_{408}
-1.9	27	0.037
-2.0	32	0.032
-2.1	38	0.027
-2.2	45	0.022
-2.3	53	0.019
-2.4	64	0.016
-2.5	76	0.013
-2.6	90	0.011
-2.7	107	0.0094
-2.8	127	0.0079

Table [5-1]: The slopes, b, of TT-plots for regions with the indicated spectral index.

The OLS bisector regression method defined according to Isobe et al. (1990) has been implemented together with other regression methods in a computer program SIXLIN by Isobe et al. (1990), which was obtained from them, as well as the later version, SLOPES, which incorporates bootstrap and jackknife resampling (Feigelson & Babu, 1992). It thus seemed that the OLS bisector was the appropriate one to use for determining the slopes of TT- plots, but the uncertainty determination in the slope provided some cause for worry.

The expected slopes i.e. b values, also known as coefficients of regression, in TT-plots for regions with temperature spectral index of 1.9 (optically thick region) to 2.7 (synchrotron radiation) in steps of 0.1 are given in table [5-1] for brightness temperatures at 408 MHz and 2300MHz. If the aim is to distinguish between a spectral index of 2.1 as opposed to 2.2 say, it is necessary to establish reliably the confidence interval of the regression coefficient b. It is standard practice to use a 95% confidence interval, i.e. 2σ, and I have followed this in the TT- plot work.

The formulae of linear regression for a straight line and associated variances in a and b given in the literature are asymptotic, i.e. derived for the number of data points tending to infinity. "These asymptotic formulae underestimate the true regression coefficient *uncertainty* in samples with small N (approximately N$\leq$ 50) or small population correlation." (Feigelson & Babu, 1992). Population correlation in this context is that of linear dependence between the data sets of the two variables i.e. how well do the data points crowd onto a straight line (cf regression which deals with the precise form of the relationship.)

The concern about the small population correlation can be dealt with by use of the statistic, r, for the strength of the linear dependence between two variables, i.e. the strength of their correlation. This is given by:

$$r = \frac{\sum_i (x_i - \bar{x})(y_i - \bar{y})}{\sqrt{\sum_i (x_i - \bar{x})^2}\sqrt{\sum_i (y_i - \bar{y})^2}} \tag{5-39}$$

where $\bar{x}$ is the mean of the x_i and $\bar{y}$ is the mean of the y_i (Sachs, 1984). r is known as the linear correlation coefficient or Pearson's r. r lies between -1 and +1. For $r = \pm 1$ all points (x_i, y_i) lie on a straight line. If $r = 0$, X and Y are uncorrelated. The closer $|r|$ is to 1 the stronger the correlation between the two variables.

Thus spectral indices and their uncertainties as calculated from the OLS bisector straight line linear regression of TT-plots could be flagged as suspect if r is below a certain value—negative slopes being meaningless in the context of spectral index determinations.

This does, however, not get around the problem of a low number of data points, which also results in an underestimate of the variance. Fifty data points at 3 samples per degree (as at critical sampling of 408 MHz survey, used extensively in this work for spectral index calculations) require a TT-plot to cover more than two square degrees, an area over which the spectral index is unlikely to be constant even if the galactic background variation did not pose a problem. The number of points in a meaningful TT-plot is thus unlikely to ever be as much as fifty. Babu & Feigelson, (1992) show that in MonteCarlo simulations with very small samples (n< 50) all regression estimators become progressively less accurate; in particular, if the population correlation is small as well, the estimates of the variances can be several times too small.

If a better estimate of the variance is required, Feigelson and Babu (1992) suggest that, for small samples, error analysis based on bootstrap and jackknife resampling should be used. As these methods, when tested on the 408 and 2300 MHz data frequently gave problems with division by zero, they were considered unsuitable.

The shortest length over which the spectral index in an image may vary is that of the resolution of the image. As the critical sampling of a region of sky is twice per resolution, this gives a minimum of three points (fence-pole effect), keeping either latitude or longitude constant, in a TT-plot to which one might want to fit a straight line, irrespective of the resolution of the map.

One might argue that the paucity of data points could be avoided by post-detection resampling of the images at a higher sampling frequency. The extra data points obtained in this manner are, however, not independent of the initial data points and merely constitute a resampling of the beams of the antennas as opposed to resampling the sky radiation. Thus nothing is gained and the confidence intervals based on an inclusion of data points from such a resampling would certainly not be indicative of the true range of the spectral index inherent in the observations.

In an extreme case one would want to fit a straight line to as little as 3 or 4 data points, although one should perhaps never go to less than 5 or 6 data points to avoid fitting lines to TT-plot peculiarities. As the assumption of a normal distribution becomes meaningless in such a small sample it was desirable for the method to be non-parametric i.e. making no assumption about the distribution of the uncertainties in the variables, as well as appropriate for a very small data set.

Thus a reliable method was required for fitting a straight line to less than 10 data points, but still appropriate for 20 to 30 data points should the spectral index be constant over a large area. The method should also give valid confidence intervals for such a small number of data points. The method that fits these criteria is known as Theil's method. It is based on the simple idea that if one had only two data points (x_1, y_1) and (x_2, y_2) the slope of the straight line joining them would be given by

$$b = \frac{y_2 - y_1}{x_2 - x_1} \tag{5-40}$$

If you have only a few more points it is an easy enough exercise to calculate the slopes resulting from applying equation (5-40) to all possible pairs of data points.

5.4 Theil's regression method

This discussion is heavily reliant on Sprent (1989), a text on applied non-parametric statistical methods. The aim of the discussion is to explore the applicability of this method to the case of regression lines for TT-plots and to give a working definition of it.

5.4.1 Terminology

Terminology of relevance to this discussion follows. It is also convenient to introduce Kendall's τ, on which the test statistic for the determination of the confidence intervals of Theil's method is based, at the same time.

Pairs of observations, (x_i, y_i) and (x_j, y_j), for which $x_i > x_j$ and $y_i > y_j$ are described as concordant. Concordance thus implies that $(y_j - y_i)/(x_j - x_i)$ is positive, as the numerator and denominator have the same sign. Another way of looking at it is that if y_j is larger than y_j then x_j is also larger than x_i i.e the ranking of the points in the pairs is the same. If the signs of the numerator and denominator are opposite, i.e. the quotient is negative, the pair is said to be discordant and their ranking is not the same. Pairs for which $x_i = x_j$ or/and $y_i = y_j$ are said to be tied.

For n observations there are $\frac{1}{2}n(n-1)$ possible pairings with n_c concordant pairs, n_d discordant pairs and t ties. Hence $n_c + n_d + t = \frac{1}{2}n(n-1)$.

Kendall's tau is given by:

$$\tau = \frac{n_c - n_d}{\frac{1}{2}n(n-1)} \tag{5-41}$$
$$= \frac{S}{\frac{1}{2}n(n-1)} \tag{5-42}$$

$\tau = 1$ if all pairs are concordant, i.e. $n_c = \frac{1}{2}n(n-1)$ and $\tau = -1$ if all pairs are discordant, i.e. $n_d = \frac{1}{2}n(n-1)$. Values of ± 1 for Kendall's τ thus imply linearity in the ranks, i.e. the order smallest to largest, denoted 1 to n, within each of the x_i, y_i, is the same. This is different to linearity in the original values on which the ranks are based. If the ranking of the X-values and Y-values is independent $n_c \approx n_d$ and τ will be close to zero.

If it is assumed that the distributions of the populations from which the X-values and Y-values are obtained are independent yet making no assumption of what this distribution is, then in a sample of n members of each population, chosen at random, any order of the chosen X-values is equally likely to appear with any order of the chosen Y-values. Thus each of the possible $n!$ arrangements of the ranks of the X-values paired with the ranks of the Y-values, giving a particular value for Kendall's τ, has the same probability $1/n!$. The number of arrangements that give a particular τ are counted and when divided by $n!$ give the probability of that value of τ. Hence the exact probability distribution of τ for a particular number n of pairs is obtained. Since τ is proportional to S, where $S = n_c - n_d$ (see equation (5-42)) it is standard practice to obtain the distribution for S rather than τ. S and hence τ has a probability distribution symmetric about zero, which is strictly distribution-free (Sen, 1968) and thus may be used as a test statistic in a non-parametric method. For large n ($n \geq 10$) the probability distribution of S approaches the normal curve (Kendall, 1970):

$$f(S) = \frac{1}{\sigma\sqrt{2\pi}} \exp^{-\frac{S^2}{2\sigma^2}} \tag{5-43}$$

where σ is given by

$$\sigma^2 = \frac{1}{18} n(n-1)(2n+5) \tag{5-44}$$

5.4.2 Method

In the non-parametric line regression method, first proposed by Theil, the slope of the regression line is estimated as the median of the slopes of all lines joining pairs of points with different X-values (Theil, 1950; Sprent, 1989). Thus a data pair (x_i, y_i) and (x_j, y_j) define a slope, b_{ij}, of

$$b_{ij} = \frac{y_j - y_i}{x_j - x_i} \tag{5-45}$$

Clearly $b_{ij} = b_{ji}$ for all i and j. For n observations there are thus only $\frac{1}{2}n(n-1)$ algebraically distinct b_{ij} that have to be computed and put into ascending order. The median, b^* is then selected as

$$b^* = \begin{cases} B_{m+1}, & n = 2m+1 \\ \frac{1}{2}(B_m + B_{m+1}), & n = 2m. \end{cases} \tag{5-46}$$

Sen (1968) extended the method to the case where not all x_i need to be distinct. The difference is that in this case b^* is the median of the N slopes for which $x_i \neq x_j$. Sen also shows that the method is still valid if both variables (as opposed to just y_i) are subject to errors, provided that the ranking of the x_i without errors is the same as that with errors, somewhat difficult to prove in practice. This suggests that in a TT-plot to which Theil's method is to be applied, it is better to use as X variable the brightness temperatures of the image that has undergone the greater amount of smoothing subsequent to the observing process, i.e. the map of higher initial resolution.

A nominal 95% (two sigma) confidence interval (i.e. of actual size 95% or higher) for b^* is formed as follows. Such a confidence interval requires testing at the 5% significance level in a two-tail test. A two-tail test is appropriate in this case, because the true value of b can be both higher or lower than the median. Sprent (1989) provides a motivation for the statistical inferences of Theil's technique that is not excessively encumbered with statistical jargon. A certain number r of all the high values and also the low values of b_{ij} are rejected, as determined from the probability distribution of Kendall's τ. This is achieved by looking up the critical value, c, for a two tail-test at the 5% level in a table of the test statistic based on Kendall's τ for the value n of the number of pairs (x_i, y_i). r is given by

$$r = \frac{1}{2}(N - c) \tag{5-47}$$

where N is the number of b_{ij}. Note that n gives the number of data pairs (x_i, y_i), whereas N gives the number of b_{ij}, with $N \leq \frac{1}{2}n(n-1)$, where the less than occurs when there are ties in the X-values of the data pairs.

If r is non-integral it is rounded down. The lower limit of the confidence interval, b_l, is then given by the $r+1$ smallest b_{ij}. By symmetry the upper limit, b_u, is obtained by rejecting the r largest b_{ij}.

The critical values, c, of such a test statistic based on an absence of ties for a two-tail test at the 5% level are tabulated in table [5-2]. These values were obtained from Kaarsemaker & van Wijngaarden (1953). For $n \leq 40$ Kaarsemaker and van Wingaarden derived the probability distribution for S from first principles rather than the approximation given above (see equation (5-43) and equation (5-44)). The critical values, c, corresponding to a nominal 95% confidence interval were selected from their tables. For $n > 40$ to $n = 100$ equation (5-44) was used. The critical values for a nominal 95% confidence interval (Kaarsemaker & van Wijngaarden, 1953) are then given by

$$c = 1.96\sigma + 1 \tag{5-48}$$

where c is then rounded up to the next even or odd number depending on whether $n = 0, 1 \pmod 4$ or $n = 2, 3 \pmod 4$ respectively (Kendall, 1970). σ is given by equation (5-44).

For n less than five there is insufficient information to form a 95% confidence interval. As a 3 point TT-plot is at the limit of the resolution of an image one may wish to determine the spectral index in such a case. For n equal to four and three (marked with a star in the table) the maximum confidence level is thus given by the lowest and highest b_{ij} and results in a 91.6% and a 66.67% confidence interval respectively.

A test statistic based on Kendall's τ will be slightly different if determined for the case of no ties as opposed to when ties are present. In the latter case the particular kind of tie (i.e. two equal x_i or three equal x_i etc) and the number of them present will further affect the form of the statistic.

If ties are present in the x_i then Kendall (1970) states that "...the distribution of τ for any fixed number of ties tends to normality as n increases, and there is probably little important error involved in using the normal approximation for n $\geq$ 10, unless the ties are very extensive or very numerous, in which case a special investigation may be necessary. For the case $n < 10$ no complete tables are available owing to the large number of possibilities. The distributions have, however, been tabulated by Sillitto (1947) for any number of tied pairs or tied triplets up to and including $n = 10$."

I expected the number of data points to be less than or equal to 10 in most situations where I intended to apply Theil's method to TT-plots. Hence I decided to incorporate the changes in the critical value c when ties are present for the case of $n \leq 10$.

n	c	n	c	n	c	n	c
1	-	26	91	51	243	76	440
2	-	27	95	52	250	77	448
3*	3	28	100	53	258	78	457
4*	6	29	106	54	265	79	464
5	10	30	111	55	271	80	474
6	13	31	117	56	280	81	482
7	15	32	122	57	286	82	491
8	18	33	128	58	295	83	501
9	20	34	133	59	301	84	510
10	23	35	139	60	310	85	518
11	27	36	146	61	316	86	527
12	30	37	152	62	325	87	537
13	34	38	157	63	333	88	546
14	37	39	163	64	340	89	556
15	41	40	170	65	348	90	565
16	46	41	176	66	357	91	573
17	50	42	183	67	365	92	584
18	53	43	189	68	372	93	592
19	57	44	196	69	380	94	603
20	62	45	202	70	389	95	611
21	66	46	209	71	397	96	622
22	71	47	215	72	406	97	630
23	75	48	222	73	414	98	641
24	80	49	230	74	421	99	651
25	86	50	237	75	431	100	660

Table [5-2]: Critical values, c, used in determining upper and lower confidence limits for the slope when determined by Theil's method from n data pairs without any ties.

n	twins	triplets	c	% (if not 95%)
3	no ties allowed			
4	1	-	5	83.4
5	1	-	9	-
	2	-	8	93.4
6	1	-	12	-
	2	-	11	-
	3	-	10	-
	-	1	12	-
7	1	-	14	-
	2	-	15	-
	3	-	14	-
	-	1	14	-
	1	1	15	-
8	1	-	17	-
	2	-	18	-
	3	-	17	-
	4	-	18	-
	-	1	17	-
	1	1	16	-
	2	1	17	-
9	1	-	21	-
	2	-	20	-
	3	-	21	-
	4	-	20	-
	-	1	21	-
	1	1	20	-
	2	1	19	-
	3	1	20	-

Table [5-3]: The critical value c when ties are present for the case of $n \leq 10$.

However, I did this only for ties whose number and kind I considered consistent with a straight line interpretation of the data points rather than a scatter plot. These critical values, as obtained from Sillitto (1947) are tabulated in table [5-3]. In some instances the combination of twins (two x values equal) and triplets (three x values equal) leads to a maximum confidence interval less than 95%. In those cases the percentage for the confidence interval is tabulated.

5.5 Discussion and Conclusion of line fitting

A good characteristic of Theil's method is that it is robust. Outliers are far less likely to affect the value of b^* than in a least squares method. Outliers do however have the effect of skewing the confidence interval, i.e. they make it non-symmetric about the value of b^*. The robustness of Theil's method is desirable for TT-plot line fits as smoothing effects at changeovers in spectral index effectively cause mild outliers which cannot always be easily rejected—rejection in such a scenario being a subjective decision made by eye.

The Theil method treats the variables symmetrically as is appropriate for TT- plot line fitting.

Intuitively one would think that Theil's method would perform better when more weight is given to the b_{ij} for pairs of points fairly far apart, i.e. to take some sort of weighted median (references to such methods are given in Sprent, 1989). This does however destroy the robustness of the method when outliers are present, a property that is desirable when doing linear regression on TT-plots.

Sprent (1989) also points out that: " In simulation studies involving outliers that effectively amounted to replacing normally distributed errors with errors from long-tail distributions, Hussain and Sprent (1983) found that Theil's method was almost as efficient as least squares when the normality assumptions were valid and that it showed a marked improvement in efficiency with a long-tail error distribution, especially with sample sizes less than 30. "

Thus I decided to use Theil's method for line fitting to TT-plots. Since it is the uncertainty interval that is more convincing for a low number of data points in the Theil method as opposed to that given by the OLS bisector method, rather than a large discrepancy in the actual estimate of the slope, I decided to also fit the lines with the OLS Bisector method (as encoded by Isobe et al. (1990) in SLOPES) in order to have an independent check on the results.

An abbreviated form of Theil's method exists which cuts down on computing time, but is not recommended unless $n \geq 12$ (Sprent, 1989). As the number of points in a TT-plot will rarely be much more than that and quite often less than 12, I decided to use the full method described above. Also, the confidence interval of the full Theil estimation procedure is reasonably expected to be shorter, as a greater amount of relevant information is used (Sprent, 1989).

As I could not find the computer code for the Theil method in the literature, I wrote a program that determines the slope and the upper and lower limits of a nominal 95% uncertainty interval for the slope using the method described above as Theil's method.

5.6 Constant latitude TT-plot spectral index image

Program TVST was applied to the 2326 MHz and 408 MHz images of the Gum Nebula. Of these two images, the 408 MHz image has the lower resolution (0.85°). Thus a resolution of 0.85° was the highest resolution at which the TVST program could be applied.

As the original 2326 MHz image had to be smoothed fairly severely to bring it to this resolution, essentially scanning effects in this image were smoothed away. The 408 MHz image did not require smoothing and thus retained all its scanning effects (see

Fig. [4-2]). Hence at this resolution faint parts of the Gum Nebula at 408 MHz are severely affected by scanning effects. Tests showed that this affected the individual TT-plots of such faint regions, as the scanning effects dominated the small inherent variation in the brightness temperatures. As a result, program TVST could not assign a meaningful spectral index to such regions. It may seem counterproductive to have used the images at this resolution at all. However, TT-plot deviations from the standard straight line become more pronounced at lower resolution. Thus there is some merit in working with as high a resolution as possible.

To obtain spectral index values for the very faint regions of the Gum Nebula, the TVST program was run a second time with data at a much lower resolution. As the 1.2° resolution linear-at-constant-latitude background method had shown that the 408 MHz image still had significant evidence of scanning effects in the fainter regions of the Gum Nebula, a resolution of 1.7° was chosen for the second application of the TVST program. This ensured an appropriate reduction in the scanning effects of the 408 MHz data.

Three pixels in latitude cover the resolved length in latitude. Thus the TVST process effectively overresolves in latitude, because it is applied to each individual pixel line in latitude. Hence a consecutive running mean over three pixels in latitude was applied to the raw TT-plot spectral index images. The final 0.85° and 1.7° resolution TVST spectral images are shown in Figs. [5-17] and [5-18]. In these the Theil method was used for the straight line fitting.

Immediately noticeable is that these spectral index images (Figs. [5-17] and [5-18]) follow the same trends as deduced from those produced from the background subtracted Gum Nebula. This is very pleasing and a more detailed comparison follows later.

Prior to discussing the results in terms of what they imply for the Gum Nebula, I wish to compare the values determined using Theil fitting with those obtained using the OLS bisector.

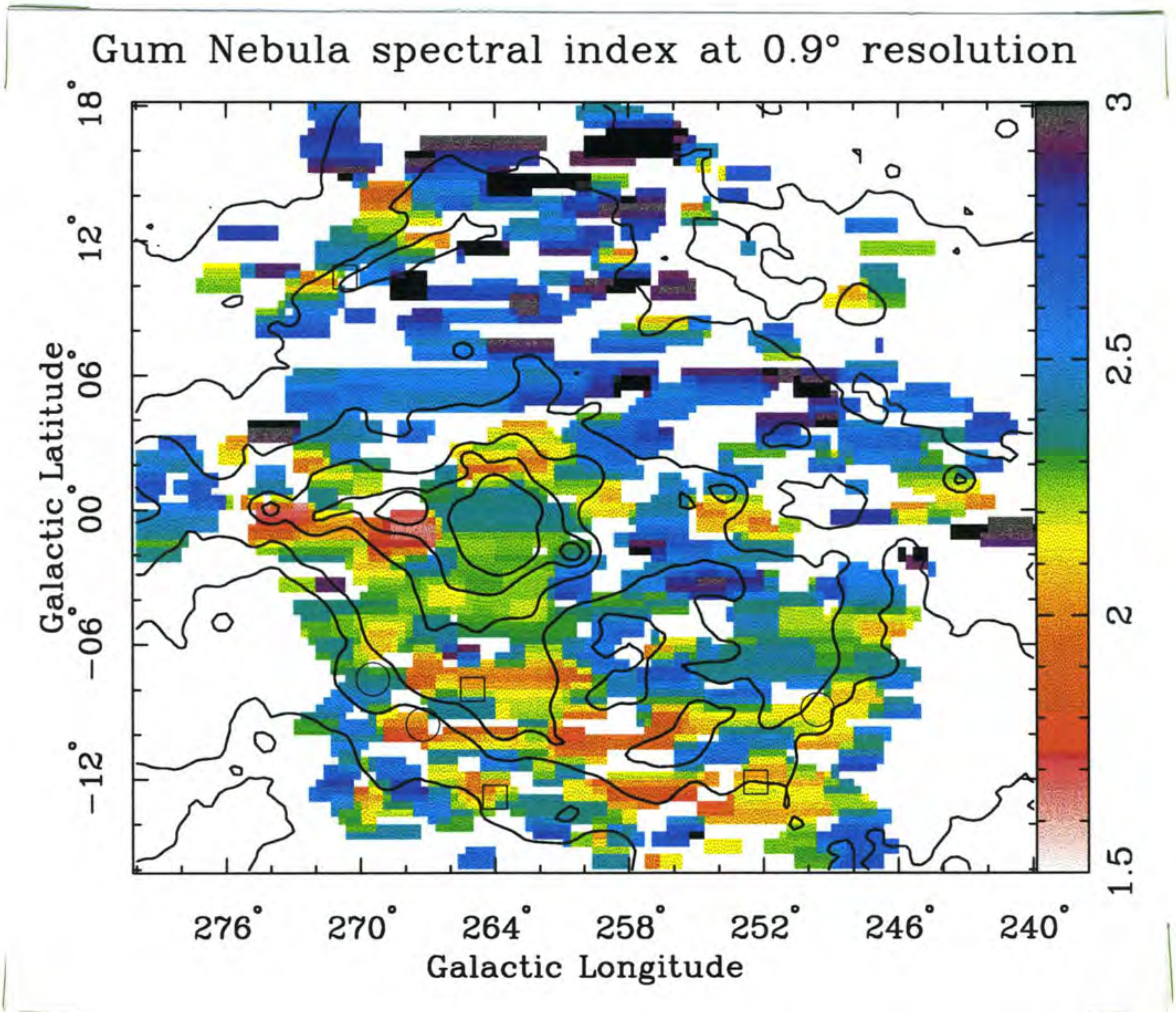

Figure [5-17]: The TT-plot spectral index image at 0.85° resolution as obtained from the Theil fit to the straight line sections of constant latitude TT-plots. The colour bar on the right gives the colour to spectral index conversion. The contour lines follow constant value brightness temperatures in the 0.85° 2326 MHz image, allowing for the identification of structures in the Gum Nebula with their spectral index values.

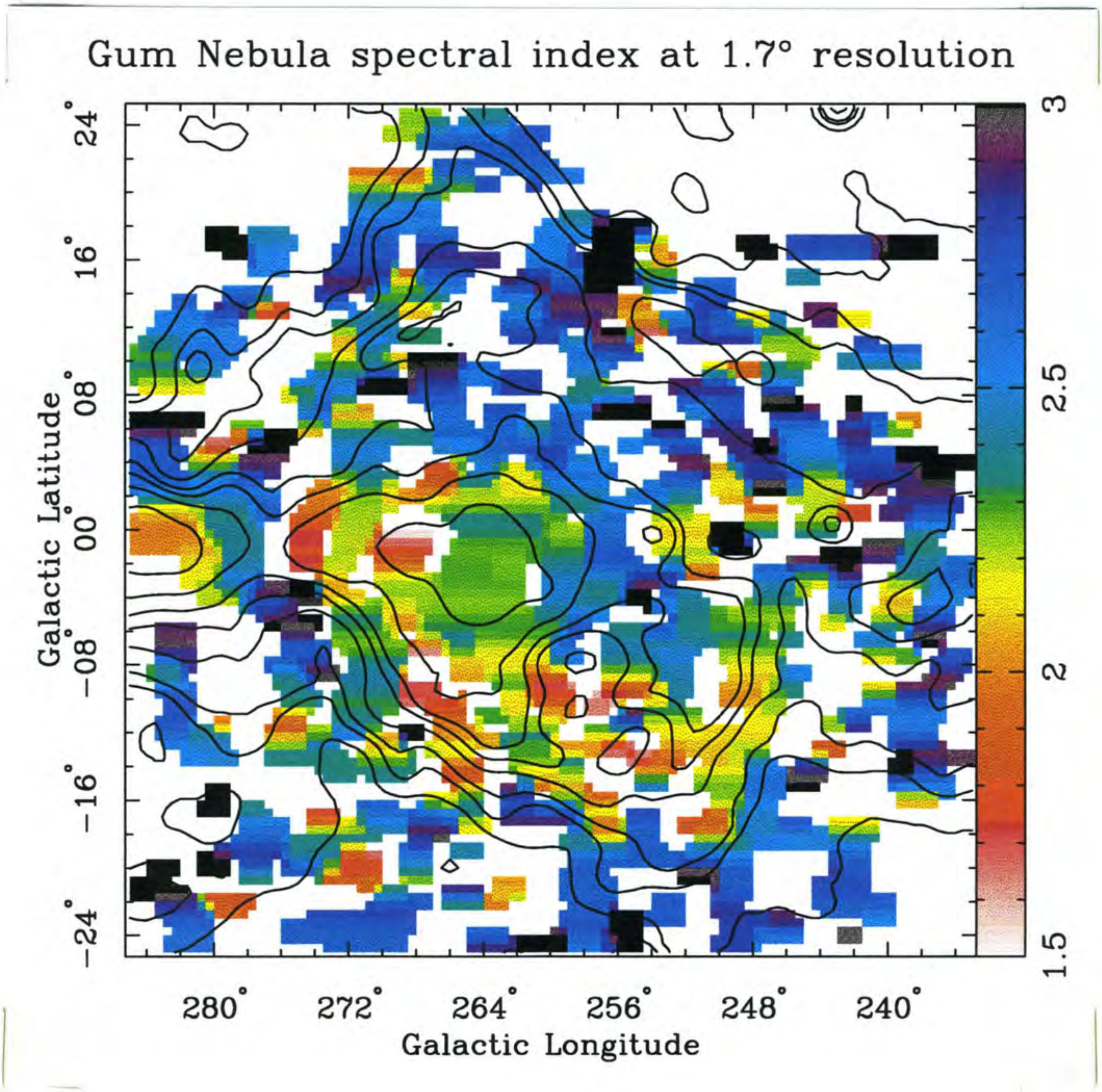

Figure [5-18]: The TT-plot spectral index image at 1.7° resolution as obtained from the Theil fit to the straight line sections of constant latitude TT-plots. The colour bar on the right gives the colour to spectral index conversion. The contour lines follow constant value brightness temperatures in the 1.7° 2326 MHz image, allowing for the identification of structures in the Gum Nebula with their spectral index values.

5.7 Comparison of OLS bisector and Theil method TT-plot spectral index and confidence interval

For these comparisons it is appropriate to use the raw results, i.e. no three pixel running mean along galactic latitude has been applied to the images discussed in this section.

The 0.85° resolution results are presented first. Fig. [5-19] shows the a) upper and b) lower limits of the spectral index determined from the 95% confidence interval given for the Theil method fit to the straight line sections of constant latitude TT-plots. Although this allows the direct reading off of these limits, it is not as instructive as the upper and lower uncertainties.

For the purposes of comparing the TT-plot Theil method uncertainty with that derived for the GUMBACK spectral index image, the difference of the upper limit Theil spectral index and the Theil estimate of the true spectral index (in future called the upper uncertainty) as well as the difference of the lower limit Theil spectral index and the Theil estimate of the true spectral index (in future called the lower uncertainty) are displayed in a) and b) of Fig. [5-20] respectively. Even though there are several regions for which this difference is greater than 0.3 for the Gum Nebula, it is generally in the range of 0.08 to 0.18. This is quite acceptable and allows one to have greater confidence in these results than the GUMBACK results where the uncertainty for the 1.2° resolution work generally is of the order of 0.5.

The Theil method is considered to give a valid confidence interval even for a TT-plot of as few as 5 data points. As the Theil confidence interval is not a nominal 95% when the number of data points are 3 or 4 or if ties are present, a percentage confidence interval map is shown in Fig. [5-21]. Note that most of the regions where a spectral index is defined have the nominal confidence interval of 95%.

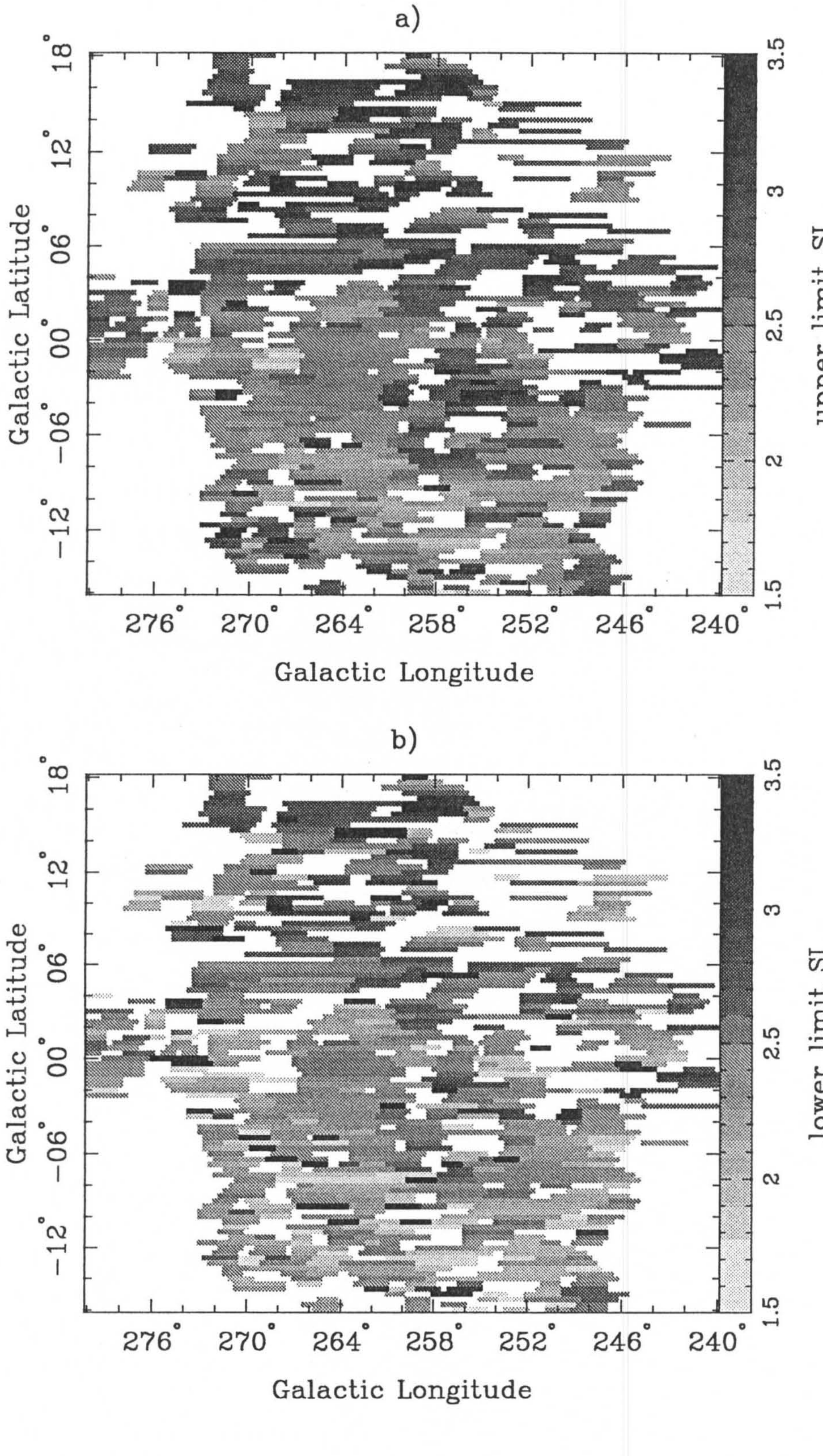

Figure [5-19]: The 0.85° resolution a) upper and b) lower limits of the spectral index (SI) determined from the confidence interval given for the Theil method fit to the straight line sections of constant latitude TT-plots.

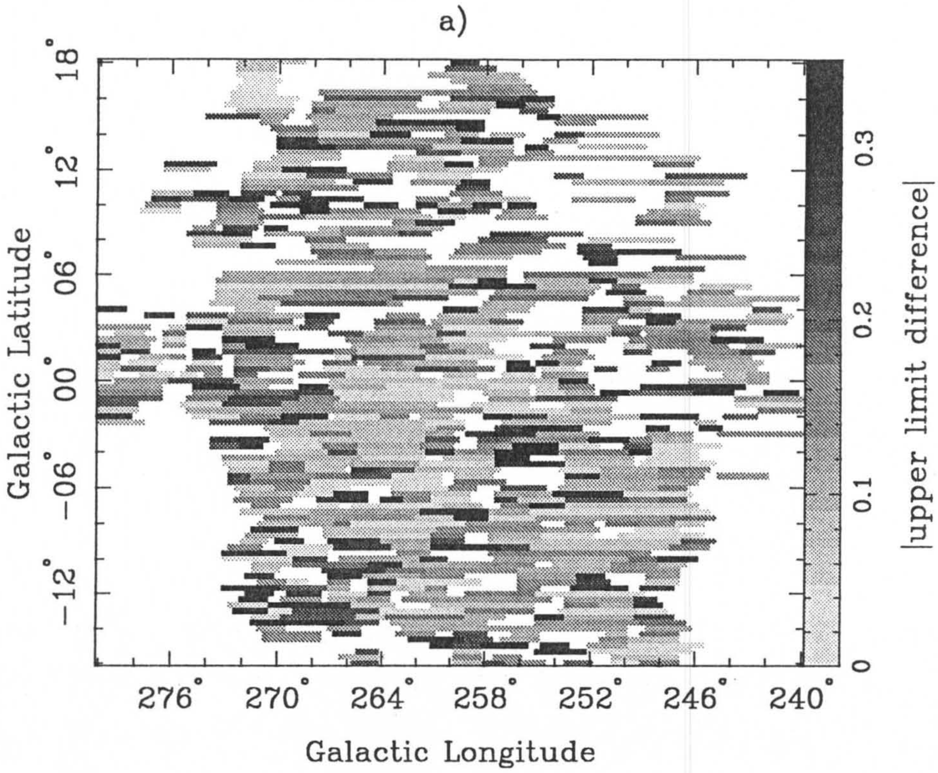

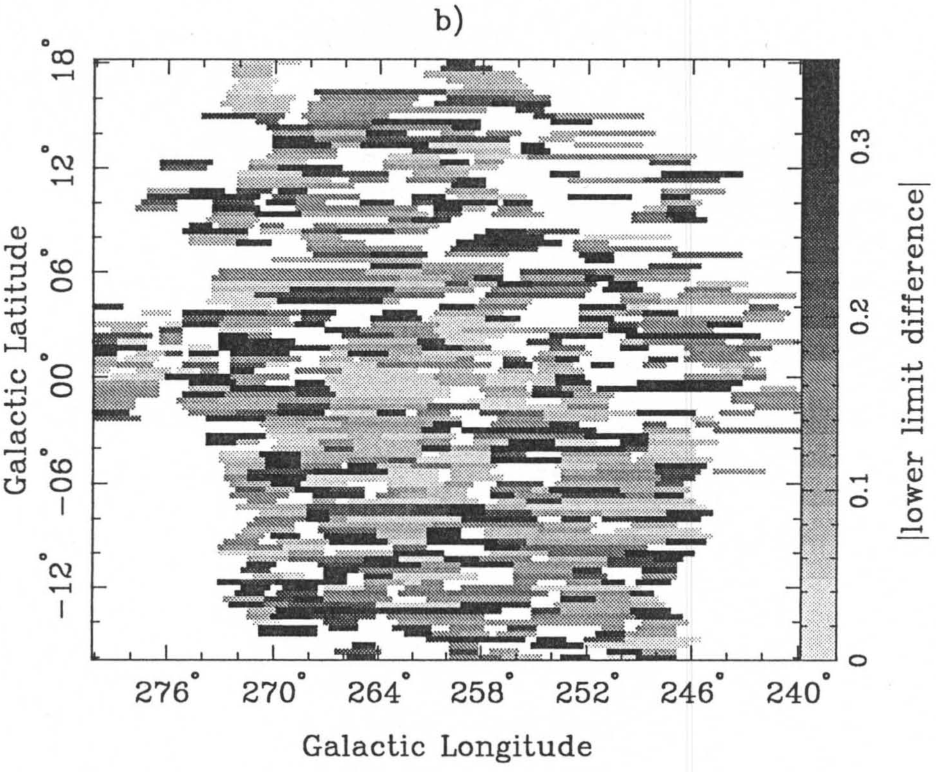

Figure [5-20]: a) The upper limit Theil spectral index minus the Theil estimate of the true spectral index at 0.85° resolution. b) The lower limit Theil spectral index minus the Theil estimate of the true spectral index at 0.85° resolution.

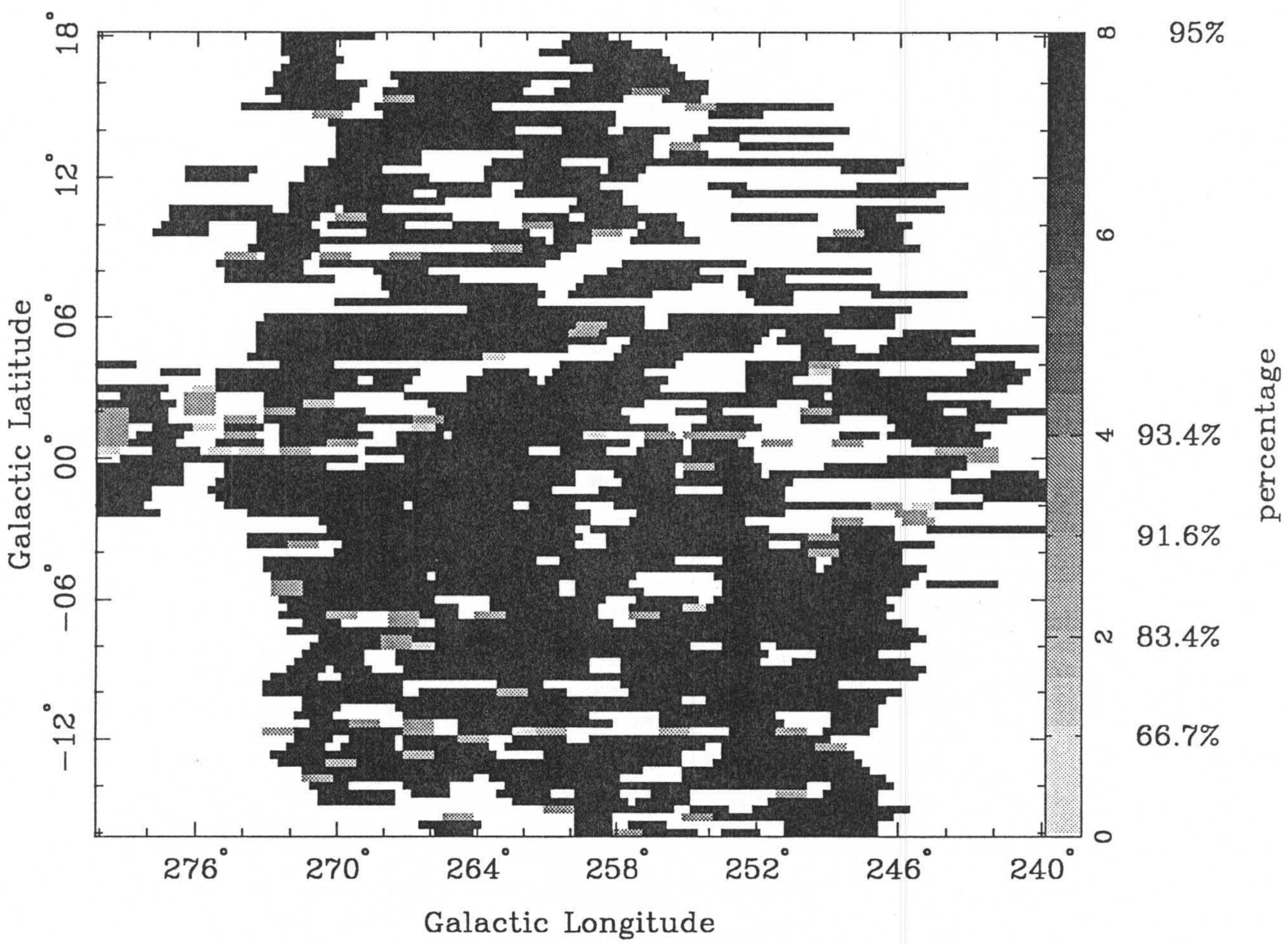

Figure [5-21]: The 0.85° resolution percentage confidence interval map of the Theil fit to straight line section of constant latitude TT- plots.

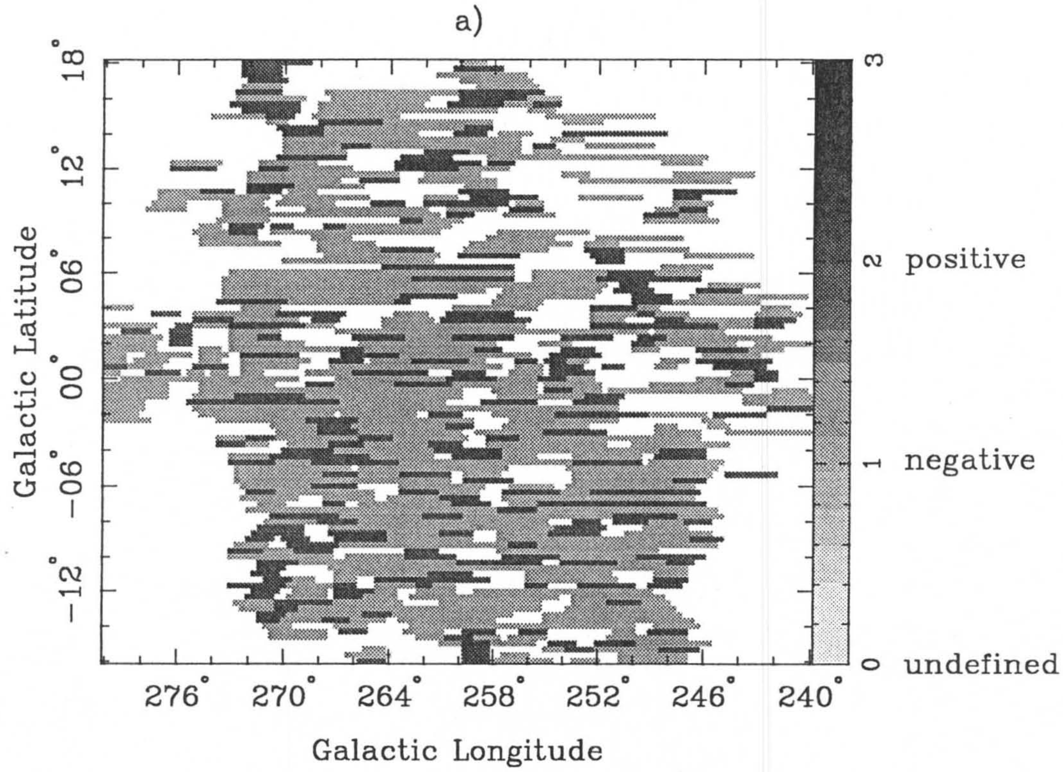

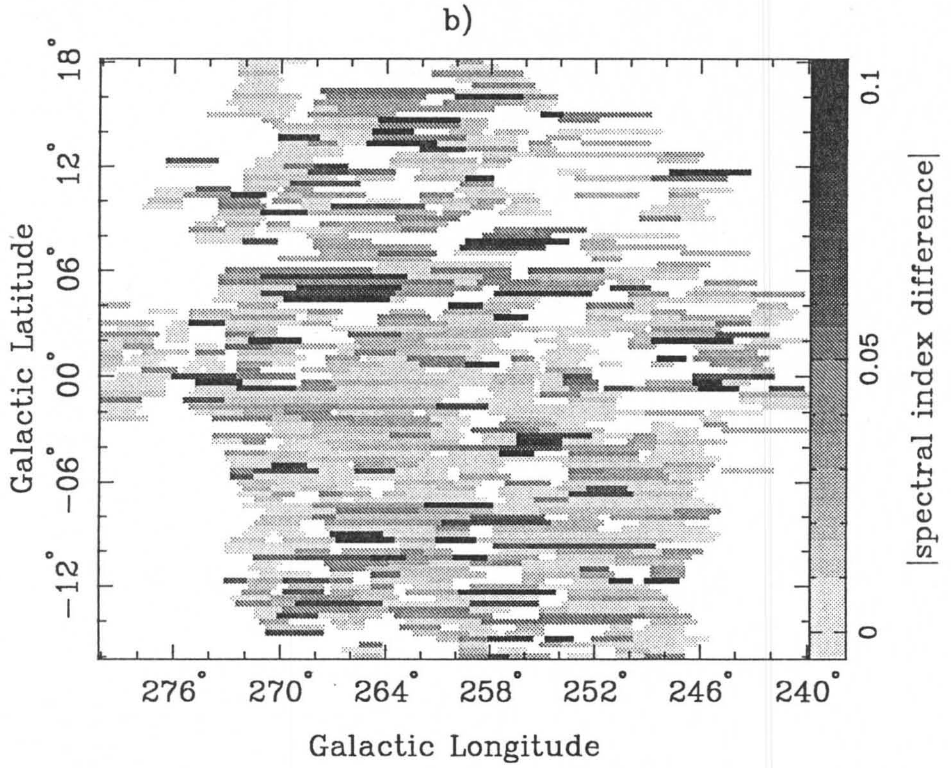

Figure [5-22]: The 0.85° resolution spectral index due to the Theil method minus the spectral index due to the OLS bisector. a) shows the sign of this difference and b) its magnitude.

For the purposes of comparing the Theil method and the OLS bisector method, several difference images were formed. Fig. [5-22] deals with the difference in the spectral index as determined with the Theil method and the OLS bisector. a) shows the sign of that difference, i.e. Theil method spectral index minus OLS bisector spectral index. It shows that this difference is predominantly negative i.e. the OLS bisector method yields a higher spectral index than the Theil method. This difference is however hardly significant, except in a few isolated cases where it is greater than 0.1, as seen in b) of the same figure. Hence the estimate of the true spectral index given by the two methods does not differ significantly.

A different picture emerges when looking at the difference in confidence intervals of the two methods. The Theil spectral index upper limit minus lower limit image is shown in a) of Fig. [5-23]. In the Gum Nebula region it is generally between 0.2 and 0.5 with a few regions having values greater than 0.8. The OLS bisector confidence interval is shown in b) of Fig. [5-23]. It is very rarely bigger than 0.2. As the OLS bisector confidence interval in known to be too small (see section 5.3), it is reassuring to see that the Theil method confidence interval is significantly larger. Yet the Theil method confidence interval is still significantly smaller than that of the GUMBACK method. The latter gave, for the 1.2° image, an uncertainty of ≈ 0.5 in the brighter regions, i.e. a confidence interval of ≈ 1.

Figs. [5-24] and [5-25] show the difference in the Theil spectral index upper limit and the OLS bisector spectral index upper limit, and the same difference for the lower limits respectively. Only in very few regions is the OLS bisector limit more extreme than the Theil limit and then by a very small margin.

The same images were formed for the 1.7° resolution work (see figures [5-26], [5-27], [5-28], [5-29], [5-30], [5-31], [5-32]). The upper and lower Theil uncertainties (Fig. [5-27]) are somewhat smaller than those of the higher resolution work. The sign of the difference of the Theil spectral index and the OLS bisector spectral index (Fig. [5-29]) is more evenly distributed in the Gum Nebula and its magnitude is generally smaller.

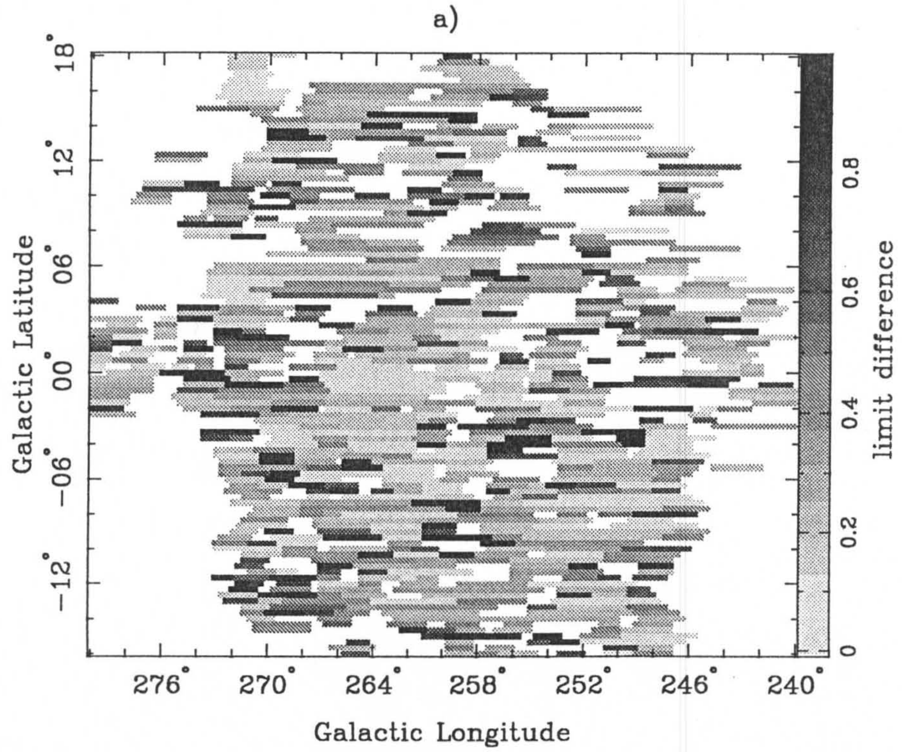

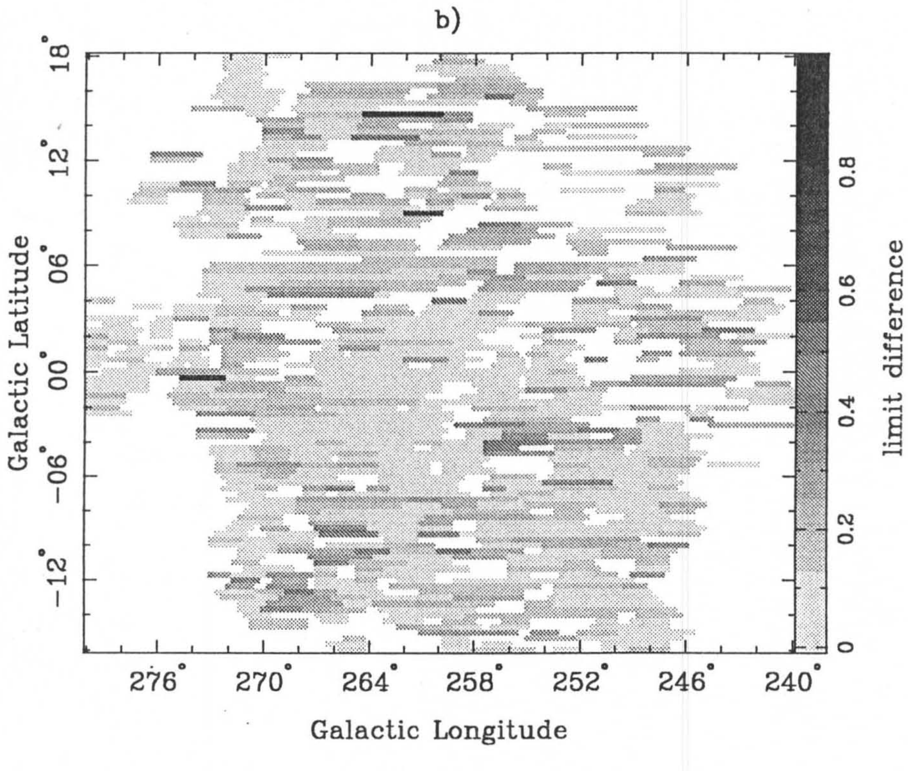

Figure [5-23]: The Theil spectral index upper limit minus lower limit image is shown in a). b) shows the corresponding OLS bisector image. The images are at a resolution of 0.85°.

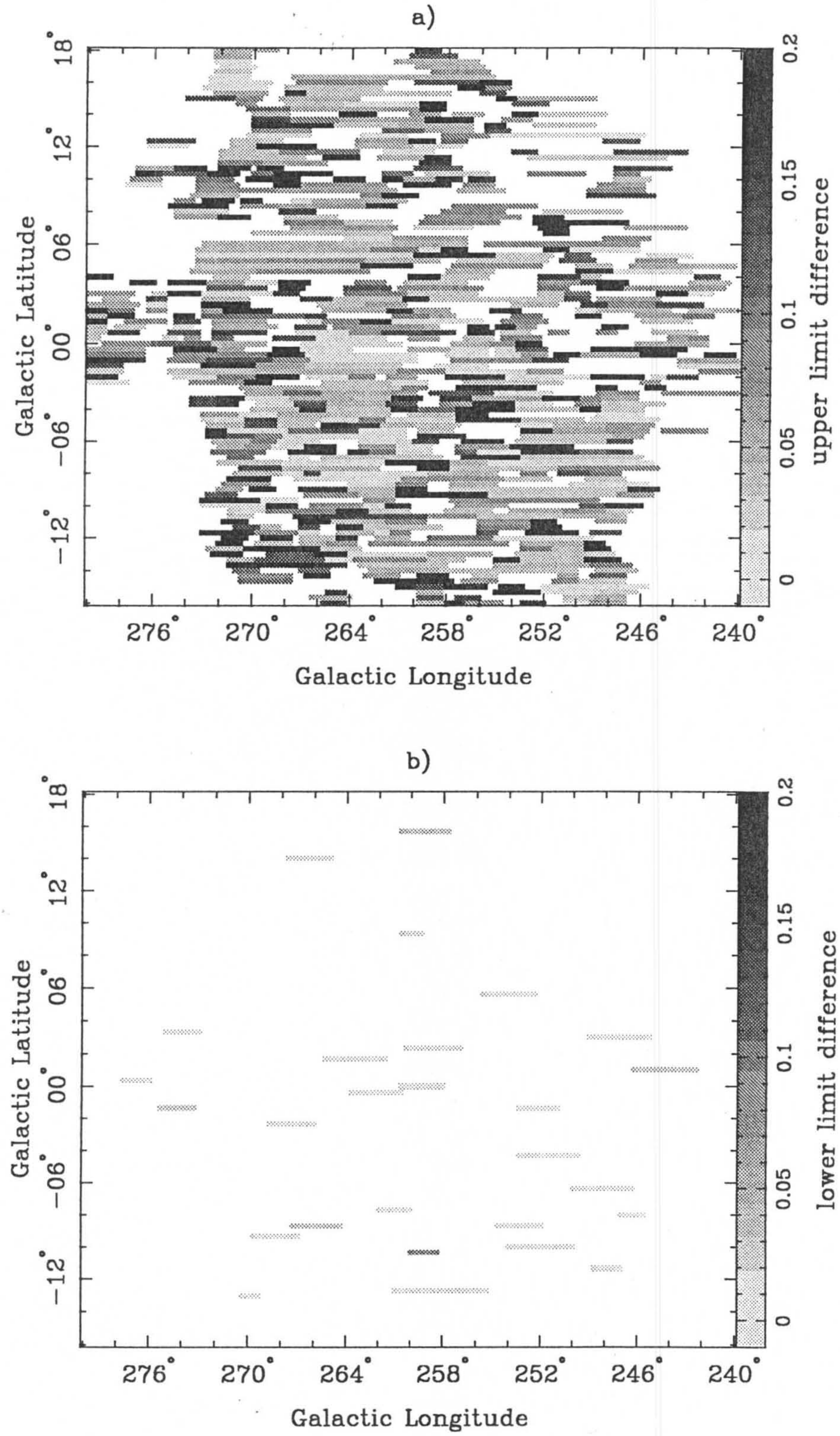

Figure [5-24]: a) and b) show respectively the magnitudes of the positive and negative values of the Theil spectral index upper limit minus the OLS bisector spectral index upper limit at 0.85° resolution.

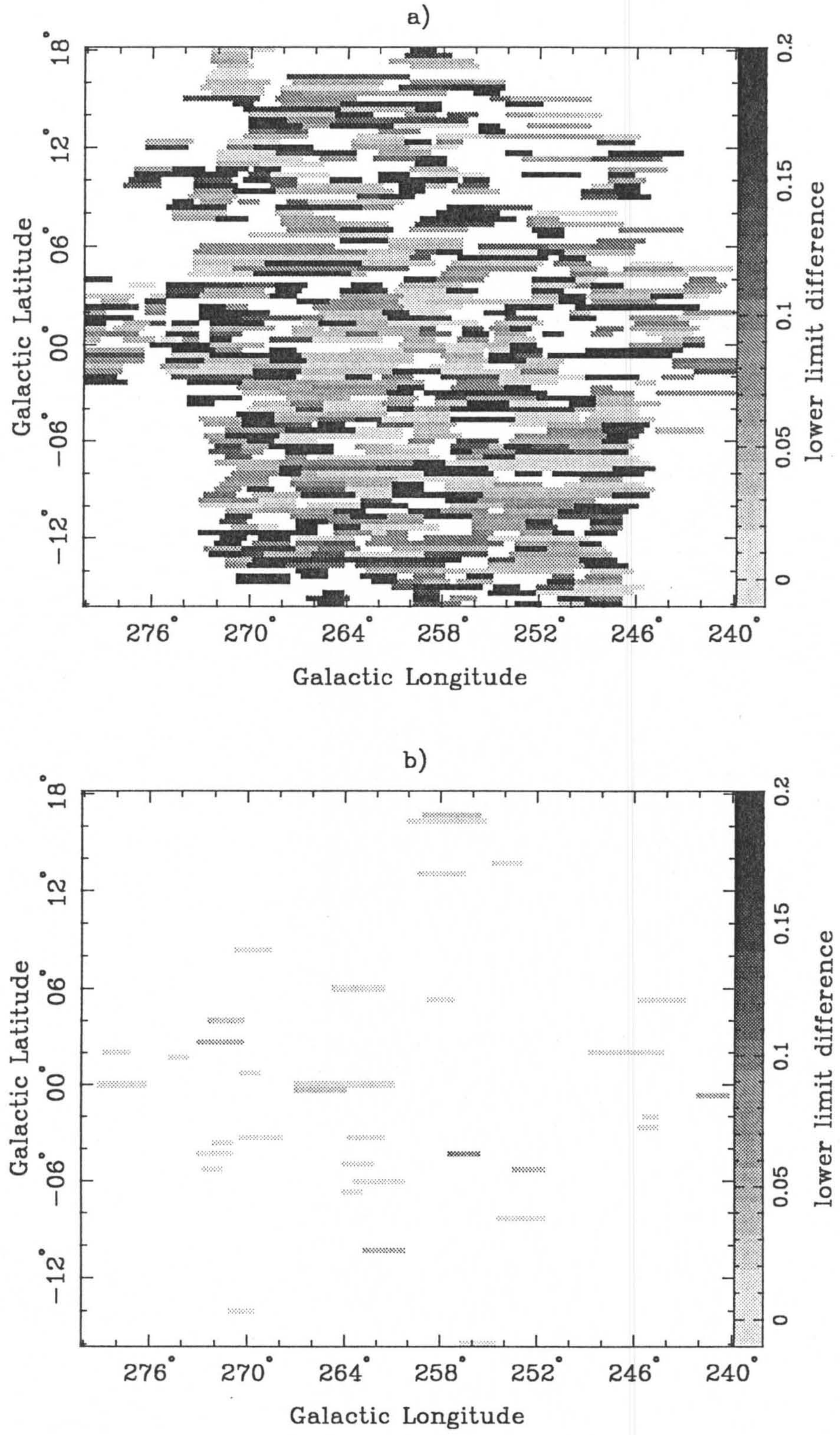

Figure [5-25]: a) and b) show respectively the magnitudes of the positive and negative values of the OLS bisector spectral index lower limit minus the Theil spectral index lower limit at 0.85° resolution.

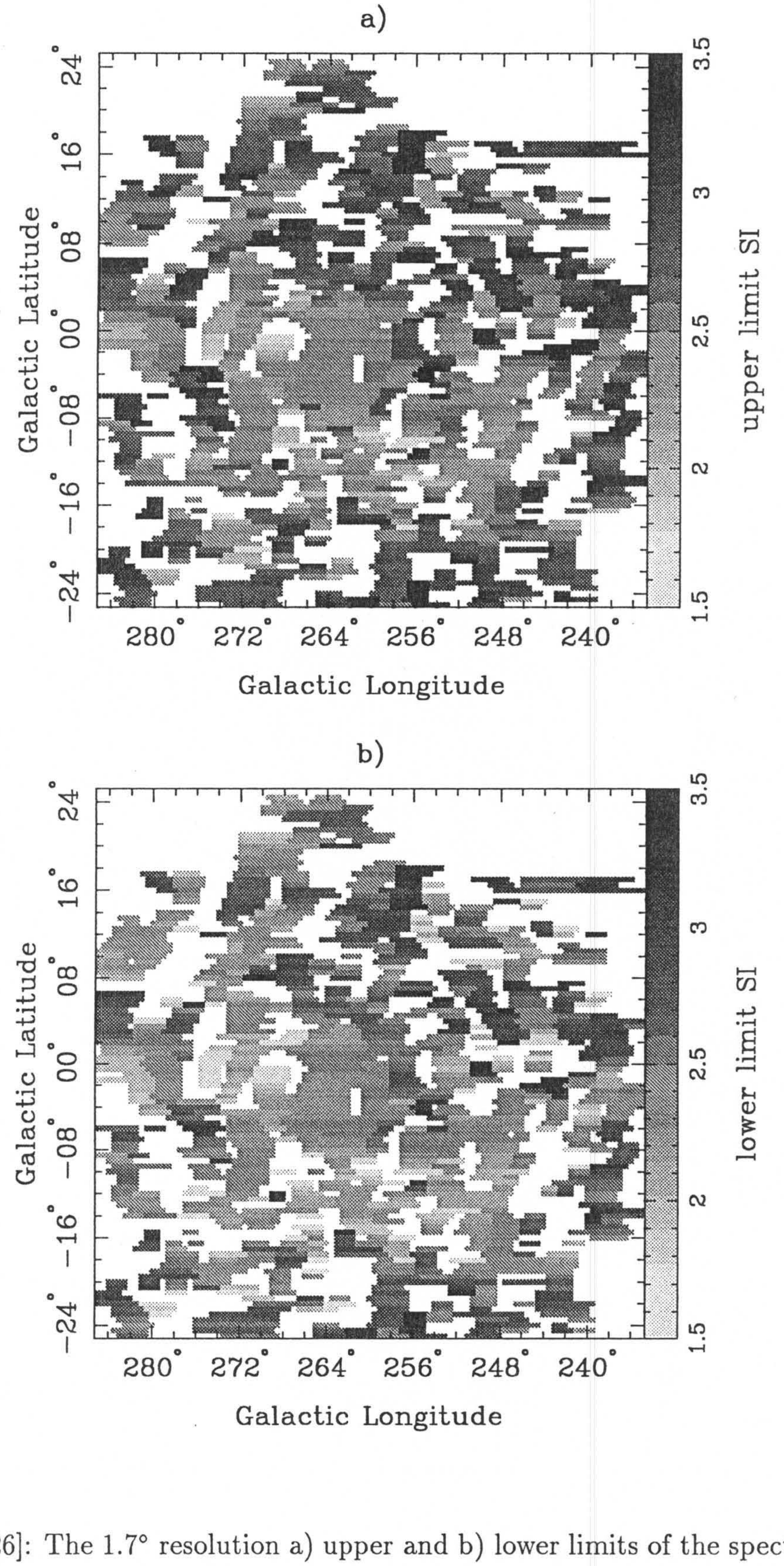

Figure [5-26]: The 1.7° resolution a) upper and b) lower limits of the spectral index (SI) determined from the confidence interval given for the Theil method fit to the straight line sections of constant latitude TT-plots.

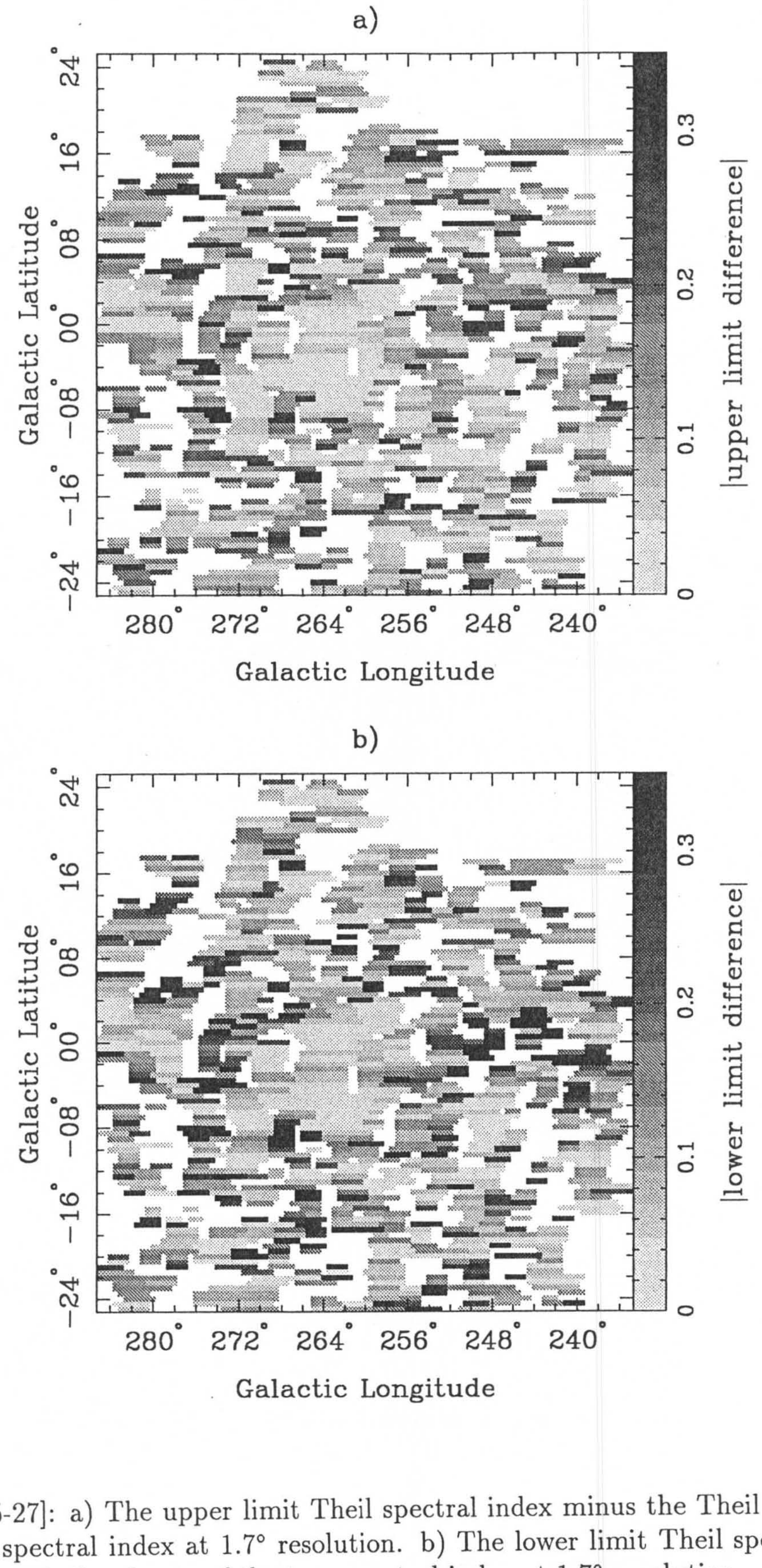

Figure [5-27]: a) The upper limit Theil spectral index minus the Theil estimate of the true spectral index at 1.7° resolution. b) The lower limit Theil spectral index minus the Theil estimate of the true spectral index at 1.7° resolution.

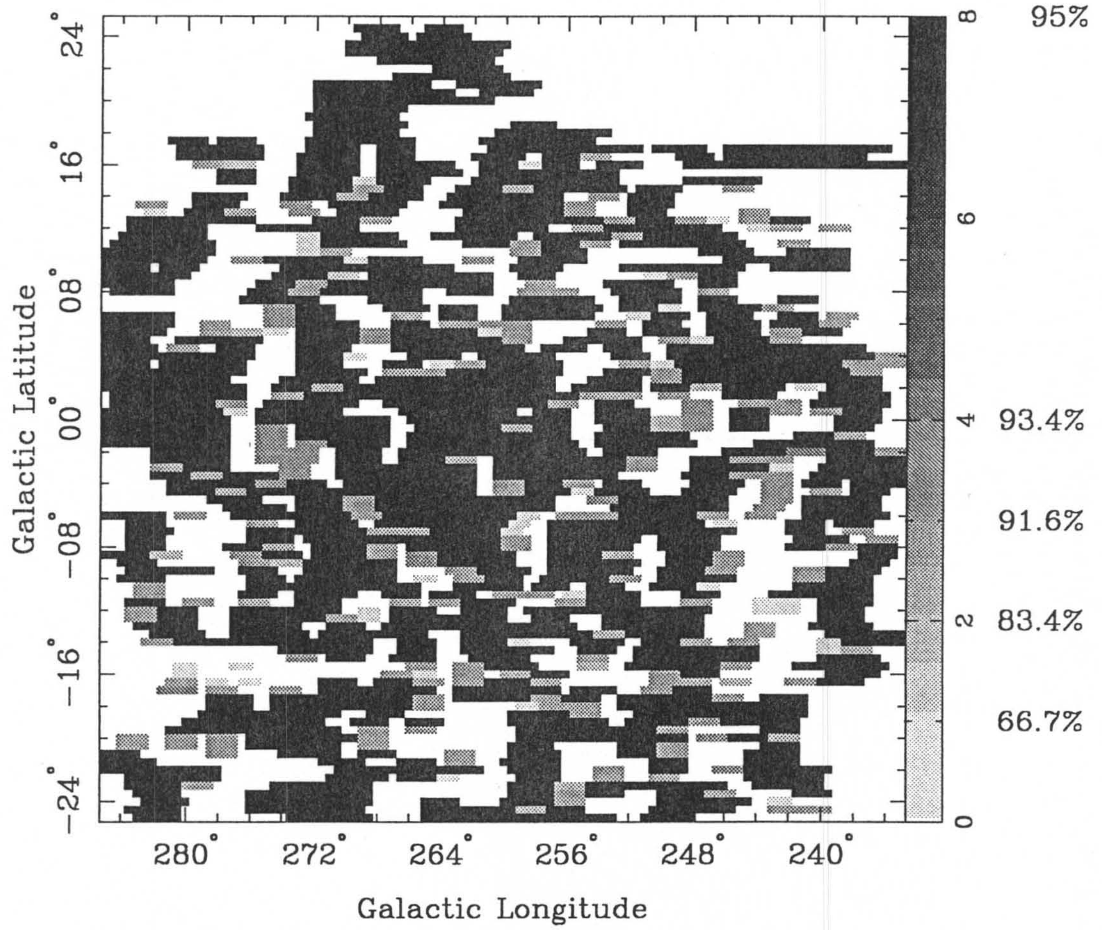

Figure [5-28]: The 1.7° resolution percentage confidence interval map of the Theil fit to straight line section of constant latitude TT- plots.

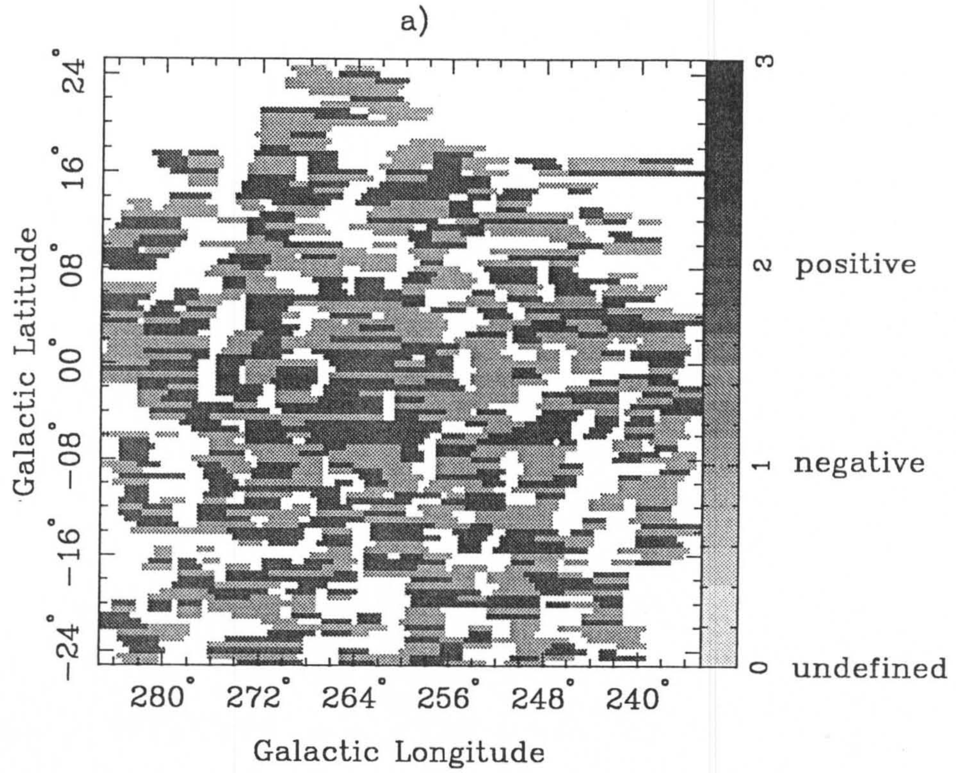

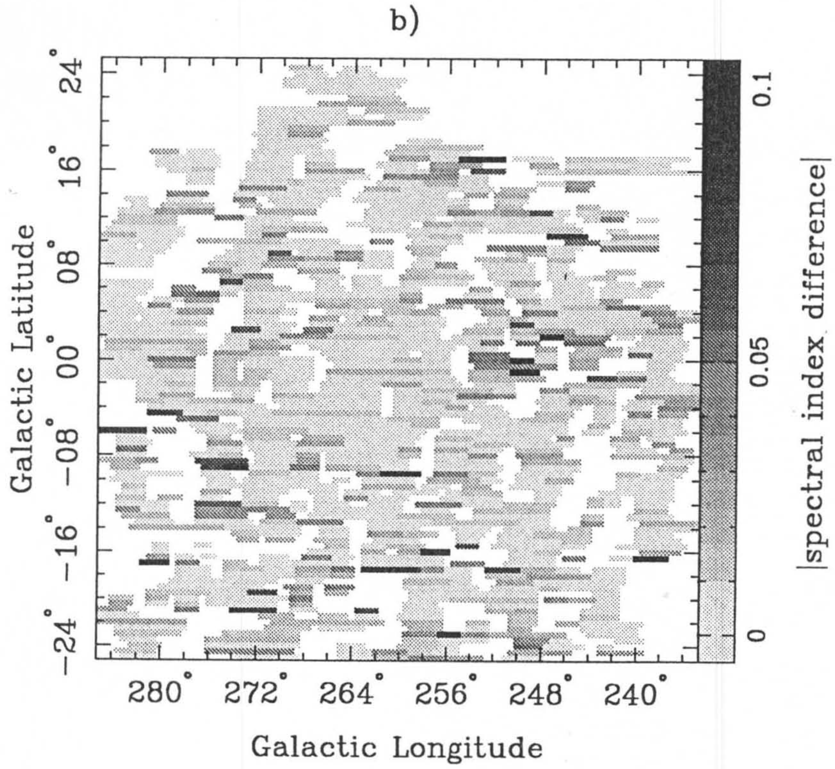

Figure [5-29]: The 1.7° resolution spectral index due to the Theil method minus the spectral index due to the OLS bisector. a) shows the sign of this difference and b) its magnitude.

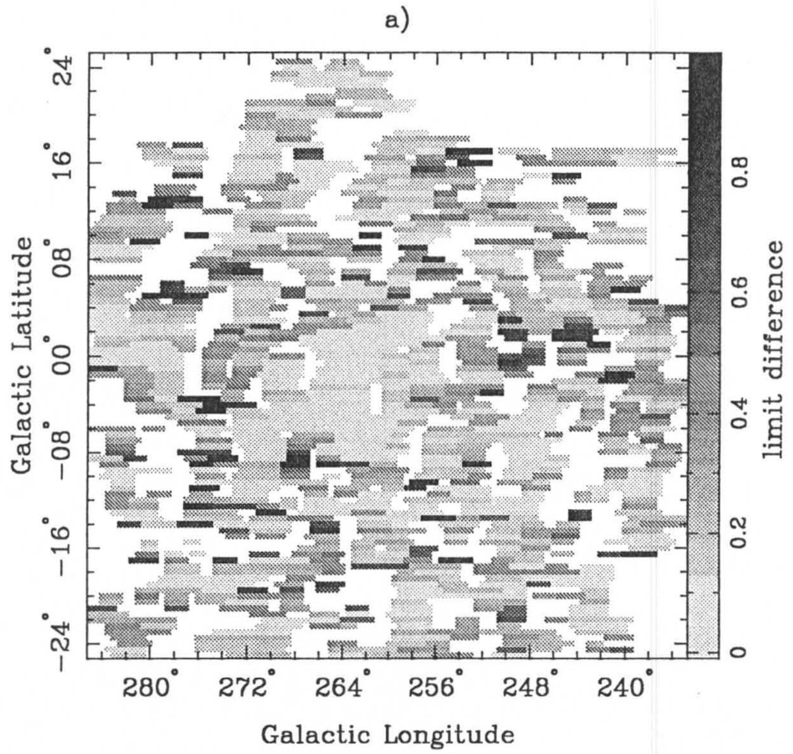

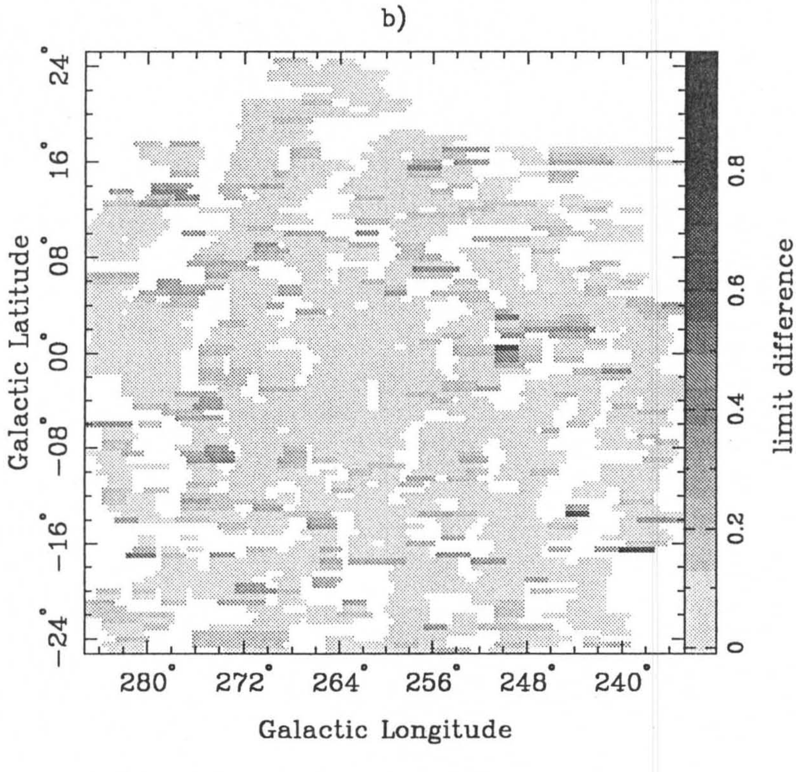

Figure [5-30]: The Theil spectral index upper limit minus lower limit image is shown in a). b) shows the corresponding OLS bisector image. The images are at a resolution of 1.7°.

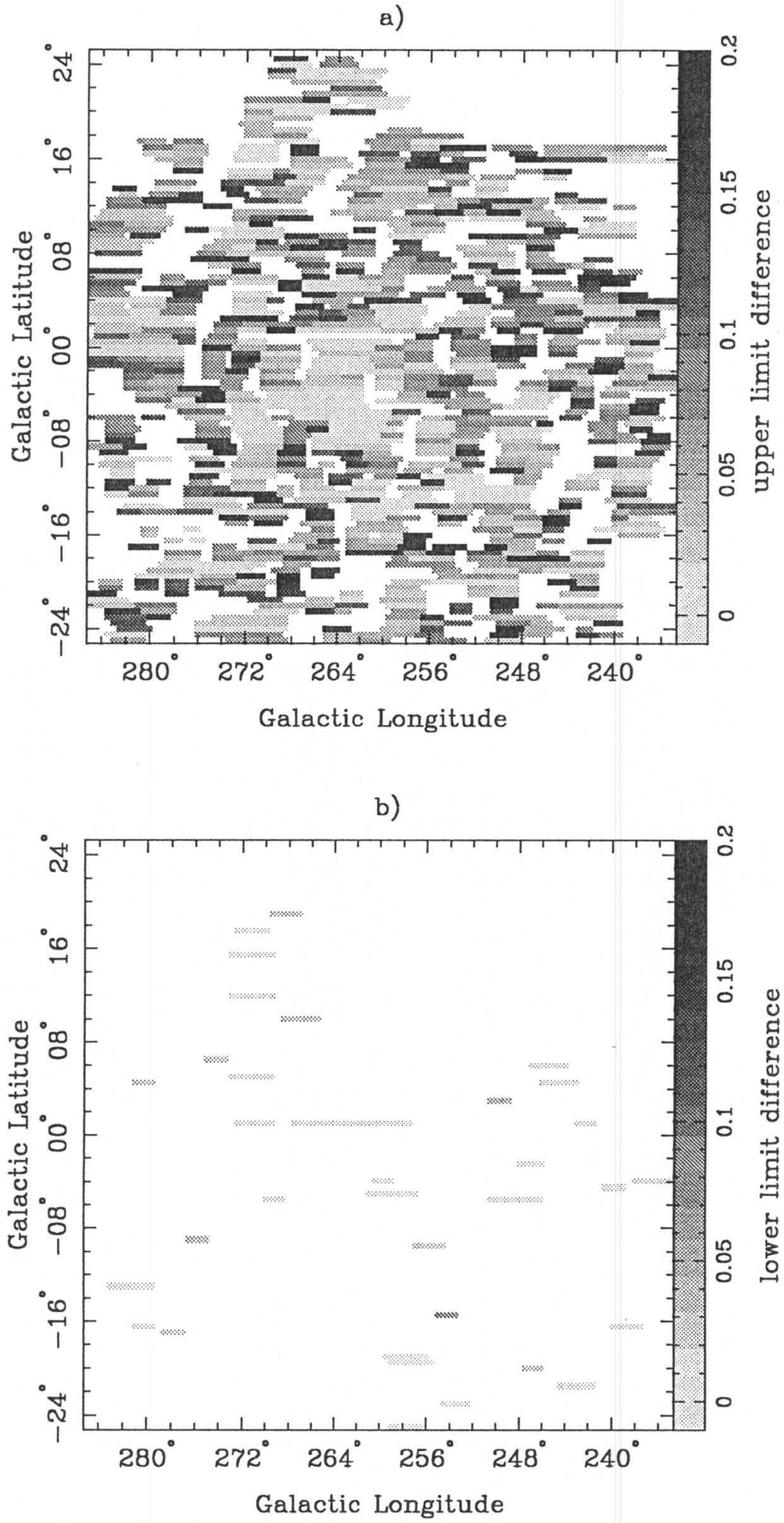

Figure [5-31]: a) and b) show respectively the magnitudes of the positive and negative values of the Theil spectral index upper limit minus the OLS bisector spectral index upper limit at 1.7° resolution.

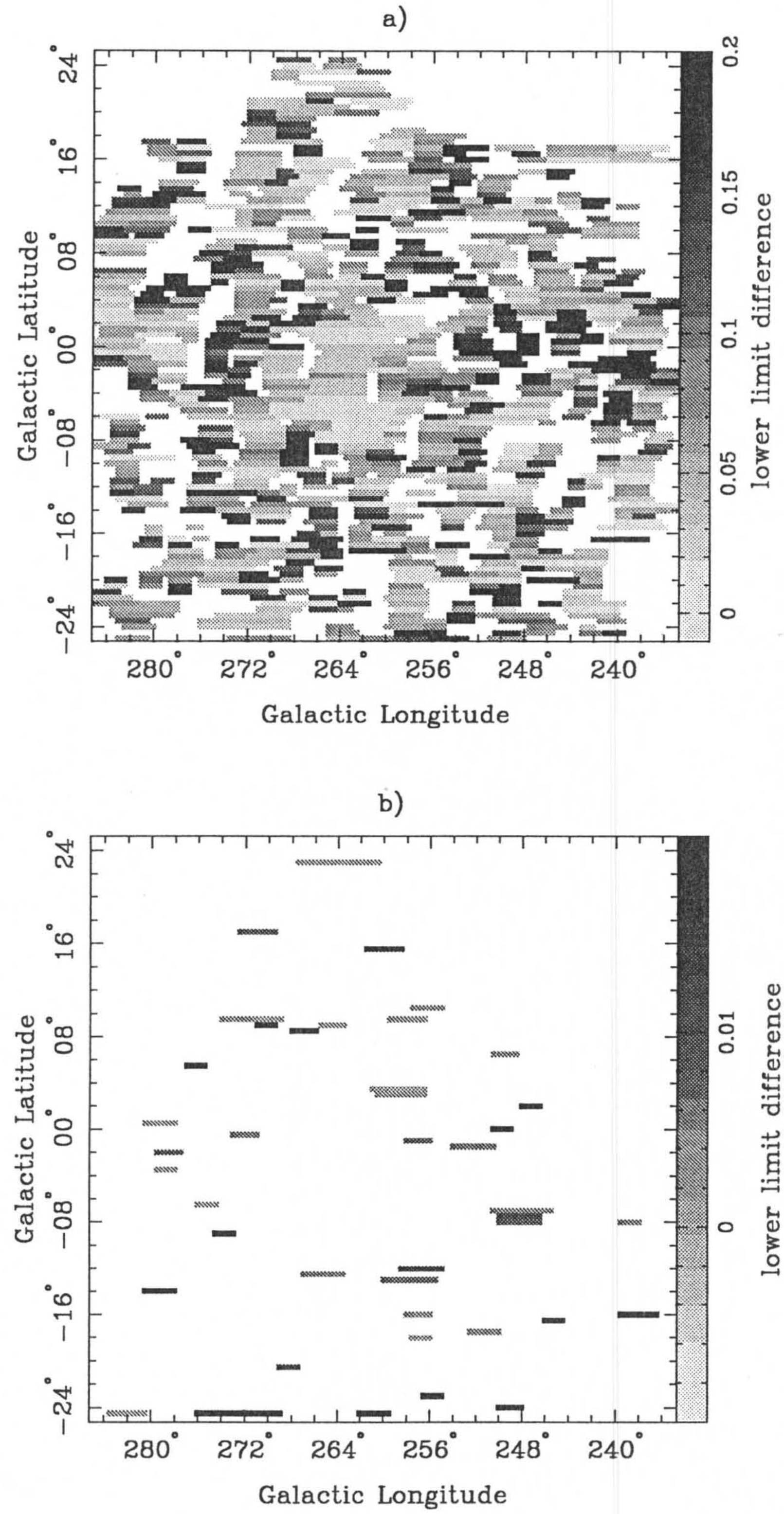

Figure [5-32]: a) and b) show respectively the magnitudes of the positive and negative values of the OLS bisector spectral index lower limit minus the Theil spectral index lower limit at 1.7° resolution.

These improved aspects of the lower resolution work are most likely due to a smaller scatter in the TT-plots caused by the reduction of scanning effects by additional smoothing. This also reduced the scatter of the TT-plots in the very faint positive galactic latitude region between longitudes 260° and 240° sufficiently for straight line fitting. In the higher resolution work almost all constant latitude TT-plots of this region were too scattered to define a plausible straight line. The Theil spectral index confidence interval in the lower resolution work is in general smaller (Fig. [5-30]). There is a down side to the lower resolution work and that is the greater number of regions that did not have a straight line constant latitude TT-plot. Also, as seen in Fig. [5-28], there are far more regions with confidence interval less than 95%. The latter is due to the poorer resolution and thus smaller number of samples for regions of definite spectral index.

5.8 Discussion and Conclusion

I made a comparison of the GUMBACK and TT-plot work. For this purpose positive and negative galactic latitude Theil TT-plot spectral index images of the same area of sky as the spectral index images produced using the GUMBACK method were made. The positive and negative galactic latitude 0.85° resolution TT-plot spectral index images are displayed together with the 1.2° GUMBACK results in Figs. [5-33] and [5-34] respectively. The positive and negative galactic latitude 1.7° resolution TT-plot spectral index images are displayed together with the 1.7° GUMBACK results in Figs. [5-35] and [5-36] respectively .

It is gratifying how closely the changes in spectral index with position correspond in the GUMBACK and the TT-plot spectral index images at both resolutions. Although the actual value of the spectral index is not exactly the same, the trend of being lower or higher relative to surrounding values is followed, with a few exceptions, very closely in the figures.

a)

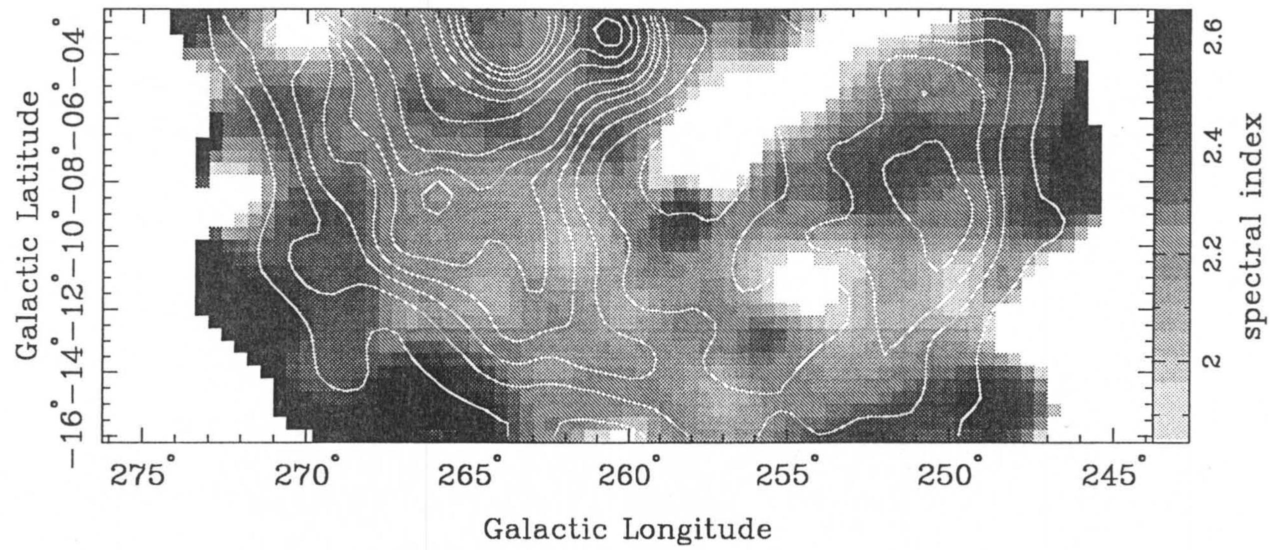

b)

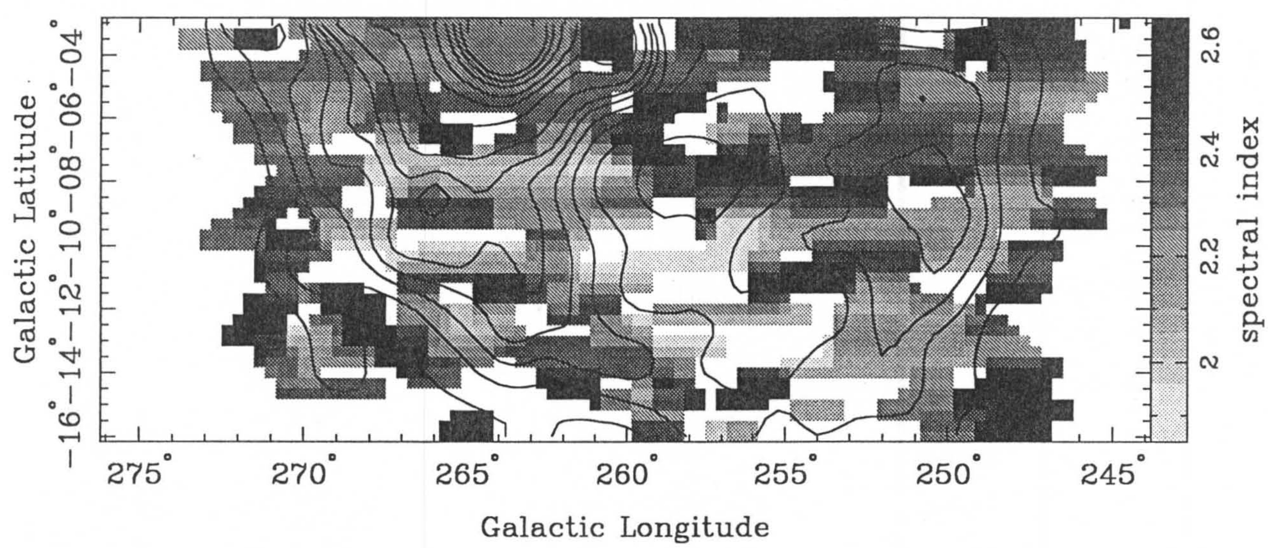

Figure [5-33]: The negative galactic latitude 0.85° resolution Theil TT-plot spectral index images in b) are displayed together with the 1.2° GUMBACK results in a). The superimposed contour levels correspond to the 2326 MHz brightness temperatures from the background-subtracted Gum Nebula at 1.2°.

a)

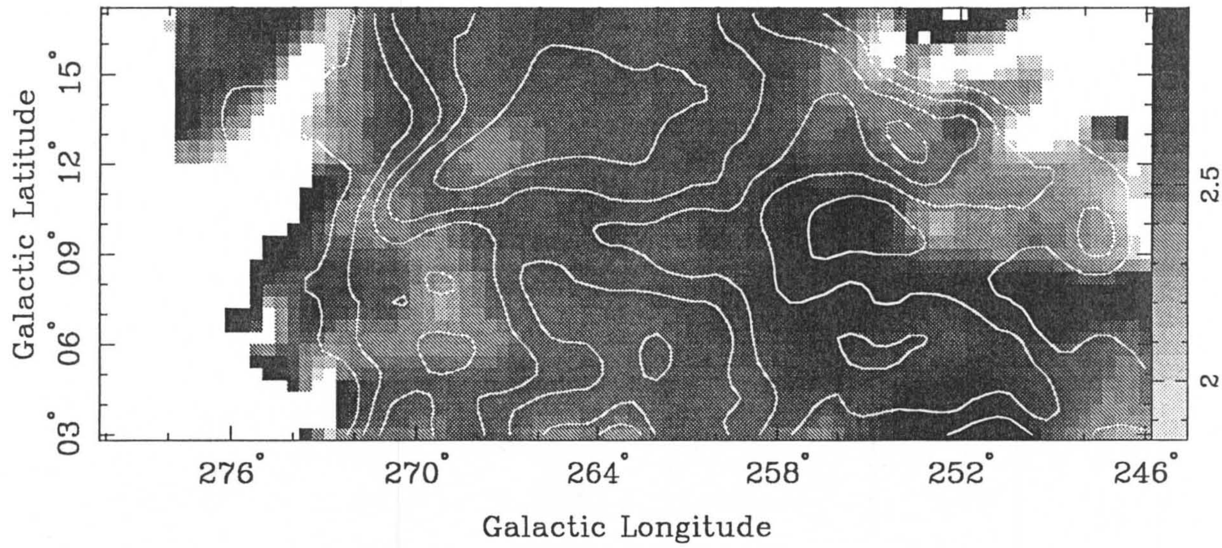

a)

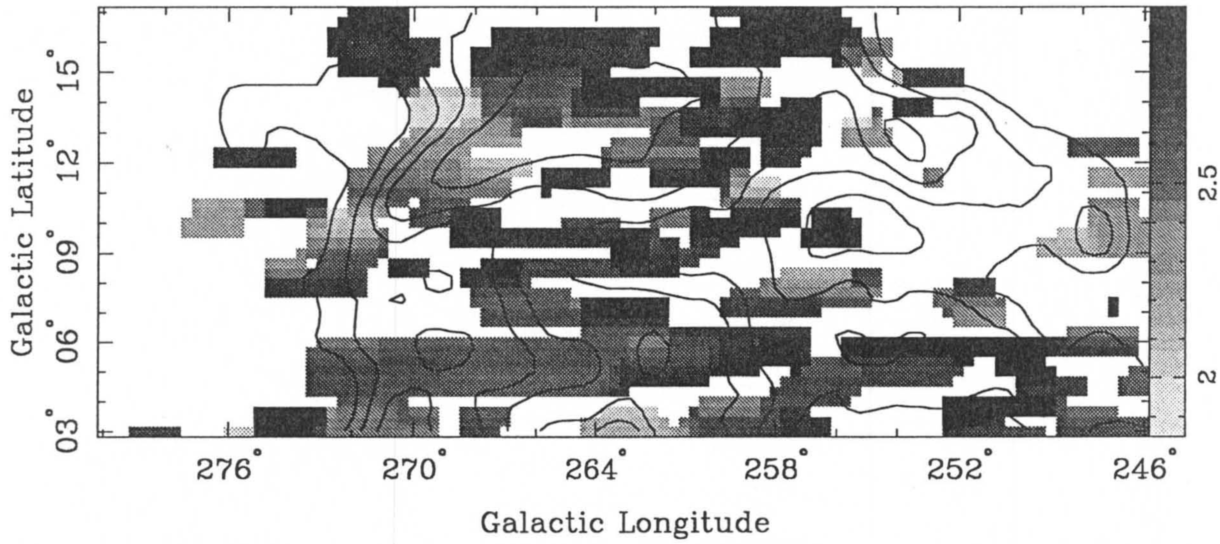

Figure [5-34]: The positive galactic latitude 0.85° resolution Theil TT-plot spectral index images in b) are displayed together with the 1.2° GUMBACK results in a). The superimposed contour levels correspond to the 2326 MHz brightness temperatures from the background-subtracted Gum Nebula at 1.2°.

The negative galactic latitude GUMBACK result at 1.2 °, which suggested the presence of a thin, nonthermal, outer shell, within which there is a somewhat broader, thermal, inner shell and again a nonthermal centre region, is present in the Theil TT-plot result. Again, both the thermal and nonthermal shells are incomplete and discontinuous in places.

In the Theil TT-plot results (Fig. [5-33] b)) there are patchy regions of spectral index less than 1.9. In the light of the investigation of TT-plot peculiarities these patches may be interpreted as regions where nonthermal and thermal regions are superimposed, with the nonthermal spectral index component having a spatial increase in brightness temperature while the thermal component is decreasing. This may also explain the intermediate spectral index (≈ 2.3) of adjacent regions. The latter may be caused by the superposition of nonthermal and thermal regions, with both the nonthermal and thermal spectral index component having a spatial increase in brightness temperature. If this interpretation is extrapolated, it leads to the idea of thermal pockets strewn along and within a nonthermal shell.

A similar interpretation adequately explains the thermal patches seen in the positive galactic latitude Theil TT-plot image in Fig. [5-34] b). The fact that the GUMBACK spectral index image does not show thermal regions, but only lower spectral index regions at the positions of most of the thermal regions in the Theil TT-plot image may be explained by assuming that in the positive galactic latitude region the thermal pockets are significantly weaker, but positioned on top of nonthermal radiation almost constant in strength, hence allowing the thermal part to dominate the TT-plot.

As none of the spectral index images shows either a uniform thermal or uniform nonthermal spectral index, one must conclude that for the Gum Nebula neither an H II region, an interstellar bubble nor a simple SNR classification is correct. The only interpretations that are plausible in the light of the spectral index images are:

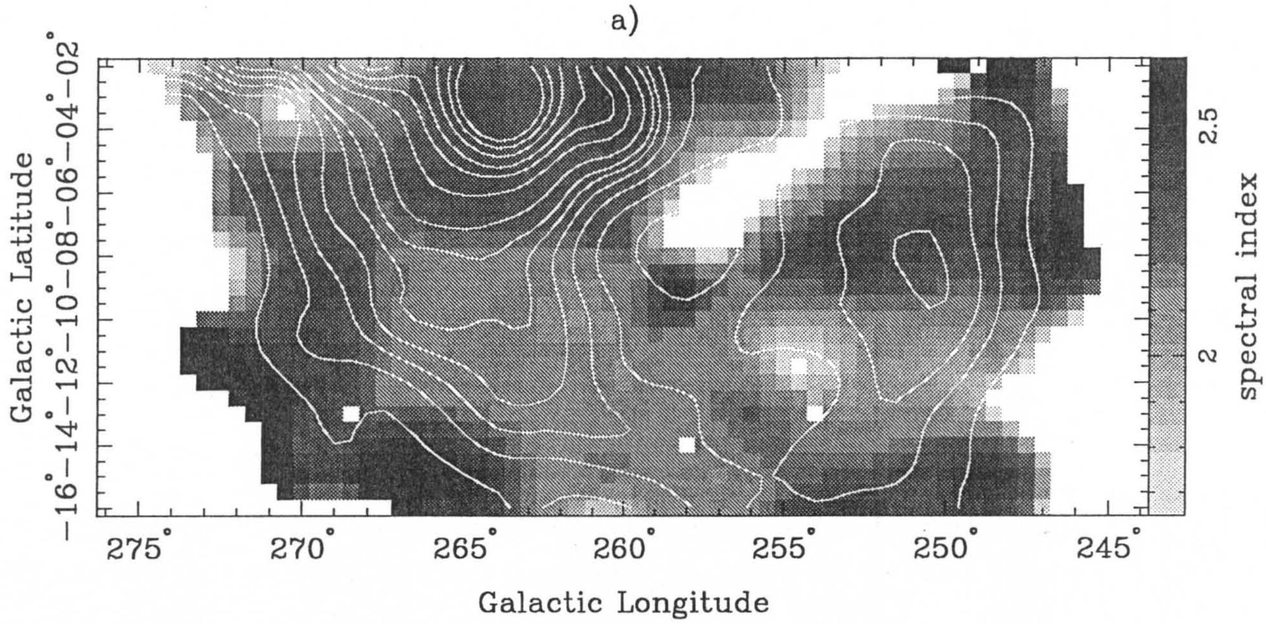

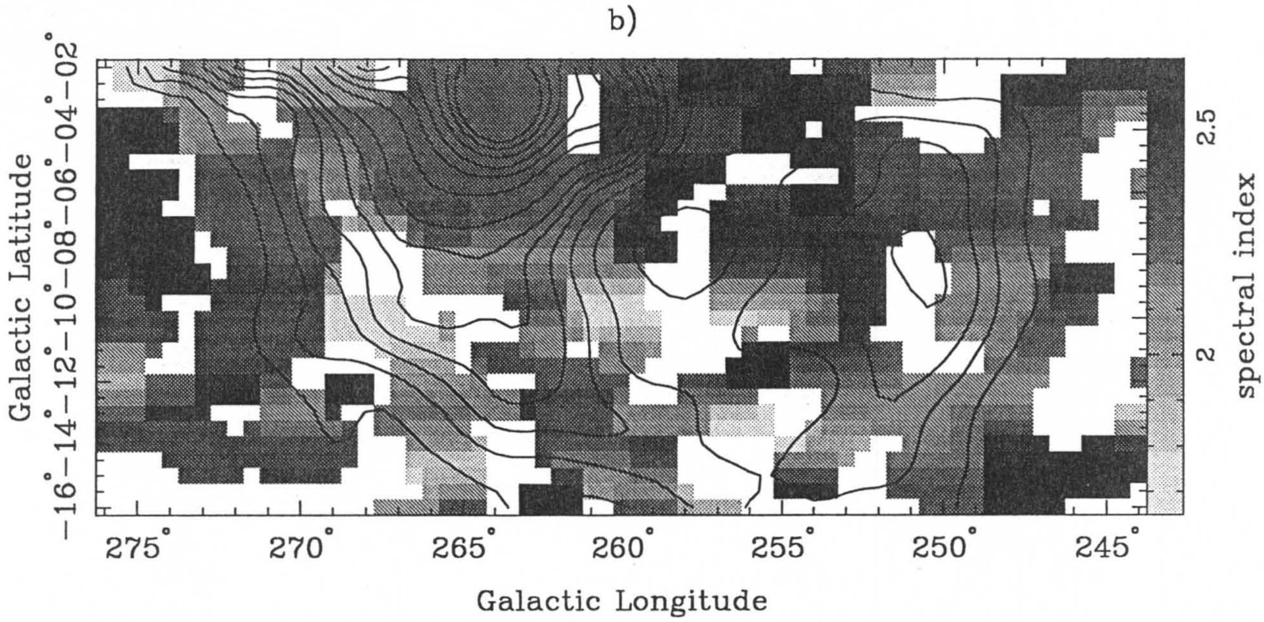

Figure [5-35]: The negative galactic latitude 1.7° resolution Theil TT-plot spectral index images in b) are displayed together with the 1.7° GUMBACK results in a). The superimposed contour levels correspond to the 2326 MHz brightness temperatures from the background-subtracted Gum Nebula at 1.7°.

a)

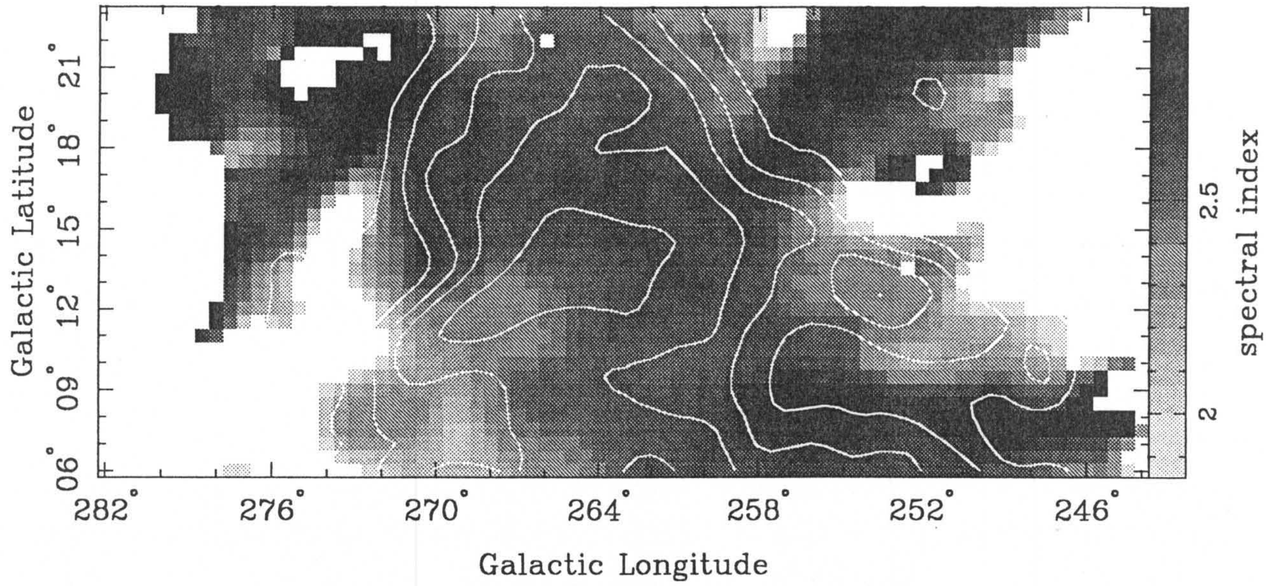

a)

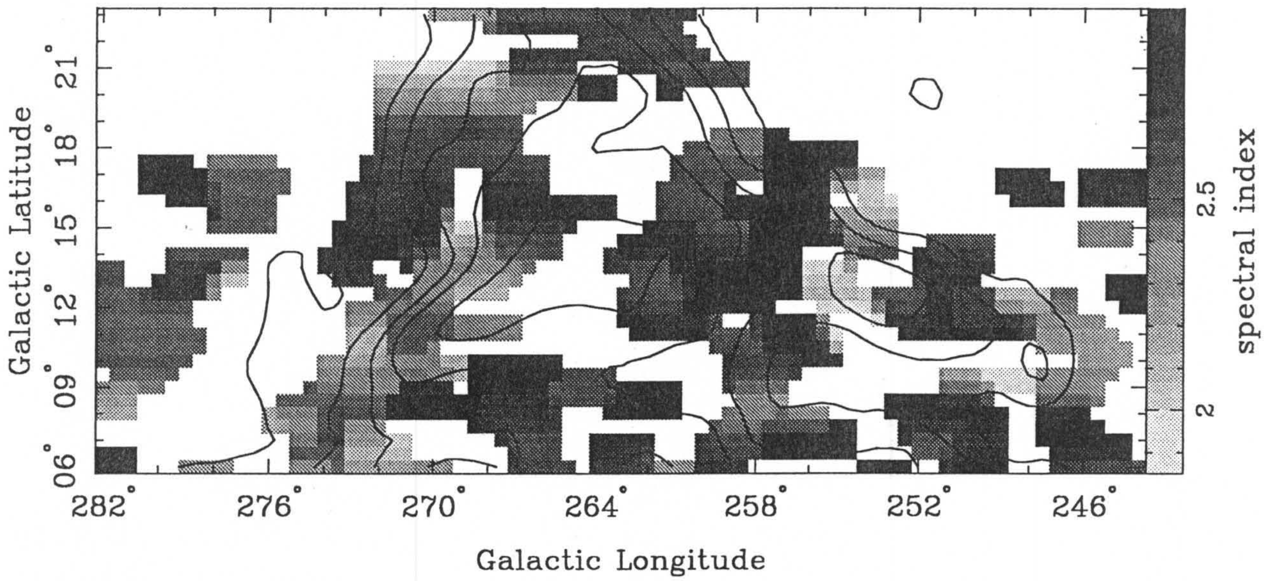

Figure [5-36]: The positive galactic latitude 1.7° resolution Theil TT-plot spectral index images in b) are displayed together with the 1.7° GUMBACK results in a). The superimposed contour levels correspond to the 2326 MHz brightness temperatures from the background-subtracted Gum Nebula at 1.2°.

- that of an extremely old SNR in which smaller regions have cooled sufficiently to be dominated by brehmsstrahlung radiation. These regions appear not to be constrained to the outer edges. They are seemingly randomly scattered throughout a very broad shell, although this effect may be simply a matter of projection onto the two-dimensional sky. The emission of the Gum Nebula is far stronger at negative than at positive galactic latitudes and the thermal patches are more ubiquitous at negative galactic latitudes. This suggests that the ISM surrounding the progenitor star was fairly non-uniform, with denser material present towards the negative galactic latitude side.

- An old SNR with the originally cold interstellar medium clouds in its immediate vicinity heated to H II region temperatures by the stars ζ Puppis and γ^2 Velorum. This suggests that the ISM surrounding the SNR is fairly non-uniform, with a greater number of such clouds present at negative galactic latitudes.

- Reynold's (1976b) model of an old SNR with a cooled outer shell presently ionised by the stars ζ Puppis and γ^2 Velorum.

This combination of thermal and nonthermal (polarized) regions is supported by Duncan et al.'s (1996) polarization survey. According to them, the power received in the polarization survey is less than the total power measured at that frequency in many parts of the nebula, indicating that the difference is due to thermal emission.

The similarity of the TT-plot and GUMBACK results indicates that the GUMBACK-determined background is a much better estimate of the true background than implied by the estimate of the uncertainty in that method.

Chapter 6

Infrared to Radio flux density ratio

Another method for distinguishing between thermal, as in HII regions, and non-thermal, as in SNRs, sources is based on the ratio of the infrared (IR) to the radio continuum flux density. As this method is independent of the spectral index method described and presented in chapters 4 and 5, it provides a valuable check on the results presented there.

This method is based on an empirical result. The infrared to radio continuum flux density ratio (IRR) assumes a unique range of values for H II regions and also for SNRs (Fürst et al., 1987, Haslam &Osborne 1987, Broadbent et al., 1989). There is a sufficiently high contrast in the IRR for H II regions and SNRs that this ratio may be used to identify these sources.

A brief review of the literature leading up to this method for identifying HII regions and SNRs is given. The extension of this method to one for separating the thermal and non-thermal radio radiation along the Galactic plane with the aid of the IRAS data is also discussed. The latter is relevant as it extends the empirically derived IRR to extended, large HII regions. Prior to this only compact HII regions had been evaluated for their IRR.

I employed the GUMBACK method of separating an extended source from its background, described in chapter 4, to obtain isolated Gum Nebula images at 2.3 GHz and 60 μm with a resolution of 0.5°. These two images were then used to generate an IRR image with a resolution of 0.5°.

6.1 Identification of SNRs and HII regions on the basis of their IRR

The theory of H II regions predicts that in a state of equilibrium each electron, given enough energy to free itself by a Lyman continuum photon, will eventually recombine. An H II region is thus optically thick to Lyman transitions. The resultant recombination cascade invariably produces one Balmer photon, one Lyman α photon plus lower energy continuum and line photons (e.g. Shu, 1982).

As the dust absorption efficiency of Lyman α photons is fairly good, one may assume that each of these Lyman α photons scattered many times by resonance in the ionized gas is eventually absorbed by dust (e.g. Krishna Swamy & O'Dell, 1968). Their energy will then be re-emitted as IR radiation. Such a model leads to the conclusion that the emission coefficient for IR radiation is equal to that of Lyman α photons. Each Lyman α photon originates from a Lyman continuum photon. The Lyman continuum flux is in turn proportional to the radio continuum flux of the HII region (Rubin, 1968). Thus theory predicts that the ratio of the infrared flux density to the radio flux density, S_{IR}/S_{radio}, should be proportional to the ratio of the Lyman α emission coefficient to the radio emission coefficient, $j_{L\alpha}/j_{radio}$.

Harper & Low (1971) set out to investigate this conjecture by making appropriate measurements on compact HII regions. Their observed proportionality coefficient is much larger than the theoretically predicted value. Thus the IR emission is larger than can be accounted for by absorption of the Lyman α photons alone. Harper & Low (1971) suggested that the dust is competing effectively with the gas for Lyman continuum photons from the central star, thereby achieving the additional heating required to explain the observational IRR. This conjecture was confirmed by Emerson & Jennings (1978).

The absorption of photons from the stellar Lyman continuum by dust thus reduces the number of ions and hence also the number of electrons in H II regions. This then reduces the radio free-free flux from the H II region. The IR excess is therefore due to a decrease in radio free-free emission and not only the result of an increase in IR emission. This interdependence of the radio and infrared emission results in a good correlation between the infrared and high-frequency radio continuum in compact H II regions. The IRR for compact H II regions is ≥ 500.

In the early eighties the IRAS data became available and made studies of the correlation between the infrared and radio emission of extended objects possible.

In most SNRs the infrared emission arises from interstellar dust that is collisionally heated by shocked gas, i.e. X-ray emitting gas. Thus there does not appear to be such a strong interrelation between the infrared and high-frequency radio continuum in SNRs. The initial set of SNRs studied individually at IR when the IRAS data became available in the early eighties (Braun, 1985) have a very low IRR, i.e. IRR <20.

This disparity in IRR for HII regions and SNRs, prompted Fürst et al. (1987) to investigate the correlation between the IRAS continuum data and radio data. Haslam and Osborne (1987) independently also embarked on the same project, though from a different perspective. They wanted to investigate the correctness of IR/submm emission models for the Galactic plane. One of these models (Cox et al., 1986) predicted a good correlation between the 60μm IRAS data and the emission of extended low-density H II regions.

Fürst et al. (1987) and independently Haslam & Osborne (1987) have shown that in general the 60 μm infrared image from the IRAS all-sky survey of the galactic plane in the longitude range of about $25° < l < 35°$ shows a detailed correlation to the 11-cm radio continuum emission of the same region observed by Reich et al.

(1986). The known compact H II regions stand out as bright sources in both maps, while SNRs are noticeable by their lack of IR in comparison to their surroundings.

Both Fürst et al. (1987) and Haslam & Osborne (1987) confirmed that the infrared flux of compact H II regions is > 500 times their radio continuum flux while SNRs in contrast only have an IR flux ≤ 20 times their radio continuum flux. Thus the ratio of IR to radio flux was proposed by both Fürst et al. and Haslam & Osborne as a means of identifying SNR candidates near the galactic plane.

The sample of SNRs on which Fürst et al. (1987) based their empirically derived IRR was heavily biased towards young SNRs. Arendt (1989) shows that these historically young SNRs are at one extreme of the range of empirically derived IRRs, with IRR < 20. For older remnants Arendt determines the IRR to be in the range of ≈ 20 to 500. The radio fluxes used for this determination are at a frequency of 1GHz.

Thus one should in principle be able to distinguish young and old SNRs and compact H II regions from each other on the basis of their IRR. This leads to the conjecture that radio radiation from HII regions, i.e. thermal radiation may be identified by its associated infrared emission, while regions of synchrotron radiation would be relatively infrared quiet. This has some bearing on the Gum Nebula which is certainly not in the category of *compact* H II region, but has at times been classified as an extended HII region.

6.1.1 Identification and/or separation of thermal and non-thermal radiation from the IRR

Haslam & Osborne (1987) as well as Broadbent, Haslam & Osborne (1989) extended the above method for distinguishing between compact H II regions and SNRs to one for separating the thermal component of the radio continuum, identified by its associated infrared emission, from the synchrotron component. This requires some justification for associating the predominant component of dust radiation at 60 μm with the thermal radio radiation of extended low-density H II regions along the galactic plane.

Several models of the IR/submm emission from the galactic disk exist. Although all such models attribute the IR emission of the galactic plane to interstellar dust heated by the absorption of starlight, they propose different locations for the dust grains and sources of interstellar radiation. An early model by Fazio & Stecker (1976) locates the dust grains in giant molecular clouds (GMCs) heated by embedded stars invisible to us. This model predicts a good correlation of ^{12}CO column density, a tracer of molecular clouds, with IR emission. This was indeed observed (Hauser et al., 1984) in IR data at 150 and 300 μm obtained from balloon flights. However, the higher resolution 60 μm IRAS survey data, Haslam & Osborne claim, has its primary correlation with the radio continuum and thus thermal emission from extended low-density (ELD) H II regions. Thus they support the model of Cox et al. (1986), which predicts precisely this correlation.

As giant H II regions are generally associated with GMCs both correlations are in principle to be expected. Further support for Cox et al.'s model comes from their detailed prediction of percentage contributions at different IR bands from dust associated with H II regions, dust associated with HI and that associated with molecular clouds. The model predicts: for 60μm 82%, 18% and 0%; for 100 μm 60%, 40% and 0% and for 200 μm 43%, 43% and 14% respectively. Thus the observed better correlation (Haslam and Osborne) of 60 μm IR to the radio is explained by the Cox et al. model which attributes most of the 60μm emission to H II regions. Furthermore, the ^{12}CO correlation reported by Hauser et al. (1984) (IR between 150 and 300 μm) also fits into the scheme of Cox et al. (1986).

Thus, if the minor contribution to the 60μm emission from the HI associated dust is modeled and removed, the remaining IR emission is associated with thermal radio emission and the empirically derived relationship between these may be used to model the thermal radio contribution. Broadbent et al. show that the IRR for ELD HII regions is the same as for compact HII regions. If the thermal radiation modeled from its infrared counterpart is subtracted from radio maps one is left with the non-thermal radio radiation.

As the IRR for ELD HII regions is also > 500, the IRR still assumes a unique range of values for H II regions (extended or compact) and SNRs.

At 60μm dust associated with HI contributes 18% of the emission according to the Cox et al. model. Even though no HI has yet been identified with the Gum Nebula, a contribution from such HI associated dust could pose a problem with the classification of the Gum Nebula. If this nebula is an SNR then it must be very old. As the IRR for older remnants is in the range of $\approx$ 20 to 500, a calculated IRR close to just greater than 500 that ignores the HI associated dust contribution could lead to an inconclusive result.

The contribution of the HI-associated dust emission depends on the distribution and density of the HI as well as the interstellar radiation field (ISRF). Broadbent et al. found that for a constant ISRF over the whole galaxy, the contribution of the HI-associated emission was typically less than 10 %, i.e. less than the 18% predicted by Cox et al., of the total infrared intensity. However for an ISRF that increases strongly towards the centre of the Galaxy (Mathis, Mezger & Panagia, 1983) the HI-associated dust contribution is no longer minor towards the centre of the Galaxy. I conclude from the discussion in Broadbent et al. that the HI-associated dust contribution in the Gum Nebula region, which is towards the anti-centre of the Galaxy, is not in excess of 10% of the 60μm emission of the Gum Nebula. Hence the infrared emission associated with the radio emission of the Gum Nebula may be overestimated, if the Gum Nebula is of thermal origin.

6.2 IRR of the Gum Nebula

I used the 60μm IRAS data and the 13 cm (2.3 GHz) Rhodes radio continuum data for the determination of the IRR of the Gum Nebula.

There are several good reasons for using the 60μm IRAS data for the determination of the IRR, rather than the IR data at other wavelengths. For one, an empirical investigation shows that the correlation of the IR with the radio emission is better if the 60 μm data is used (Haslam & Osborne, 1987). Furthermore there is evidence that the 60μm data is most closely associated with the thermal radio radiation as predicted by the model of Cox et al. (1986) (Haslam & Osborne, 1987; Broadbent et al., 1989) Also, SNRs are most clearly defined at 60 μm according to Arendt (1989). Lastly, both the work of Broadbent et al. (1989) and Fürst et al. (1987) was done using 60μm and thus the empirically derived ratios quoted there are best used in the same context.

Furthermore, the 13 cm (2.3 GHz) Rhodes radio continuum data is not that significantly different in wavelength (frequency) to the surveys used by Fürst et al. (11cm, i.e 2.7 GHz) and Broadbent et al. (11 cm and 6 cm, i.e 2.7 and 5 GHz). The flux density for a thermal source, i.e. of flux density spectral index 0.1, at 13 cm is 1.02 times that at 11 cm. This difference is not significant for the IRR.

The revised IRR for SNRs due to Arendt (1989) was made using SNR fluxes at 1 GHz. A nonthermal source with flux spectral index 0.7 has a flux density at 1 GHz that is 1.8 times that at 2.3 GHz. Thus the IRR derived using 2.3 GHz data should be multiplied by 0.56 to compare it to the IRR values obtained from 1 GHz radio flux densities. The lower the flux spectral index of the SNR, the closer to 1 this adjustment factor becomes. This should be kept in mind when drawing conclusions about an IRR determined using data at a frequency other than 1 GHz.

6.2.1 The 60 μm data from the ISSA images

The infrared astronomical satellite (IRAS) surveyed 98% of the sky in four broad infrared bands centred at 12, 25, 60, and 100 μm and with resolution $\approx 5'$ (Beichmann et al., 1988; Wheelock et al., 1994). Most of the sky was observed three times in order to obtain hours-confirmation, i.e. verifying that sources were detected at the same positions and brightnesses on different passes of the satellite separated by one or more orbits. The scans from these independent coverages were combined to form co-added images with higher resolution and sensitivity. The resultant data, co-added and independent single pass coverages, from this survey was reprocessed by the Infrared Processing and Analysis Center (IPAC) to improve calibration and remove zodiacal emission. It was published in the reprocessed form as the two volume CDrom IRAS Sky Survey Atlas (ISSA). The units of these images are MJy/sr.

Images for which the IPAC cannot guarantee sufficient removal of the zodiacal emission and which are thus of reduced quality are classed as the ISSA reject set. The ISSA images give differential brightness for objects outside the solar system and thus are not absolutely calibrated.

Unfortunately the Gum Nebula is in the region of sky that contains some of the 2% not observed. Furthermore a fair portion of the Gum Nebula region falls within the region made up of the ISSA reject set images. Thus in those regions the IR emission would be slightly overestimated as they contain some residual zodiacal emission. However, this residual emission is smaller at 60 and 100μm than at 12 and 25 μm. As IPAC (1994) claims that the reject images are still useful at longer wavelengths, the work presented here, based on these observations is meaningful. Also the portion of the region investigated containing the reject images only skirts the outer boundary of the Gum Nebula (with RA approximately 3 to 13 hrs and dec from approximately $-15°$ to $-3°$, which is approximately between galactic longitudes 240° to 260° and at latitudes greater than +20°). None of this is contained within the background subtracted image (see Fig. [6-2]) used for the IRR determination.

Mosaicking of the individual 12.5° by 12.5° ISSA images to form a larger image was done with a multipurpose program for mosaicking written by Jonas of Rhodes University. According to IPAC this can be done without additional adjustments to an accuracy of 0.1 MJy/sr, except where images from the $|\beta| > 50°$ sky join those from the $|\beta| < 50°$ sky, β being the ecliptic latitude. In those regions, the field boundary discrepancy is of the order of 1 to 2 MJy/sr at 60 μm. Although the Gum Nebula straddles these two regions of sky, no significant change in brightness is noticeable across the $\beta = -50°$ boundary.

6.2.2 Jy/beam determination

The IRR of the Gum Nebula was determined pixel by pixel, resulting in an IRR image. For a pixel by pixel IRR determination one has to use units of Jansky per beam.

The units of the 13 cm (2.3 GHz) Rhodes radio continuum data are brightness temperature in Kelvin. Dividing by 1.5 converts this back to antenna temperature (see chapter 3) in Kelvin. If this is multiplied by the beam sensitivity, 9.72 Jy/K, of the HartRAO antenna at 13 cm one obtains Jy/beam for this 20′ beam.

The 60μm IRAS data is in MJy/steradian. This thus has to be multiplied by the beam area in steradian and divided by 10^6 to convert it to Jy/beam. As both surveys have to be at the same resolution for any meaningful comparative work, the 60μm was convolved with a gaussian function of appropriate half power beam width (HPBW) to bring it to the 20′ resolution of the radio survey. Thus the beam area, Ω_A, to multiply by is that of a gaussian beam with HPBW of 20′. This is given by the formula $\Omega_A = 1.133(HPBW)^2$ (Baars, 1973), where the HPBW is in radians. Ω_A is 3.835×10^{-5} sr when the $HPBW$ is 20′.

Scanning effects present in the 2.3 GHz data at its observation resolution of 20′were reduced by smoothing both the radio and the IR images to a resolution of 0.5°. The IRR work was thus done at that resolution. This further effective increase in beam area meant multiplying both surveys by the same factor, 2.25, after they had both already been calibrated for a resolution of 20′.

6.2.3 Method and Results

There are at least two methods of obtaining an IRR image of the Gum Nebula. One is based on the TT-plot method used for the spectral index image determination. In this case the IRR ratio for a region is given by the slope of the FF-plot i.e. the slope of the plot of the IR flux per beam at each pixel position versus the radio flux per beam. Detailed investigations of this method showed that the only way to obtain good results was to adjust the TVST program to give the slopes of straight line sections of FF-plots at constant latitude, rather than the spectral index defined by the slope of such TT-plots.

FF-plots are also prone to smoothing and superposition effects, although some of these are of a different nature to those investigated for the spectral index determinations. The FF-plot peculiarites are at present under investigation. A preliminary IRR image I produced from the slopes of FF-plots effectively gives the same results as those presented below, except that the image is intermittent. This is due to the presence of many scatter and negative slope FF-plot sections resulting in an undefined IRR. It is the need to understand the origin of the negative slope FF-plots that has held back the FF-plot results. Many of these negative slope sections are too extended in longitude to be due to the smoothing of the beam over two severely different IRR ratio regions. The latter is the explanation of one of the negative slope TT-plot effects in spectral index determinations.

The method whose results are presented here relies on the determination of an approximate background for both the 60μm image as well as the 2.3 GHz radio image of the region from the Rhodes/HartRAO 2326 MHz Survey. The IRR image is then obtained by simple division of the radio image into the IR image.

I used the program GUMBACK described in chapter 4 for the background determination of the 0.5° resolution images. The thus isolated Gum Nebula is shown in Fig. [6-1] and Fig. [6-2] at 2.3 GHz and 60μm respectively. The background removal was not entirely successful between latitudes of $\approx -3°$ and $\approx 4°$, where there has been an unavoidable oversubtraction, thus hiding the nature of the Gum Nebula in that region.

Contours at constant Jy/beam values of the 2.3 GHz image have been superimposed on the false colour 60 μm image in Fig. [6-2]. This superposition highlights the fairly close correspondence of the morphology of the Gum Nebula at 2.3 GHz and 60 μm. The close correspondence at negative galactic latitudes of the 60 μm data to Sivan's Hα image had already been noticed by Srinivasan Sahu (1992). Srinivasan Sahu assumed that there is no IR radiation corresponding to the Gum Nebula at positive galactic latitudes. These two facts form the basis of her argument for the existence of the IRAS-Vela ring.

However, as seen in Fig. [6-2], there is faint IR emission at positive galactic latitudes. As the 2.3 GHz contours show, this has a fairly close correspondence to the radio emission and thus the Hα emission. In particular, the relatively strong radio structure between galactic longitudes 272° and 258° and galactic latitudes +9° and +15° is clearly also present in the IR. Unfortunately this cuts across an unobserved region in the IR.

The much fainter radio spur between galactic longitudes 254° and 246° and galactic latitudes +15° and +9° does not show such close correspondence. One reason for this was discovered from the IRR image which clearly shows that some confusion is present in the 60 μm image in this area due to the presence of a cirrus cloud (see later discussion).

There is thus no need for postulating the existence of a separate IRAS-Vela ring. Just as the 2.3 GHz radio emission of the Gum Nebula at positive galactic latitudes is much fainter than that at negative latitudes, so is the 60μm IR emission.

I obtained the IRR image by division of the two images in Figs. [6-2] and [6-1]. It is shown in Fig. [6-3] as a false colour image, with superimposed contours of constant Jy/beam from the 2.3 GHz image. The contours are there to aid in the identification of IRR values for features and objects in the 2.3 GHz image.

Immediately noticeable in the false colour image of the IRR is that the Gum Nebula is red bordering on yellow, which corresponds to a value of at most 250, with large areas in the colours corresponding to the range below 100. The Gum Nebula is thus definitely an old SNR, especially if one takes into account that this value has to be multiplied by a factor less than one, depending on the radio spectral index, to account for using 2.3 GHz data rather than 1 GHz data.

There are three regions on the edge of the Gum Nebula that have an IRR > 500. These are cirrus cloud A approximately covering longitude 249° to 242° and latitude $-12°$ to $-15°$, cirrus cloud B approximately covering longitude 272° to 270° and latitude $-7°$ to $-13°$ (on the 60μm image it is not evident below 11°) and cirrus cloud C approximately covering longitude 254° to 242° and latitude 12° to 16°. As these are also regions that have essentially no corresponding features in the radio image, I conclude that the 60 μm features in these three regions are isolated cirrus clouds.

I made hydroxyl 1667 MHz spectral line observations (see next chapter) at positions in these three regions. The observed positions, their line velocities and corresponding kinematic distance range as given by the uncertainty in the line velocity (from the Wouterloot & Brand (1989) galactic rotation model) assuming no local motions are tabulated in table [6-1]. Also tabulated is the range kinematic distances from us, assuming local motions to or away from us of the order of 5 km/s, which is typical of interstellar molecular clouds. A distance is quoted as zero when, even if the cloud

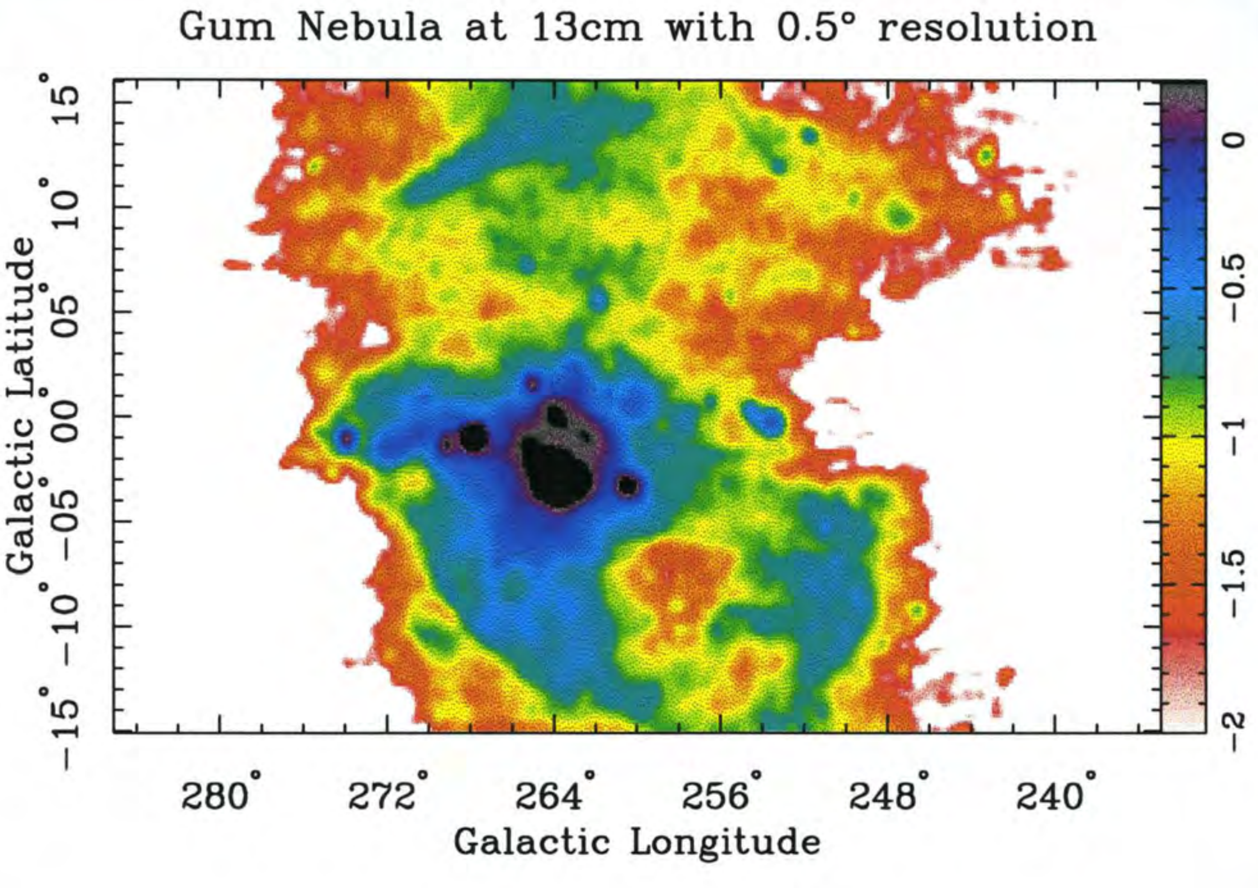

Figure [6-1]: The background subtracted Gum Nebula at 2.3 GHz with a resolution of 0.5°. The background removal was not entirely successful between $\approx -3°$ and $\approx 4°$, where there has been an unavoidable oversubtraction, thus hiding the nature of the Gum Nebula in that region. The false colour scale is logarithmic. Inversion of this logarithmic scale and multiplication by 2.25 yields values in units of Jy/beam.

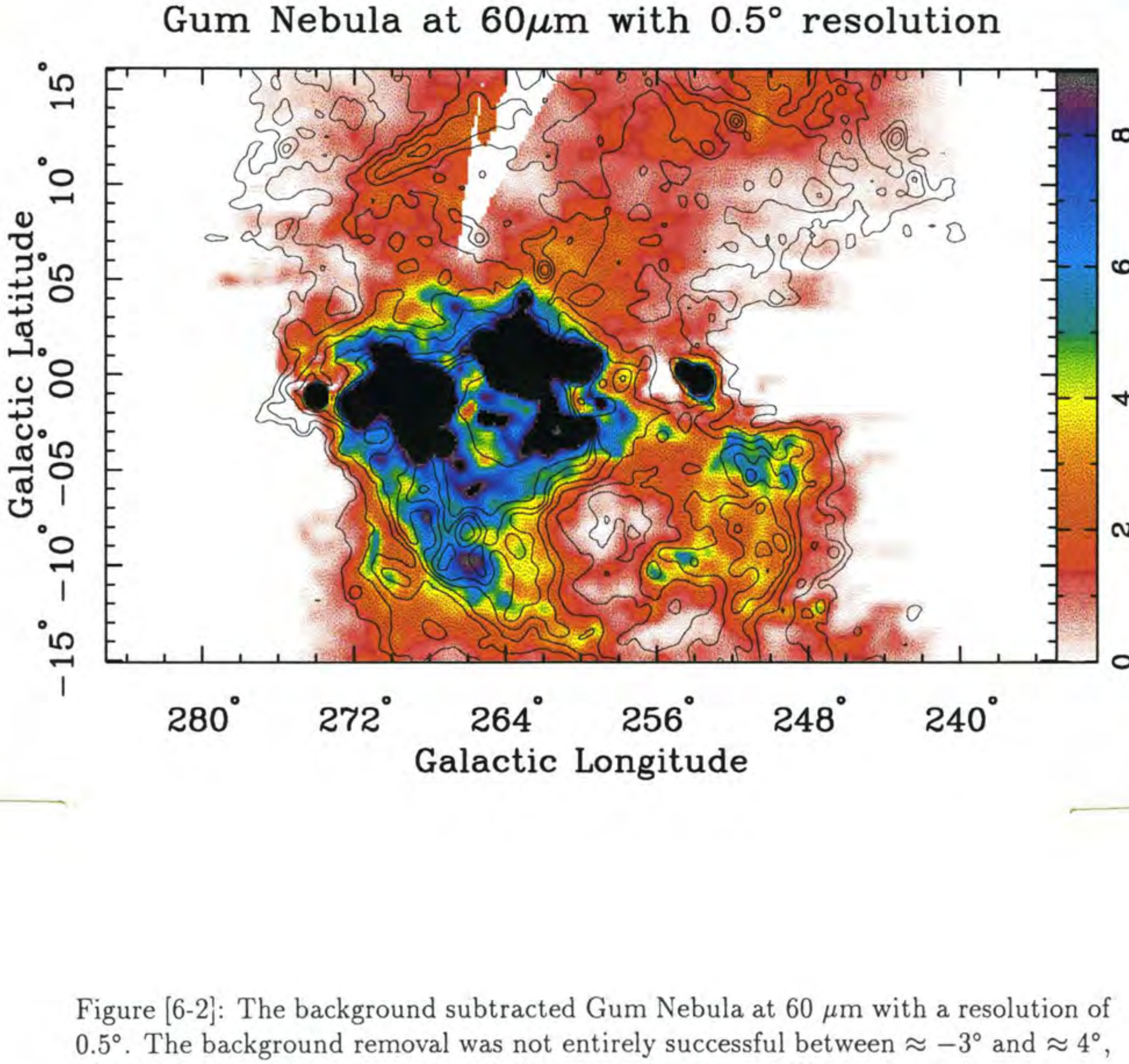

Figure [6-2]: The background subtracted Gum Nebula at 60 μm with a resolution of 0.5°. The background removal was not entirely successful between $\approx -3°$ and $\approx 4°$, where there has been an unavoidable oversubtraction. The contours at constant Jy/beam values of the corresponding 2.3 GHz image in the previous figure. False colour values must be multiplied by 2.25 to give values in units of Jy/beam.

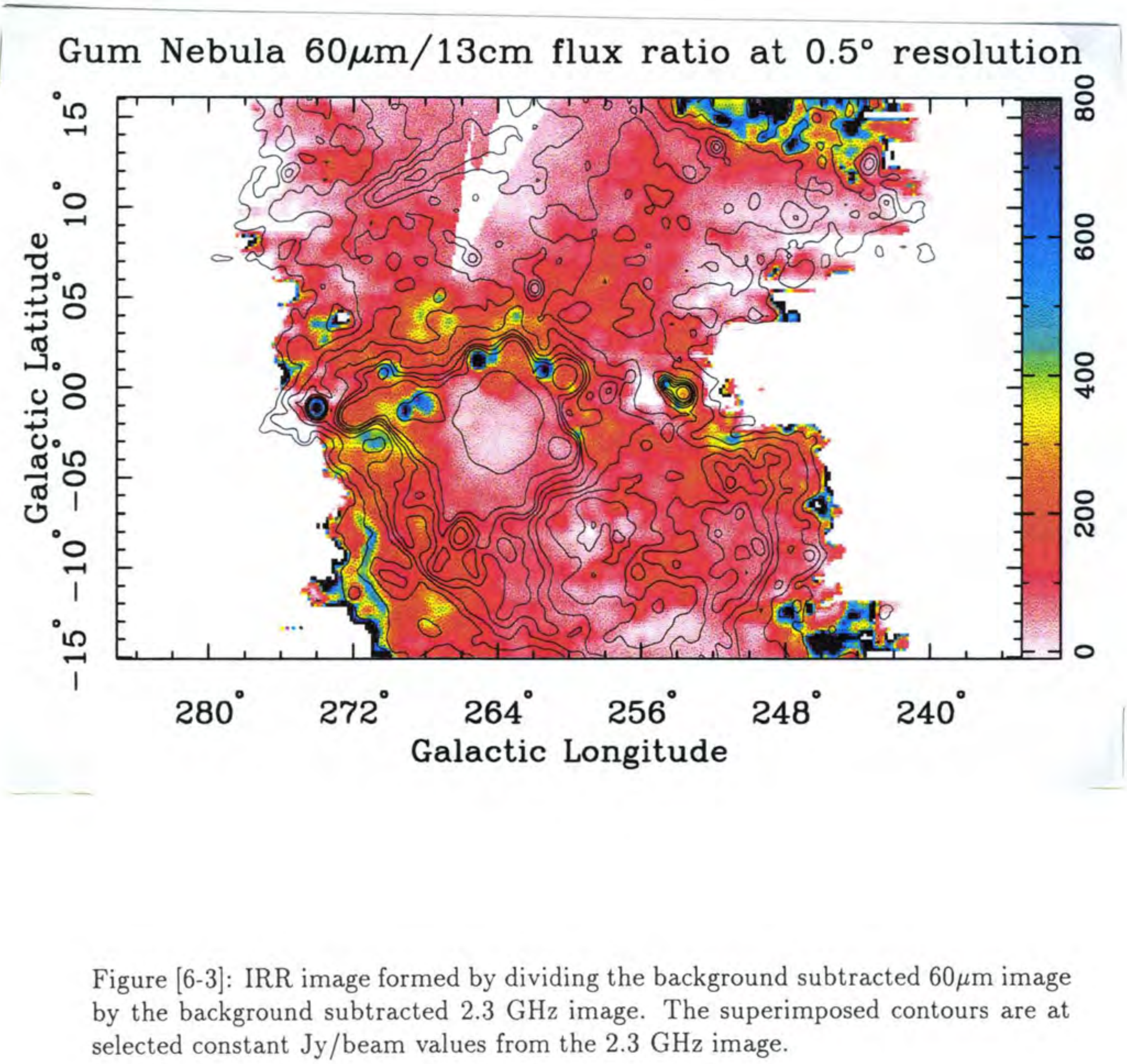

Figure [6-3]: IRR image formed by dividing the background subtracted 60μm image by the background subtracted 2.3 GHz image. The superimposed contours are at selected constant Jy/beam values from the 2.3 GHz image.

is assumed to be at our position in the galaxy, it still has to be moving towards us in order to account for the velocity or assumed velocity in the case where local motions are included. Essentially all these distances fall into the range of distances quoted in the literature for the Gum Nebula. Thus one may conclude that they are close to the Gum Nebula, but, as they do not share the IRR of this nebula, presumably not interacting with it. The fact that some of the constant Jy/beam contours from the 2.3 GHz image follow the IRR morphology of these identified cirrus clouds is simply an artifact of the method (division by the 2.3 GHz image) and as such cannot be considered as evidence for any interaction of the nebula with these cirrus clouds.

cirrus cloud	position	V_{lsr}/[km/s]	D/[kpc]	D range/[kpc]
A	G247.5 − 12.225	2.562 ± 0.087	0.3	0.9 to 0.0
B	G270.9 − 8.4	0.26 ± 0.12	0.59	2.1 to 0.05
C	G250.45 + 13.6	-0.34 ± 0.19	0.0	0.6 to 0.0

Table [6-1]: OH line velocities obtained at positions in the three cirrus clouds A,B and C. The kinematic distances were determined using the galactic rotation model of Wouterloot & Brand (1989).

6.2.4 IRR for HII regions and young SNRs along the plane

Although the background subtraction, as far as the Gum Nebula is concerned, is very unsatisfactory in the region between $\approx -3°$ and $\approx 4°$, it nevertheless is a reasonable first order approach for the more intense objects along the galactic plane. Thus although this background subtraction is by no means perfect, the IRR for the known HII regions, whose positions are shown as squares in Fig. [6-4] of the IRR image, and for the younger SNRs (shown as circles in Fig. [6-4]) has the expected range. An exception is the extended HII region at G 260, 0, which is very faint at 2.3 GHz and thus the background subtracted at its position is unlikely to be correct—keeping in mind the manner in which this is determined.

Noticeable in this figure are the patches with IRR > 500 without squares around them. Of these, the IRR features at G271 − 3; G273 + 4 and G251 − 2.5 are

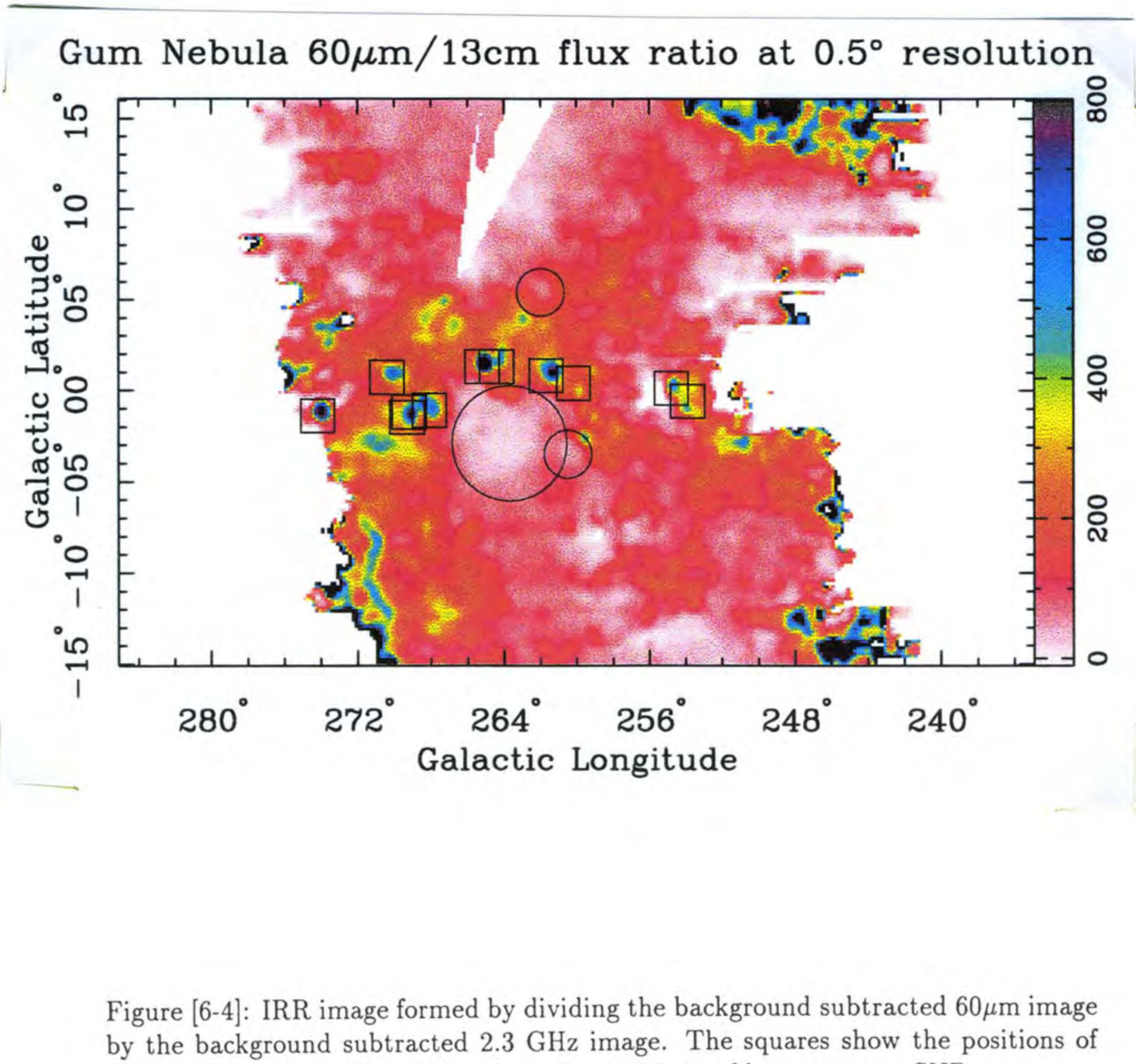

Figure [6-4]: IRR image formed by dividing the background subtracted $60\mu m$ image by the background subtracted 2.3 GHz image. The squares show the positions of known HII regions. The circles show the positions of known young SNRs.

fairly definitely artifacts of the method, caused by subtraction of an overestimated background at 2.3 GHz, as closer investigation of the 2.3 GHz image shows. The IRR features around G268 + 3.5 may also be artifacts of the method. If not, then they are objects obscured in the IR and radio images.

However, the patches with IRR ≈ 450 at approximately G263.5 + 3.5 and approximately G259.5 − 2.5 could not be definitely classified as artifacts of the method. A search for strong 60 μm IRAS point sources at these positions was negative for the position G263.5 + 3.5. Thus this feature may be an artifact of the method after all, or perhaps a small, but extended HII region hidden by confusion and/or obscuration near the plane. Close to G259.5 − 2.5 a strong 60 μm point source was identified in the IRAS point source catalogue, source 08211-4158 (G259.9 − 2.7) with fluxes of 11 Jy, 32 Jy, 210 Jy and 625 Jy at 12 μm, 25 μm, 60 μm and 100 μm respectively and with flux quality numbers given as 3 at all 4 wavelengths. These flux values and flux quality numbers match the criteria for compact IRAS HII regions given by Hughes & Macleod (1989). Thus the feature at G259.5 − 2.5 is probably a compact HII region.

6.2.5 Uncertainty in IRR of the Gum Nebula

An IRR uncertainty image was generated in similar manner as for the GUMBACK spectral index images. It is displayed in Fig. [6-5] b). For comparison purposes the IRR image is displayed in a) of the same figure. As expected, the uncertainties in the very faint regions of the 2.3 GHz and 60 μm are large. But across the main body of the Gum Nebula the uncertainty in the IRR is less than 80. Thus even in the worst case scenario one would classify the Gum Nebula as an old SNR.

6.2.6 Infrared emission of SNRs

A supernova remnant (SNR) is the composite of the exploded star's ejecta and the swept-up surrounding material. These are all heated to temperatures of the order of

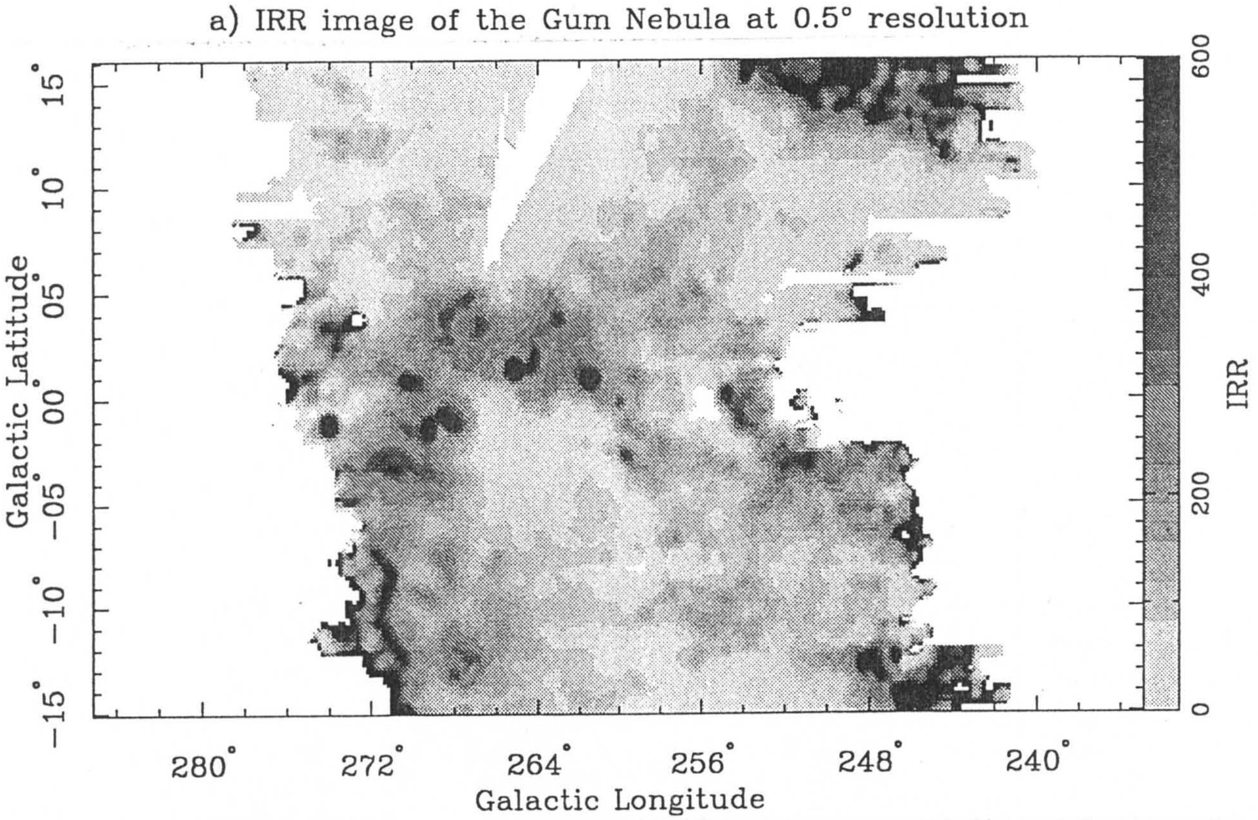

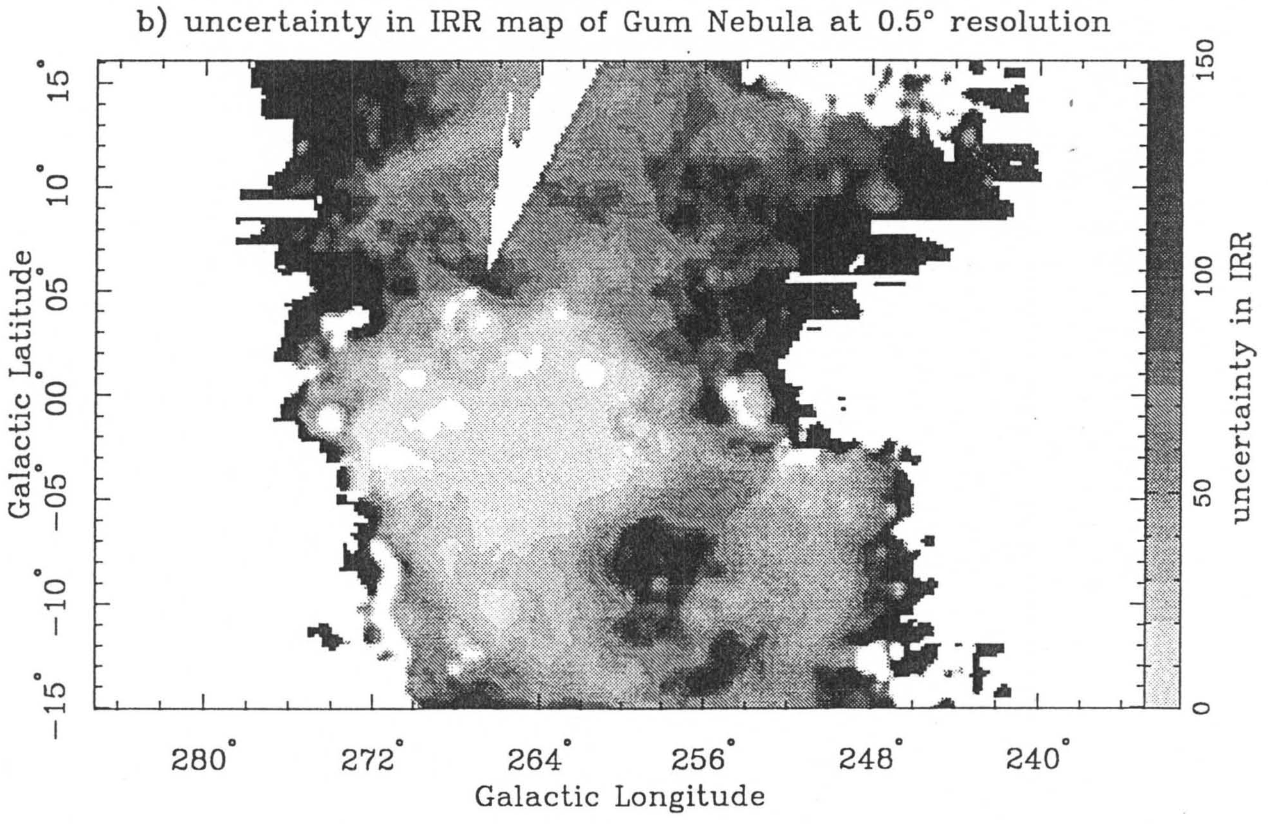

Figure [6-5]: a) shows the IRR image for ease of reference to the image in b) which shows the IRR uncertainty image.

10^6 K in the explosion and shock front formed by the high speed outward expansion. Dust, either from pre-explosion stellar origin or the surrounding interstellar medium, collisionally heated by the shocked plasma, is considered responsible for most of the infrared emission of an SNR. Theoretical considerations predict this emission to be the main cooling mechanism of the plasma. (Ostriker & Silk, 1973; Silk & Burke, 1974). The IRAS data has confirmed that many remnants do indeed emit most brightly at IR wavelengths. This is certainly the case for the Gum Nebula whose 60 μm infrared emission is about 80 to 250 times greater than its 2.3 GHz radio emission.

In older remnants IR dust emission is considered to be dominated by swept-up interstellar dust (Saken et al., 1992). Furthermore, as the dust is heated mainly by electrons in the hot plasma, which are at temperatures greater than or equal to 10^6 K and thus emit X- rays, one expects there to be a good correlation between the IR and X-ray emission of SNRs. (Dwek et al., 1987). Although the Gum Nebula has been observed with the ROSAT satellite and Aschenbach et al. (1995) have reported the existence of X-ray emission from it, no details are available yet.

As the dominant infrared emission from an SNR is from collisionally heated dust, the quantity of dust engulfed by the expanding remnant determines the brightness of its infrared emission. Thus remnants at high galactic latitudes, where the ISM density is relatively low, remain undetected in the infrared. (Dwek et al., 1987; Braun & Strom, 1986). Unfortunately where the ISM has a high density i.e. generally along the galactic plane at low galactic latitudes, other strong infrared sources are common and detection of infrared emission from SNR is difficult due to confusion with these other objects.

A further consequence of the dust density dependence of the infrared emission from SNRs is that the distribution of the dust in the surrounding interstellar medium has a direct bearing on the infrared appearance of the remnant. If the SNR progenitor had a strong stellar wind, this would have made the surroundings dust-deficient.

Consequently the resultant SNR will show little or no detectable IR.

If this is indeed the case, then the wide range in brightness of the Gum Nebula at 60 μm points to this supernova remnant having expanded into regions of very different density. Indeed, the disparity in the brightness above and below the plane may well be explained by the progenitor of this SNR having formed at the edge of a large molecular cloud, with the molecular cloud towards the negative galactic latitude side of the star.

The fact that there is a relatively good correlation between the morphologies of SNRs at radio and IR wavelengths, but not a constant value for the IRR, is taken to imply that radio and IR emission mechanisms in SNRs depend in different ways on the local conditions. The IRR image of this old SNR clearly shows that the IRR varies significantly across the face of this SNR. It is hoped that the present investigation of the IRR with FF-plots may shed some light on this.

Young remnants are brightest at 12 and 25μm while older remnants are brightest at 60 and 100 μm (Saken et al., 1992). Arendt (1989) comments that most identified remnants appear with the greatest clarity at 60 μm, even though SNRs may be intrinsically brighter at 100 μm. At the latter wavelength they are more easily confused with the cool dust of the Galactic cirrus as well as other sources that emit strongly at that wavelength. At the other extreme of the observed IRAS wavelengths, 12 and 25 μm, emission from warm dust in the ecliptic plane obscures SNRs.

6.3 IRAS point sources associated with SNRs

Rengarajan et al. (1989) report that there is a statistical excess of IRAS point sources with IR spectra of young stellar objects (YSOs) associated with SNRs in general and that a few of these remnants show a large excess. These point sources also show a preference for the shells of the SNRs rather than their central regions.

As only the point sources with spectra characteristic of heated dust were considered, those situated in SNRs may either be dusty knots heated by the shock in the hot plasma or possibly protostars whose birth was triggered by the supernova shock. Rangarajan et al. argue that while most of these point sources associated with SNRs are probably due to emission from dusty knots heated by the shock, some could indeed be protostars.

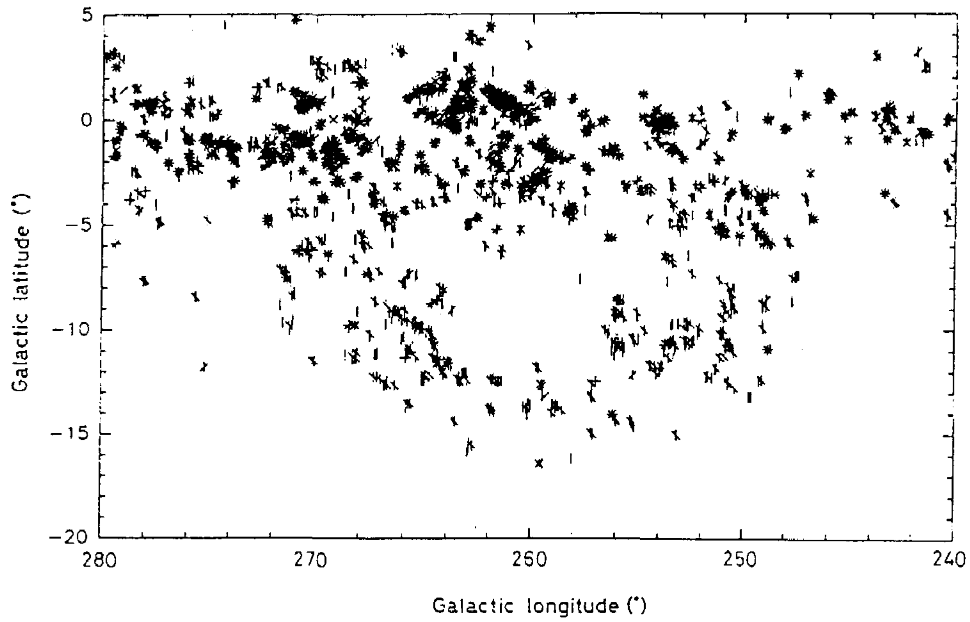

Figure [6-6]: Young stellar objects, YSOs, selected by Prusti et al. (1992) from the IRAS point source catalogue in the Gum Nebula region. Note the high incidence of these within the shell of the Gum Nebula at negative galactic latitudes.

Prusti et al. (1992) have shown that possible YSOs selected from the IRAS point source catalogue, have a high incidence within the shell of the Gum Nebula at negative galactic latitudes (see Fig. [6-6]). This is in agreement with an old SNR classification of the Gum Nebula according to its IRR. The fact that these selected IRAS point sources are only evident below the galactic plane probably indicates a density gradient in the original ISM.

6.4 Estimate of Dust mass of the Gum Nebula, an old SNR

A characteristic temperature T_{34} of the blackbody spectra modified by $\lambda^{-1.5}$ emissivities which fit the observed spectra between 60μm and 100μm may be determined for an SNR. This temperature together with an estimate of the flux density, S_μ at 60 μm may be used to obtain an estimate of the SNR's dust mass, M_d, in terms of solar masses (Arendt, 1989).

$$M_d = \pi D^2 S_\nu / B_\nu(T_d)\kappa_\nu \tag{6-1}$$

where $T_d = T_{34}$, $\kappa_\nu(60\mu\text{ m}) \approx 120\text{ cm}^2/\text{g}$, $B_\nu(T_d)$ is the Planck function evaluated at the dust temperature T_d and D is the distance to the SNR. The calculated masses are uncertain by at least a factor of 2.

Without having to analyse the 100μm image of the Gum Nebula, a first order guess at the mass of dust within it may be obtained by assuming that its characteristic temperature T_{34} is that of the average for "old" SNRs, quoted by Arendt as $\approx$ 30 K. This seems reasonable as Srinivasan Sahu quotes a value of $\approx$ 25 K for this temperature for the IRAS-Vela ring, which is part of the Gum Nebula (reasons given above and elsewhere).

I made a first order estimate of the flux density of the Gum Nebula at 60 μm from the background subtracted 60 μm image, excluding the region between latitude $-5°$ and $+5°$, as well as the region between latitudes -7° and -5° and between longitudes 266° and 258°. Most of the latter region is part of the Vela XYZ SNR. The contributions to the flux density from the three cirrus clouds were also excluded. Such an estimate gives a flux density at 60μm of 2.8 $\times 10^5$ Jy. This results in a dust mass of 0.12 $M_\odot$. This is similar to that quoted for other SNRs in Arendt (1989).

6.5 IRR from total flux density values

It was a simple matter to also obtain an estimate of the radio flux density for the Gum Nebula.

For the negative galactic latitude region between latitudes $-15°$ to $-5°$, excluding the cirrus clouds A and B and the part of the Vela XYZ SNR between latitudes $-7°$ and $-5°$ and between longitudes 266° and 258°, the radio flux density came to 1.7 $\times 10^3$ Jy. The corresponding 60 μm flux density is 1.9 $\times 10^5$ Jy. This gives an IRR of 112.

For the region between latitudes $+4°$ to $+16°$ excluding cirrus cloud C, the radio flux density came to 1.5 $\times 10^3$ Jy. The corresponding 60 μm flux density is 9.4 $\times 10^4$ Jy. This gives an IRR of 63.

For the combined regions, the radio flux density is 3.2 $\times 10^3$ Jy and the 60 μm flux is 2.8 $\times 10^5$ Jy. This gives an IRR of 88.

On the basis of these results there can be no doubt about the old SNR classification of the Gum Nebula.

6.6 Discussion and Conclusion

A global IRR representative of the IRR image of the Gum Nebula is 120 with an uncertainty of about 80. This puts the Gum Nebula into the category of old SNR. As there is no information on the IRR of an interstellar bubble, some skepticism about this result is appropriate. However, this old SNR classification is further supported by the spectral index results in chapters 4 and 5.

There is one aspect about this old SNR that the spectral index result does not answer. Are the thermal regions identified in the spectral index map due to material cooled sufficiently to be emitting bremsstrahlung radiation and H recombination lines or are they cold material (either in an outer shell of the SNR with which the

SNR never interacted, or the outer layer of the SNR that cooled to below 1000 K) now heated by the centrally situated stars γ Velorum and ζ Puppis?

Suppose that one makes the assumption that cold material heated by the Lyman continuum radiation of the stars has the same IRR characteristics as H II regions. Then this material would have an IRR > 500. Suppose that the corresponding radio emission has a Jy/beam value of X and thus an IR Jy/beam value of 500X. Suppose that this is superimposed on an old SNR with an IRR of 100 with Jy/beam value Y for its radio emission and thus Jy/beam value of 100 Y for its IR emission. The total radio Jy/beam value is thus (X+Y) and the total IR Jy/beam (500X +100Y). After some manipulation the IRR is given by $(500 + 100Y/X)/(1 + Y/X)$. In the GHz range, judging from the appearance of the Gum Nebula at 2.3 GHz, it is reasonable to assume that $Y \approx X$ and $Y/X \approx 1$. Since the identified thermal regions of the Gum Nebula tend to be in its brighter parts at 2.3 GHz, Y/X is probably less than one. Hence giving an IRR for this superposition of > 500.

No such regions corresponding to the identified thermal spectral index regions are apparent in the IRR image. Thus I conclude that the thermal regions in the Gum Nebula are unlikely to have originated from material in the immediate vicinity of the nebula that never interacted with the nebula and was only heated by the stars γ^2 Velorum and ζ Puppis. If this had been the case these regions would have the infrared excess seen in ordinary H II regions. I thus conclude that the thermal regions must have been processed by the Gum Nebula SNR, and thus lack the infrared excess usually seen in such thermal regions. This may be due to a smaller amount of dust in these regions than found in ordinary H II regions—the dust having been destroyed in the SNR shock front. Alternately, these thermal regions may have a larger amount of radio free-free emission than in ordinary H II regions as the gas has cooled to thermally emitting temperatures, rather than competing with the dust for Lyman contiuum photons from a star.

Thus there is also no evidence for the existence of the IRAS-Vela ring, as this is supposed to have properties similar to an H II region.

There are three other data sets, the 12, 25 and 100 μm images, available from the IRAS. However, using infrared spectra to identify SNRs is not feasible, as the IR spectra of SNRs are not unique. Young SNRs and planetary nebulae (PNs) have similar infrared spectra, while old SNRs and compact HII regions have similar spectra, though the latter are quite distinct from those of young SNRs and PNs. Thus the use of the IRAS data alone would not have allowed me to clearly identify the Gum Nebula as an old SNR.

As the IR dust emission in older SNRs is considered to be dominated by swept-up interstellar dust, the noticeable disparity in the IRR above and below the plane points to an expansion of the SNR into inhomogeneous interstellar material. This is further supported by the three identified cirrus clouds in the vicinity of the Gum Nebula. These may be representative of the type of material present at the location of the nebula prior to its birth.

Chapter 7

Spectral line observations

I also made radio spectral line observations at selected positions within and adjacent to the Gum Nebula. For these observations I used the 13 cm and 18 cm systems at HartRAO as well as the 20 cm system of the Mopra antenna near Coonabarabran, NSW, Australia.

Spectral line observations require a different receiver configuration to that for continuum observations. The spectral line receiver operates in what is known as the total power mode and the signal is fed through a correlator. The basic hardware of the 2 bit 3-level autocorrelation spectrometer at Hartebeesthoek and a test program were developed by Woodhouse (1980). Since then Gaylard (1989) has been responsible for fine-tuning, debugging and enhancing the system. The details of operating the spectrometer and post-detection analysis can be found in Gaylard (1981).

The correlator bandwidths available at HartRAO are 0.32, 0.64, 1.28, 2.56 and 5.12 MHz. The maximum correlator channel number is 512 channels.

The Mopra 22-m antenna is part of the Australia Telescope National Facility (ATNF), operated by the CSIRO. Though intended for use with other ATNF antennas to form the Long Baseline Array, it is also used for single dish observations. It is in the latter configuration that I used it for this work. The Mopra antenna has an alt-azimuth mount with the azimuth drive supplied by wheels on a circular track. Like the HartRAO antenna it has a Cassegrain or secondary reflector. The feedhorns for the various radio astronomy bands are operated with both feed horn and subreflector placed on axis. The relevant feed horn is rotated into position for observations by means of a rotating turret system which allows each feed horn to be brought on axis as required.

For my work I only required the 20 cm system. At the time of my observations (January to April, 1994) the antenna was still in its testing phase and some facilities were not yet in working order, such as doing continuum drift scans. The latter are important for the determination of electron temperature from hydrogen recombination lines. Drift scans also yield a more reliable calibration of the antenna parameters.

During January to April, 1994 the 20 cm system of the Mopra antenna at 1665 MHz had a system temperature of 34 K (the average for the two polarizations) and a beam sensitivity of 12.7 Jy/K as measured on Virgo A (A. Tzioumis, private communications). At 1665 MHz the resolution of the Mopra antenna is similar to that of the HartRAO antenna, $\approx 0.5°$.

The bandwidths available then were 64, 32, 16, 8 and 4 MHz at 1 or 2 bit sampling. The digital correlator is usually operated with 2-bit digitization for spectral line work. It can be set up such that two spectra, one from each polarization, are obtained simultaneously. Various combinations of bandwidth with number of channels are possible—the maximum number of channels available at the time of my observations being 4096. Spectra can be obtained in either the frequency or the position switching mode.

Observations at Mopra proved complicated as the system there did not have a doppler-tracking synthesizer. Furthermore the available local oscillator could only be set in quanta of one MHz. The lack of a doppler-tracking synthesizer meant that if the observing time on a single position lasted more than a day, (see chapter 8 for a report on single position observations of such length) the line would become smeared out. In addition, the line position velocity would be incorrect, as the line rest frequency could not be precisely positioned in the passband. It was thus necessary to correct the individual spectra for doppler tracking post detection, as well as correcting for observing at the frequency closest in MHz to the line rest frequency rather than observing at the latter frequency.

As the spectral line data reduction program used at HartRAO was not capable of handling data of more than 512 channels, I installed the spectral line data reduction program SLAP, provided by L. Stavely-Smith for Mopra users, at Rhodes. I then wrote a SLAP subroutine for post observation doppler tracking based on an existing program rv (Wallace,P.T., Starlink) for determining the appropriate doppler velocity and calling on another SLAP subroutine for the appropriate interpolation between channels.

The gaussian line fitting of the Mopra data was however done with the HartRAO program to ensure consistency of the line fitting of all spectral line data reported on in this work. As the Mopra spectra could be reduced in bandwidth once the line position had been found, the latter presented no problems to the HartRAO program.

There are two methods of spectral line observing, frequency switching and position switching. In both position switching and frequency switching, the objective is to isolate the line, which takes up only a portion of the passband and sits on top of the continuum radiation, from this continuum.

In position switching this is achieved by pointing the antenna for half the integration time at the chosen source position and for the other half at a position outside the source. The latter position should have essentially the same continuum as on source, but be without line emission in the observation passband. As only half the integration time is spent observing on source, this method is not very observing-time efficient. However, it has the advantage of producing a spectrum with a good baseline, as both on-source and off-source observations have the same frequency-dependent standing waves in the antenna and receiver. A good baseline is particularly desirable when faint broad lines are observed in order to avoid mistaking instrumental effects for such a line. Although such faint, broad lines were expected for the hydrogen recombination line observations in the Gum Nebula, this method was not used. As the Gum Nebula is an extended source, a suitable off-source position would be on average 5 to 10 degrees away from the on-source position. Thus driving the antenna to such an off-source position and returning it to the on-source position would add substantially to the observing time. Furthermore the hydrogen recombination lines (and also the OH lines) in the nebula were expected to be very faint. Hence spending half the observing time off-source was not an option, when use of the frequency-switching method guaranteed that all the observing time was spent on-source.

Removal of the continuum in the frequency-switching method is achieved by changing the frequency the observation passband is centred on, for half of the integration time, while remaining at the same source position. The removal of the continuum with the frequency-switching method is however usually not entirely successful due to the frequency-dependent standing waves in the antenna and receiver. The residual baseline curvature is removed by fitting orthogonal polynomials to user specified regions outside the line emission. As one does not want to turn an instrumental effect into an artificial line detection, it is generally desirable for this polynomial to be of as low an order as possible and preferably no higher than 4.

All spectra, both OH and hydrogen recombination line, presented in this work resulted from subtracting polynomials of order 2 to 4 prior to fitting the detected line with one or more gaussians.

Chapter 8

Hydrogen recombination line observations

8.1 Introduction

The detection of a hydrogen recombination line indicates the presence of ionised material in the temperature range 5000 K to 10000 K. The continuum emission from such regions is thermal. In general these regions are associated with O and B stars that emit a large enough number of Lyman continuum photons to ionise a significant amount of the circumstellar medium. Such thermally emitting regions are however also thought to exist in very old SNRs that have cooled sufficiently to emit detectable H recombination lines. Furthermore, if Reynolds' model of the Gum Nebula is correct, then the outer thermal shell of the old SNR, predicted by this model, would also emit H recombination lines.

The line velocity of an H recombination line observed near the edge of the nebula would allow one to estimate the heliocentric distance to the nebula by means of a galactic rotation model.

An estimate of the required on source integration time for a positive detection was made, given the continuum antenna temperatures measured in the 2.3 GHz survey and assuming typical values for the electron temperature and line width. The worst case scenario gave an estimate of one and a half days for the integration time.

As a detection at any one position would allow one to determine the electron temperature, emission measure and turbulent velocity of the emitting region, the project was nevertheless considered worthwhile. Even the failure to detect an emission line would allow one to determine a lower limit to the electron temperature.

8.2 Hydrogen recombination lines

The rest frequency, ν, in Hz of a hydrogen recombination line, H$n\alpha$, is given by the Rydberg formula:

$$\nu = cZ^2 R_a[n^{-2} - (n+dn)^{-2}] \tag{8-1}$$

where c = speed of light = 299792.5×10^3 m/s

Z = charge on the nucleus = 1 for hydrogen

$R_a = R_\infty(1 + m_e/m_a)$ = Rydberg constant for atom a

R_∞ = Rydberg constant for infinite mass = 10973731 m^{-1}

m_e = mass of the electron = 5.48597×10^{-4} amu

m_a = mass of the atom = 1.007825 amu for hydrogen

n = principal quantum number of the lower energy level

dn = number of levels jumped = 1 for α line, 2 for β line etc.

The ratio of the line antenna temperature integral, $\int T_{AL} dv$, to continuum temperature of the source, T_{AC}, for $H_{n\alpha}$ transitions has been derived by Brown, Lockman & Knapp (1978) for a model where:

1. The nebular structure is plane-parallel, homogeneous and isothermal.

2. All optical depths (that of the line as well as the continuum) are small: $\mid \tau_L + \tau_C \mid \ll 1$ and $\tau_C \ll 1$.

3. The lines can be treated as if they were formed and transferred in local thermodynamic equilibrium (LTE).

This gives

$$\frac{\int T_{AL}dv}{T_{AC}} \simeq 6.67 \times 10^3 \nu^{1.1} T_e^{-1.15} \quad (8\text{-}2)$$

where T_e is the electron temperature of the emitting region and the frequency ν is in GHz.

For a Gaussian line shape (Brown,Lockman and Knapp, 1978)

$$\int T_{AL}dv = 1.065 T_{AL} \Delta v \quad (8\text{-}3)$$

where Δv is the line width in km/s at half maximum.

Substituting equation (8-3) into equation (8-2) gives, for the H$n\alpha$ recombination line antenna temperature,

$$T_{AL} \simeq 6350 \Delta v^{-1} \nu^{1.1} T_e^{-1.15} T_{AC} \quad (8\text{-}4)$$

When an observation of a radio recombination line is made, the signal from the antenna is passed through the spectral line receiver. The resultant root mean square noise, δT_{rms}, in the spectrum is given by (Gaylard, 1989):

$$\delta T_{rms} = K_s T_{sys} \left(\sqrt{\delta f W_s t} \right)^{-1} \quad (8\text{-}5)$$

where δT_{rms} is in Kelvin and

K_s = 1.235 for 3 levels = quantization correction factor

T_{sys} = system temperature (K)

δf = correlator bandwidth per channel (Hz)

= 5.12 MHz over 256 channels for the HartRAO observations

W_s = correction for smoothing function

= 1.0 (rectangular), 1.36 (Hamming), or 1.5 (von Hann window)

t = observing time (seconds).

The line antenna temperature, T_{AL}, must be at least three times δT_{rms} for it to be considered a positive detection.

Equation (8-5) shows that an increase in integration time reduces the root mean square noise temperature and thus decreases the minimum detectable line temperature. If one combines equation (8-5) with equation (8-4) one obtains the minimum on source observing time, t, needed for a positive detection.

$$t > (3K_s T_{sys} \Delta v T_e^{1,15})^2 [\delta f W_s (6350 \nu^{1,1} T_{AC})^2]^{-1} \tag{8-6}$$

For a source with weak radio continuum emission, such as the Gum Nebula, equation (8-2) thus implies that the line antenna temperature will be small and hence will require a long integration time for detection (see equation (8-6)).

By contrast, the line temperature is inversely related to the electron temperature in the H II region—the lower the electron temperature the shorter the integration time for detection. The electron temperature of H II regions lies in the range 5000 to 10000 K. It may be determined from equation (8-4), giving

$$T_e = \left(6350 \nu_{GHz}^{1.1} T_{AC} \ /(T_{AL} \Delta v)\right)^{0.87} \mathrm{K} \tag{8-7}$$

The observed line width is the product of the instrumental resolution, the thermal width of the line, the turbulent velocity and pressure broadening, which is frequency dependent. The instrumental broadening is removed as part of the data reduction process. Without pressure broadening the line has a Gaussian profile. A hydrogen recombination line has thermal (a function of the electron temperature) and turbulent (which are assumed to be the same for each component) contributions to the full width at half maximum of the line, given by

$$\Delta v = \sqrt{1.85 < v_{turb} >^2 + 0.0457 T_e} \qquad \mathrm{km/s} \tag{8-8}$$

where $< v_{turb} >$ is the rms turbulent velocity. This equation allows one to determine the turbulent velocity of the emitting gas.

The normalized signal-to-noise ratio, S/N, of the Gaussian fitted to the detected line is used as a criterion for the reality of the line. This is defined as (von Hoerner, 1967):

$$S/N = (\frac{T_{AL}}{\delta T_{rms}})\Delta v^{\frac{1}{2}} \tag{8-9}$$

where T_{AL} = the line antenna temperature (K)

T_{rms} = the rms noise in the spectrum (K)

Δv = the halfpower width of the line in units of the spectrum resolution.

The S/N should be greater than 10 for a 3-σ detection of a spectral line.

8.3 Estimate of required integration time for detection

The on source observing time required for the detection of a hydrogen recombination line of rest frequency near 2.3 GHz in the Gum Nebula was estimated. I assumed that all the continuum emission at 2.3 GHz from the Gum Nebula is thermal. The continuum antenna temperatures of the brighter parts of the Gum Nebula were determined. Subtraction of a linear fit to the low points on the boundary at opposing sides of the Gum Nebula removed the background continuum. The brighter parts of the nebula isolated from its background were found to be $\approx$ 200 mK at 2.3 GHz and a resolution of 0.33°. For this continuum antenna temperature, a typical line width of 30 km/s and T_e = 10000 K, the estimated integration time given by equation (8-6) is about 40 hrs. A lower electron temperature of 5000 K would reduce this estimate to 9 hrs.

An observation of a hydrogen recombination line of 40 hour duration is clearly not easy. In observations lasting only a few hours, small instrumental effects are hidden in the comparatively large noise. In much longer integration times these instrumental effects are no longer negligible compared to the size of the much reduced electronic noise. Thus such long integration times make stringent requirements on the stability of the system over a period of days. However, observations of 24 hour duration with the HartRAO 13cm system had previously resulted in detections (Gaylard, 1984). Thus, provided the electron temperature of the Gum Nebula is closer to 5000 K than 10 000 K, the detection of a hydrogen recombination line in the Gum Nebula was feasible.

8.4 Observations

I made observations of the H141α line (rest frequency 2321.2 MHz) at three positions, G249.6 $-$ 9.56, G267.22 $-$ 9.56 and G269.45 $-$ 7.53, during Nov 1987 at HartRAO.

The positions of the H recombination lines observed at HartRAO are indicated in the TT-plot spectral index image in Fig. [5-17] by circles. The spectral index images were generated after the H recombination line observations at HartRAO were made. One of the positions observed at HartRAO has a non-thermal spectral index. Thus it is not surprising that it yielded a non-detection. In the light of the detections obtained at Mopra, the other two observations at HartRAO should have yielded detections as they are in regions of thermal spectral index and at positions of high continuum antenna temperature.

The spectra I obtained at HartRAO after more than 30 hrs of integration time were dominated by instrumental effects. This conclusion was reached as follows. No obvious line was evident in the spectra prior to the polynomial fitting. Fitting 8th order polynomials to these spectra resulted in fairly flat baselines, but gave rise to spectral lines with severely non-gaussian line shapes and in one case unrealistically large line width. Fitting such high order polynomials to the baselines is known to result in spectral lines that are artifacts of the fitting process. Insisting on a polynomial fit not exceeding the 4th order resulted in lines so narrow that the derived turbulent line velocity was negative. This is physically inconsistent, unless the lines are strongly pressure-broadened, which is unlikely in the Gum Nebula. Furthermore the signal to noise ratio of these narrow lines was significantly less than 10. Thus a conservative interpretation of the HartRAO spectra is that they are non- detections. As the lines/wobbles arising from instrumental effects in the spectra can be quantified by antenna temperatures of the order of 10 mK, an upper limit on any real lines masked by these instrumental effects is 5 mK.

The system at Mopra provided dual polarization spectra. As hydrogen recombination lines are unpolarized, the two polarizations are independent and can be added. This effectively doubles the on source time for a particular observing time and thus reduces the noise level by $\sqrt{2}$. Thus I made another attempt at detecting the hydrogen recombination line at Mopra in April 1994 after the hydroxyl observing programme (see next chapter) had been completed.

All observed positions were chosen to be at positions with a relatively high continuum antenna temperature and where the spectral index, as determined in chapter 5, is essentially thermal (see open squares in Fig. [5-17]). Three of the four observed positions were chosen to be near the edge of the nebula. These sample the material of the Gum Nebula at positive galactic latitudes, G $270.65° + 10.4°$, and at high, G$264.0 - 12.8$, and low, G$252.36 - 12.15$, longitudes at negative galactic latitudes. A large disparity in the kinematical distances determined from the line velocities at these positions, would support a model of this region where the Gum Nebula is not a single object.

The fourth position, G$265.0 - 8.0$, was chosen to be as near the centre of the nebula as consistent with a thermal spectral index and a relatively high continuum antenna temperature. This was to test whether the turbulent velocity near the centre is greater than at the edges; as expected if the emitting material is expanding from a common centre.

As the system at Mopra was set up for observations at 18 cm, this meant choosing a hydrogen recombination line in that receiver passband. Thus the 8 MHz band was tested for interference levels at four different H recombination line frequencies between 1620 MHz and 1716 MHz. The band around the H156α transition (rest frequency 1715.67 MHz) at 1716 MHz proved to be the cleanest.

The Mopra observations at G264.0$-$12.8 and G265.0$-$8.0 were made at a bandwidth of 8 MHz with 1024 channels. For the subsequent two Mopra observations, G252.36 $-$ 12.15 and G270.65 + 10.4, the number of channels was halved in order to reduce the integration time required (see equation (8-6)).

Fourth order polynomials, obtained from a fit to the residual baseline between $\approx$ $-$130km/s and $\approx$ +130 km/s, were subtracted from the spectra obtained at G265.0$-$8.0, G252.36$-$12.15 and G270.65+10.4 and a third order polynomial was subtracted from the spectrum at G264.0 $-$ 12.8. The residual baseline error was $\approx$ 1.5 mK in all cases and thus of the order of the rms noise in the spectra. The resultant spectra are shown in Fig. [8-1].

The line parameters as determined from single gaussian fits to the lines are listed in table [8-1]. As the observation at G265.0 $-$ 8.0 is towards the centre of the Gum Nebula, one would expect a broader line there.

position	S/N	resol /[km/s]	T_{AC} /[mK]	T_{AL} /[mK]	v /[km/s]	Δv /[km/s]
252.36 $-$12.15	10.0	3.28	210 $\pm$ 40	5.19 $\pm$ 0.50	0.91 $\pm$ 1.8	31.5 $\pm$ 3.9
264.00 $-$12.80	18.9	1.64	310 $\pm$ 70	7.97 $\pm$ 0.43	2.96 $\pm$ 0.61	22.9 $\pm$ 1.5
265.00 $-$8.00	16.7	1.64	380 $\pm$ 80	4.93 $\pm$ 0.30	-2.60 $\pm$ 1.3	43.1 $\pm$ 2.8
270.65 +10.40	11.8	3.28	265 $\pm$ 60	4.69 $\pm$ 0.40	-7.77 $\pm$ 1.3	30.2 $\pm$ 2.8

Table [8-1]: The positions and line parameters of H recombination line observations made on the Gum Nebula.

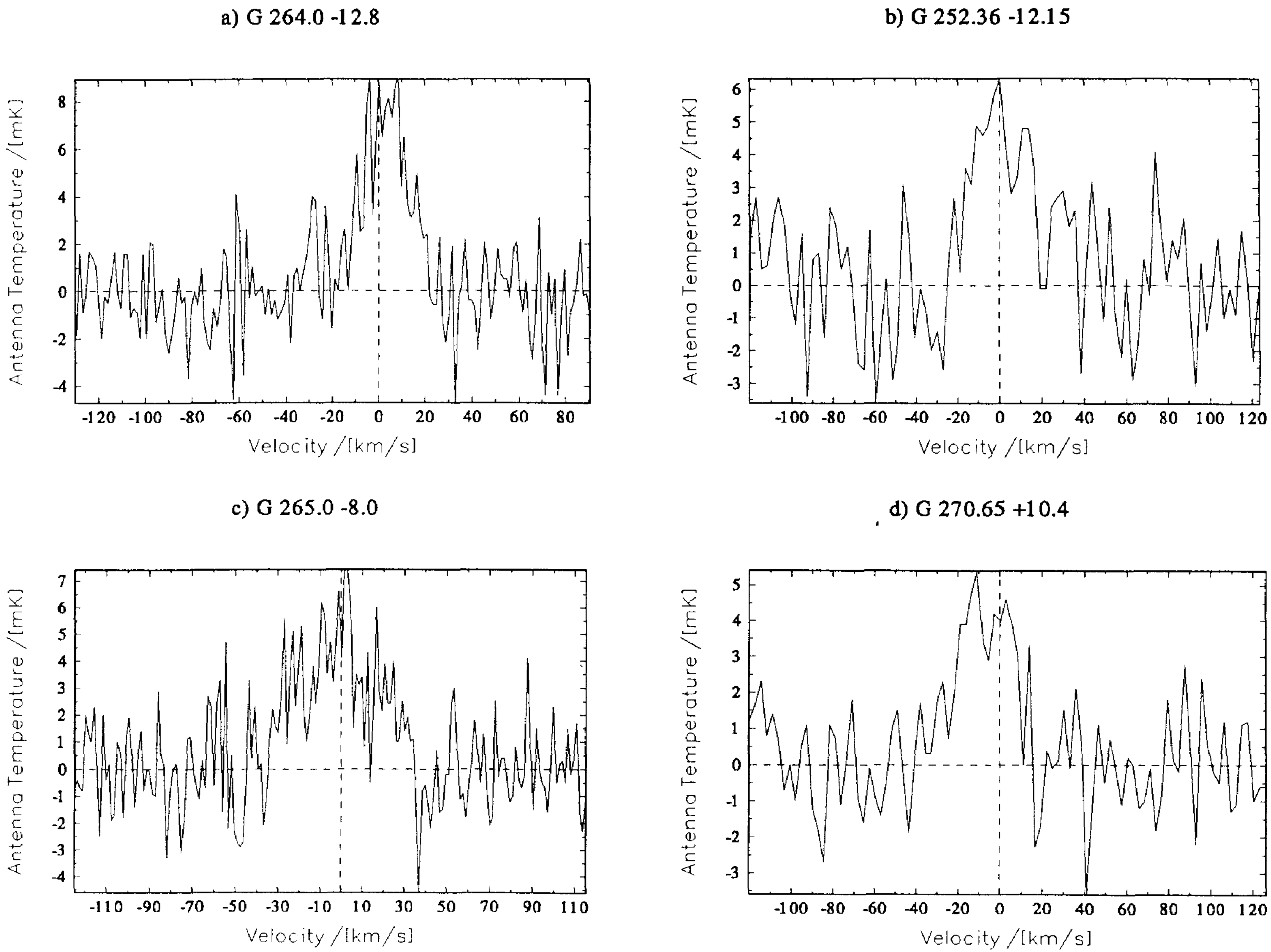

Figure [8-1]: The unsmoothed H recombination line spectra obtained at the four positions observed with the Mopra antenna.

8.5 Kinematic distances from line velocities

The uncertainties in the line velocities were used to obtain a range of possible kinematic distances from us for each observed position. The galactic rotation curve of Wouterloot & Brand (1989) was used to convert the line velocities to kinematic distances from us.

position	distance/[kpc]
252.36 -12.15	0.1 to 0.4
264.00 -12.80	0.7 to 1.0
265.00 -8.00	moving towards us
270.65 +10.40	0.01 to 0.2

Table [8-2]: The range of kinematic distances to the observed positions as consistent with the uncertainties in the lines velocities of the hydrogen recombination lines.

From the derived kinematic distances listed in table [8-2] it is obvious that the velocities are dominated by internal motions.

8.6 Continuum antenna temperature for the Mopra observations

The positive detection of hydrogen recombination lines at Mopra meant that continuum antenna temperatures of the source positions obtained with the same system at the same frequency were required for electron temperature determinations. As there was a bug in the scanning software at Mopra (the antenna was running on a trial basis) that could not be fixed before my observing time was up, I had to obtain estimates of the continuum antenna temperature at the positions where hydrogen recombination lines were detected by other means. Attempts were made by measuring the system temperature (using the spectral line observing program, SPECTRA) at points along a line passing through the position where the line was detected. This did not give rise to useful data. The terrestrial background dominated the measurements and there was no means of determining its contribution. Thus an educated guess at the appropriate continuum antenna temperature was made using the 2.3 GHz HartRAO data.

I used the 2.3 GHz Rhodes HartRAO continuum image of the region convolved to a 0.5° resolution with a linear background subtracted from the Gum Nebula, as presented in chapter 6. This image is at the same resolution as that of the HartRAO system at 18 cm (HPBW = 0.5°). Thus the 2326 MHz HartRAO antenna temperatures could simply be read off at the appropriate positions. The next step was to convert the 2326 MHz HartRAO antenna temperature to one at the rest frequency (1715.67 MHz) of the observed hydrogen recombination lines. Assuming the continuum emission to be thermal with a spectral index of 2.1, this is given by

$$T_{A,1715.67} = T_{A,2326}\left(\frac{2326}{1715.67}\right)^{2.1} \tag{8-10}$$

The calculated 1715.67 MHz HartRAO antenna temperature had to be converted to the Mopra antenna temperature at 1715.67 MHz. Thus the relationship between the Mopra antenna beam efficiency and that of the HartRAO antenna had to be determined. The determination of the beam efficiency of an antenna requires mapping the antenna beam pattern at the observation frequency. No such beam map could be made with the Mopra antenna nor was one available at this frequency. As the Mopra and HartRAO antennas are both Cassegrain antennas with similar illumination and sidelobes, it is reasonable to assume that they have similar beam efficiencies. Thus for this work it is assumed that the Mopra antenna temperature continuum at 1715.67 MHz is equal to that derived from equation (8-10) for the HartRAO antenna temperature continuum at 1715.67 MHz. It is difficult to quantify the uncertainty in this assumption, given that the Mopra antenna has a slightly smaller dish (22m diameter) than the HartRAO antenna (26m diameter) and that the Mopra antenna is likely to have smaller sidelobes and hence a higher beam efficiency than the HartRAO antenna as its support tetrapod legs are thinner than those of the HartRAO antenna and its feed is positioned on axis rather than off axis. The uncertainty is systematic rather than random and is assumed to be about 20%.

The 1715.67 MHz continuum antenna temperature at the observed positions is listed in table [8-3].

8.7 Derived parameters

The derived electron temperature, turbulent velocity and emission measure (EM) are listed in table [8-3].

position	T_e /[K]	v_{turb} /[km/s]	EM /[pc cm^{-6}]
252.36 −12.15	4200 ± 900	20.8 ± 3.3	220 ± 60
264.00 −12.80	5500 ± 1100	12.2 ± 1.9	360 ± 100
265.00 −8.00	5800 ± 1100	29.3 ± 2.3	460 ± 130
270.65 +10.40	6000 ± 1300	18.6 ± 2.6	320 ± 100

Table [8-3]: The positions and derived parameters of H recombination line observations made on the Gum Nebula.

8.7.1 Electron Temperatures

The electron temperatures derived from the Mopra spectra compare reasonable well with those quoted in the literature. Other than the very hot ($\geq 10^5$) temperatures required to explain the existence of highly ionised species (see chapter 2), most temperature values reported in the literature are in the accepted range for H II regions. Hippelein & Weinberger (1975) report 11800 ± 5200 K at $l = 250°$, $b = -10°$ and 11600 ± 4500 K at $l = 266°$, $b = -9°$. Reynolds obtained a temperature range of 3000 K to 17000 K at seven positions with a least-squares fit to these temperatures giving an average temperature of 11300 K. Chanot & Sivan (1983) report an electron temperature of 8000 K and Vidal (1979) derived values of T = 5940 K and T = 7260 K. The range for the electron temperature derived from the absorption of background radiation by the Gum Nebula at very low radio frequencies is 8500K +4500K -3500K (Beuermann, 1973).

8.7.2 Emission measure

The emission measure (EM) at frequency ν may be derived from the electron and brightness temperatures at the observed H recombination line positions using the formula (Mezger & Henderson, 1967):

$$EM = 12.14 T_e^{0.35} \nu^{2.1} T_b \qquad (8\text{-}11)$$

It is assumed that the conversion factor from antenna temperature to brightness temperature of the Mopra and the HartRAO observations is the same, i.e 1.5. The calculated emission measures are listed in Table [8-3].

Reynolds (1976a) published calibrated Hα derived emission measures of the Gum Nebula. He reported a range of 8 to 320 cm^{-6} pc, as given by a subsequent improvement in the absolute calibration (private communication). A similar range, also absolutely calibrated, is reported by Chanot & Sivan (1983), with an average of about 100 cm^{-6} pc.

The emission measures derived from the H recombination lines are, within the uncertainties, in agreement with these values. That the H recombination line derived emission measures are consistently high is due to the fact that the observed positions were chosen for their high brightness temperatures.

8.7.3 Turbulent Velocities

The turbulent velocities of the three positions, G264.0 − 12.8 , G252.36 − 12.15 and G270.65 + 10.4, compare favourably with the average turbulent velocities for H II regions quoted in the literature. Gaylard (1989) reports 26.5 ± 6.1 km/s for H142α

(2.3 GHz) lines. Caswell & Haynes (1987) report 26.6 ± 5.6 km/s for H109α (5 GHz) lines.

The turbulent velocity of 43.2 km/s at G265.0 − 8.0 is considerably larger. This large turbulent velocity probably has systematic components due to a contribution from an expansion of the nebula. The contribution from an expansion of the nebula would be large towards the centre of the nebula and essentially zero at its edge. Thus this is a plausible explanation of this large turbulent velocity.

8.8 Discussion and Conclusion

Hydrogen recombination lines were detected at four positions with the Mopra antenna in the Gum Nebula. This confirms the thermal spectral indices at these positions. As the HartRAO spectra, which include observed positions with non-thermal spectral index, were dominated by instrumental effects, the non-detections at these non-thermal positions are not conclusive.

The detection of the Hydrogen recombination lines does not negate an SNR classification of the Gum Nebula. It does however support the models in which the old SNR is surrounded by an H II shell. The latter is not uniformly distributed around the SNR, as seen in the spectral index images shown in chapter 4 and 5.

The line velocities of the H recombination line data are dominated by internal motions. They do not provide any usefull information on the distance to the Gum Nebula. At best one can conclude that it is unlikely for the nebula to be further than 1 kpc from us.

The derived electron temperatures, 4200 to 6000 K, and emission measures, 220 to 460 pc cm^{-6}, are in agreement with values listed in the literature.

The large turbulent velocity estimated from the detection at G265.0 − 8.0, a position closer to the centre than the other three observed positions, is indicative of a non-zero expansion of the nebula.

Chapter 9

Hydroxyl observations towards the Gum Nebula

9.1 Introduction

One motivation for studying the Gum Nebula in the Hydroxyl (OH) lines was to search for evidence of the interaction of the Gum Nebula with molecular material in the form of shocked molecular lines. The detection of such shocked molecular lines would strengthen an SNR classification of the nebula. Shocked hydroxyl lines have been observed towards the SNR IC443 by DeNoyer (1979) and DeNoyer & Frerking (1981). Similar line profiles were seen in CO, CS, HCN and HCO+. The OH line in IC443 was confirmed by Green (1989), but he made no definite detections with similar properties in 15 other observed SNRs. In general the characteristic traits of the shocked molecular lines in IC443 are that they are broad and asymmetric. In particular, the hydroxyl is anomalously excited, having strong narrow-line OH emission at 1720 MHz and broad-line absorption at 1612, 1665 and 1667 MHz. Such OH emission is now considered as indicative of the interaction of an SNR with molecular material by Frail et al. (1996), who detected the OH 1720 MHz line in emission towards 20 out of 66 observed SNRs.

Several molecular line studies within the Gum Nebula region have been reported in the literature (Goss et al., 1980; de Vries et al., 1984; Zealey et al., 1983 and

Sridharan, 1992). The positions of the reported detections (solid symbols) and non-detections (empty symbols) are shown in Fig. [9-1]. Clearly molecular material is present near the plane, as a large proportion of the detections are within 5° of the plane. However a definite association with the Gum Nebula is not guaranteed there, because of confusion with other objects situated near the plane. Those detections falling outside this region are predominantly observations of the cometary globules (CGs, square symbol of Sridharan's data in Fig. [9-1]). For an improved sampling of molecular material unambiguously associated with the nebula, observations away from the plane were required.

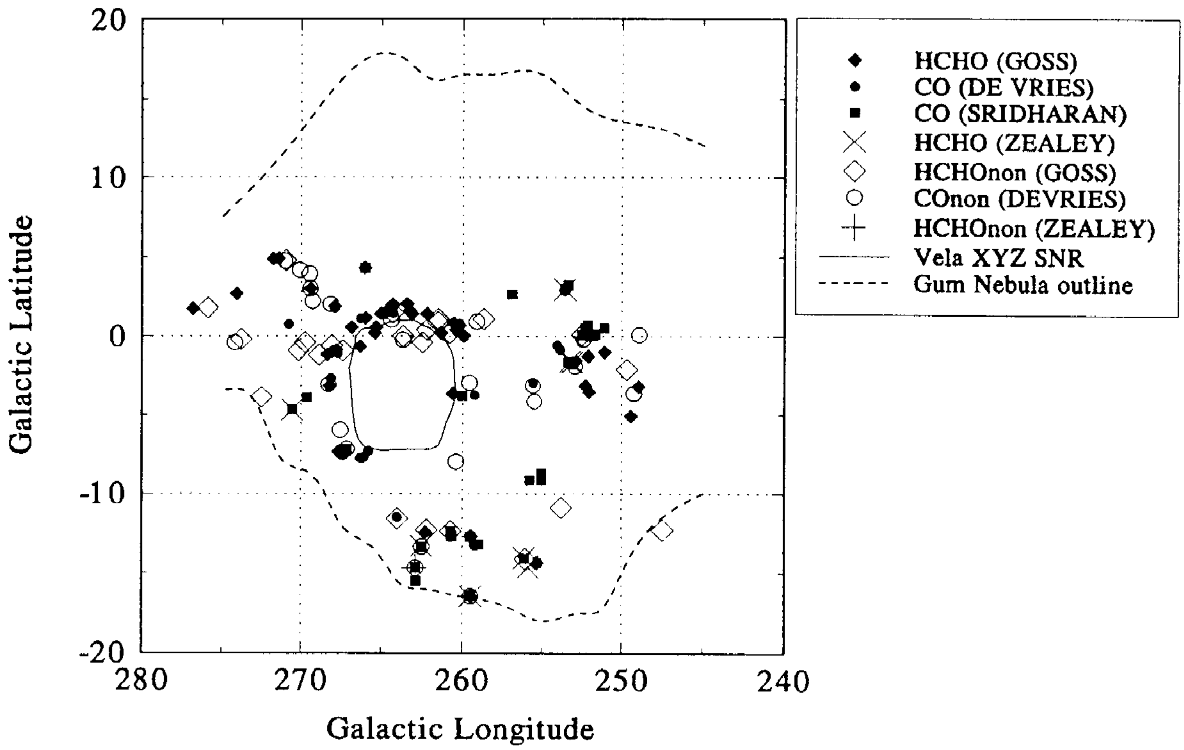

Figure [9-1]: A schematic map of the Gum nebula region, showing where molecular line observations, reported in the literature, were made. The approximate extent and position of the Gum nebula and Vela XYZ SNR are indicated by the dashed line and solid line respectively.

The Gum Nebula is too large to attempt a complete coverage of it in OH with the $\approx 0.5°$ beam size of the HartRAO and Mopra antennas. As there are a large number of reported non-detections, some criterion for selecting observing positions that would favour detections of the molecular material had to be obtained.

Large concentrations of molecules are known to occur in dense, very cold (≤ 100 K) and dusty clouds (e.g. Hoyle 1957 and Heiles, 1968). The dust in these clouds is a strong emitter in the infrared wavelength regime, because of its low temperature. Thus, in principle, concentrations of molecular material should be at positions with high infrared intensity. Cox et al. (1986) have shown that the longer wavelength infrared has a better correlation with concentrations of molecular material than that at shorter wavelength. An inspection of the IRAS images of this region displayed in Srinivasan Sahu (1992) shows that there are no marked differences in the positions of local intensity maxima between the 60 μm and 100 μm data. Thus I could use the existing 60 μm map to isolate positions with high infrared intensity signalling concentrations of molecular material. I also used dark cloud catalogues (Feitzinger & Stüwe, 1984; Hartley et al., 1986) of this region to pinpoint positions with concentrations of molecular material.

The characteristics of shocked OH lines are not the only possible departures from LTE line ratios. Thus the broader aim of this part of this project was, in the first instance, to investigate the excitation of the OH associated with the Gum Nebula. For the identification of observed events with departures from LTE line ratios a brief summary of OH line theory and radiative transfer is presented. This is followed by the presentation and discussion of the observed spectra.

On average 6 hr integration times were necessary for positive detections. Thus only a limited number of positions were observed at the two or more OH line frequencies necessary to establish the type of excitation present. The majority of positions were observed only in the 1667 MHz line, predicted to be the strongest unless the OH excitation is severely anomalous. Shocked gas producing broad-line absorption and asymmetric line shapes at 1667 MHz can still be identified in observations at this single frequency.

I also analysed the line velocities of the detections for evidence of an expansion of the nebula as a whole with this associated molecular material. Details of that investigation are given in the next chapter. This dual purpose of the OH observations meant that observing positions were also selected according to criteria appropriate for such an investigation of the expansion.

9.2 The line-ratios of the four OH Λ-doublet ground state transitions

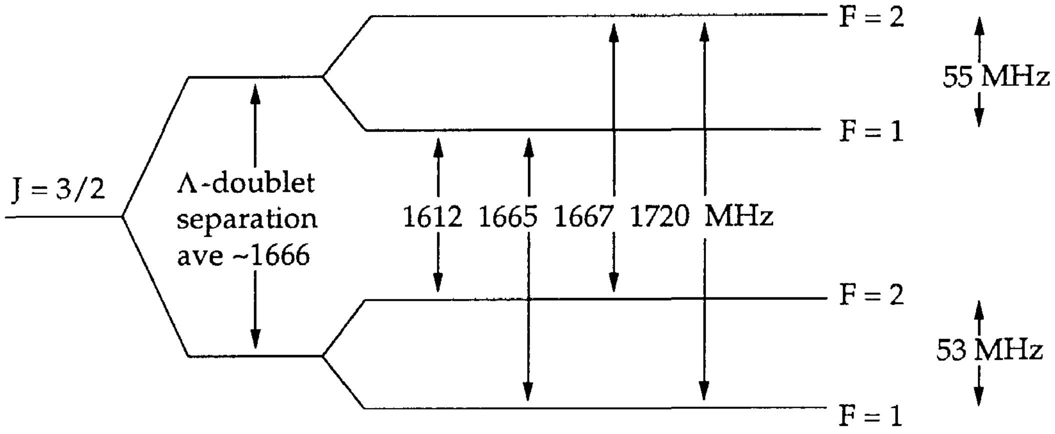

Figure [9-2]: Diagram showing transitions for OH radio lines at 1612, 1665, 1667 and 1720 MHz (Kraus, 1986).

In OH the lowest energy levels all belong to the $^2\Pi_{3/2}$, J=3/2 ground state. A schematic diagram of the four energy levels of this ground state produced by Λ-doubling and the hyperfine interaction is shown in Fig. [9-2]. Transitions between the four levels give rise to radio lines at approximately 1612, 1665, 1667 and 1720 MHz.

In local thermodynamic equilibrium (LTE) the 1665 and 1667 MHz lines are strongest and thus known as the main lines. The weaker 1612 and 1720 MHz lines are known as the satellite lines.

The quantity, T_x, known as the excitation temperature, describes the population density ratios for the upper and lower levels of a transition. Anomalous excitation occurs when the excitation temperatures for the four lines differ from each other.

Rogers & Barrett (1967) have shown that these four lines obey the the excitation-temperature sum rule:

$$\frac{\nu_1}{T_{x,1}} + \frac{\nu_4}{T_{x,4}} = \frac{\nu_2}{T_{x,2}} + \frac{\nu_3}{T_{x,3}} \tag{9-1}$$

where the numbers 1,2,3 and 4 refer to the 1612, 1665, 1667 and 1720 MHz OH lines respectively, such that ν_1 and $T_{x,1}$ are the frequency and excitation temperature of the 1612 MHz line respectively etc. As no assumptions about thermal equilibrium or optical thickness of the emitting source were made in deriving this equation, it holds under all conditions.

For each of the four OH lines, $i = 1..4$, there are equations of the form of equation (9-2) and equation (9-3) below (Goss, 1968).

Radiative transfer of these lines yields

$$T_{A,i} = \eta_B \, F \, (T_{x,i} - T_c) \, \tau_i \tag{9-2}$$

where $T_{A,i}$ is the line antenna temperature, T_c is the brightness temperature of the background continuum, η_B the beam efficiency, τ_i is the optical depth and F is the beam filling factor. The latter has a value of one if the OH cloud fills the antenna beam. For clouds of angular size smaller than the antenna beam F is less than one.

N_{OH}, the OH column density in cm^{-2}, is given by

$$N(OH) = C_i \, T_{x,i} \, \tau_i \, \Delta V_i \qquad (9\text{-}3)$$

where ΔV_i is the full width at half maximum of the optical depth profile i.e the line profile in km/s. C_i is equal to 22.21, 4.299, 2.385 and 20.84 in units of 10^{14} cm^{-2} K^{-1} (km/s)$^{-1}$ for 1612, 1665, 1667 and 1720 MHz respectively.

Together with equation (9-1) this gives a total of nine equations. If all four OH lines have been observed at a position, then $T_{A,i}$, η_B, T_c and ΔV_i are known for each line. That leaves four line excitation temperatures, four line optical depths, the OH column density and the filling factor as unknowns—a total of 10 unknowns. If the nine equations are solved for different assumed values of the filling factor, the solutions for the other nine unknowns may be chosen as those giving the smallest errors overall in the resultant excitation temperatures, optical depths and column densities.

One does not necessarily have to solve these equations to identify the presence of anomalous excitation. Unless the latter is masked by optical depth effects, the line ratios themselves indicate if anomalous excitation is present. If an OH cloud is in LTE, i.e. all four OH lines have the same excitation temperature, and optically thin, the line ratios for the lines are $T_{A,1612} : T_{A,1665} : T_{A,1667} : T_{A,1720} \approx \tau_{1612} : \tau_{1665} : \tau_{1667} : \tau_{1720} \approx 1 : 5 : 9 : 1$ (e.g. Weaver et al., 1965). A cloud in LTE of intermediate optical thickness has line ratios of an intermediate value between the extremes of the optically thin and thick case. For the latter extreme, which is essentially never encountered in practice $T_{A,1612} : T_{A,1665} : T_{A,1667} : T_{A,1720} = 1 : 1 : 1 : 1$. For example, in LTE the OH line ratio, $T_{A,1667}/T_{A,1720}$, ranges from 9 to 1 as the optical depth goes from zero ($T_{A,1667} : T_{A,1665} \approx 9 : 1$) to thick ($T_{A,1667} : T_{A,1665} = 1 : 1$). Thus if this line ratio lies outside the 9 to 1 range there are definitely anomalies, i.e. the excitation temperatures are not equal. Obviously mild departures from LTE line ratios may be present even when this line ratio is between 9 and 1, but these are masked by optical depth effects. Provided one has sufficient data and can thus solve the equations above, even the latter anomalies may be determined.

The aim of this work was, in the first instance, to identify detections of anomalous excitation. This may be done without observing all four ground state OH lines, as the satellite lines are more sensitive to anomalous excitation than the main lines. Thus a departure from the LTE line ratio 9:1 of the 1667 MHz line to one of the satellite lines is usually more apparent than a departure from LTE values in the main line ratio. Hence, in a search for anomalous excitation, it is best to observe the 1667 and either the 1720 or 1612 MHz lines. However interference from the group of artificial earth satellites, known as Glonass, is so severe in the 1612 MHz band, that observations at this frequency are usually avoided. Also, in this case we are interested in detecting a particular type of anomaly where the 1667 MHz line is in absorption, while the 1720 MHz line is in emission. Thus observations were restricted to 1667 and 1720 MHz. At 3 positions the 1665 MHz line was also observed.

9.3 Search for anomalous excitation

The OH 1667 and 1720 MHz spectra I obtained at fifteen positions in the Gum Nebula are shown in Fig. [9-3] a) to o). Supplementary observations at 1665 MHz were made at three positions and are shown in g) to i).

The spectra shown in p) were obtained at a position on the SNR IC443 to serve as an example of the particular anomalous excitation and asymmetric line shape characteristic of shocked gas.

The observation j) at G264.0 -3.3 has a ratio $T_{A,1667} : T_{A,1720}$ of $2:1$. This is indicative of an intermediate optical depth, which may be masking anomalous excitation in the 1720 MHz line. Nevertheless, the spectra lack the specific characteristics of shocked OH lines. The 1667 MHz spectrum is fitted easily by three gaussians and thus does not qualify as having an asymmetric line shape of the kind looked for. As this position is also along the line of sight to the Vela XYZ SNR and close to the galactic plane a definite association with the Gum Nebula cannot be made.

Anomalous excitation is only identified unambigously from line ratios if $T_{A,1667}/T_{A,1720}$ lies outside the 9 to 1 range. Thus the 1720 MHz line must be greater than the 1667 MHz line or the 1720 MHz line must be less than 1/9 the 1667 MHz line for such an identification. The former case is not seen in any of the observed spectra. The indentification of the latter case is not possible from these observations as the 1720 MHz lines are still hidden within the noise after approximately 6 hours of integration time. Thus observations at 1720 MHz were discontinued as totally prohibitive integration times would have to be spent at each position in order to obtain unambiguous data.

Hence in these observations there is no evidence of an interaction of the Gum Nebula with a molecular cloud.

Thus I decided to limit the subsequent OH observing programme to 1667 MHz observations. The positions observed only at 1667 MHz were selected for suitability in a test for expansion of the OH emitting material with the Gum Nebula. Detections were nevertheless examined for the type of broad asymmetric absorption line at 1667 MHz observed in IC443.

Figure [9-3]: On the next 3 pages are the 1667, 1720 and 1665 MHz OH spectra obtained with the HartRAO antenna at positions within the Gum Nebula. An exception is p) which shows spectra obtained at a position on the SNR IC443.

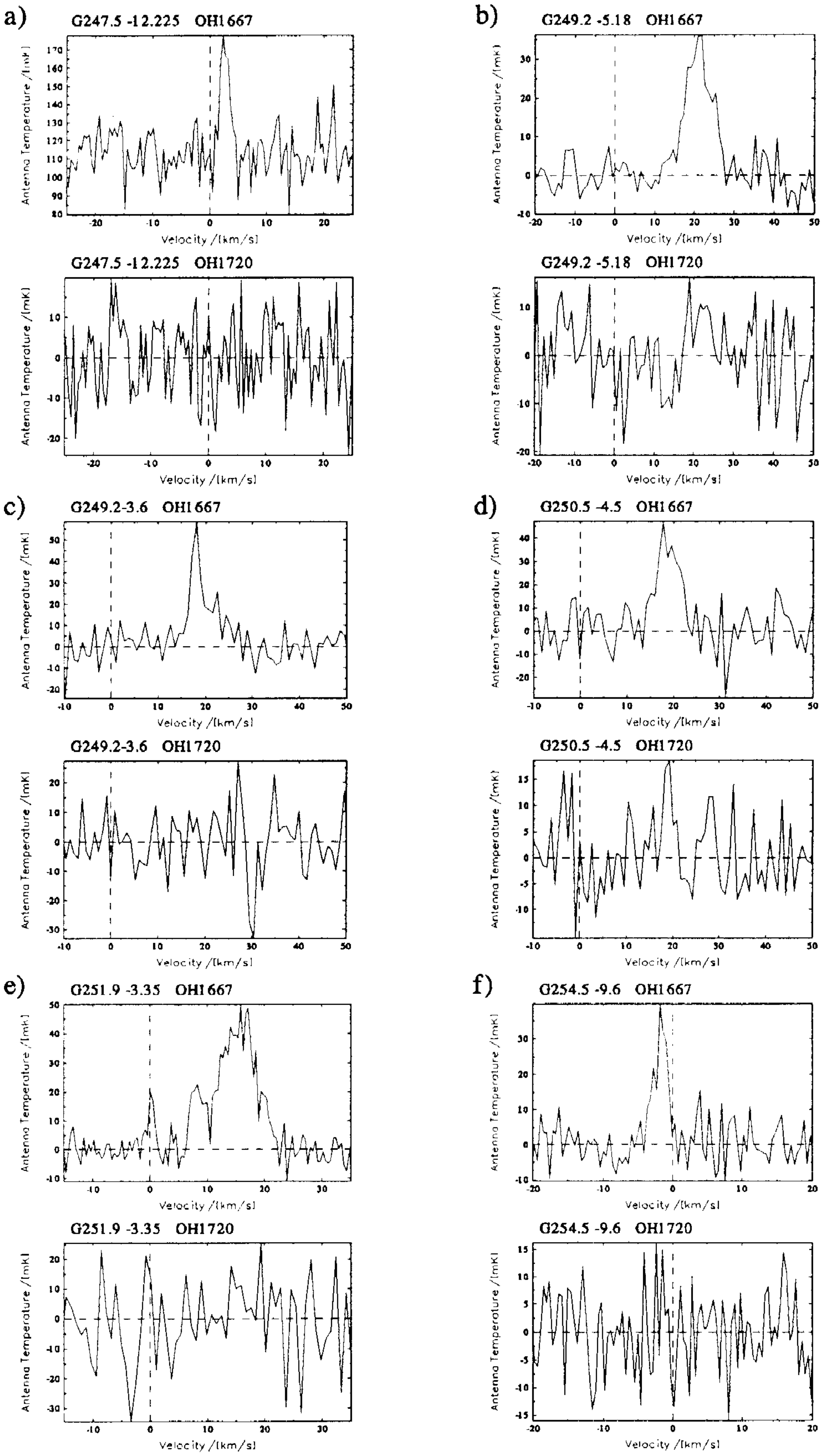

a)
G247.5 -12.225 OH1667
G247.5 -12.225 OH1720
b)
G249.2 -5.18 OH1667
G249.2 -5.18 OH1720
c)
G249.2-3.6 OH1667
G249.2-3.6 OH1720
d)
G250.5 -4.5 OH1667
G250.5 -4.5 OH1720
e)
G251.9 -3.35 OH1667
G251.9 -3.35 OH1720
f)
G254.5 -9.6 OH1667
G254.5 -9.6 OH1720
Antenna Temperature /[mK]
Velocity /[km/s]

g)

G256.1 -10.5 OH1665

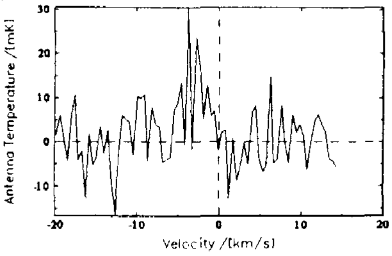

G256.1 -10.5 OH1667

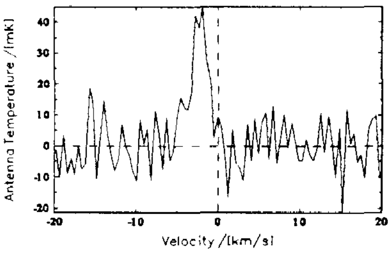

G256.1 -10.5 OH1720

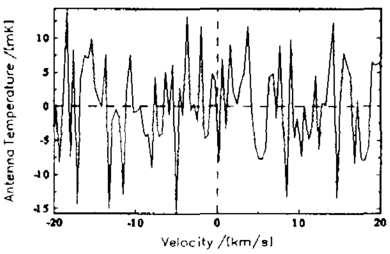

h)

G258.25 -3.1 OH1665

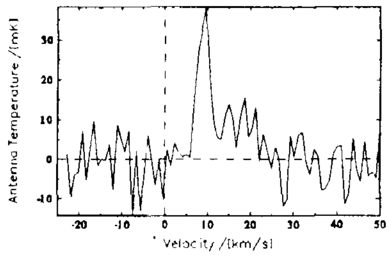

G258.25 -3.1 OH1667

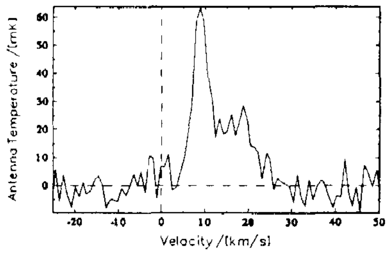

G258.25 -3.1 OH1720

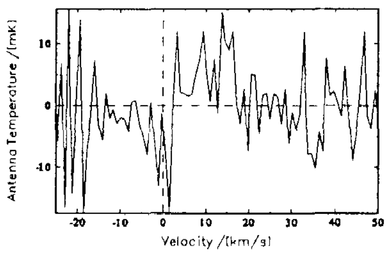

i)

G259.25 -13.25 OH1665

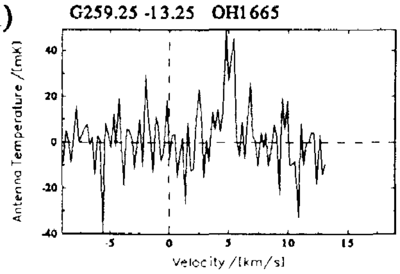

G259.25 -13.25 OH1667

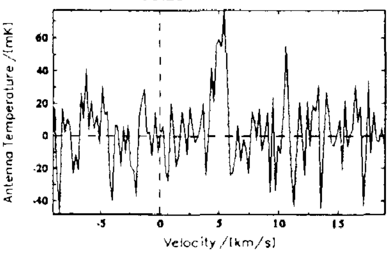

G259.25 -13.25 OH1720

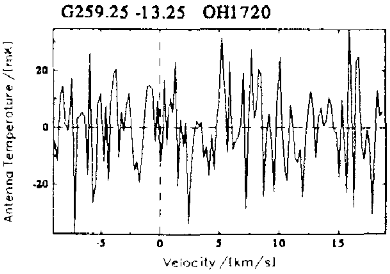

j)

G264.0 -3.3 OH1667

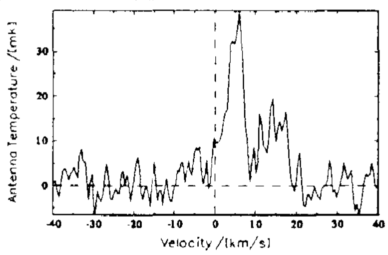

G264.0 -3.3 OH1720

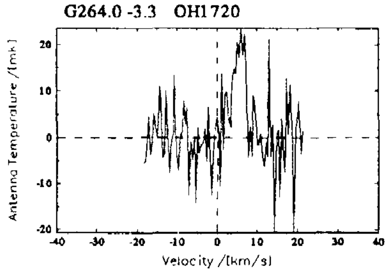

k)

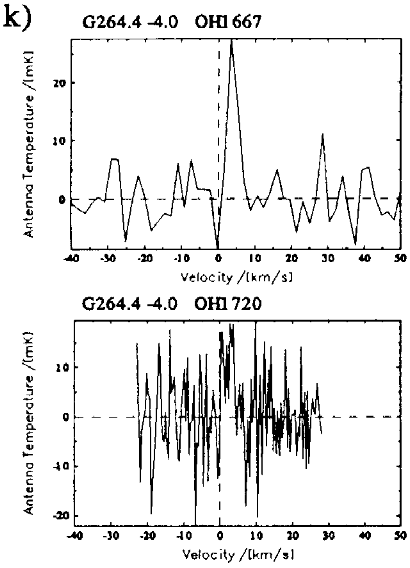
G264.4 -4.0 OH1667
G264.4 -4.0 OH1720
Antenna Temperature /[mK]
Velocity /[km/s]

l)

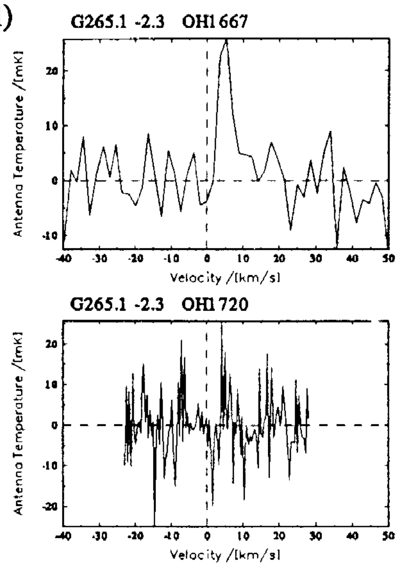
G265.1 -2.3 OH1667
G265.1 -2.3 OH1720
Antenna Temperature /[mK]
Velocity /[km/s]

m)

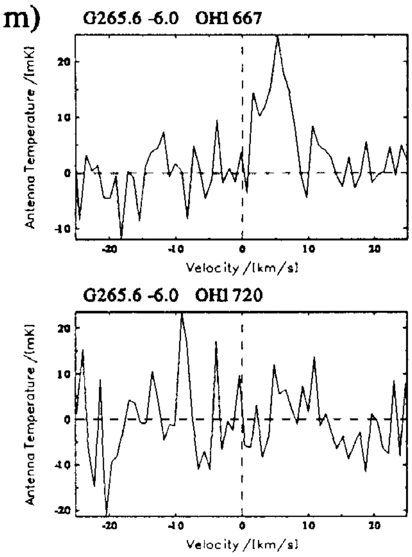
G265.6 -6.0 OH1667
G265.6 -6.0 OH1720
Antenna Temperature /[mK]
Velocity /[km/s]

n)

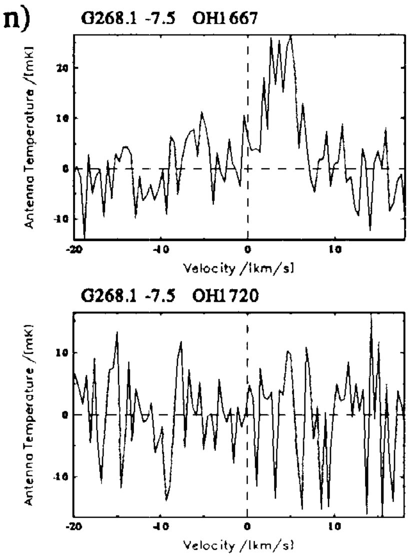
G268.1 -7.5 OH1667
G268.1 -7.5 OH1720
Antenna Temperature /[mK]
Velocity /[km/s]

o)

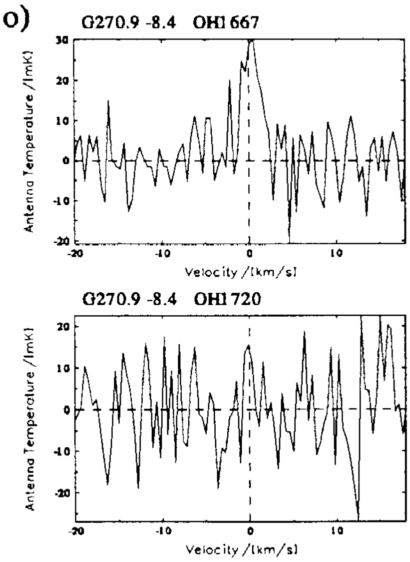
G270.9 -8.4 OH1667
G270.9 -8.4 OH1720
Antenna Temperature /[mK]
Velocity /[km/s]

p)

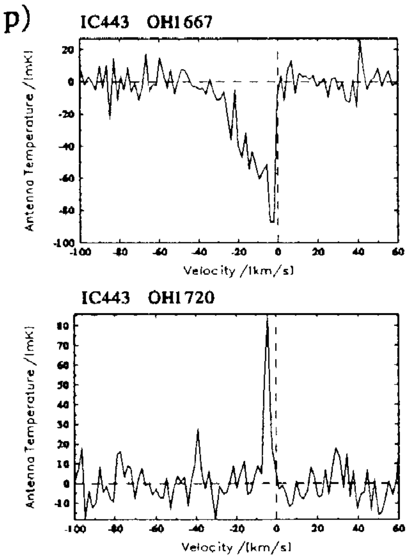
IC443 OH1667
IC443 OH1720
Antenna Temperature /[mK]
Velocity /[km/s]

9.4 Choice of observing positions for testing against an expansion model

The positions observed at 1667 MHz in the search for anomalous excitation gave a good detection rate. They resulted in a distribution of observed positions concentrated near the edge of the Gum Nebula at negative galactic latitudes where the 60 μm intensities are significantly higher than elsewhere in the nebula. However, any expansion of the Gum Nebula is expected to be perpendicular to the line of sight at these edge positions. Thus these cannot provide significant information on an expansion of the nebula.

If the outer layer of the Gum Nebula is a homogeneous, spherical, expanding shell of molecular material, observed positions along the line of sight through the centre of the nebula should show two lines, one due to material on the far side of the nebula receding from us, the other due to material on the near side approaching us. However, as the molecular material in the Gum Nebula has a patchy distribution, as deduced from the IRAS 60μm map and supported by the non-detection of CO at some positions in the Gum Nebula by de Vries et al. (1984), a lack of one, or both, of these lines at one position in the Gum nebula does not rule out an expansion of the nebula. It is the overall picture formed by observed line velocities at positions reasonably distributed across the face of the Gum Nebula that would allow one to come to a conclusion about the expansion of the nebula.

Complete sampling at all projected velocities, assuming a spherical, uniformly expanding shell geometry, was attempted in the following manner. The observed positions are chosen to lie along a line in the sky, perpendicular to our line of sight, through the approximate centre, G258 − 2 (Chanot & Sivan, 1983), of the nebula. This line was chosen to be on an axis through positions which had already been observed, at intervals giving almost complete sampling at 1667 MHz. Thus this line (see Fig. [9-4]) is at negative galactic latitudes where most of the detections had been made.

The Gum Nebula straddles the Galactic plane. Hence positions that lie within $\approx 4°$ of the plane should be excluded to avoid confusion problems. However, to test the hypotheses that the Gum Nebula is expanding at a rate of up to 20 km/s (Reynolds, 1976), or at 12 km/s (Sridharan, 1992), or 5 km/s (Zealey et al., 1983) or not at all (Wallerstein et al., 1980; Hippelein & Weinberger, 1975), one should make observations at positions close to the centre of the nebula. The line-of-sight component of the expansion velocity is largest on the centre position, assuming uniform spherical expansion of the nebula. As the centre of the nebula is somewhere within 5° of the plane and close to the Vela XYZ SNR and even closer to Puppis A, the restraints imposed by confusion problems in this area had to be ignored to some extent. It was hoped that at positions closer to the plane, where there is more molecular material with which the expanding nebula could interact, the observed spectra might show evidence of interaction. This evidence would then be a criterion for eliminating confusion problems, especially if such detections were made throughout the Gum Nebula along the plane, but not outside the nebula along the plane. If evidence for interaction were observed only at positions within the Vela XYZ SNR or Puppis A, then it is most likely these SNRs that are causing the interaction with the material.

The need to observe at positions towards the centre of the Gum Nebula made observations towards Puppis A (almost centre position according to Sridharan (1992)) and the Vela XYZ SNR unavoidable. As a result two essentially separate investigations were spawned by the Gum Nebula OH project. One of these, an investigation of OH towards Puppis A, gives a lower limit on the distance towards Puppis A (to be published). The other, an investigation of the molecular material towards the Vela XYZ SNR suffers from interpretative difficulties as a result of confusion with foreground and background molecular material near the galactic plane.

The few positions, observed at negative galactic latitudes, picked without a criterion such as a local 60 μm intensity maximum or the position of a dark cloud in one of the dark cloud atlases (Feitzinger & Stüwe, 1984; Hartley et al., 1986), resulted in non-detections. In order to obtain an overall picture of the expansion of the nebula, one should also sample the material at positive latitudes. This region is very faint at 60 μm and does not contain dark clouds. Thus it was very difficult to find observing positions with a fair chance of producing detections at positive galactic latitudes.

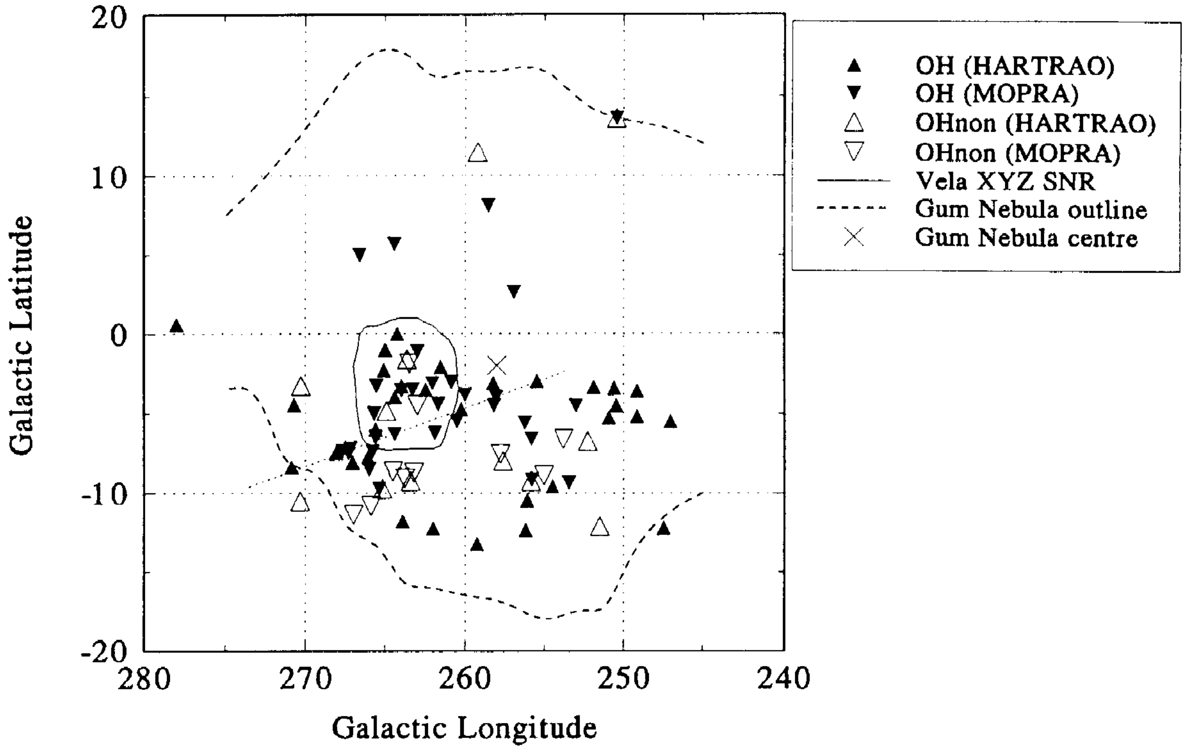

Figure [9-4]: A schematic map of the Gum nebula region, showing detections and non-detections of my OH observations. The approximate extent and position of the Gum Nebula and Vela XYZ SNR are indicated by the dashed line and solid line respectively. Some observations were made on the dotted line approximately passing through the centre of the nebula.

9.5 Observations

The observed OH 1667 MHz positions are shown in Fig. [9-4]. The observations were made at HartRAO and completed at Mopra. Frequency switching was used as the observation method.

Several different bandwidths were used for the spectra obtained at HartRAO. Some of them were also smoothed with the Hamming function for the determination of line parameters. The resultant velocity resolutions are indicated in table [9-1] at the end of this chapter together with the line parameters derived from fitted gaussian functions. A few of these observations were Hamming (HM) smoothed before line fitting, as indicated in the table.

All OH 1667 MHz Mopra observations were made with a resolution of 0.843 km/s. Those of the Mopra spectra that were smoothed with such a function are marked HM in the column headed HM? in table [9-2] at the end of this chapter. This table also lists the derived line parameters of the Mopra spectra.

The unsmoothed 1667 MHz spectra from HartRAO and Mopra are shown at the end of this chapter in Fig. [9-5] and Fig. [9-6] respectively. None of the spectra show broad absorption lines, characteristic of shocked OH lines in SNRs.

9.6 Discussion and Conclusion

No anomalous excitation unambiguously associated with the Gum Nebula was detected in the 1720 and 1667 MHz observations.

The 1667 MHz feature corresponding to the 1720 MHz inversion, which is characteristic of shocked gas, is a broad absorption line. No such 1667 MHz absorption lines are present in the observations made at HartRAO and Mopra. Thus there is no evidence for shocked OH in the Gum Nebula. As the inversion of the 1720 MHz line occurs only under special conditions, the non-detection of shocked gas does not in itself rule out an interaction of an SNR with its surrounding molecular material (Frail et al., 1996).

OH was detected in a large number of positions in the Gum Nebula. In general OH has a much lower abundance than that of neutral hydrogen. Thus the lack of a feature corresponding to the position, extent and likely distance from us of the

Gum Nebula in the surveys of the 21 cm neutral hydrogen line (Cleary, 1977; Kerr et al., 1986; Dubner et al., 1992) is puzzling.

It has been suggested that the reason the Gum Nebula does not feature in 21 cm neutral hydrogen surveys is the paucity of neutral hydrogen in this region of sky (Bohlin et al., 1978). There are two reasons why OH could nevertheless be detected, if this is true. The ground state OH lines involve electric dipole transitions as opposed to the magnetic dipole transition of the hydrogen 21 cm line and are thus more intense.

If the reported paucity of hydrogen in this region is not responsible for the lack of a Gum Nebula feature in the 21 cm surveys, another explanation may be the following. Hydrogen is the most abundant element in the universe. This large abundance is a problem as line emissions from warm gas in spatially unrelated regions blend in velocity (Dickey et al., 1981). Thus 21 cm line emission from the gas situated behind the Gum Nebula may be masking the cavity that one would expect to see in 21 cm surveys at the position of the Gum Nebula. Furthermore, the thermal line width of hydrogen from gas with a kinetic temperature of 50 to 200 K is 1.5 to 4 km/s, i.e. of the order of the internal velocity structure of such gas. By comparison the thermal line width of the heavier OH lines ranges from 0.5 to 1 km/s over the same kinetic temperature range. Thus if the expansion velocity of the nebula is very small, the thermal width of the 21 cm could be masking the expected Gum Nebula cavity. Nothing definite can be said about the latter argument, because of the existing contradictory evidence on the expansion velocity of the Gum Nebula.

As the OH 1667 MHz line velocities provide further data on the kinematics of the nebula, I used this, together with molecular line data from the literature for a determination of the global expansion velocity of the Gum Nebula. The work is presented in the next chapter.

Galactic coords	S/N	res./[km/s]	T_A/[mK]	v_{lsr}/[km/s]	Δv/[km/s]
$247.50 - 12.225$	10.5	0.55	64.5 ± 5.9	2.562 ± 0.087	1.7 ± 0.18
$247.07 - 5.50$	8.0	2.2	32.6 ± 4.1	21.08 ± 0.28	4.1 ± 0.70
$249.20 - 5.18$	22.1	1.1	33.4 ± 1.5	20.99 ± 0.17	7.7 ± 0.42
$249.20 - 3.60$	8.4	1.1	44.6 ± 5.7	17.88 ± 0.10	1.4 ± 0.28
	7.9	1.1	18.8 ± 3.0	20.39 ± 0.73	8.7 ± 1.3
$250.45 + 13.60$		1.1	≤ 20		
$250.50 - 4.50$	12.4	1.1	40.2 ± 3.2	18.75 ± 0.23	5.7 ± 0.53
$250.60 - 3.40$	19.8	1.1	49.6 ± 3.0	17.872 ± 0.099	3.9 ± 0.36
$250.95 - 5.25$	9.7	1.1	25.9 ± 2.8	18.21 ± 0.45	8.7 ± 1.2
$251.50 - 12.10$		2.2	≤ 20		
$251.90 - 3.35$	7.0	0.55	20.3 ± 3.2	0.314 ± 0.086	1.0 ± 0.26
	9.8	0.55	20.9 ± 2.1	8.01 ± 0.12	2.12 ± 0.23
	38.4	0.55	44.4 ± 1.2	15.44 ± 0.10	7.39 ± 0.25
$252.25 - 6.75$	4.8	1.1	≤ 16		
$254.50 - 9.60$	13.5	0.55	34.0 ± 2.6	-1.681 ± 0.086	2.27 ± 0.21
$255.50 - 3.00$	9.9	1.1	34.1 ± 3.5	9.19 ± 0.29	5.69 ± 0.71
$255.85 - 9.25$		1.1	≤ 20		
$256.10 - 10.50$	11.2	0.55	41.5 ± 4.0	-2.21 ± 0.11	2.42 ± 0.33
$256.20 - 12.375$	10.3	1.1 then HM	17.8 ± 1.8	-1.73 ± 0.15	3.12 ± 0.40
$257.60 - 8.00$		1.1	≤ 20		
$258.25 - 3.10$	24.8	1.1	59.1 ± 3.4	8.808 ± 0.097	3.77 ± 0.30
	16.5	1.1	23.8 ± 1.6	16.94 ± 0.62	10.6 ± 1.6
$259.20 + 11.50$		1.1	≤ 20		
$259.25 - 13.25$	7.4	0.27	69.5 ± 8.9	5.097 ± 0.070	0.94 ± 0.13
$260.25 - 4.75$	6.4	1.1	12.1 ± 2.0	3.72 ± 0.36	3.78 ± 0.85
	9.9	1.1	18.6 ± 2.0	11.55 ± 0.20	3.79 ± 0.62
$261.55 - 2.10$	11.9	1.1	19.5 ± 2.1	6.70 ± 0.84	15.0 ± 1.3
	5.5	1.1	26.7 ± 4.9	8.39 ± 0.18	1.30 ± 0.24
	7.5	1.1	31.6 ± 3.8	12.64 ± 0.16	2.02 ± 0.40
$262.00 - 12.25$	9.7	1.1 then HM	22.2 ± 2.2	5.17 ± 0.12	2.30 ± 0.24
$262.50 - 3.50$	11.6	1.1	31.2 ± 3.5	4.96 ± 0.13	2.52 ± 0.31
	8.4	1.1	23.3 ± 2.9	14.93 ± 0.16	2.33 ± 0.36
	13.7	1.1	18.5 ± 2.6	6.59 ± 0.53	10.76 ± 1.24
$263.40 - 9.25$		1.1	≤ 25		
$263.65 - 1.60$		1.1	≤ 15		
$263.90 - 11.80$	5.4	1.1	33 ± 19	3.70 ± 0.076	0.00 ± 0.45
$264.00 - 3.30$	10.8	0.81	7.1 ± 1.1	0.31 ± 1.4	12.2 ± 1.8
	27.9	0.81	32.7 ± 2.2	5.213 ± 0.078	3.82 ± 0.26
	17.1	0.81	15.4 ± 0.87	14.76 ± 0.23	6.52 ± 0.46
$264.25 + 0.00$	9.8	2.2	31.9 ± 3.2	6.75 ± 0.47	9.1 ± 1.1
$264.40 - 4.00$	9.4	2.2	29.8 ± 3.3	3.92 ± 0.16	1.86 ± 0.38
$264.90 - 4.85$		2.2	≤ 10		
$265.10 - 2.30$	7.6	2.2	28.4 ± 3.8	4.83 ± 0.27	3.21 ± 0.59
$265.15 - 9.75$		1.1	≤ 10		
$265.60 - 6.00$	10.3	1.1	20.5 ± 2.0	5.04 ± 0.24	4.65 ± 0.58
$266.10 - 7.75$	11.2	1.1	116 ± 19	3.494 ± 0.063	0.90 ± 0.37
$267.05 - 8.10$	11.2	1.1 then HM	17.3 ± 1.5	1.71 ± 0.17	3.76 ± 0.40
$268.10 - 7.50$	11.8	0.55	23.6 ± 2.0	3.91 ± 0.17	3.94 ± 0.41
$270.30 - 3.25$		1.1	≤ 16		
$270.35 - 10.50$		1.1	≤ 20		
$270.75 - 4.45$	11.5	1.1	22.6 ± 3.0	2.15 ± 0.54	7.9 ± 1.1
$270.90 - 8.40$	9.7	0.55	29.4 ± 3.1	0.26 ± 0.12	2.40 ± 0.32
$278.00 + 0.60$	7.3	2.2	31.8 ± 4.2	-1.89 ± 0.42	5.65 ± 0.85

Table [9-1]: The line parameters of the OH 1667 MHz line observations made at HartRAO. Note that the S/N for position G263.90 − 11.80 is low because the line is not resolved.

Galactic coords	S/N	HM?	T_A/[mK]	v_{lsr}/[km/s]	Δv/[km/s]
250.45 + 13.60	9.7	HM	10.3±1.5	-0.34±0.19	3.61±0.93
253.00 − 4.50	12.1		26.6±2.1	16.24±0.17	4.02±0.36
	12.0		38.4±3.3	11.419±0.084	1.73±0.22
253.42 − 9.38	9.5		37±14	-1.171±0.058	0.00±0.23
253.78 − 6.60			≤17		
255.06 − 8.91			≤10		
255.79 − 9.18	9.7		17.2±1.9	-4.51±0.11	1.98±0.28
255.83 − 6.59	9.5		18.2±2.0	10.89±0.23	4.37±0.59
256.26 − 5.60	14.2		45.9±3.1	9.594±0.075	2.05±0.17
256.95 + 2.65	9.9	HM	7.05±0.91	8.97±0.55	7.9±1.7
257.75 − 7.55			≤8		
258.07 − 4.00	17.0		21.5±1.8	10.17±0.20	6.01±0.55
	18.1		11.0±1.4	11.52±0.73	26.6±3.4
258.20 − 4.50	11.6	HM	17.4±2.1	8.14±0.16	3.00±0.51
	17.2	HM	13.5±1.1	13.02±0.61	11.2±1.1
258.54 + 8.13	10.5		24.6±2.3	2.055±0.15	2.84±0.33
260.02 − 3.82	9.0		10.9±1.2	11.53±0.55	10.0±1.0
260.53 − 5.50	15.0		28.5±2.0	12.63±0.11	3.09±0.29
260.88 − 3.03	23.0		32.6±1.4	13.60±0.14	6.58±0.33
261.70 − 4.40	19.2		27.4±1.5	10.29±0.15	5.87±0.42
261.90 − 6.25	12.4	HM	8.01±0.63	10.27±0.42	10.47±0.84
262.07 − 3.10	12.1		25.8±2.8	6.46±0.22	4.79±0.94
	10.4		27.3±3.0	13.72±0.20	3.10±0.63
263.00 − 4.50			≤10		
263.00 − 1.10	12.6		25.9±2.0	8.94±0.44	11.38±0.99
263.20 − 8.73			≤14		
263.30 − 3.50	17.4		27.6±1.7	4.51±0.15	5.06±0.43
263.50 − 1.90			≤8		
263.75 − 9.10			≤12		
264.00 − 3.55	11.9		30.5±2.5	4.70±0.16	3.65±0.38
264.40 − 6.30	16.0		15.5±1.0	6.32±0.18	5.78±0.47
264.42 + 5.71	22.0	HM	32.5±1.5	10.094±0.078	2.86±0.19
	10.3	HM	14.4±1.4	5.39±0.18	3.24±0.46
264.50 − 8.65			≤12		
265.38 − 9.75	8.0		13.9±2.1	-6.67±0.31	4.3±1.1
265.56 − 3.24	25.2	HM	30.2±1.2	2.406±0.065	3.10±0.15
	7.4	HM	11.6±1.5	7.31±0.14	1.66±0.28
265.60 − 6.50	9.4		10.0±1.0	5.55±0.55	10.6±1.2
265.70 − 5.00	8.5		10.5±1.3	1.33±0.37	6.3±1.1
265.80 − 7.40	29.8		84.3±3.2	3.409±0.033	1.70±0.10
265.90 − 10.85			≤14		
266.00 − 8.50	8.0		16.7±2.0	3.72±0.12	1.70±0.22
266.63 + 4.98	26.0		89.9±4.4	2.673±0.026	0.932±0.068
	20.4		34.3±3.2	1.91±0.15	5.23±0.36
267.00 − 11.40			≤12		
267.20 − 7.20	11.3	HM	16.2±1.4	3.86±0.23	4.69±0.46
267.33 − 7.53	8.7	HM	13.7±1.9	3.98±0.20	3.51±0.76
	7.2		23.0±3.1	1.50±0.25	3.26±0.57
	11.5		52.1±4.6	5.283±0.077	1.42±0.20

Table [9-2]: The line parameters of the OH 1667 MHz line observations made at Mopra.

Figure [9-5]: The unsmoothed 1667 MHz OH spectra obtained at HartRAO.

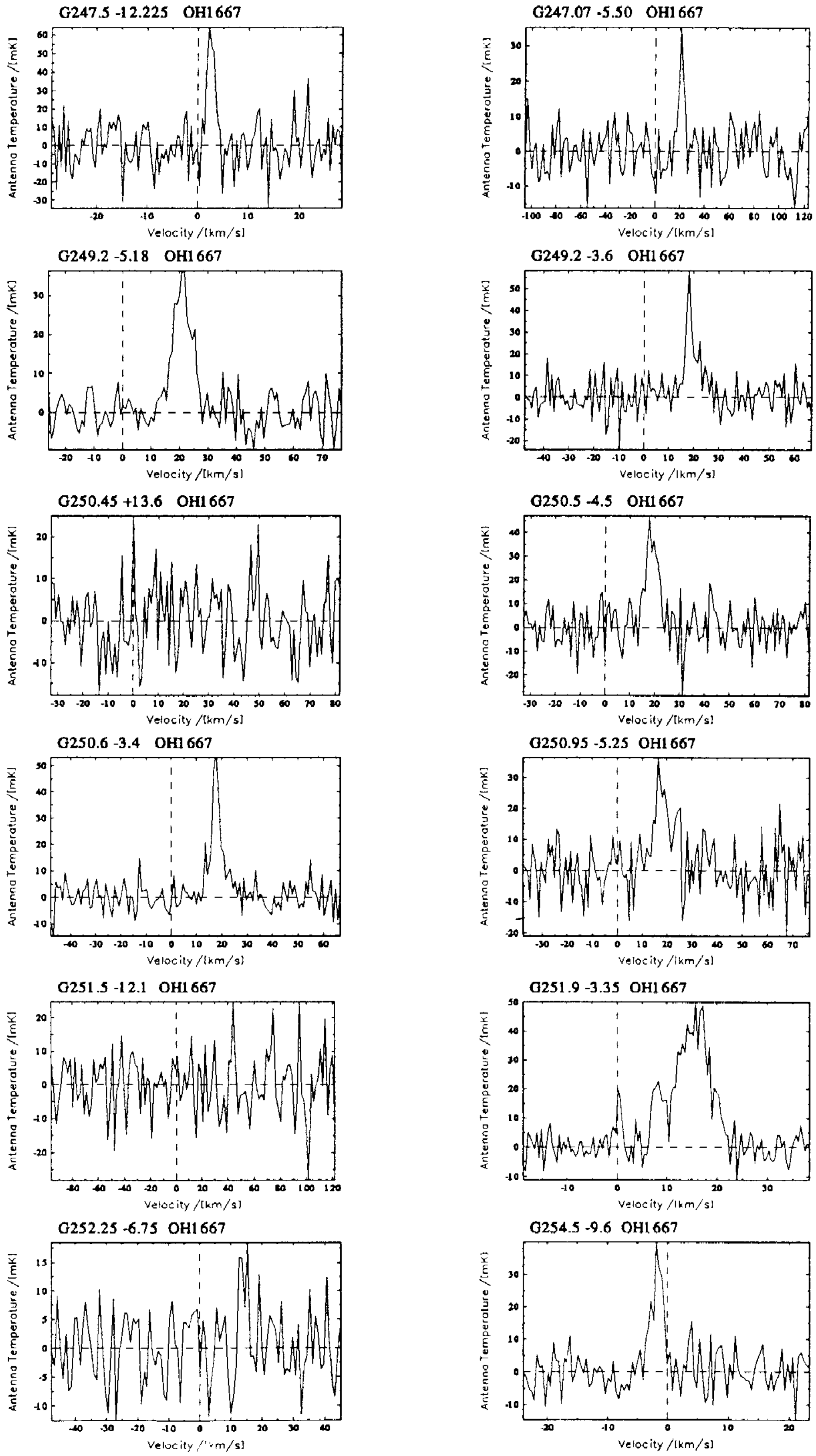

G255.5 -3.0 OH1667

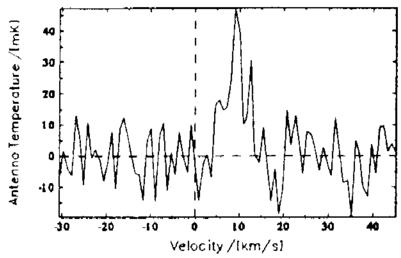

G255.85 -9.25 OH1667

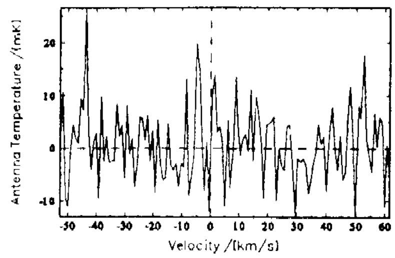

G256.1 -10.5 OH1667

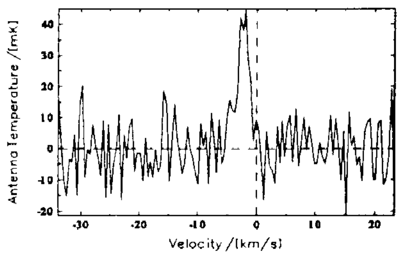

G256.2 -12.375 OH1667

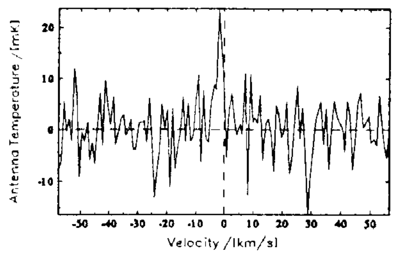

G257.6 -8.0 OH1667

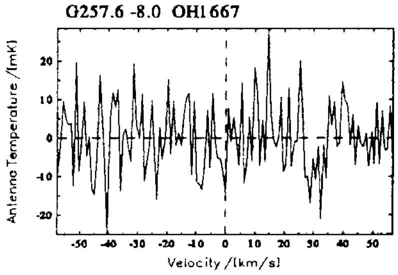

G258.25 -3.10 OH1667

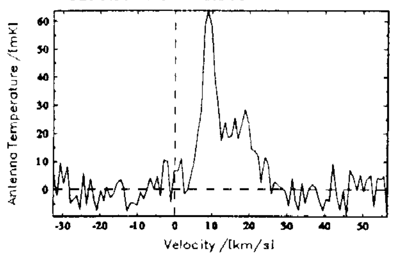

G259.2 +11.5 OH1667

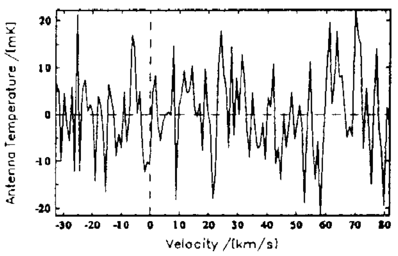

G259.25 -13.25 OH1667

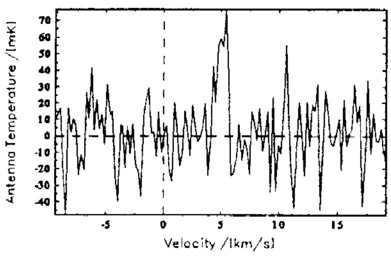

G260.25 -4.75 OH1667

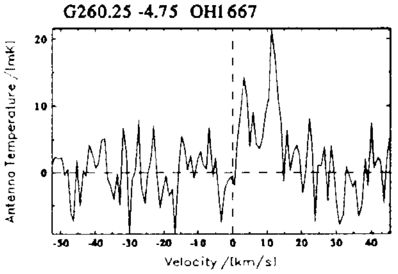

G261.55 -2.1 OH1667

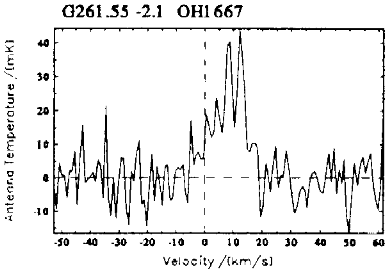

G262.0 -12.25 OH1667

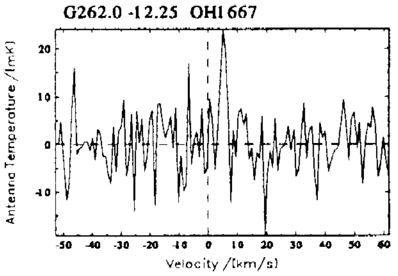

G262.5 -3.5 OH1667

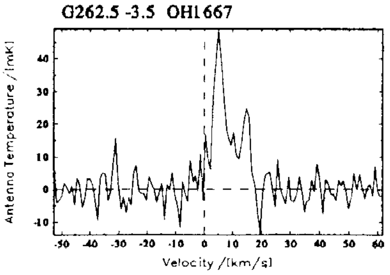

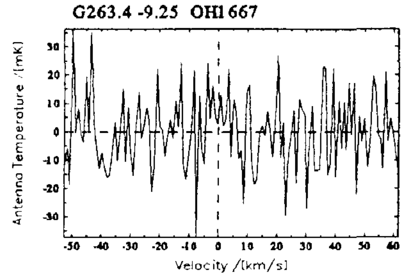
G263.4 -9.25 OH1667
Antenna Temperature /[mK]
Velocity /[km/s]

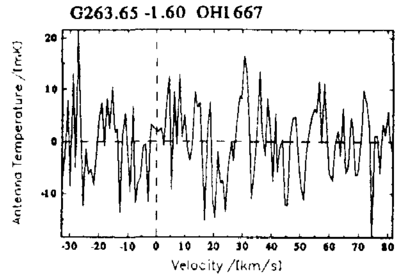
G263.65 -1.60 OH1667
Antenna Temperature /[mK]
Velocity /[km/s]

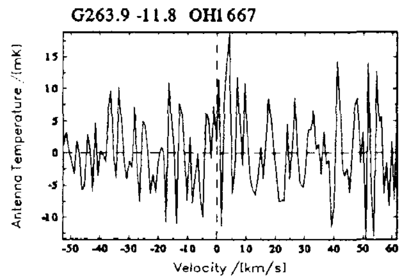
G263.9 -11.8 OH1667
Antenna Temperature /[mK]
Velocity /[km/s]

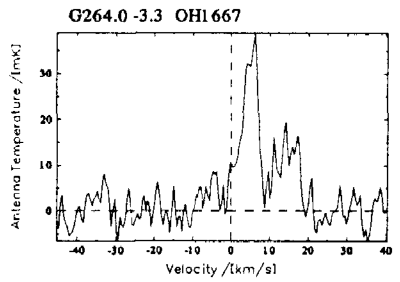
G264.0 -3.3 OH1667
Antenna Temperature /[mK]
Velocity /[km/s]

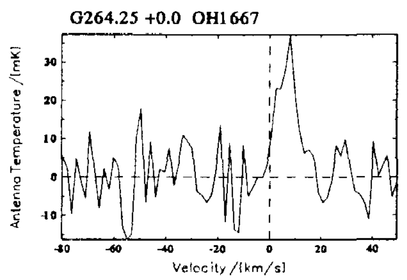
G264.25 +0.0 OH1667
Antenna Temperature /[mK]
Velocity /[km/s]

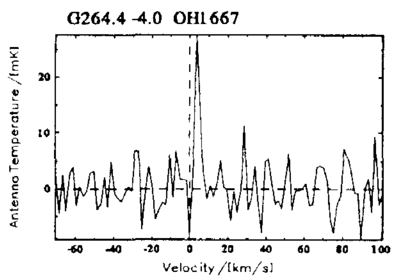
G264.4 -4.0 OH1667
Antenna Temperature /[mK]
Velocity /[km/s]

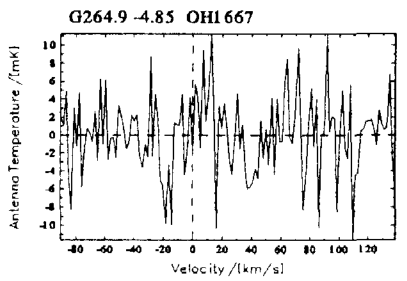
G264.9 -4.85 OH1667
Antenna Temperature /[mK]
Velocity /[km/s]

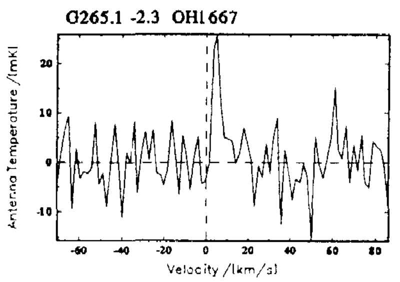
G265.1 -2.3 OH1667
Antenna Temperature /[mK]
Velocity /[km/s]

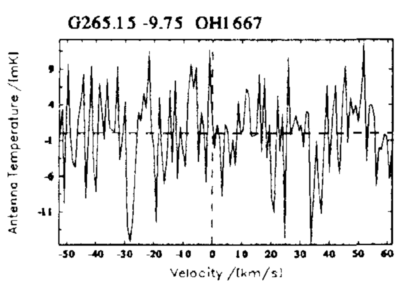
G265.15 -9.75 OH1667
Antenna Temperature /[mK]
Velocity /[km/s]

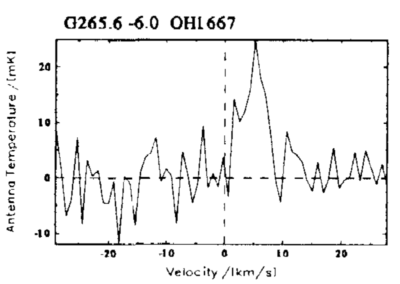
G265.6 -6.0 OH1667
Antenna Temperature /[mK]
Velocity /[km/s]

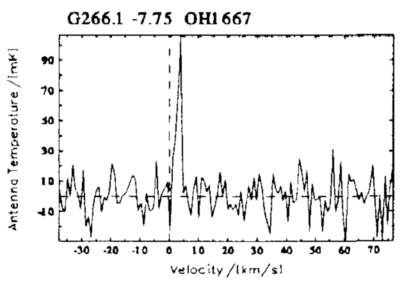
G266.1 -7.75 OH1667
Antenna Temperature /[mK]
Velocity /[km/s]

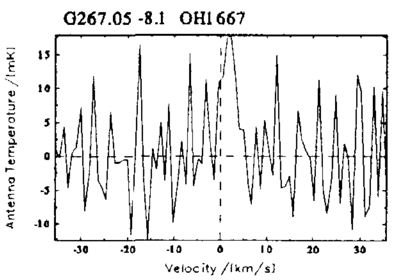
G267.05 -8.1 OH1667
Antenna Temperature /[mK]
Velocity /[km/s]

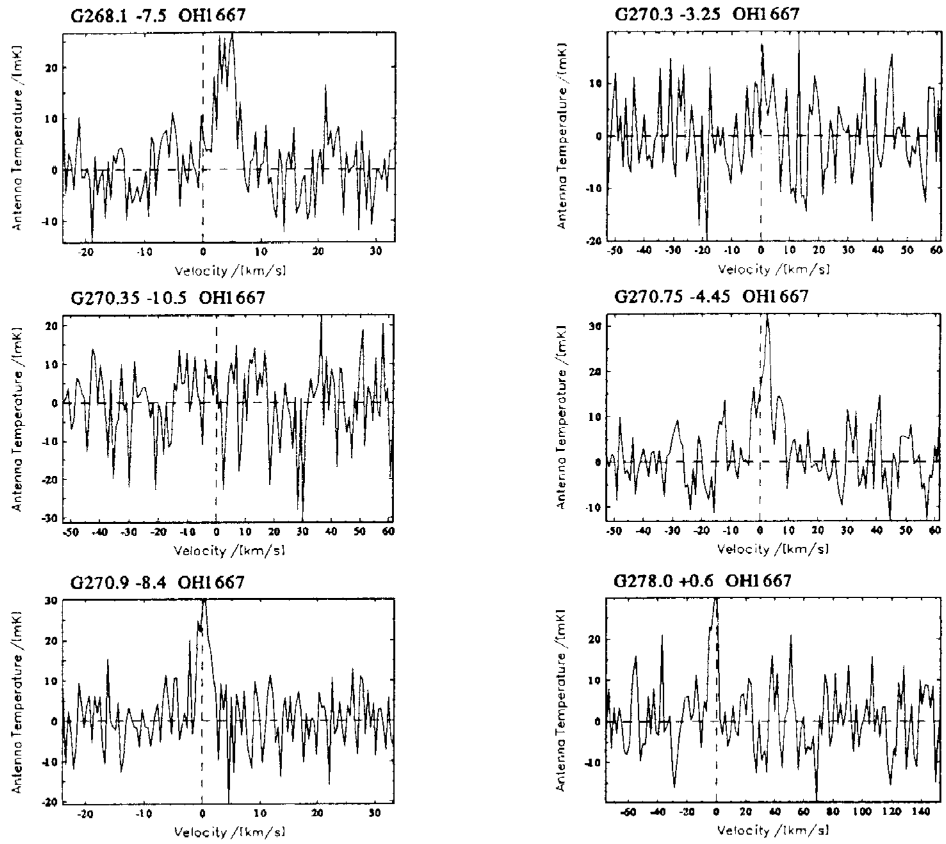
G268.1 -7.5 OH1667
G270.3 -3.25 OH1667
G270.35 -10.5 OH1667
G270.75 -4.45 OH1667
G270.9 -8.4 OH1667
G278.0 +0.6 OH1667
Antenna Temperature /[mK]
Velocity /[km/s]

Figure [9-6]: The unsmoothed 1667 MHz OH spectra obtained at Mopra.

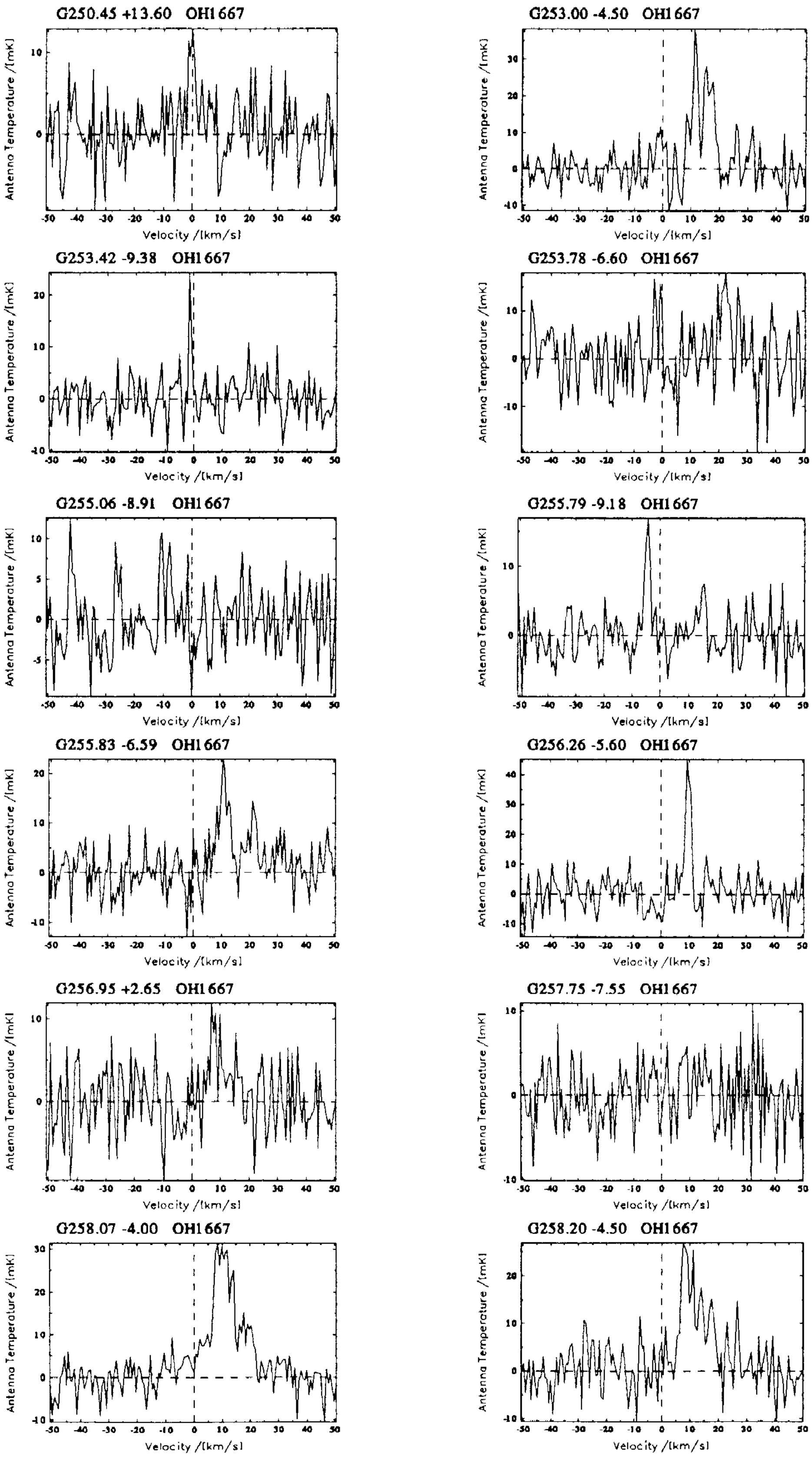

G258.54 +8.13 OH1667

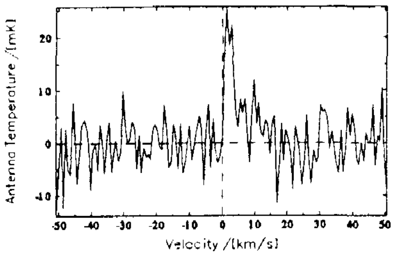

G260.02 -3.82 OH1667

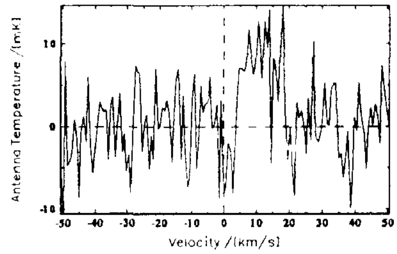

G260.53 -5.50 OH1667

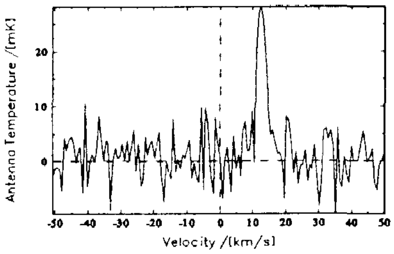

G260.88 -3.03 OH1667

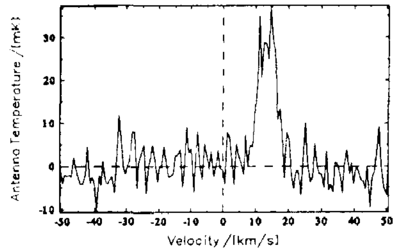

G261.70 -4.40 OH1667

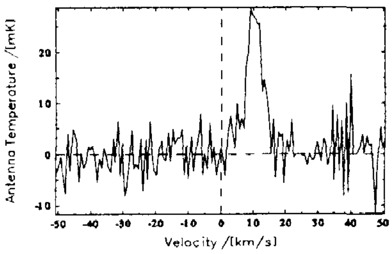

G261.90 -6.25 OH1667

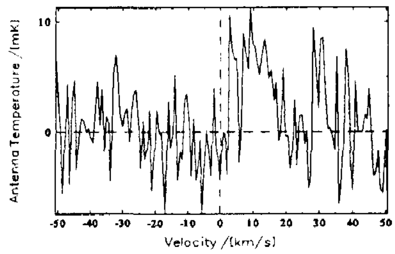

G262.07 -3.10 OH1667

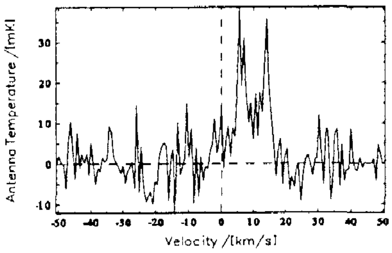

G263.00 -4.50 OH1667

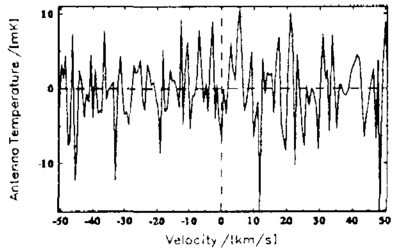

G263.00 -1.10 OH1667

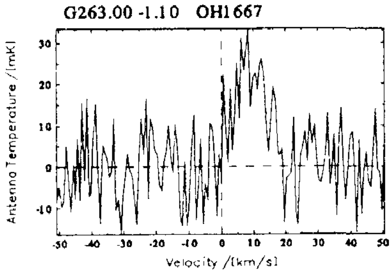

G263.20 -8.73 OH1667

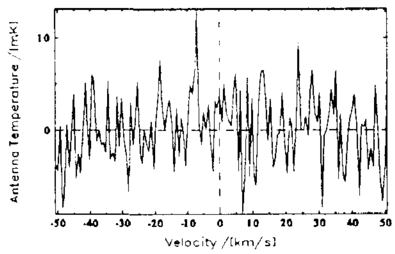

G263.30 -3.50 OH1667

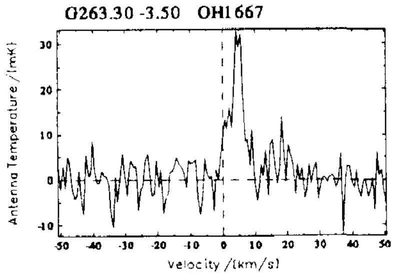

G263.50 -1.90 OH1667

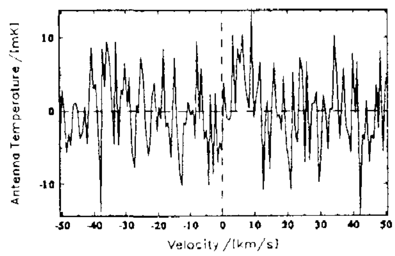

G263.75 -9.10 OH1667

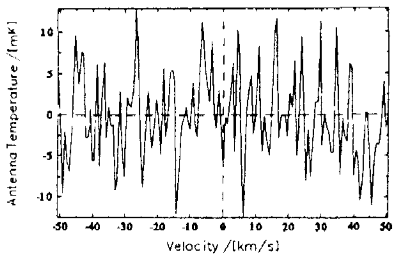

G264.00 -3.55 OH1667

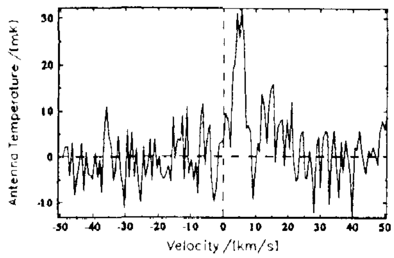

G264.40 -6.30 OH1667

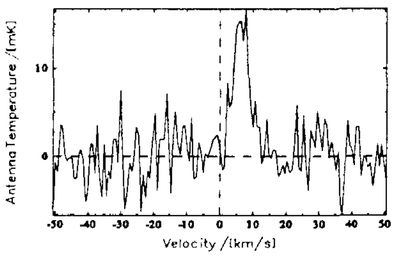

G264.42 +5.71 OH1667

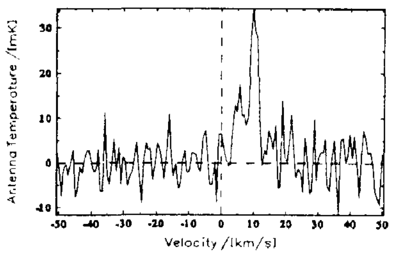

G264.50 -8.65 OH1667

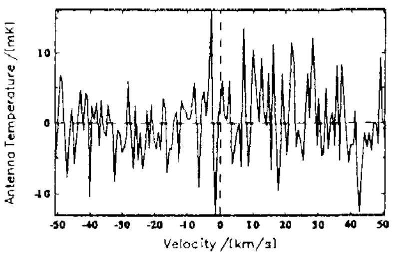

G265.38 -9.75 OH1667

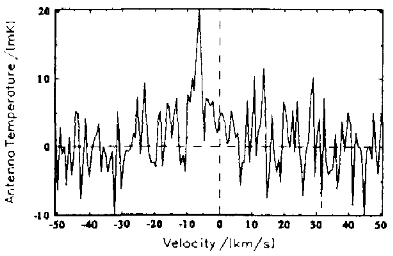

G265.56 -3.24 OH1667

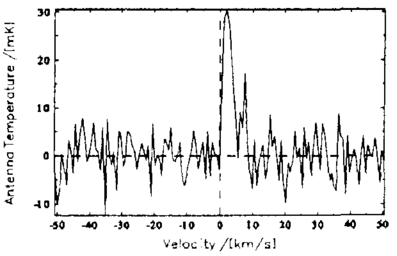

G265.60 -6.50 OH1667

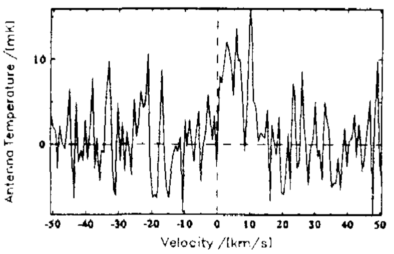

G265.70 -5.00 OH1667

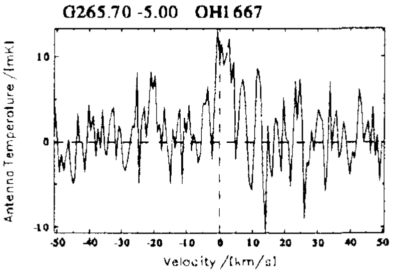

G265.80 -7.40 OH1667

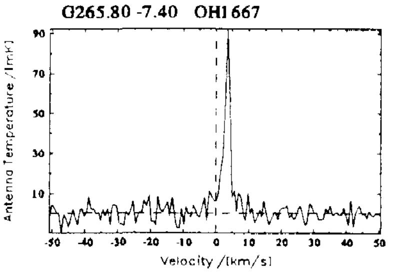

G265.90 -10.85 OH1667

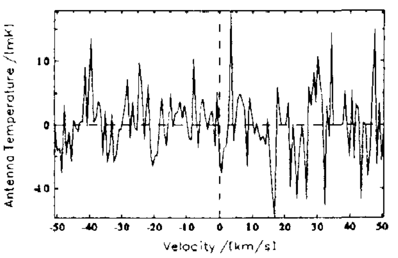

G266.00 -8.50 OH1667

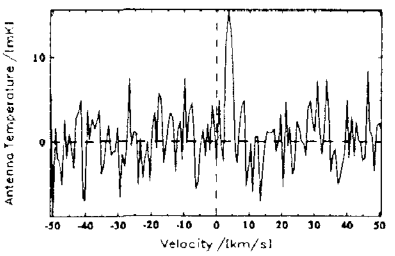

G266.63 +4.98 OH1667

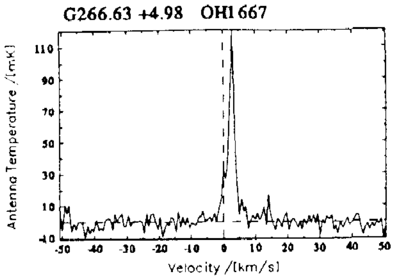

G267.00 -11.40 OH1667

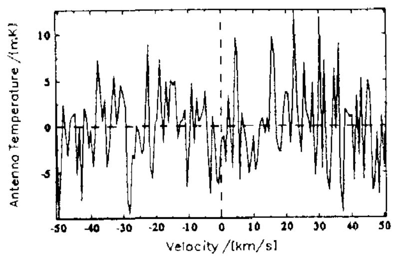

G267.2 -7.20 OH1667

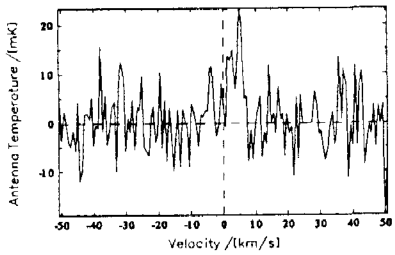

G267.33 -7.53 OH1667

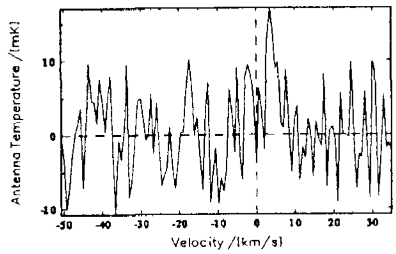

G267.70 -7.35 OH1667

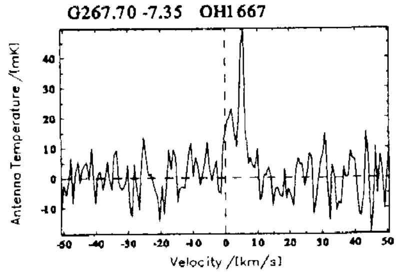

Chapter 10

Expansion model of the Gum Nebula

The 1667 MHz line velocities at positions unambiguously identified with the Gum Nebula were used, together with those reported in the literature, to determine whether an expansion of this molecular material from a common centre is present. The expansion model is discussed prior to presenting the results of this kinematic investigation.

10.1 The kinematics of a homogeneous, spherical, expanding shell

Suppose that a spherically symmetric shell of material is expanding radially from its centre and that a spectral line is detected from the shell material. As seen by us, this line is doppler shifted from its rest frequency by an amount corresponding to the component of the expansion velocity of the shell along our line of sight to the observed position. From the viewing geometry depicted in Fig. [10-1], the line of sight component of the expansion velocity, v_{rad}, is given by :

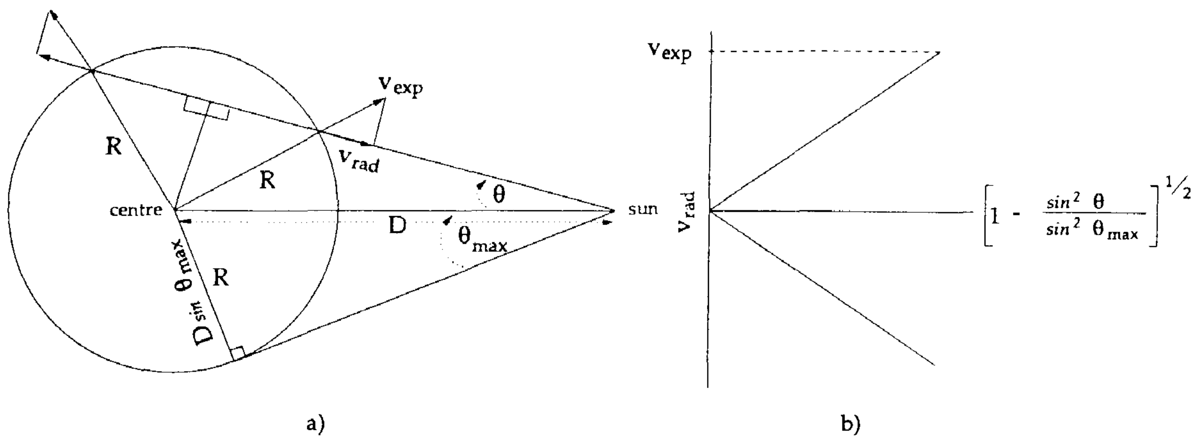

Figure [10-1]: Schematic diagram of the viewing geometry for a spherical, uniformly expanding shell with centre a heliocentric distance D from us and radius $D \sin \theta_{max}$, where θ_{max} is the angular radius of the shell. v_{rad} is the observed radial component of the expansion velocity, v_{exp}, at a position an angular distance θ from the centre of the shell. b) The graph of the radial velocity, v_{rad}, plotted against $(1-\sin^2\theta/\sin^2\theta_{max})^{\frac{1}{2}}$.

$$v_{rad} = \pm v_{exp}(1 - \sin^2\theta/\sin^2\theta_{max})^{\frac{1}{2}} \tag{10-1}$$

where v_{exp} is the expansion velocity of the shell, θ is the angular distance of a position relative to the line of sight to the centre of the shell, and θ_{max} is the angular distance to the position on the shell farthest from the centre as seen by us. As the Gum Nebula has a large angular radius, the angular distance θ was calculated using the great circle distance between two points on a sphere. A plot of v_{rad} versus $(1 - \sin^2\theta/\sin^2\theta_{max})^{\frac{1}{2}}$ should then result in the bimodal distribution shown in Fig. [10-1] b).

If we set $y = \sin\theta$ and $a = \sin\theta_{max}$, equation (10-1) becomes, after some manipulation,

$$y^2 = a^2(1 - v_{rad}^2/v_{exp}^2). \tag{10-2}$$

Since θ does not exceed 90°, even for a nebula as large as the Gum Nebula, y is always positive. Thus

$$y = a(1 - v_{rad}^2/v_{exp}^2)^{\frac{1}{2}}. \tag{10-3}$$

Fig. [10-2] is an idealised plot of y, i.e $\sin\theta$, versus the radial velocity, v_{rad}, obtained from the doppler shift of the observed spectral lines.

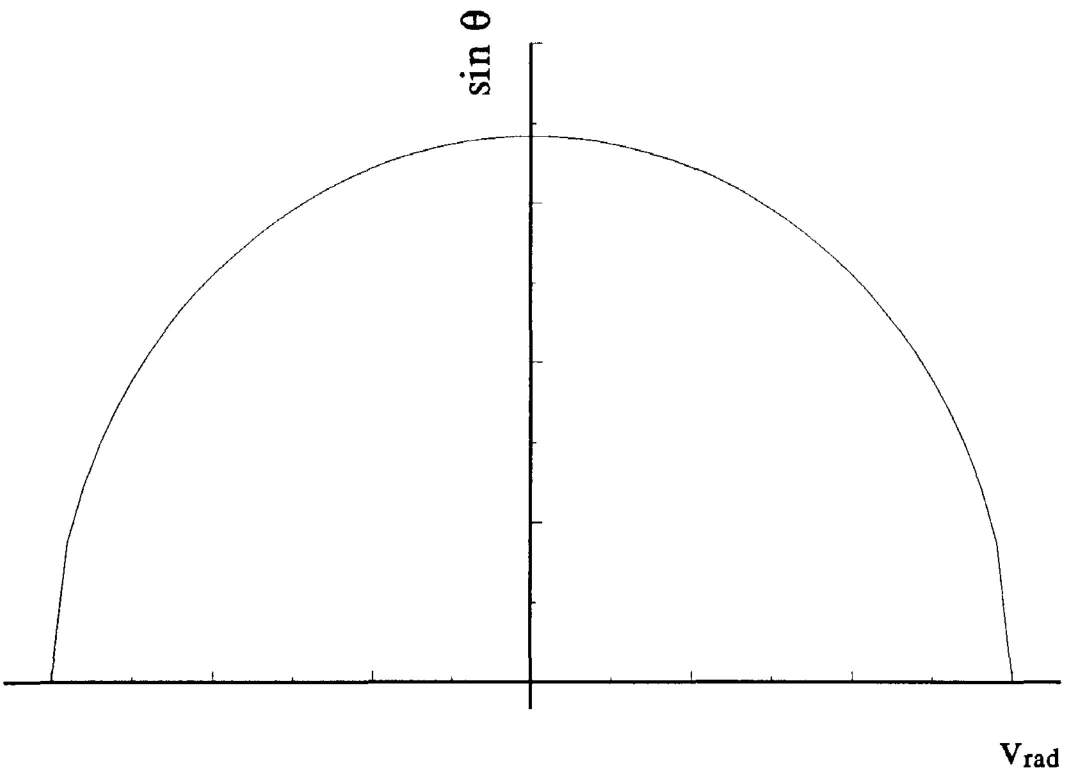

Figure [10-2]: An idealised plot of $\sin\theta$ (the sine of the angle that the observed position makes with the line of sight towards the centre of the shell, see the previous figure) versus the line of sight velocity, v_{rad}, obtained from the doppler shift of the observed spectral lines.

In general the material at different positions on the shell, especially if clumpy rather than homogeneous, will have some peculiar velocity relative to the overall expansion velocity. In addition to this, the observed radial velocities will also contain a contribution due to the galactic rotation, v_{gal}, at the position of the observed nebula. If the nebula is small enough for this contribution to be essentially constant throughout the nebula, the appropriate value of v_{gal} is determined from the heliocentric distance to the nebula, the galactic coordinates of its centre and a galactic rotation model. The residual velocities, $v_{res,i}$, for each observed position i are then obtained by subtracting v_{gal} from each observed radial velocity of the nebula, $v_{rad,i}$. The residual velocities, $v_{res,i}$, and their corresponding angular positions, θ_i, are then used for analysing the data for evidence of expansion.

However, in the case of the Gum Nebula, which spans almost 40° in longitude, one cannot assume that the contribution from galactic rotation to the radial velocity is essentially constant throughout the nebula. Thus, at each observed position, i, one has to determine the contribution of the galactic rotation, $v_{gal,i}$ to the radial velocity, $v_{rad,i}$, subtract the former from the latter, and use the resultant residual velocities, $v_{res,i}$ for an investigation of the kinematics of the nebula alone. The manner in which the galactic rotation contribution is determined is dealt with in subsection 10.1.1.

Once the residual velocities have been determined, applying a chi-squared fit (Bevington, 1969) of the data points ($v_{res,i}$, $\sin\theta_i$) i.e. ($v_{res,i}$, y_i), to equation (10-3) should yield the expansion velocity of the nebula, provided the centre and angular radius of the nebula are known. If the latter two are not known, these may also be determined from a reduced chi-squared fit by searching parameter space.

The paucity of line velocity data at positive galactic latitudes in the Gum Nebula gave rise to a shape in parameter space not suited to an automated search for the minimum χ^2. Thus repeated applications of the reduced chi- squared test for different values of the expansion velocity, the centre position and angular radius were made. Contour maps of parameter space were used to obtain uncertainties in the fitted parameters.

The least-squares fit of the expansion model to the data was obtained as follows. For each datum the distance d_i was obtained by drawing the straight line passing through the two points $(0,0)$ and $(y_i, v_{res,i})$, as shown in the Fig. [10-3]. Clearly the slope, m_i, of this straight line is given by $y_i/v_{res,i}$. Since the straight line passes through the origin, a point (y, v) on this straight line is given by

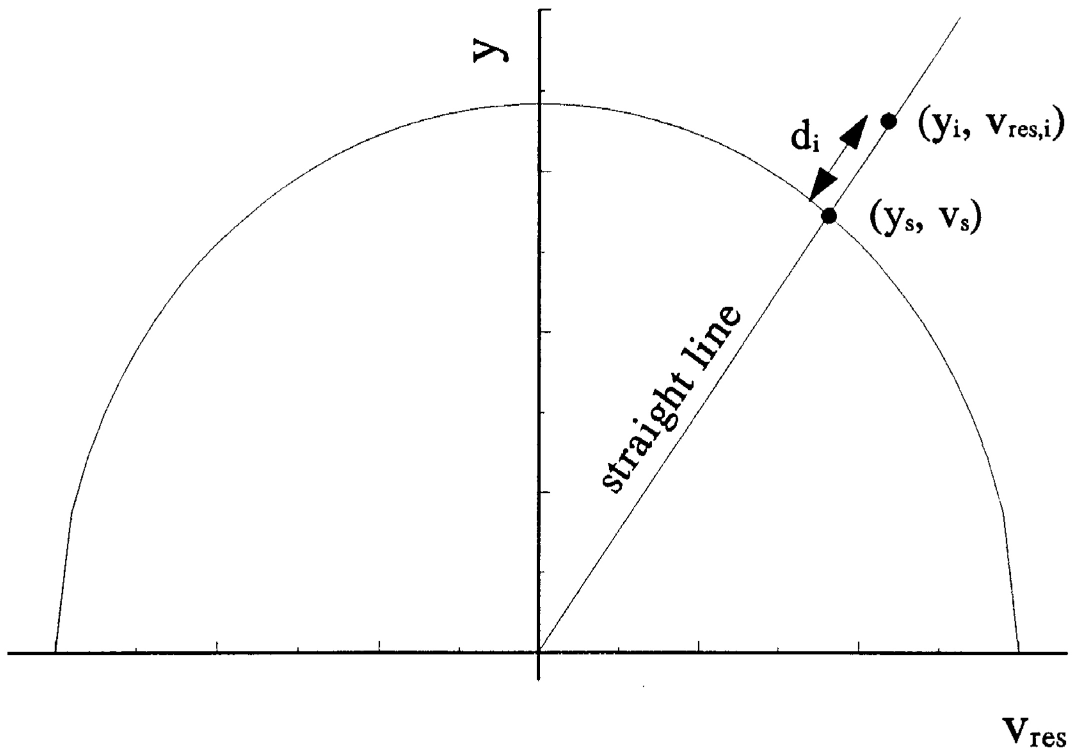

Figure [10-3]: Schematic diagram showing the criterion used for applying the Chi-squared test to the expansion model.

$$y = m_i v = \frac{y_i}{v_{res,i}} v \tag{10-4}$$

Substituting equation (10-4) for y in equation (10-3) gives for the v value of the intersection point (y_s, v_s) of the straight line and the function given by equation (10-3)

$$v_s = \pm \left[(a^2 v_{exp}^2)/(a^2 + v_{exp}^2 \frac{y_i}{v_{res,i}}) \right]^{\frac{1}{2}} \tag{10-5}$$

where v_s has the same sign as $\frac{y_i}{v_{res,i}}$. y_s of the intersection point is then determined from equation (10-4) by substituting v_s for v.

The reduced χ_ν^2 that one wants to minimize in determining the best fit of equation (10-3) to the N data points $(y_i, v_{res,i})$ with their associated standard deviations σ_i is then

$$\chi_\nu^2 = \chi^2/\nu \tag{10-6}$$

where

$$\chi^2 = \Sigma_{i=1}^{N}[(y_i - y_{s,i})^2 + (v_{res,i} - v_{s,i})^2]/\sigma_i^2 \tag{10-7}$$

and

ν is the number of degrees of freedom given by the number of data points N minus the number of parameters of the distribution determined from those data points.

The expansion velocity, centre of the nebula and angular radius are given by the values that give rise to the minimum. Confidence limits for each of these taken separately may be obtained by use of constant χ^2 boundaries. A 1-σ confidence level is given by projecting onto the axis of the parameter of interest the region in parameter space that encloses all χ^2 that differ from the minimum χ^2 by a $\Delta\chi^2 = 1$. A 2-σ confidence level is given by the projection onto the parameter of interest's axis of the region in parameter space that encloses all χ^2 that differ from the minimum χ^2 by a $\Delta\chi^2 = 4$. (Press et al., 1992)

The chosen centre of the expansion effectively defines the values of θ and thus the angular radius. Thus one can also deduce the centre by running the model through all possible values of expansion velocity and angular radius for different centre positions. As the centre position is defined by two numbers such a procedure would then increase the number of parameters determined from the data points to four.

The expansion test run in this manner without adjusting the velocities for a galactic rotation contribution, a first order approach, will in future be referred to as the model 1 expansion test. Two other versions, model 2 and model 3, include an adjustment to the velocities for the galactic rotation according to an assumed distance. The manner in which this distance is determined is described below.

10.1.1 Galactic rotation contribution to line of sight velocity

The approach for model 2 is to assume that all molecular clouds are at the distance to the centre of the shell, irrespective of their location on the shell. The radial velocity contribution due to galactic rotation may then be determined for each observed position from its galactic coordinates and the assumed distance using one of the galactic rotation models.

Another approach is to assume that all observed molecular clouds for which the angular distance from the centre of the shell, θ, is less than the angular radius, θ_{max}, of the shell, are situated on the front or back face of an infinitely thin shell. The distance, s, to the assumed position on the shell, whose centre has heliocentric distance D, is then derived from simple geometric arguments illustrated in Fig. [10-4] as

$$s = D\cos\theta \pm \sqrt{D^2(\sin^2\theta_{max} - \sin^2\theta)} \qquad (10\text{-}8)$$

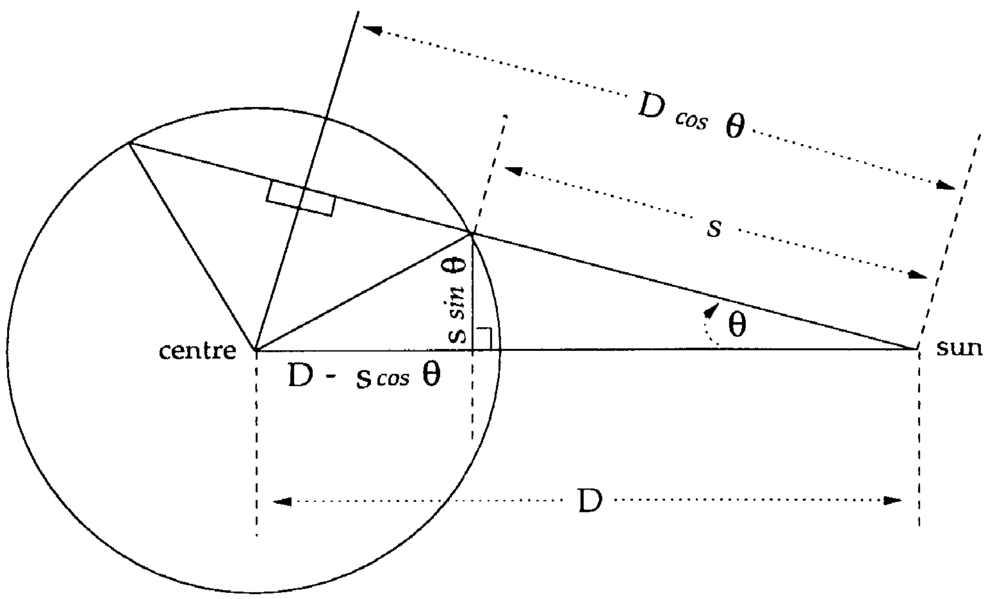

Figure [10-4]: Schematic diagram illustrating how the heliocentric distance s to a point on a spherical shell is determined.

The observed cloud is positioned on the front face of the shell (i.e. the minus sign in the above formula is used) if the radial velocity due to galactic rotation at that position at a heliocentric distance $D\cos\theta$ is larger than the observed velocity and vice versa. The radial galactic rotation contribution to the observed radial velocity is then determined using the appropriate distance s given by equation (10-8).

For positions that have θ greater than θ_{max}, which is a fairly frequent occurrence as θ_{max} is the mean angular radius, a distance to the cloud of $D\cos\theta$ is assumed. This is model 3.

For the case of the Gum Nebula, which lies in the outer part of the Galaxy, a galactic rotation curve model based on data obtained in that region of the Galaxy is most appropriate. Thus the model of Wouterloot & Brand (1989) was chosen for this work.

10.2 Data selection for testing against expansion model

A first attempt at fitting the expansion models was made with only the 1667 MHz OH data obtained at HartRAO and Mopra. To minimise the inclusion of data actually associated with other objects along the line of sight, all data points at positions within 4° of the galactic plane were excluded. Parameter space was searched for the centre position that gave the minimim reduced χ^2 for some value of distance, angular radius and expansion velocity. No minimum was found.

Sridharan's CO data on the cometary globule positions were then added, as these objects are definitely associated with the Gum Nebula, even when at positions within 4° of the plane. Now a search of parameter space gave a minimum χ^2_ν at a position near the centre determined from Hα photographs of the nebula. Further investigation showed that data near the centre position is crucial to obtain a plausible fit. Thus the search, during the observations of the 1667 MHz OH line, for data near the Hα geometric centre of the Gum Nebula, with a signature that unambiguously associates it with the nebula, was important even though it yielded no positive results.

As the inclusion of Sridharan's data was necessary for the expansion model to yield plausible results for the centre position, I decided to include all available molecular data in the literature. As is evident from the Figs. [9-1] and [9-4], there is some overlap in observing positions. Such identical observing positions would result in dependent data, as would adjacent observing positions effectively unresolved in terms of their observing HPBWs. I thus tried to make sure that the data set used for the expansion model contained only independent data.

Both the HartRAO and Mopra data have a resolution of $\approx 0.5°$. That of the molecular observations in the literature is $5'$ (De Vries et al. (1984) CO), $5'$ (Goss et al. (1980) HCHO), $4.4'$ (Zealey et al. (1983) HCHO) and $1'$ (Sridharan (1992) CO).

The final data set for testing against the expansion models 1, 2 and 3 was thus selected in the following order:

- All of Sridharan's CO cometary globule data was included, because of having the most definite association with the Gum Nebula, as well as having the highest resolution.

- All other observed positions that coincided with the Sridharan CG positions or contained those positions within their beams were deleted with a few exceptions. This meant that all but one of the observations of Zealey et al. were excluded.

  The exceptions were positions at which the non-Sridharan data has velocities very different to that reported by Sridharan, a plausible scenario if the emission is from opposite sides of the expanding shell, even if this disparity is difficult to explain.

The exceptions were:

- on CG16 at G262.857 −15.479 Sridharan reports a velocity of −0.7 km/s while De Vries et al. report +3.30 km/s also in CO.
- on CG17 at G270.588 −4.686 Sridharan reports a velocity of +3.7 km/s while Zealey et al. report −6.7 km/s in HCHO.
- on CG22 at G260.022 −3.825 Sridharan reports a velocity of −12.5 km/s while I obtained +11.53 km/s in OH at Mopra.
- on CG36 at G256.947 +2.649 Sridharan reports a velocity of −8.5 km/s while I obtained at Mopra +8.97 km/s.

• From all non-Sridharan data all positions within 4° latitude of the galactic plane were deleted, except for the CG coincident observations noted above. Also, any data lying outside the longitude range 275° to 245° was deleted. The latter are considered as conservative boundaries of the Gum Nebula in longitude. No data points significantly outside the Gum Nebula in latitude exist (see the comments below on the cirrus clouds).

• At all other coincident or unresolved adjacent positions the HartRAO and Mopra data were chosen in preference to other data, unless the reported velocities were sufficiently different to be possibly from opposite sides of the expanding shell. The latter situation did not exist in the given data set.

• Some other data positions were also deleted from the expansion model data.

  - The HartRAO observations G247.07 −5.5, G249.2 −5.28, G250.5 −4.5, G250.95 −5.25, G252.25 −6.75 and the Mopra observation G253.0 −4.5 are all at positions on the dark cloud (Feitzinger & Stüwe, 1984) complex between longitude 245° and 255° and latitude −7° and 0°. These positions have absolute velocities greater than or of the order of that of the CGs towards the middle of the Gum Nebula. As these positions are nearer to the edge of the nebula, the velocities do not fit into an expansion model.

A run of the expansion models with these positions and velocities included in the data set, always ended with this group isolated in a separate region from the expansion data in parameter space. Thus these positions are obviously not part of the expanding Gum Nebula and were justifiably excluded.

- Also the Mopra position at G 265.7 -5.0 with velocity 1.3 km/s was obviously not part of the expansion of the Gum Nebula and was thus excluded from the expansion model data set.
- The detections (HartRAO G247.500 -12.225 and G270.900 -8.4 and Mopra G250.450 $+13.6$) on the three cirrus clouds identified in the IRR work were also excluded.

The final data set used for testing against the three versions of the expansion model is plotted in Fig. [10-5] and tabulated below in table [10-1].

10.3 Model 1 fitting

The data set listed in table [10-1] was tested against the expansion model 1 to determine the centre position with the minimum reduced χ^2 in the longitude range 254° to 267° and latitude range $-10°$ to $+7°$ at intervals of 0.5° in latitude and longitude. A contour map of the minimum reduced χ^2 value is shown in a) of Fig. [10-6]. The lowest minimum is 0.50 and occurs at G261.0 $-$ 1.5 when the angular radius is 10° and the expansion velocity is 12 km/s. The dashed contour shows the 1-σ confidence level, i.e the region in parameter space that encloses all χ^2 that differ from the minimum χ^2 by a $\Delta\chi^2 = 1$.

If only Sridharans' CO cometary globule data are tested against expansion model 1, the contour map of the minimum reduced χ^2 shown in a) of Fig. [10-7] is obtained. The dashed contour, enclosing the 1-σ confidence area, in this case does not close on itself in the region shown, and opens up towards positive galactic latitudes. Thus

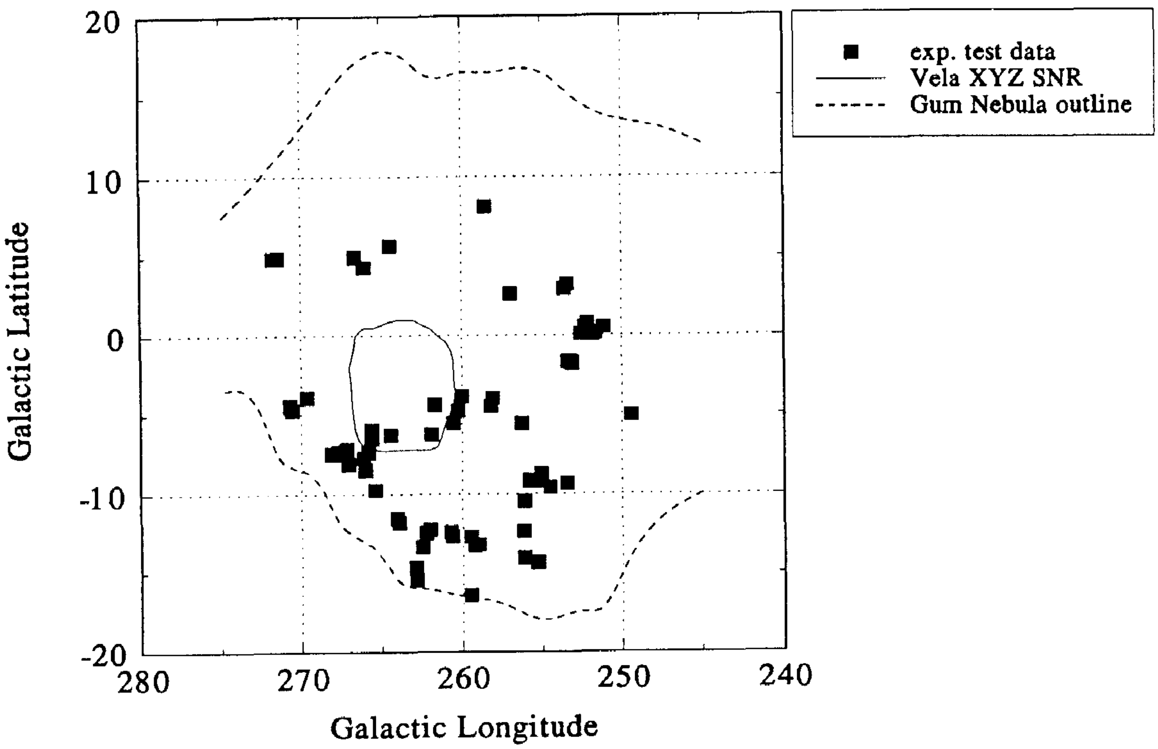

Figure [10-5]: A schematic diagram showing the data used for testing against the expansion models.

position	v_{lsr} /[km/s]	reference
258.07 − 4.00	10.17	MOP
258.07 − 4.00	11.52	MOP
256.26 − 5.60	9.59	MOP
261.70 − 4.40	10.29	MOP
265.80 − 7.40	3.41	MOP
264.42 + 5.71	5.38	MOP
266.63 + 4.98	2.67	MOP
266.63 + 4.98	1.91	MOP
253.42 − 9.38	-1.17	MOP
258.54 + 8.13	2.05	MOP
265.38 − 9.75	-6.66	MOP
266.00 − 8.50	3.72	MOP
265.60 − 6.50	5.54	MOP
264.40 − 6.30	6.32	MOP
267.70 − 7.35	5.28	MOP
261.90 − 6.25	10.27	MOP
260.53 − 5.50	12.63	MOP
258.20 − 4.50	8.14	MOP
258.20 − 4.50	13.02	MOP
256.95 + 2.65	8.97	MOP
260.02 − 3.82	11.53	MOP
254.50 − 9.60	-1.68	HART
256.10 − 10.50	-2.21	HART
256.20 − 12.38	-1.73	HART
259.25 − 13.25	5.10	HART
260.25 − 4.75	11.55	HART
262.00 − 12.25	5.17	HART
263.90 − 11.80	3.57	HART
265.60 − 6.00	5.04	HART
266.10 − 7.75	3.49	HART
267.05 − 8.10	1.71	HART
268.10 − 7.50	3.91	HART
270.75 − 4.45	2.15	HART
256.14 − 14.07	3.30	SRID
255.32 − 14.35	4.10	SRID
260.72 − 12.40	0.10	SRID
259.48 − 12.73	1.70	SRID
258.99 − 13.21	0.90	SRID
266.04 + 4.31	-1.10	SRID
255.06 − 8.76	-5.80	SRID
255.06 − 9.17	-4.20	SRID
255.79 − 9.18	-5.50	SRID
259.48 − 16.43	3.70	SRID
262.49 − 13.37	-0.90	SRID
262.88 − 14.67	-0.80	SRID
262.86 − 15.48	-0.70	SRID
270.59 − 4.69	3.70	SRID
269.66 − 3.92	2.00	SRID
253.58 + 2.96	6.50	SRID
253.37 + 3.24	6.80	SRID
260.02 − 3.82	-12.50	SRID
260.65 − 12.70	-1.80	SRID
252.14 + 0.73	2.00	SRID
251.66 + 0.15	5.00	SRID
251.80 + 0.05	5.20	SRID
251.88 + 0.01	5.20	SRID
253.29 − 1.61	5.80	SRID
253.18 − 1.66	6.00	SRID
253.18 − 1.72	6.00	SRID
253.11 − 1.73	6.30	SRID
253.11 − 1.80	6.90	SRID
252.52 + 0.08	4.90	SRID
252.48 + 0.08	4.80	SRID
252.29 + 0.51	1.60	SRID
256.95 + 2.65	-8.50	SRID
251.11 + 0.52	6.20	SRID
253.38 − 1.64	7.00	SRID
267.38 − 7.51	5.30	SRID
267.46 − 7.39	6.00	SRID
267.29 − 7.32	5.90	SRID
267.15 − 7.20	4.90	SRID
262.85 − 15.48	3.30	DEV
262.27 − 12.50	5.30	DEV
264.01 − 11.52	1.60	DEV
265.84 − 7.36	3.20	DEV
249.44 − 5.09	7.70	GOSS
262.25 − 12.46	5.50	GOSS
266.02 + 4.32	1.50	GOSS
267.40 − 7.52	5.30	GOSS
271.43 + 4.90	-3.30	GOSS
271.78 + 4.88	-3.00	GOSS
270.59 − 4.69	-6.70	ZEA

Table [10-1]: The molecular line data used for testing against the expansion models. MOP = Mopra OH 1667, HART = HartRAO OH 1667, SRID = Sridharan's CO, DEV = CO of DeVries et al., GOSS = HCHO of Goss et al., ZEA= HCHO of Zealey et al. .

a)

Contour map of min χ^2 (model 1) at given centre positions
$\chi^2 = 0.50$ at G261.0 -1.5 (+) with $\theta = 10°$, $v_{ex} = 12$ km/s

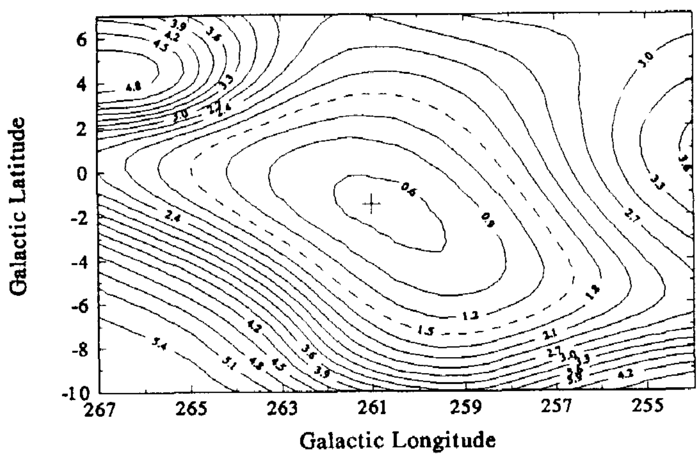

b)

expanding shell model 1 of angular radius 10° and v_{exp} 12 km/s
with expansion centre at G261.0 -1.5 fitted to molecular data

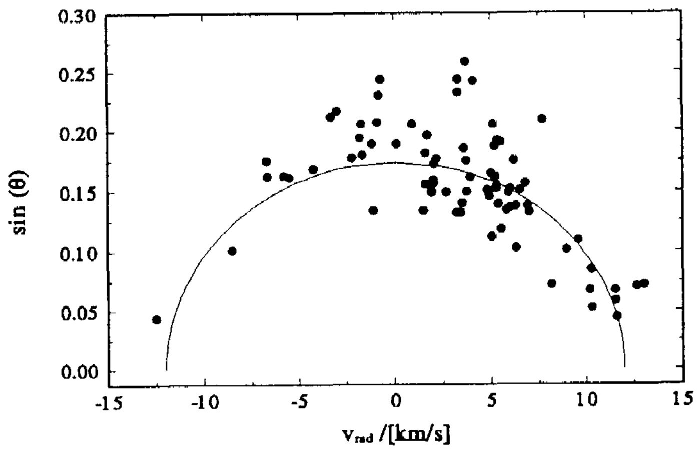

c)

Contour map of χ^2 (model 1) at centre position G261.0 -1.5
minimum χ^2 is at $\theta = 10°$, $v_{exp} = 12$ km/s (+)

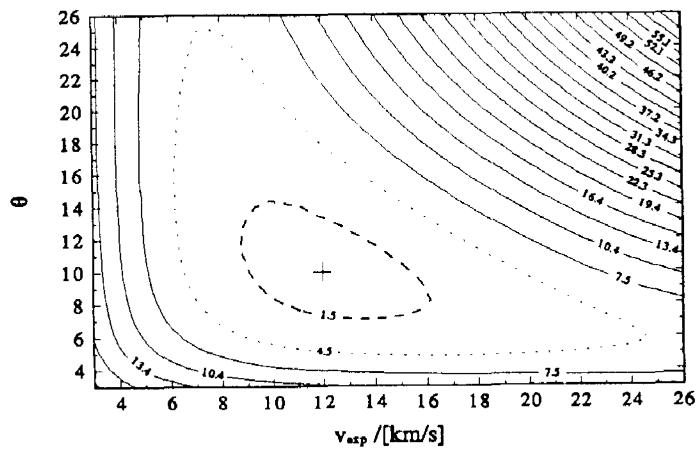

Figure [10-6]: All molecular data tested against model 1.

a)

Contour map of min χ^2 (model 1) at given centre positions
$\chi^2 = 0.21$ at G261.0 -2.5 (+) with $\theta = 10°$, $v_{ex} = 12$ km/s

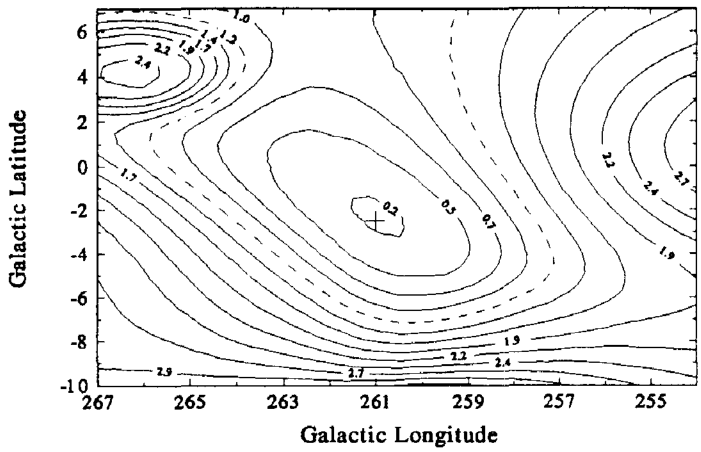

b)

expanding shell model of angular radius 10° and v_{exp} 12 km/s
with expansion centre at G261.0 -2.5 fitted to cometary globule data

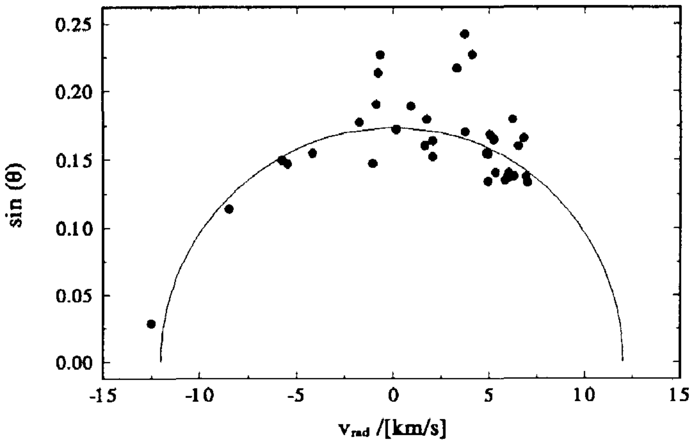

c)

Contour map of χ^2 (model 1) at centre position G261.0 -2.5
minimum χ^2 is at $\theta = 10°$, $v_{exp} = 12$ km/s (+)

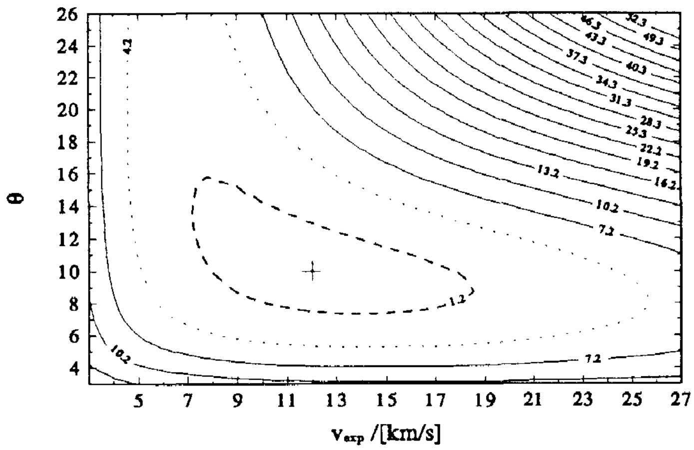

Figure [10-7]: Only the Sridharan CO cometary globule data tested against model 1.

the additional data obtained at HartRAO and Mopra, as well as from the literature, are not superfluous.

Also noticeable is the decided lack of cometary globules moving with high velocity away from us, as seen in the plot of the CG data for the parameters at the minimum χ^2 shown in b) of Fig. [10-7].

The same plot for all the molecular data, (b) of Fig. [10-6], shows better sampling at positive velocities, although the fit of the model to these positive velocities is not that good.

In the plots shown in b) of both figures, the scatter of data points about the best fit value of θ at $v_{exp} = 0$ is an indication that the molecular material is distributed in a thick shell. For all molecular data (Fig. [10-6] b)) at $v_{exp} = 0$, the range of $\sin(\theta)$ in the data points is ≈ 0.12 to 0.25. This gives a range for θ of 6.9° to 14.5°. If one also takes into account that there is a paucity of positions on the edge of the nebula (Fig. [10-5]) in the data points used, the apparent disparity between the best fit θ value and the known angular radius of $\approx 16°$ is explained.

The 1-σ confidence level (first solid contour) and the 2-σ confidence level (dashed contour) for χ^2 in the parameter space of angular radius (θ) and expansion velocity (v_{exp}) are shown in c) of Figs. [10-6] and [10-7]. These contours show quite clearly that the additional molecular data help to confine the plausible range of these parameters.

10.4 Model 2 and 3

Next all molecular data was tested against expansion models 2 and 3. The results are presented in Figs. [10-8] and [10-9]. The contour maps of minimum χ^2 for these tests shown in a) of these figures indicate that the dashed contour (1-σ confidence level) for model 3 does not close on itself within the region shown. This may indicate that the increased complexity in determining the galactic rotation contribution in model

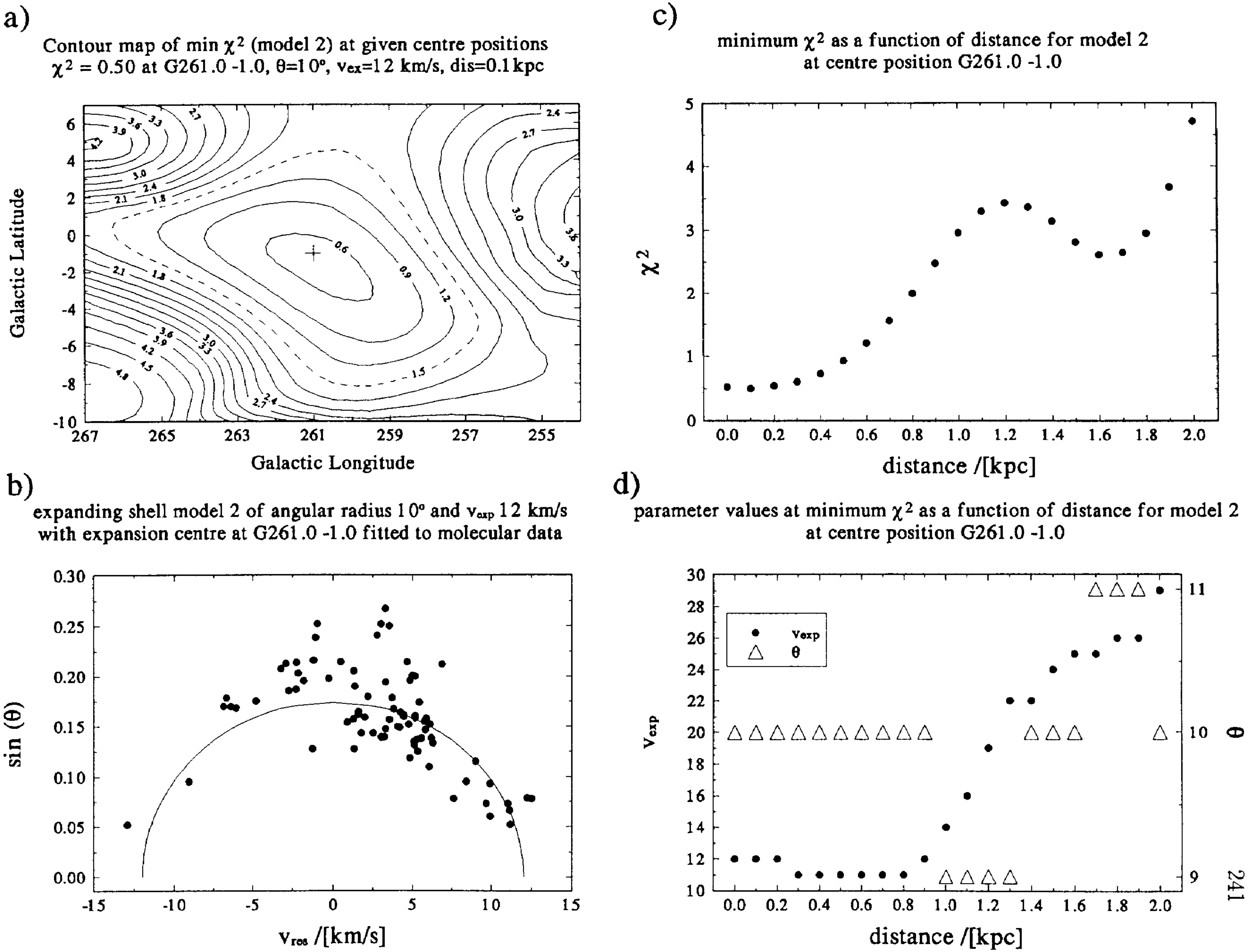

Figure [10-8]: All molecular data tested against expansion model 2.

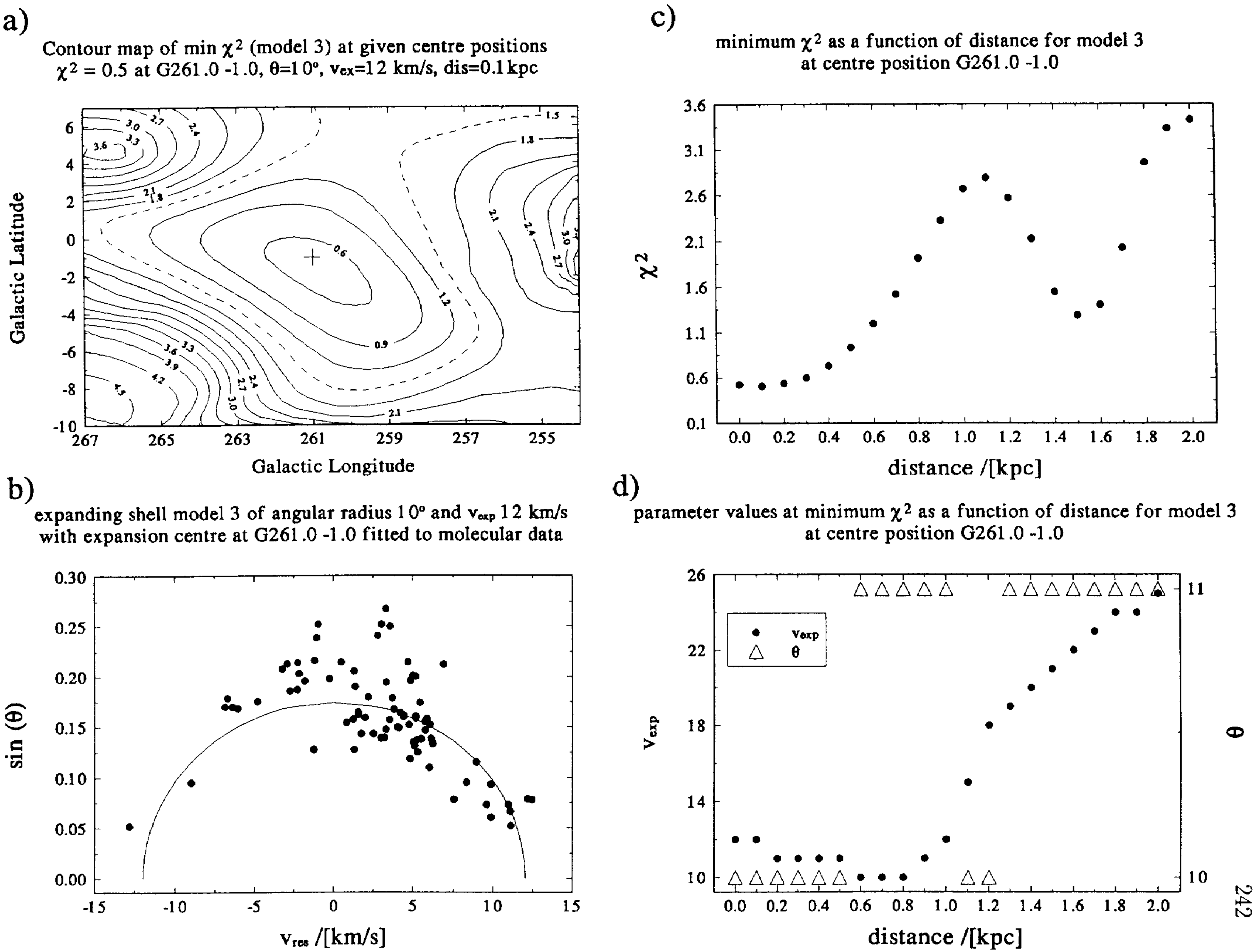

Figure [10-9]: All molecular data tested against expansion model 3.

3 is not warranted, or perhaps even wrong. However, as the minimum χ^2 values for the two models hardly differ from each other, one cannot make any definitive conclusions on the basis of the larger region enclosed by the dashed contour (the area where the χ^2 differ from the minimum χ^2 by a $\Delta\chi^2 = 1$).

For both models the the best fit, shown in b), is poor for positive velocities.

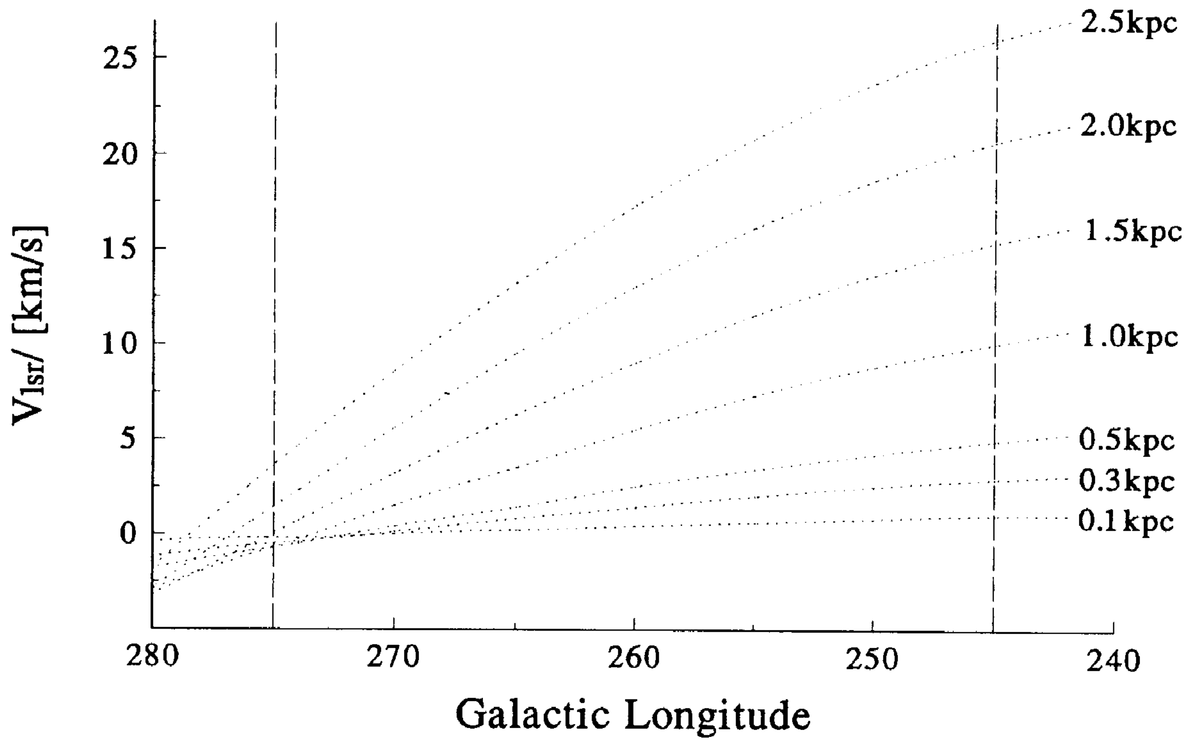

Figure [10-10]: The dotted lines show velocities relative to the local standard of rest due to galactic rotation at fixed distances and at zero galactic latitude. The long-dashed lines enclose the region of interest.

Also, for both these models the minimum χ^2 occurs at a distance of 0.1 kpc, but is basically flat out to 0.4 kpc. A look at Fig. [10-10] shows that this effectively means that the models are not able to make any decision on the distance of the nebula from us, as the galactic contribution at over this distance range (0 to 0.5 kpc) is essentially constant over the longitude range of interest (275° to 245°) and very small. Another possibility is that the models are inadequate or wrong in modelling some aspect of the data.

The best fit values of θ only range between 9° and 11° with assumed distance at the best fit centre position (see d) in both figures). Thus θ is not significantly affected by the assumed distance in either model. For both models the expansion velocity however changes from a value of $\approx$ 11 km/s to 25 km/s very rapidly beyond an assumed distance of 1 kpc.

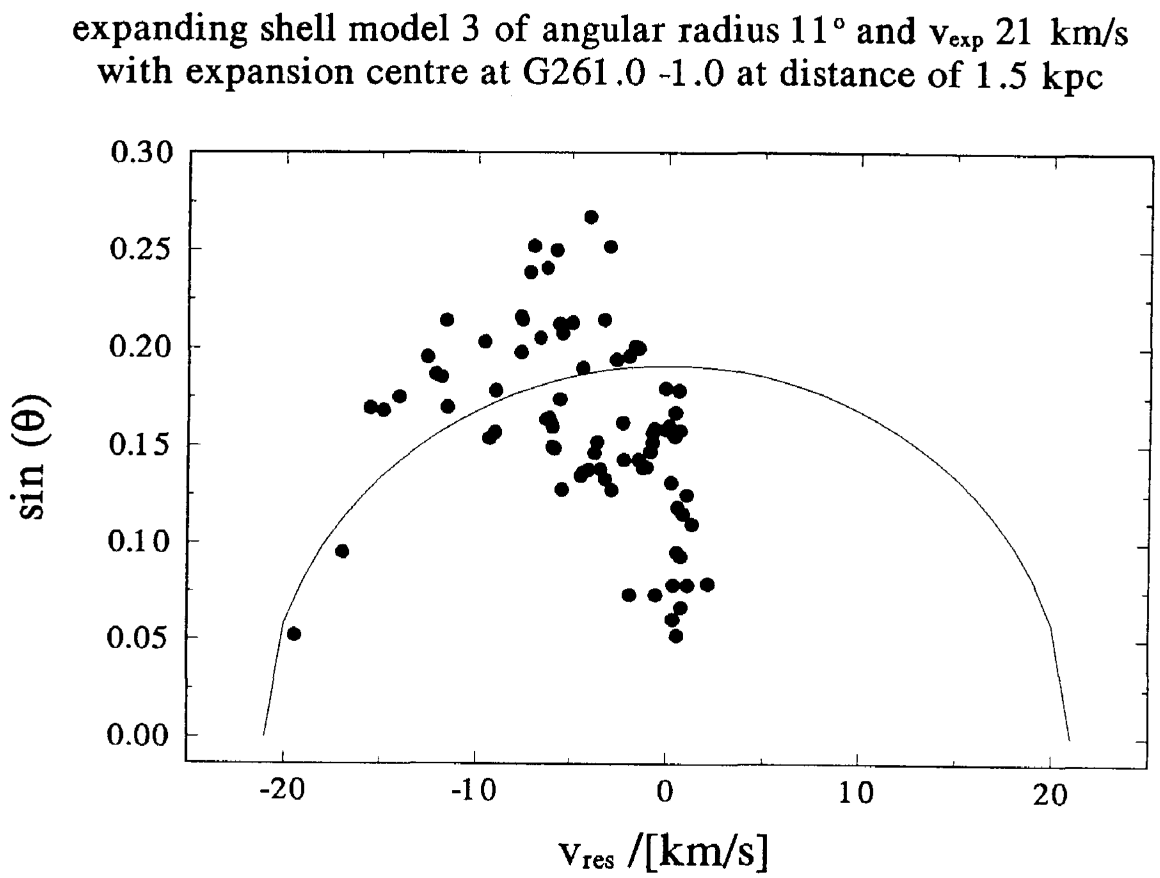

Figure [10-11]: Expanding shell model with parameters chosen by a minimum χ^2 within the dip of the secondary minimum with distance for model 3.

It is evident from the secondary minimum in χ^2 as a function of distance at the centre position (the latter was selected as the overall minimum χ^2 value) shown in c) for both models that there is a problem with the distance determination. In order to determine whether these secondary minima are likely to give the distance to the nebula, the data for the parameters given by model 3, angular radius 10° and v_{exp} 20 km/s, at a distance of 1.4 kpc and expansion centre G261.0 − 1.0, is shown in Fig. [10-11].

Obviously these secondary minimum χ^2 regions in distance do not define parameters that describe the data well. At this secondary minimum the data has been shifted to negative velocities, with the remaining positive velocity data points closely scattered near the positive velocity side of zero velocity.

This is reminiscent of the behaviour of the cometary globule data shown in Fig. [10-7] b) for model 1. It was thus investigated to what extent Sridharan's CO data of the CGs was responsible for this effect in model 2 and 3. Thus this data alone was tested against both these models. The results are shown in Figs. [10-12] and [10-13].

For the CGs alone, it is seen that the minimum χ^2 is no longer at a distance of 0.1 kpc, but at 0.8 kpc for model 2 and 0.7 kpc for model 3. This minimum is also the only one found up to a distance of 1.9 kpc as seen in Figs. [10-12] and [10-13]. However, as the value of χ^2 as a function of distance is almost flat out to 1 kpc, this minimum is not very significant.

At this minimum, with the galactic rotation velocity contribution subtracted, the CGs show predominantly negative residual velocities, i.e. the model predicts that they are moving towards us. This could be explained, if the expansion velocity of the material moving towards us is significantly different from the expansion velocity of material moving away from us. Furthermore this difference could perhaps account for the formation of the CGs predominantly in the material on the front face of the nebula.

If one assumes that this is the case, then the complete data set should be tested against different expansion velocities for the side of the nebula moving towards us and that moving away from us.

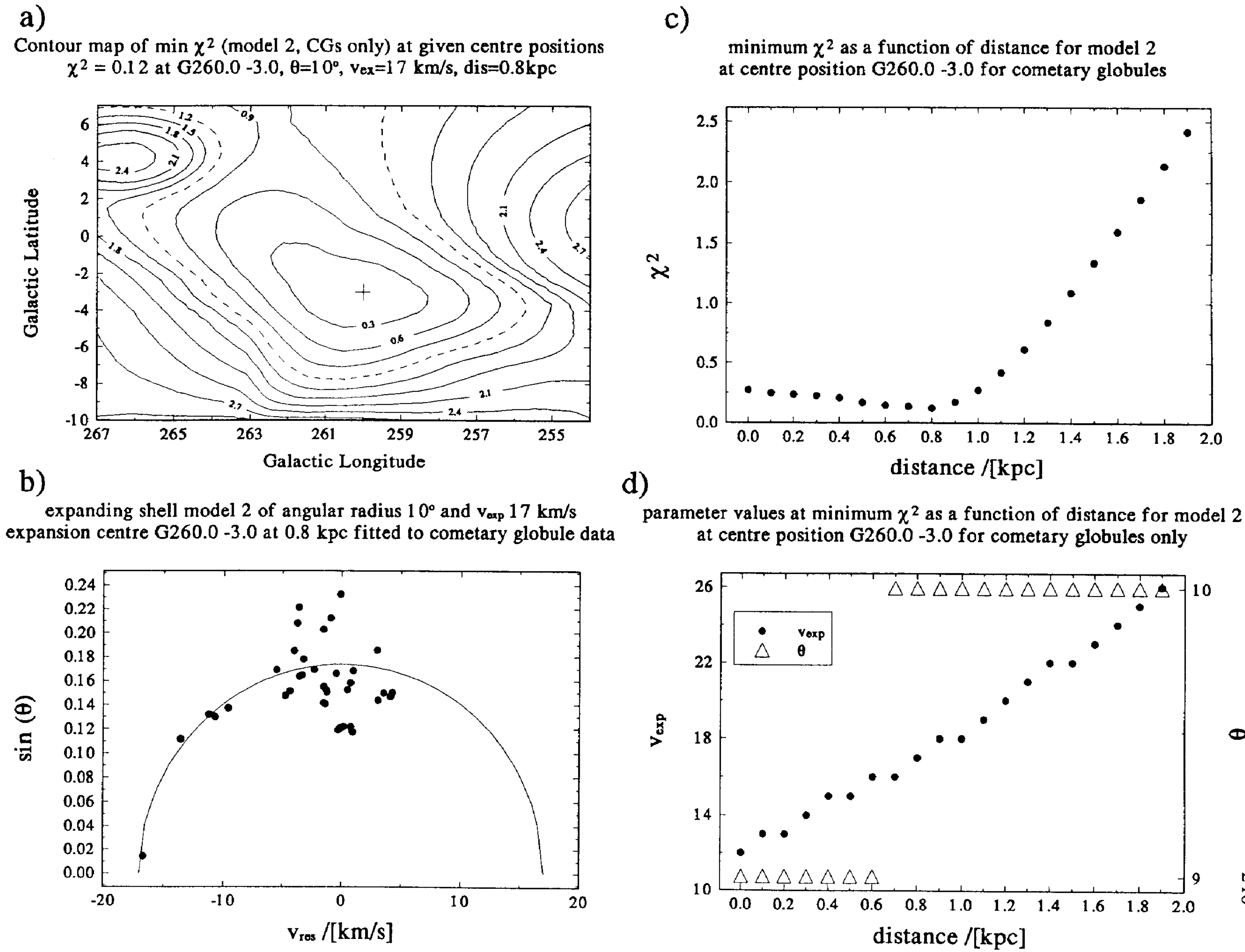

Figure [10-12]: The CG data (Sridharan) only tested against expansion model 2.

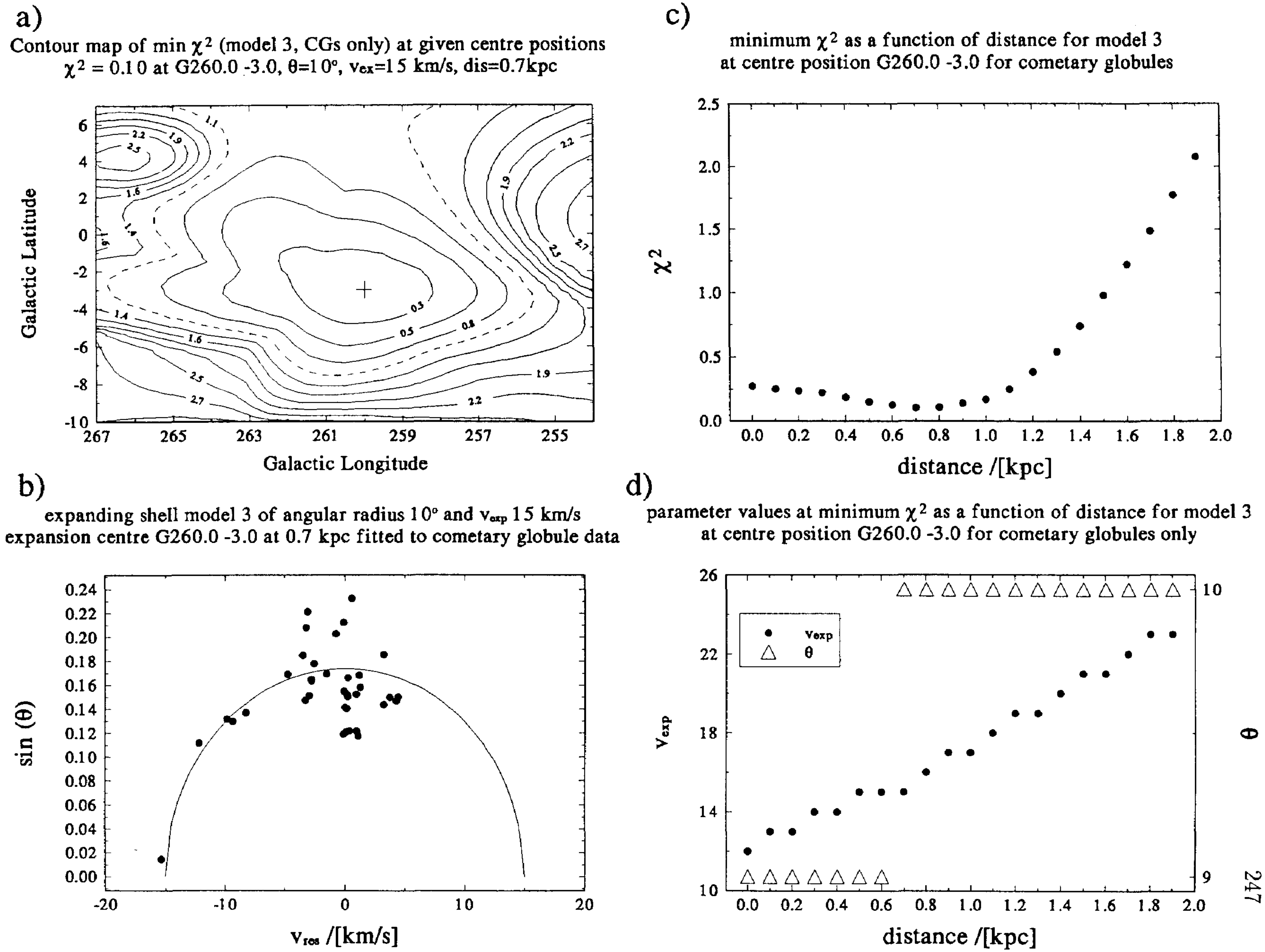

Figure [10-13]: The CG data (Sridharan) only tested against expansion model 3.

10.5 Different expansion velocities for the front and back faces of the nebula

The programs that had been written to determine the reduced χ^2 values for parameter ranges of model 2 and 3 were adjusted to determine the best fit values of the angular radius and the expansion velocity independently for the front and back faces of the nebula for a chosen range of centre position and distance (centre location). The search for the minimum reduced χ^2 had to include different angular radii for the front and back faces, as a difference in expansion velocity of the two faces would inevitably give rise to a different size in the front and back faces. As running such programs is very time consuming, the centre positions between longitude 254° and 266° and between latitude $-10°$ and $+7°$ were only searched at 1° intervals, rather than at 0.5° as was done previously.

The resultant contour maps of minimum χ^2 for these tests are shown in a) and b) of Fig. [10-14] for model 2 and 3 respectively. Compared to the fitting with one overall expansion velocity and one overall angular radius (see Figs. [10-6], [10-7], [10-8], [10-9], [10-12] and [10-13]), the region enclosing the 1-σ confidence level (dashed contour) is smaller. Hence this two faced model appears better at homing in on the centre position.

The value of the minimum χ^2 in the contour map (Fig. [10-14]) for each of the two adjusted models is closer to 2 than 1. The models in the previous sections had minimum χ^2 values approximately equally far from 1, but towards the zero side of 1. As a good fit of a model to data should give a minimum χ^2 value close to 1, these minimum χ^2 values do not allow one to choose one of these models above the others.

For the adjusted model 3, the minimum χ^2 of 1.783 occurs at the centre position G261 -3 (centre 1) at a distance of 1 kpc with an angular radius of 11° and an expansion velocity of 17 km/s for the front face. At this centre location, the best fit angular radius and expansion velocity of the back face are 7° and 5 km/s respectively

a) Contour map of min χ^2 (model 2 adj.) at given centre positions
$\chi^2 = 1.81$ at G261.0 -2 (+)

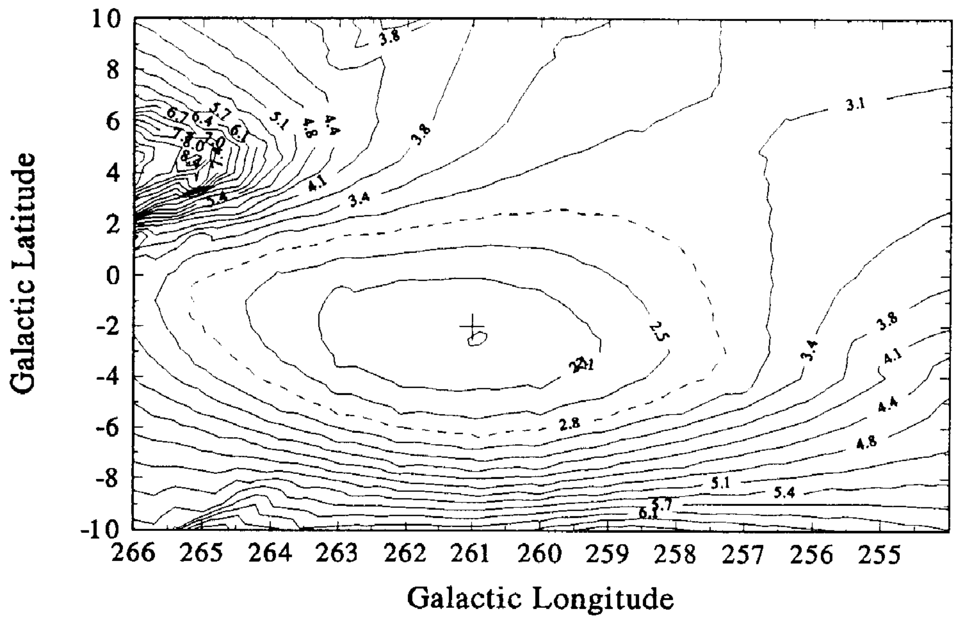

b) Contour map of min χ^2 (model 3 adj.) at given centre positions
$\chi^2 = 1.783$ at G261.0 -3 (+)

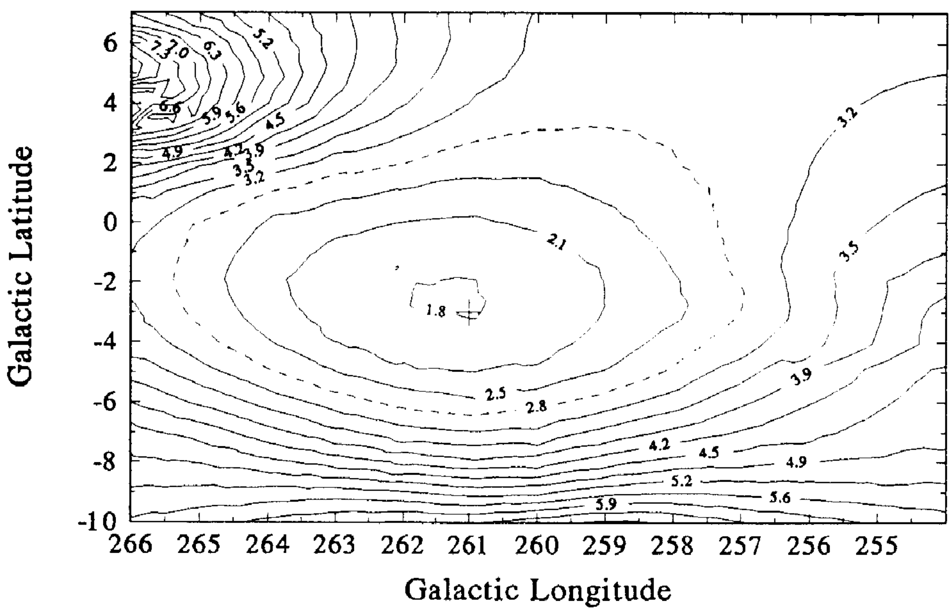

Figure [10-14]: Contour maps of minimum χ^2 at the given centre positions for models 2 and 3 adjusted to fit different expansion velocities and angular radii to the front and back face of the nebula.

(see Fig. [10-15] a)). The minimum χ^2 at position G261 -2 (centre 2) and distance 0.6 kpc is only very slightly larger at 1.785, giving an angular radius of 11° and an expansion velocity of 15 km/s for the front face and a best fit angular radius and expansion velocity for the back face of 9° and 8 km/s respectively (see Fig. [10-15] b)). The large disparity in these parameters for these two adjacent positions is disquieting. As the CG data has the best association with the Gum Nebula, the centre location, G260 -3 (centre 3) and distance 0.7 kpc, selected for model 3 by the CG data alone (see Fig. [10-13]) may be considered equally valid as centre location. At this centre location the adjusted model 3 gives a minimum χ^2 value of 1.932 and an angular radius and expansion velocity of 10° and 15 km/s respectively for the front face. The angular radius and expansion velocity of the back face are given by 9° and 7 km/s respectively (see Fig. [10-15] c)).

a) to c) of Fig. [10-15] show that the fit of the data to the adjusted model 3 is unsatisfactory near $v_{res} = 0$. Thus although this adjusted model is probably more representative of the data than the single expansion velocity and angular radius model, the data does suggest a continuous variation of these parameters with direction from the centre of the nebula. This also accounts for the somewhat large minimum χ^2 values derived for the adjusted model 3.

A plot of minimum χ^2 versus distance for the three centre positions given above (see Fig. [10-16]), shows that for all these the minimum χ^2 curve is essentially flat out to $\approx$ 1 kpc. Thus this adjusted model 3 does not improve on the distance estimates given by the unadjusted models (see previous sections). The cause of this does not lie in the adjusted model 3, but in the nature of the galactic rotation curve in this region of sky (see Fig. [10-10]).

For the adjusted model 2, the minimum χ^2 of 1.81 occurs at centre position G261 -2 (centre 4) at a distance of 0.5 kpc with an angular radius of 11° and an expansion velocity of 15 km/s for the front face. At this centre location, the best fit angular radius and expansion velocity of the back face are 9° and 9 km/s respectively (see

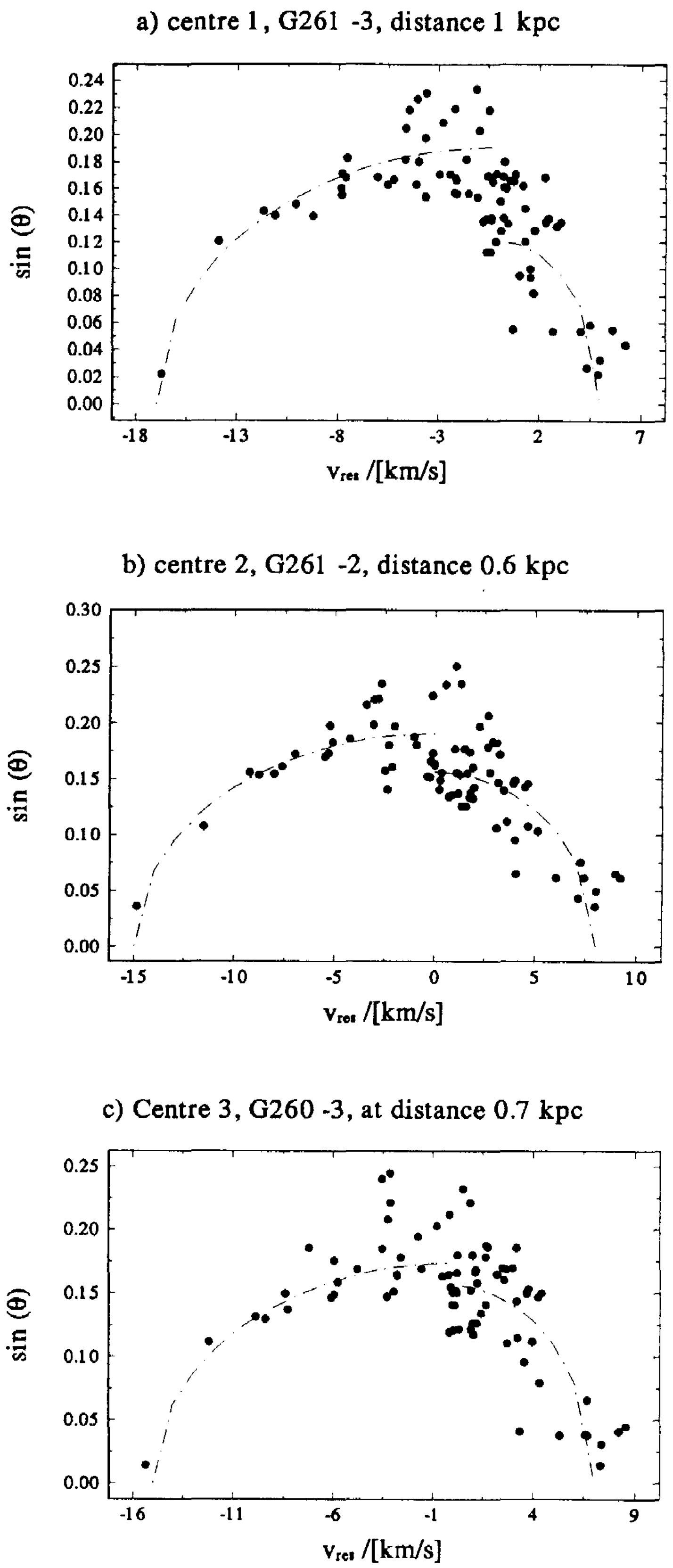

Figure [10-15]: Expanding shell model 3, adjusted to fit different expansion velocities and angular radii to the front and back face of the nebula, fitted to the data with the given centre locations

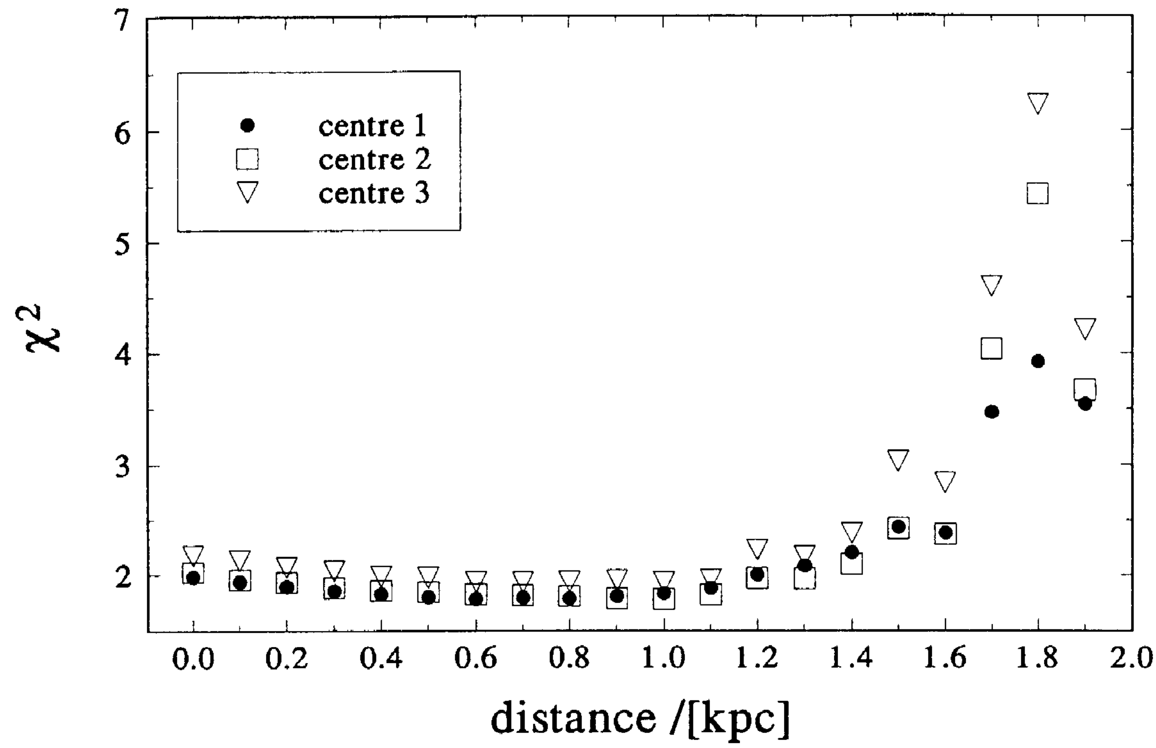

Figure [10-16]: A plot of minimum χ^2 versus distance for the three centre positions of the adjusted model 3

Fig. [10-17] a)). The CG data alone selected for the unadjusted model 2 the centre location, G260 −3 (centre 5), at a distance of 0.8 kpc. For this centre location, the χ^2 value from the adjusted model 2 is 1.94. For the front face this selects an angular radius of 10° and an expansion velocity of 17 km/s. The best fit angular radius and expansion velocity of the back face are 9° and 7 km/s respectively (see Fig. [10-17] b)).

The distance selection at the centre location using the adjusted model 2 is also poor, as shown in Fig. [10-17] c). This is the case even for a position, G260 −5 (centre 6), significantly removed from the selected best centre position. Again, the cause of this lies in the nature of the galactic rotation curve in this region of sky.

For comparison purposes the parameter values at minimum χ^2 for the unadjusted models are given in table [10-2]. These unadjusted models consistently select an angular radius of 10°. The one interesting aspect is that these unadjusted models

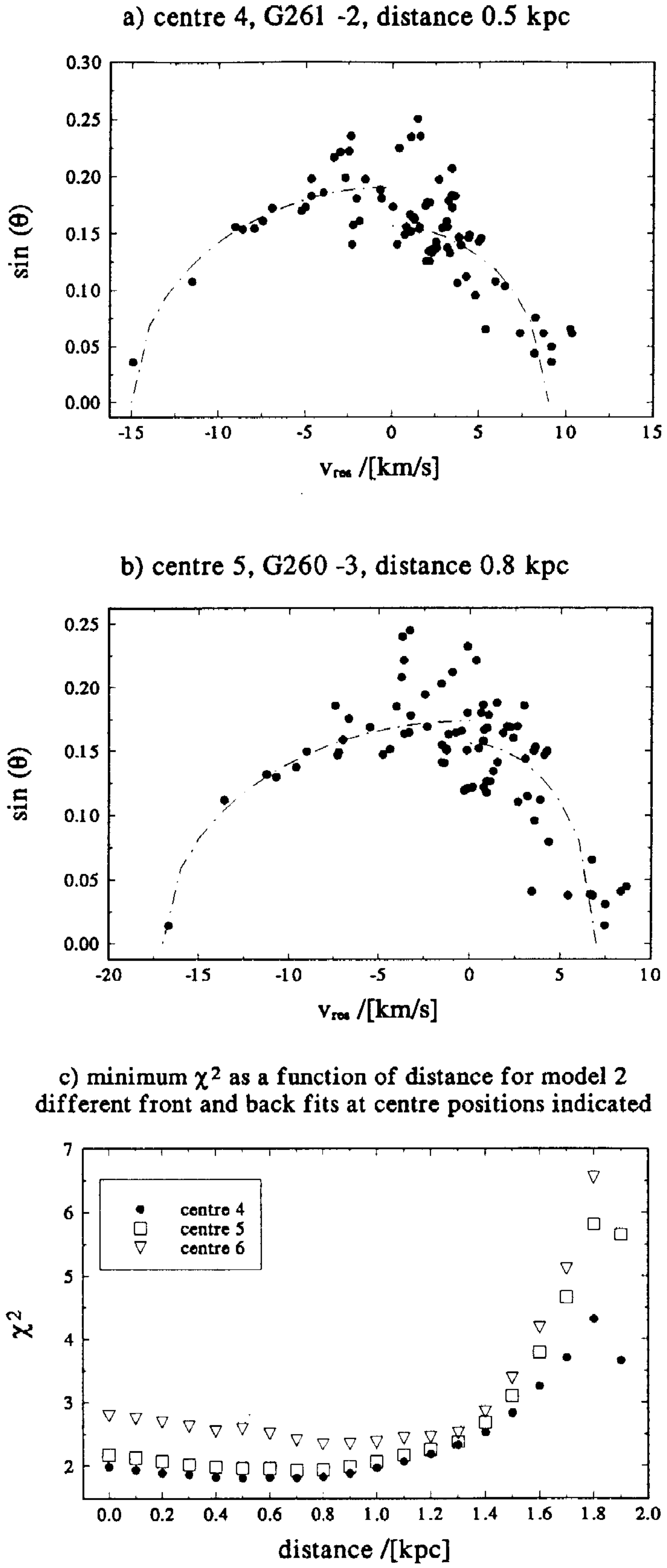

Figure [10-17]: a) and b) The expanding shell model 2, adjusted to fit different expansion velocities and angular radii to the front and back face of the nebula, fitted to the data with the given centre locations. c) A plot of χ^2 versus distance for the adjusted model 2 at the given centre positions.

applied to the CG data only give values similar to those selected by the adjusted models from all data. This gives strong support to accepting the "average result" given by these adjusted models, keeping in mind that the CG data, as seen in Figs. [10-12] and [10-13], is almost exclusively spread across the front face of the nebula.

Table [10-3] summarises the results from these adjusted models. This gives a "mean" centre position of say G260.5 −2.5 ($\pm$ 1° for both longitude and latitude). Averaging the tabulated parameter values results in a distance of $\approx$ 0.7 kpc, $\approx$ 10.5° and $\approx$ 16 km/s for the front face angular radius and expansion velocity respectively and $\approx$ 8.5° and $\approx$ 7 km/s for the back face angular radius and expansion velocity respectively.

model	centre	distance/[kpc]	θ	v_{exp}/[km/s]
1 (all)	G261 −1.5	-	10	12
1 (CGs)	G260 −2.5	-	10	12
2 (all)	G261 −1.0	0.1	10	12
3 (all)	G261 −1.0	0.1	10	12
2 (CGs)	G260 −3.0	0.8	10	17
3 (CGs)	G260 −3.0	0.7	10	15

Table [10-2]: Expansion parameters selected by the unadjusted models.

model	centre	distance/[kpc]	Front θ	Front v_{exp}/[km/s]	Back θ	Back v_{exp}/[km/s]
2	G261 −2	0.5	11	15	9	9
2	G260 −3	0.8	10	17	9	7
3	G261 −3	1	11	17	7	5
3	G261 −2	0.6	11	15	9	8
3	G260 −3	0.7	10	15	9	7

Table [10-3]: Expansion parameters selected by the adjusted models.

10.6 Optical spectral line data

The success of the fitting of the molecular line data to an expansion model prompted me to investigate whether there is any evidence for such an expansion in the published optical line data of the Gum Nebula ([N II] Hippelein & Weinberger, 1975; Hα and [N II] Reynolds, 1976a; Ca II and Na I Wallerstein et al., 1980; Hα and [N II] Srinivasan Sahu, 1992; Hα and [N II] Srinivasan Sahu & Sahu, 1993). The positions at which such optical lines were detected are shown in Fig. [10-18] a).

All optical line data was published with velocities relative to the local standard of rest, as required for a test against an expansion model. Those data points at positions towards the Vela XYZ SNR exhibiting line velocity magnitudes in excess of 50 km/s were excluded from testing against an expansion model. Such high velocity lines are very probably associated with material in the Vela XYZ SNR rather than the Gum Nebula (Hipppelein & Weinberger, 1975). Lower line velocity data at positions within the Vela XYZ SNR were not excluded, as the work on the molecular line data had shown that data position close to the centre position of the expansion are important for successful fitting to a model.

Thus I used all the optical data at the positions shown in Fig. [10-18] a) in a test against model 1. The resultant contour map of the minimum reduced χ^2 at given centre positions in the longitude range 254° to 267° and latitude range -10° to 7° at intervals of 0.5° in latitude and longitude is shown in Fig. [10-18] b). This contour map looks promising as it shows a strong minimum at a plausible centre position. The short-dashed contour shows the 1-σ confidence level, and encircles a far smaller region than the corresponding contour for the molecular line data. Even the 2-σ confidence level shown by the longer-dashed contour shows a better constraint than the 1-σ confidence level contour of the molecular data. (This may be due to better sampling at positive galactic latitudes and the larger number of optical data points available.) However, the fact that the minimum reduced χ^2 value is 6.5 does not bode well for the fit of the model to the optical data. A good fit of data to a model should give a minimum reduced χ^2 of approximately 1. That model 1 does not fit the data is evident in Fig. [10-18] c). There are at least two reasons for this unacceptable fit of the data to the model.

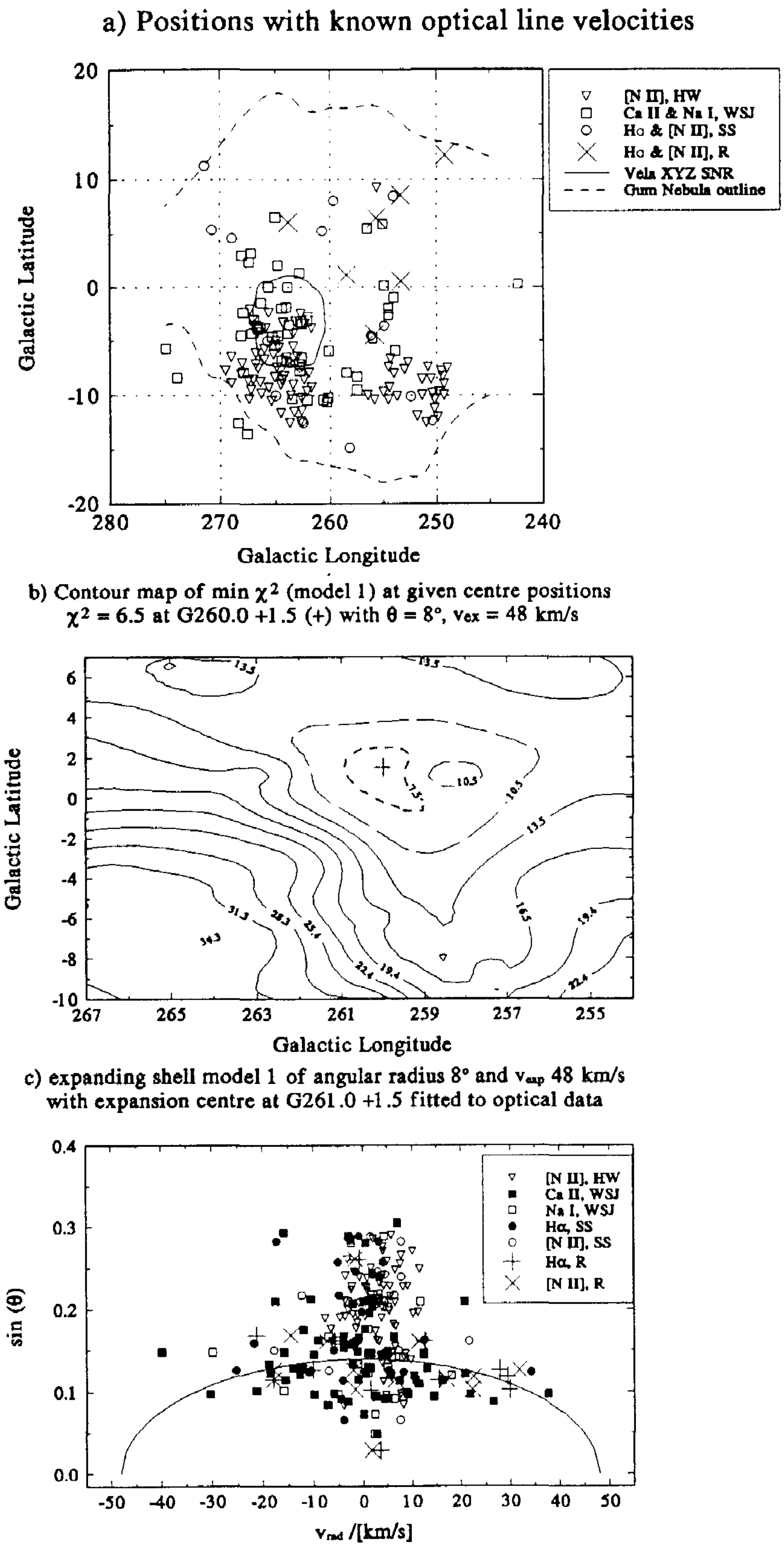

Figure [10-18]: Optical line data tested against expansion model 1. HW = Hippelein & Weinberger, 1975; R = Reynolds, 1976a; WSJ = Wallerstein et al., 1980; SS = Srinivasan Sahu, 1992.

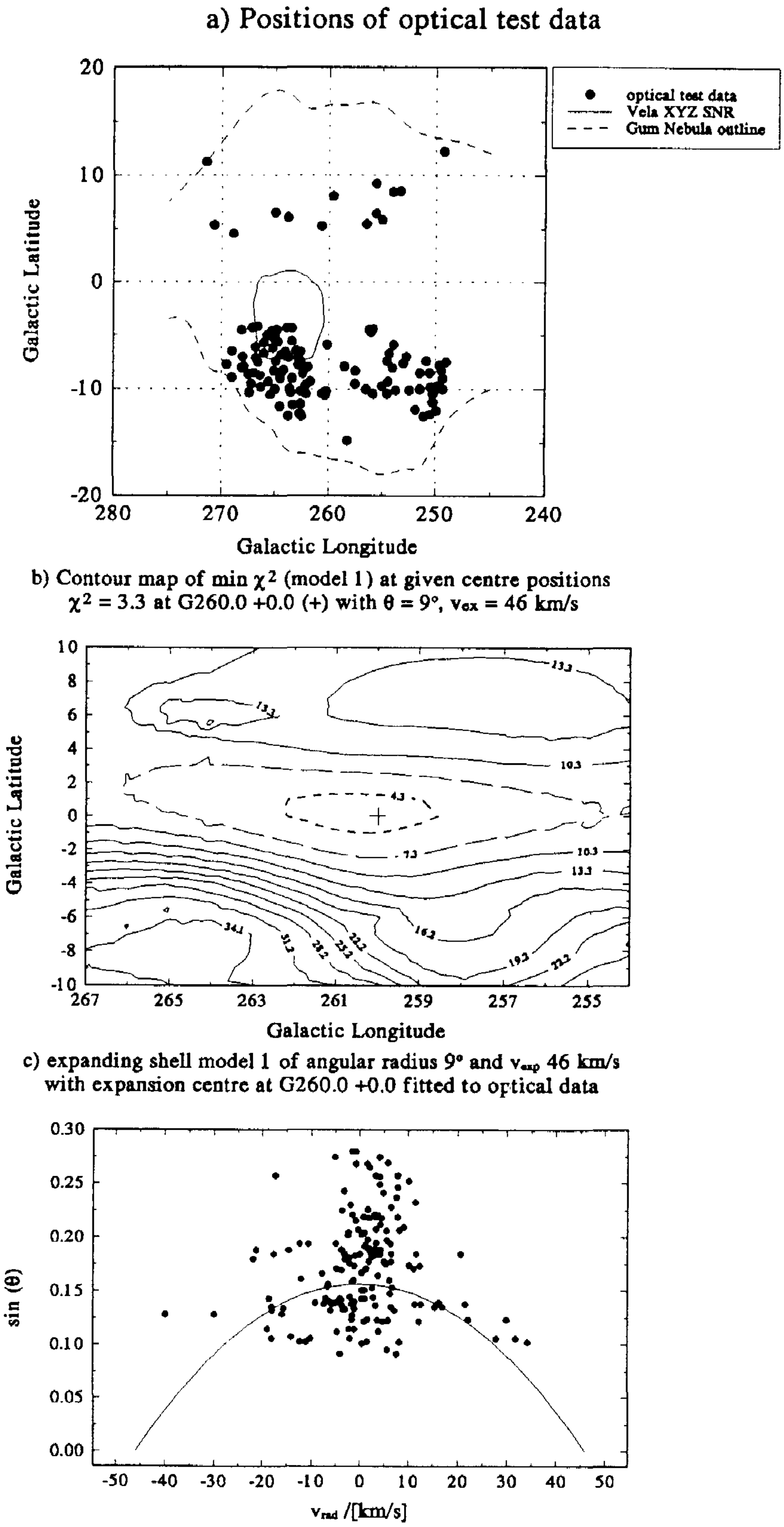

Figure [10-19]: Optical line data outside the region within 5° of the galactic plane tested against expansion model 1. Data points at positions outside the Gum Nebula were also excluded.

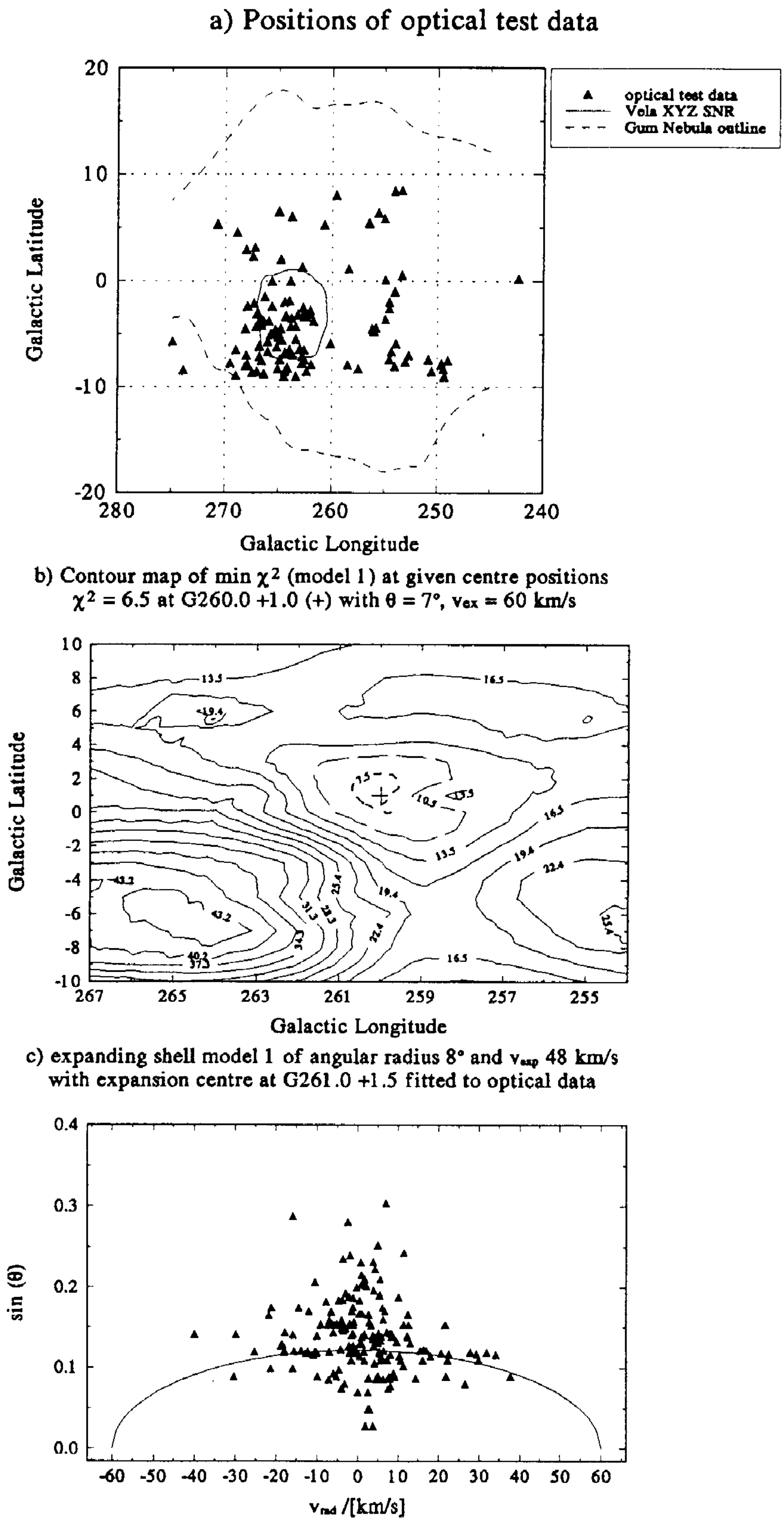

Figure [10-20]: Optical line data within 9° of the galactic plane tested against expansion model 1.

The data set may be excessively contaminated by spectral line detections from material that is not part of the Gum Nebula. In this case excluding data within 5° of the galactic plane, where confusion with other sources is most likely, may eliminate this problem. As seen in Fig. [10-19], this strategy was not successful. This is not unexpected, as a data set that lacks positions near the expansion centre is not appropriate in a search for the expansion velocity of the nebula. However, as Fig. [10-19] c) shows that the data is clustered at v = 0 km/s at the best fit parameters, I wondered whether the opposite strategy, in spite of confusion problems, might be successful with the optical data.

I thus excluded all data points outside the region within 9° of the galactic plane, as shown in Fig. [10-20] a), hoping that a fit of model 1 to this data set would show some indication of an expansion. Even though the reduced minimum χ^2 contour map (Fig. [10-20] b)) shows 1-σ and 2- σ regions of very small extent, the actual fit of the data to the best fit parameters is not good, as seen in Fig. [10-20] c). At this best fit, the data points are loosely arranged in a '+' shape rather than a '$\frown$' shape. This '+' shape arrangement of the data points is also seen in Fig. [10-18] c) where all optical data is shown with the best fit parameters of model 1.

Although the problem of confusion with unrelated data cannot be totally ruled out, there is another plausible reason for the lack of evidence for an expansion in the optical data. If the optically emitting material within the Gum Nebula is very turbulent one would expect a large range in line velocity at any particular angular distance θ from the centre and also a large range of θ for a particular velocity. Such a data set is likely to distribute itself loosely as a '+' at the best fit to model 1, as the '-' part of this distribution is best fitted by making the expansion velocity so large that the top of the $\frown$ is approximately flat. This is particularly evident in Fig. [10-20] c) where the best fit expansion velocity is the largest (60 km/s) included in the expansion velocity range searched.

a) expanding shell model 2 of angular radius 7° and v_{exp} 32 km/s with expansion centre at G260 -3 and dis 0.8kpc fitted to optical data

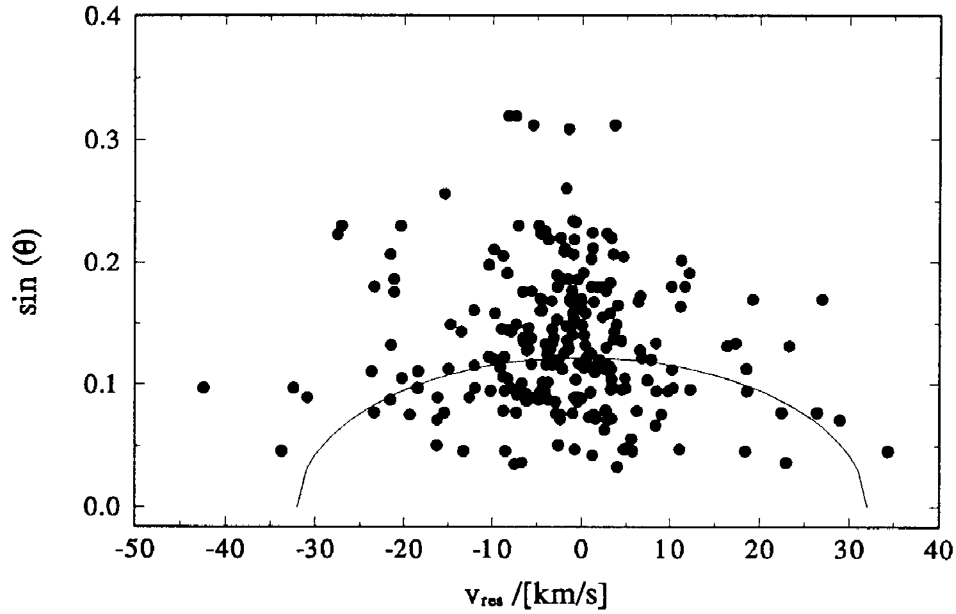

b) expanding shell model 3 of angular radius 7° and v_{exp} 32 km/s with expansion centre at G260 -3 and dis 0.7kpc fitted to optical data

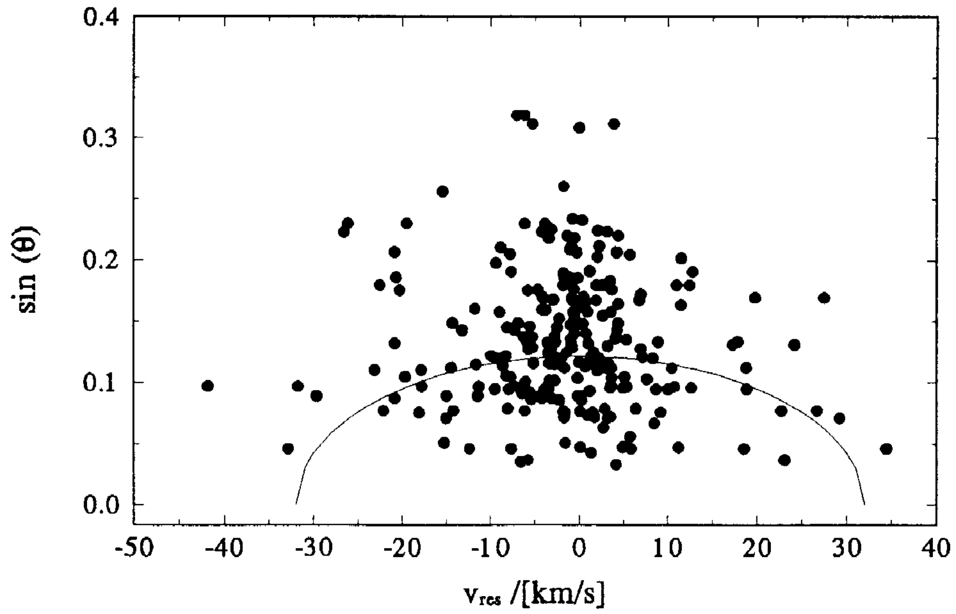

Figure [10-21]: The best fit of expansion models 2 and 3 to the optical data at the given centre locations.

As the Gum Nebula is an old SNR it is quite likely that the residual expansion of the optically emitting material is dominated by turbulence. If this is the case, then plotting the optical data for the expansion centre, in terms of position and distance from us, given by the molecular data should give the most likely representation of this optical data. Thus all optical data is shown with a best fit of the unadjusted models 2 and 3 at the centre locations selected by the CG data alone (see section 10.4) in Fig. [10-21] a) and b) respectively. The shown distributions are adequately explained by a slow expansion (not more than 30 km/s, perhaps as low as for the molecular data) with a similar turbulent velocity. Only Reynolds (1976a) and Srinivasan Sahu (1992, also Srinivasan Sahu & Sahu, 1993) determined turbulent velocities from their line data. Both quote values of the order of 20 km/s.

10.7 Conclusion

The molecular data clearly shows evidence of expansion of this molecular material. There is also fairly good evidence that the expansion velocity and angular radius of this material is nonuniform. A reasonable approximation to this situation is given by models 2 and 3 adjusted to fit different expansion velocities to the front and back face of the nebula. These models give a "mean" centre position of G260.5 -2.5 ($\pm 1^\circ$ for both longitude and latitude) for this expanding shell of molecular material. This centre is at a distance of ≈ 0.7 kpc from us. The front face angular radius and expansion velocity are $\approx 10.5^\circ$ and ≈ 16 km/s respectively and the back face angular radius and expansion velocity are $\approx 8.5^\circ$ and ≈ 7 km/s respectively.

Thus if one supports the theory that the molecular material is connected with the Gum Nebula and the cometary globules, and that the expansion is nonuniform, then the above parameters also hold for the Gum Nebula.

Several double component Hα lines in the Gum Nebula have been reported by Srinivasan Sahu & Sahu (1993) and Reynolds (1976a). This, in combination with the results of Fig. [10-21] a) and b) showing the optical data from the literature fitted by an expansion model, is best explained by a slow expansion ($\approx$ 30 km/s) combined with a similar ($\approx$ 20 km/s) turbulent velocity. Thus the optically emitting material in the Gum Nebula is also expanding, but the evidence for this is not as clear cut as for the molecular data because the turbulent velocity of this material is of the same order as its expansion velocity.

If one determines a distance to the expansion centre using model 2 or 3, the residual velocities of the CGs are predominantly negative and so towards the side with greater expansion velocity. This may indicate that CGs are only formed in a particular range of expansion velocities and that the material moving away from us expanded at velocities below the lower cutoff when the CGs were formed.

It is clear from all the expansion model graphs of the data that the $\approx 10°$ angular radius for the nebula is a lower limit. At zero residual velocity the data points extend quite far above and below the line indicating the model parameters. This implies that the molecular material is distributed throughout a thick shell.

Chapter 11

Conclusion

11.1 Morphology of the Gum Nebula

In order to generate the spectral index images (chapter 4 and 5) and IRR image (chapter 6), I had to observe the Gum Nebula region at a high radio frequency. The resultant radio continuum map at 2326 MHz is now part of the Rhodes/HartRAO 2326 MHz radio continuum survey.

In all frequencies at which the Gum Nebula has been observed, Hα (Sivan, 1974), 408 MHz radio continuum (Haslam et al., 1982), 2326 MHz radio continuum and the 60 νm IRAS data (Beichman et al., 1988; Wheelock et al., 1994), it is brighter at negative galactic latitudes than at positive galactic latitudes.

The stacked constant latitude plot diagram in Fig. [3-5], which I made from the 2326 MHz data at 0.5° resolution, shows that the nebula has a shell morphology.

11.2 The Gum Nebula, an old SNR

From the values of the infrared to radio flux density ratio (IRR) it is clear that the nebula is an old SNR. Thus the main aim of my work, to obtain a definite classification for this nebula, was achieved.

This classification cannot explain the observational evidence for H II region characteristics reported in the literature. Reynolds (1976b) had proposed a model of combined old SNR with H II region shell that allowed for such H II region characteristics. In the IRR chapter I argue that if the thermal shell has the IRR characteristics of an ordinary H II region, the IRR image should reveal such a shell by its markedly different IRR compared to that of the rest of the old SNR. In the IRR image there is no evidence for such a shell.

However, the spectral index images I produced showed that this thermal shell does exist. Thus the thermal shell proposed by Reynolds (1976b) must have non-H II region IRR characteristics. It is therefore most likely that this H II shell is cooled SNR material, rather than material surrounding the SNR heated only by the central stars.

11.3 The spectral index of the Gum Nebula

The spectral index images I derived using two different methods (TT-plot method and background-isolated-source method) give similar results. In both the positive and negative galactic latitude parts of the Gum Nebula large areas have nonthermal spectral indices. There is also a broad ring-like region of flat spectral index which is non-continuous across the plane and wider at negative galactic latitudes.

At positive galactic latitudes this thermal region is not as clearly defined. Here the TT-plot method shows up definite thermal patches, while that produced from the background-subtracted images only gives regions of lower (but not thermal) spectral index compared to the surroundings. The latter, i.e. a region of intermediate spectral index, is what one would expect from a superposition of thermal and steep non-thermal regions in a spectral index image obtained by straight division of the two frequency maps. The former also fits this picture provided that there is essentially no variation with position in the brightness temperature of the non-thermal component.

The picture revealed by the spectral index image is thus very close to the model proposed by Reynolds (1976b), an old SNR with a thermal shell. The latter is thought to be either cooled SNR material and/or material heated by the centrally situated stars, γ^2 Velorum and ζ Puppis. The fact that this shell lacks H II region IRR characteristics does point to the material having undergone some processing within the SNR, rather than having originated in a neutral surrounding shell heated by these stars.

11.4 The role of γ^2 Velorum and ζ Puppis

The debate in the literature about the role of these two stars in heating the Gum Nebula has been extensive. From the spectral index image it is clear that not all radio radiation from the Gum Nebula is synchrotron emission. Only the thermal regions could in principle be dependent on the stars as an energy source. As seen from the calculations of Chanot & Sivan (1983) the Lyman continuum from these stars can just account for the Hα radiation. The fact that the fluxes match approximately is not a good enough reason for definitely associating the thermal component with heating by these stars. However, as the stars do emit ionizing radiation in the Gum Nebula region, it is unlikely that they are not responsible for at least some heating of the thermal region.

The nebula may have engulfed most of the material (neutral or heated by the stars, including its precursor) in the region while still expanding fast enough to heat the encountered material through shocks to temperatures higher than 10000 K. This material is now cooling off. The latter may be happening more slowly than in a scenario unaided by additional heating from the central stars.

The scenario in which the nebula never engulfed all the surrounding neutral material, which thus became heated by the stars, forming the H II shell, is less likely as it is not supported by evidence in the IRR image.

As there are no direct observational means of deciding whether the stars are responsible for the heating and ionization of the thermal regions, one will never know exactly what is happening with regard to the contribution made by the stars.

11.5 H Recombination lines towards nebula

The H recombination line observations made at Mopra show the thermal regions to have a temperature of 4000 to 6000 K, a turbulent velocity of $\approx$ 20 km/s, typical of ionized hydrogen regions, and an emission measure of 220 to 460 pc cm^{-6} in the brightest regions. The latter is in agreement with published values (Chanot & Sivan, 1983; Reynolds, 1976a).

11.6 Hydroxyl observations

The search for shocked OH was negative. A large number of unshocked OH lines were detected. As the large angular size of the nebula made complete sampling of the molecular material, at the resolution of 0.5° used for this work, impossible, this does not rule out the existence of regions with shocked molecular gas.

11.7 Kinematics

The OH 1667 MHz lines were also used, in conjunction with data from the literature, to determine the expansion velocity of the nebula. This investigation successfully shows that the molecular material is undergoing expansion and that this expansion is non-uniform. The data indicates that the front face of the nebula is on average expanding faster than the back face. The expansion centre is at G260.5 −2.5 and at a distance of 0.7 kpc from us. The front face angular radius and expansion velocity are 10.5° and 16 km/s respectively. The back face angular radius and expansion velocity are 8.5° and 7 km/s respectively. This difference, in a nebula as old as the Gum Nebula, is most likely due to expansion into a non-uniform interstellar medium, with the side closer to us having a lower density.

If one determines a distance to the expansion centre using the unadjusted model 2 or 3, the residual velocities of the CGs are predominantly negative and so towards the side with greater expansion velocity. This may indicate that CGs are only formed in a particular range of expansion velocities and that the material moving away from us expanded at velocities below the lower cutoff at which the CGs form.

The investigation of the expansion of the nebula with the molecular line data also shows that the centre of this molecular material associated with the nebula is within a degree or two of the Hα emission centre, further confirming the association of the molecular material with the nebula. The distance dependent models also confirm that the nebula's centre is within 1 kpc of us.

The scatter of the molecular data in the expansion plots shows that the molecular material associated with the nebula is distributed throughout a broad shell of $\approx 5°$. If any neutral hydrogen is present amongst this molecular material, this broad distribution together with the low expansion velocity may well explain why 21 cm hydrogen emission from physically separate regions of sky easily blend out any evidence of the nebula in 21 cm line surveys.

A search for evidence of uniform expansion in the optical line data available in the literature gave negative results. The most plausible explanation of the optical data is that the emitting material has turbulent velocities of the order of the expansion velocity of this material.

11.8 Evidence for inhomogeneous ISM in the region

Inhomogeneity in the pre-expansion ISM is predicted by the difference in the front and back face expansion velocities of the molecular material, as the shock front would move faster through rarer material. Thus the face closer to us has/had a lesser density compared to the back face. A similar disparity in the ISM density above and below the plane is evident in the large difference in the brightness of the nebula at positive and negative galactic latitudes.

The much broader structure of the H II shell at negative galactic latitudes, compared to positive galactic latitudes, shown in the spectral index images, further supports such a pre-explosion scenario of density disparity above and below the plane. I argue that the thermal region is once hot, now cooled, SNR material. Such cooling is expected to be more efficient in denser regions.

Furthermore, the identification of 3 cirrus clouds in the IRR image in the vicinity of the Gum Nebula also hints at this inhomogeneity having been present on a smaller scale.

The picture that emerges is one in which the precursor star was situated near the edge of a molecular cloud, with the bulk of the cloud to the far and to the negative galactic latitude side of the star.

11.9 X-ray emission

Aschenbach et al. (1995) mention that X-ray emission associated with the Gum Nebula is present in the ROSAT data. The only details given by them are that the centre of this emission is somewhere in the Vela XYZ SNR and that the radius of this emission is 10°. This radius is significantly smaller than that of the Gum Nebula at other wavelengths. Thus there seems to be a discrepancy.

However, if the Gum Nebula belongs to the group of SNR that have a centrally brightened X-ray and a limb brightened radio morphology (Long et al. 1991, Leahy & Aschenbach 1995 and 1996), this discrepancy looses importance. The difference in the X-ray and radio morphology of this group of SNRs is thought to be due to the presence of evaporating clouds (White & Long 1991 etc.), i.e density inhomogeneity in the interstellar medium. Although the similarity solutions of White & Long for a SNR in a cloudy interstellar medium, predicting the centrally peaked X-ray emission, are for remnants between 10^3 and 2×10^4 years, i.e. much younger than the Gum Nebula, they certainly are in agreement with other data on the Gum Nebula. Density inhomogeneities are still present in the uneven distribution of the CGs, as well as the large differences in IR emission across the remnant. One problem with this interpretation is that the model of White & Long predicts a similarly centrally brightened IR morphology, whereas the Gum Nebula is limb brightened in the IR and has a morphology similar to that of the radio emission.

11.10 The IRAS-Vela ring

No evidence for the IRAS-Vela ring can be seen in the IRR image. If this ring did exist, one would expect there to be a distinct change in the IRR value from negative to positive galactic latitudes, as the ring is supposedly confined to negative latitudes, extending at most to about $+5°$ (Srinivasan Sahu, 1992; Srinivasan Sahu & Sahu, 1993) in latitude. No such abrupt change is evident in the IRR image (see Fig. [6-3]). As argued in chapter 6, a superposition of an object with IRR in the H II region range on an SNR should show up noticeably in an IRR image, unless the H II region like object is extremely faint—an impression not given by the interpretation of the IRAS-Vela ring by Srinivasan Sahu.

The existence of IR emission at positive galactic latitudes (see Fig. [6-2]) of similar morphology to that of the radio and Hα emission of the Gum Nebula at these latitudes also invalidates some of the evidence given by Srinivasan Sahu for the separate identity of the IRAS-Vela ring.

Also, something not mentioned in chapter 10, which deals with the kinematics of the molecular material associated with the Gum Nebula, is that there is no evidence for a minimum in the minimum χ^2 values at the position of the proposed centre (G263 -7) of the IRAS-Vela ring. Thus Srinivasan Sahu's (1992) claim that the cometary globules are associated with the IRAS-Vela ring cannot be supported with concrete evidence.

11.11 Spectral index determination methods

I showed that valid spectral index images of a faint extended source can be produced.

The uncertainty in the TT-plot-at-constant-galactic-latitude method, using the Theil method of straight line fitting, is sound, yet small enough to allow definite conclusions to be drawn from the results. One negative aspect of this method is that a spectral index cannot be defined for all positions in an image. Also, the determination of the spectral index image using this method is very time consuming and laborious.

The spectral index determination by isolating the source from its background radiation using program GUMBACK is less time consuming than the TT-plot method. However, this method is not successful near the galactic plane and in very faint regions. Furthermore, it is difficult to quantify an uncertainty for this method.

11.12 Miscellaneous

The nonthermal, separate, faint circular structure seen in the background subtracted radio images at very positive galactic latitudes (approximately centred at G263 +14), and the two possible compact H II regions identified on the IRR image at G263.5 +3.5 and G259.5 −2.5 warrant further investigation.

References

Abt,H.A., Landolt,A.U., Levy,S.G., Mohnacki,S., 1976, AJ, 81, 541

Alexander,J.K., Brandt,J.C., Maran,S.P., Stecher,T.P., 1971, ApJ, 167, 487

Alexander,J.K., 1973, see NASA Symposium, p31

Arendt,R.G., 1989, ApJS, 70, 181

Aschenbach.B., Egger.R., Trümper,J., 1995, Nature, 373, 587

Baars,J.W.M., 1973, IEEE Trans. Ant. Propagat., AP-21, 461

Baart,E.E., de Jager,G., Mountfort,P.I., 1980, A&A, 92, 156

Babu,G.J., Feigelson,E.D., 1992, Commun.Statist.Comput.Simul., 22, 533

Baschek,B., 1970, A&A, 7, 318

Beichman,C.A., Neugebauer,G., Habing,H.J., Clegg,P.E., Chester,T.J., 1988, IRAS Explanatory Supplement (NASA RP-1190) (Washington,D.C.: GPO)

Beuermann,K.P., 1973, Astrophys. Space Sci., 20, 27

Bevington,P.R., 1969, Data Reduction and Error Analysis for the Physical Sciences, McGraw-Hill Book Company

Blaauw,A., 1993, Symposium on Massive Stars: Their Lives in the Interstellar Medium as Part of the 104 Annual Meeting of the Astronomical Society of the Pacific, 207

Bohannan,B., Voels,S.A., Hummer,D.G., 1990, ApJ, 365, 729

Bohlin,R.C., Savage,B.D., Drake,J.F., 1978, ApJ, 224, 132

Bok,B.J., 1971, Sky and Telescope, 42, 64

Brand,P.W.J.L., Hawarden,T.G., Longmore,A.J., Williams,P.M., Caldwell,J.A.R., 1983, MNRAS, 203, 215

Brandt,J.C., 1973, see NASA Symposium, p4

Brandt,J.C., Stecher,T.P., Crawford,D.L., Maran,S.P., 1971, ApJ, 163, L99

Brandt,J.C., Roosen,R.G., Thompson,J., Ludden,D.J., 1976, ApJ, 208, 109

Braun,R., 1985, Doctoral Thesis, Sterrewacht Leiden

Braun,R., Strom,R.G., 1986, A&A, 164, 193

Bridle,A.H., 1967, MNRAS, 136, 219

Broadbent,A., Haslam,C.G.T., Osborne,J.L., 1989, MNRAS, 237, 381

Brown,R.L., Lockman,F.J., Knapp,G.R., 1978, Ann. Rev. Astr. Astrophys., 16, 445

Bruhweiler,F.C., Kondo,Y., McCluskey,G.E., 1979, ApJ, 229, L39

Bruhweiler,F.C., Kafatos,M., Brandt,J.C., 1983, Comments Astrophys., 10, 1, 1

Burton,W.M., Evans, R.G., Griffin,W.G., 1974, MNRAS, 169, 307

Cane,H.V., 1973, Proc. ASA 2 (4), 197

Castor,J., McCray,R., Weaver,R., 1975, ApJ, 200, L107

Caswell,J.L., Haynes,R.F., 1987, A&A, 171, 261

Chanot,A., Sivan,J.P., 1983, A&A, 121, 19

Cleary,M.N., 1977, Doctoral Thesis, Australian National University, Canberra

Cox,P., Krügel,E., Mezger,P.G., 1986, A&A, 155, 380

de Boer,K.S., Pottasch, S.R., 1973, A&A, 28, 155

de Vries,C.P., Brand,J., Israel,F.P., de Graauw,Th., Wouterloot,J.G.A., van de Stadt,H., Habing,H.J., 1984, A&ASS, 56, 333

DeNoyer,L.K., 1979, ApJ, 228, L41

DeNoyer,L.K., Frerking,M.A., 1981, ApJ, 246, L37

Dickey,J.M., Crovisier,J., Kazès,I., 1981, A&A, 98, 271

Dopita,A., 1978, A&A, 63, 237

Dubner,G., Giacani,E., Cappa de Nicolau,C., Reynoso,E., 1992, A&ASS, 96, 505

Duncan,A.R., Stewart,R.T., Haynes,R.F., Jones,K.L., 1996, MNRAS, 280, 252

Dwarakanath,K.S., Udaya Shankar,N., 1990, J. Astrophys. Astr., 11, 323

Dwek,E., Petre,R., Szymkowiak,A., Rice,W.L.,1987, ApJ, 320, L27

Eggen,O.J., 1980, ApJ, 238, 627

Eggen,O.J., 1982, ApJS, 50, 199

Ellis,G.R.A., 1972, Proc.ASA 2 (3), 158

Emerson,J.P., Jennings,R.E., 1978, A&A, 69, 129

Fazio,G.G., Stecker,F.W., 1976, ApJ, 207, L49

Feigelson,E.D., Babu,G.J., 1992, ApJ, 397, 55

Feitzinger,J.V., Stüwe,J.A., 1984, A&ASS, 58, 365

Flanagan,C.S., 1981, Honours project, Rhodes University, South Africa

Frail,D.A., Goss,W.M., Reynoso,E.M., Giacani,E.B., Green,A.J., Otrupcek,R., 1996, AJ, 111, 1651

Franco,G.A.P., 1990, A&A, 227, 499

Fürst,E., Reich,W., Sofue,Y., 1987, A&ASS, 71, 63

Gaylard,M.J., 1981, RAO Correlator Operation and Test Manual, HartRAO

Gaylard,M.J., 1984, MNRAS, 211, 149

Gaylard,M.J., 1989, Doctoral Thesis, Radio Studies of Ionized Hydrogen in the Southern Milky Way, Rhodes Universty, Grahamstown, South Africa

Goss,W.M., 1968, ApJS, 15, 131

Goss,W.M., Manchester,R.N., Brooks,J.W., Sinclair,M.W., Manefield,G.A., 1980, MNRAS, 191, 533

Gott,J.R.III, Ostriker, J.P., 1973, see NASA Symposium, p42

Graham,J.A., ApJ, 1986, 302, 352

Green,D.A., 1989, MNRAS, 238, 737

Green,D.A., 1995, A Catalogue of Galactic Supernova Remnants (1995 July version), Mullard Radio Astronomy Observatory, Cambridge, United Kingdom

Grewing,M., Lamers,H.J., Walmsley,C.M., Wulf-Mathies,C., 1973, A&A, 27, 115

Gum,C.S., 1952, Observatory, 72, 151

Gum,C.S., 1955, Mem. Roy. Astron. Soc., 67, 155

Gum,C.S., 1956, Observatory, 76, 150

Hanbury Brown,R., Davis,J., Herbison-Evans,D., Allen,L.R., 1970, MNRAS, 148, 103

Harper,D.A., Low,F.J., 1971, ApJ, 165, L9

Hartley,M., Manchester,R.N., Smith,R.M., Tritton,S.B., Goss,W.M., 1986, A&ASS, 63, 27

Haslam,C.G.T., Klein,U., Salter,C.J., Stoffel,H., Wilson,W.E., Cleary,M.N., Cooke,D.J., Tomasson,P., 1981, A&A, 100, 209

Haslam,C.G.T., Salter,C.J., Stoffel,H., Wilson,W.E., 1982, A&ASS, 47,1

Haslam,C.G.T., Osborne,J.L., 1987, Nature, 327, 211

Hauser,M.G. et.al,, 1984, ApJ, 285, 74

Hawarden,T.G., Brand,P.W.J.L., 1976, MNRAS, 175, 19P

Heiles,C., 1968, ApJ, 151, 919

Herbst,W., 1975, AJ, 80, 503

Hippelein,H.H., Weinberger,R., 1975, A&A, 43, 405

Hoyle,F., 1957, The Black Cloud, New York: Harper & Bros.

Hughes,V.A., Macleod,G.C., 1989, AJ, 97, 786

Humphreys,R.M., 1978, ApJS, 38, 309

Hussain,S.S., Sprent,P., 1983, J. R. Statist. Soc. A, 146, Part 2, 182

Isobe,T, Feigelson,E.D., Akritas,M.G., Babu,G.J., ApJ, 1990, 364, 104

Jenkins,E.B., 1971, ApJ, 169, 25

Jonas,J.L., 1982, Observation and Processing of 2.3 GHz Radio Astronomy Survey Data, Masters thesis, Rhodes University, South Africa

Jonas,J.L., de Jager,G., Baart,E.E., 1985, A&ASS, 62, 105

Jonas,J.L., Baart,E.E., 1995, Astrophysics & Space Science, 230, 351

Kafatos,M.C. Morrison,P., 1971, ApJ, 168, 195

Kaarsemaaker,L. and van Wijngaarden,A., 1953, Statistica Neerlandica, 7,41

Kendall,M.G., 1970, Rank Correlation Methods, Charles Griffin & Company Limited, 4th edition.

Kerr,F.J., Bowers,P.F., Jackson,P.D., Kerr,M., 1986, Fully Sampled Neutral Hydrogen Survey of the Southern Milky Way, Astronomy Program, University of Maryland, College Park, Maryland, U.S.A.

Kraus,J.D., 1986, Radio Astronomy, 2nd edition, Cygnus-Quasar Books, Powell, Ohio

Krishna Swamy,K.S., O'Dell,C.R., 1968, ApJ, 151, L61

Kudritzki,R.P., Simon, K.P.,Hamann, W.-R., 1983, A&A, 118, 245

Kudritzki,R.P., Hummer,D.G., 1990, Ann. Rev. Astron. Astrophys., 28, 303

Lamers,H.J.G.L.M., Leitherer,C., 1993, ApJ, 412, 771

Leahy,D.A., Aschenbach,B., 1995, A&A, 293, 853

Leahy,D.A., Aschenbach,B., 1996, A&A, 315, 260

Leahy,D.A., Nousek,J., Garmire,G., 1992, ApJ, 385, 561

Long,K.S., Blair,W.P., White,R.L., Matsui,Y., 1991, ApJ, 373, 567

Mathis,J.S., Mezger,P.G., Panagia,N., 1983, A&A, 128, 212

Maran,S.P., 1971, Sci. American, Vol. 225, NO. 6, 20

Maran,S.P., Brandt,J.C., Stecher,T.P., 1971, Physics Today 24, No.9, 42

Mezger,P.G., Henderson,A.P., 1967, ApJ, 147, 471

Miller,E.W., 1972, AJ, 77, 216

Morrison,P., Sartori,L., 1969, ApJ, 158, 541

Morton,D.G., 1978, ApJ, 222, 863

Morton,D.G., Bhavsar,S.P., 1979, ApJ, 228, 147

Mountfort,P.I., 1989, The Observation of Extended Sources with the Hartebeesthoek Radio Telescope, Doctoral Thesis, Rhodes University, South Africa

Mountfort,P.I., Jonas,J.L., de Jager,G., Baart,E.E., 1987, MNRAS, 226, 917

Murphy,D.C., May,J., 1991, A&A, 247, 202

NASA Symposium, 1973, The Gum Nebula and Related Problems, The Proceedings held at the NASA Goddard Space Flight Center during May18, 1971, Editors: Maran,S.P., Brandt,J.C., Stecher,T.P., National Aeronautics and Space Administration, Washington, D.C.

Ostriker,J.P.,Silk,J., 1973, ApJ, 184, L113

Panagia, N., 1973, AJ, 78, 929

Pettersson,B, 1987, A&A, 171, 101

Press,W.H., Teukolsky,S.A., Vetterling,W.T., Flannery,B.P., Numerical Recipes in Fortran The Art of Scientific Computing, Second Edition, Cambridge University Press, 1992

Prusti,T., Adorf,H.-M., Meyrs,E.J.A., 1992, A&A, 261, 685

Reich,P., Reich,W., 1986, A&ASS, 63, 205

Reich,P., Reich,W., 1988, A&ASS, 74, 7

Reipurth,B., 1983, A&A, 117, 183

Rengarajan,T.N., Verma,R.P., Iyengar,K.V.K., 1989, MNRAS, 237, 1047

Reynolds,R.J., 1976a, ApJ, 203, 151

Reynolds,R.J., 1976b, ApJ, 206, 679

Rogers,A.E.E, Barrett,A.H., 1967, Radio Astronomy and the Galactic System, ed. H. van Woerden, Amsterdam, North-Holland Publishing Co.

Rohlfs,K.R.,1986, Tools of Radio Astronomy, Springer-Verlag

Rubin,R.H.,1968, ApJ, 154, 391

Sachs,L., 1984, Applied Statistics A Handbook of Techniques, 2nd edition, Springer Verlag New York Inc. Translated by Reynarowych,Z.

Sahu,M., Pottasch,S.R., Sahu,K.C., Wesselius,P.R., Desai,J.N., 1988, A&A, 195, 269

Saken,J.M., Fesen,R.A., Shull,J.M., 1992, ApJS, 81, 715

Salter,C.J., Brown,R.L., 1988, Galactic and Extragalactic Radio Astronomy, Second edition, Editiors Verschuur,G.L. and Kellermann,K.I. Springer-Verlag

Sandqvist,Aa., 1976, MNRAS, 177, 69P

Schlickeiser,R., Fürst,E., 1989, A&A, 192-194

Sen,P.K., 1968, J. Amer. Statist. Assoc., 63, 1379

Shu,F.H., 1982, The Physical Universe An Introduction to Astronomy, University Science Books, Mill Valley, California

Silk,J., Burke,J.R.,1974, ApJ, 190, 11

Sillitto,G.P., 1947, Biometrika, 34, 36

Sivan,J.P., 1974, A&ASS, 16, 163

Sky Catalogue 2000.0 Volume 2, 1985, Edited by Hirschfeld,A. and Sinnott,R.W., Cambridge University Press & Sky Publishing Corporation

Slawson,R.W., Reed, B.C., 1988, AJ, 96, 988

Smith, A.M., 1970, ApJ, 160, 595

Smith,L.F., 1968, MNRAS, 140, 409

Smoot,G.F., De Amici,G., Friedman,S.D., Witebsky,C., Sironi,G., Mandolesi,N., Cortiglioni,S., Morigi,G., Partridge, Danese,L., De Zotti,G., 1985, ApJ, 291, L23

Sprent,P., 1989, Applied Nonparametric Statistical Methods, Chapman and Hall Ltd.

Sridharan,T.K., 1992, J. Astrophys. Astr. 13, 217

Srinivasan Sahu, 1992, Doctoral Thesis, Rijksuniversiteit Groningen, Netherlands

Srinivasan Sahu, M., Sahu, K.C., 1993, A&A, 280, 231

Strong,A.W., Riley,P.A., Osborne,J.L., 1982, MNRAS, 201, 495

Theil,H., 1950, Proc. Kon. Nederl. Akad. Wetensch. A, 53, 386-392, 521-525, 1897-1912

Turtle,A.J., Pugh,J.F., Kenderdine,S., Pauliny-Toth,I.I.K., 1962, MNRAS, 124, 297

Upton, 1973, see NASA Symposium, p119

Vidal,J.-L., 1979, A&A, 79, 93

von Hoerner, S., 1967, ApJ, 147, 467

Wallerstein,G., Silk,J., Jenkins,E.B., 1980, ApJ, 240, 834

Weaver,H., Williams,D.R.W., Dieter,N.H., Lum,W.T., 1965, Nature, 208, 29

Weaver,R., McCray,R., Castor,J., 1977, ApJ, 218, 377

Wells,D.C., Greisen,E.W., Harten,R.H., 1981, A&ASS, 44, 363

Wheelock S.L. et al., 1994, IRAS Sky Survey Altas Explanatory Supplement, JPL Publication 94-11 (Pasadena,JPL)

White,R.L., Long,K.S., 1991, ApJ, 373, 543

Whiteoak,J.B., 1961, Dissertation, Australian National University

Woermann,B., Jonas,J.L., 1988, MNRAS, 234, 971

Woermann,B., Gaylard,M.J., 1993, Poster at IAU Colloqium 145 on Supernovae and Supernova Remnants, Xian, China

Woodhouse,G.F.W., 1980, Trans. S. Afr. Inst. Elec. Eng., 70, 188

Woodward,P.R., 1976, ApJ, 207, 484

Woodward,P.R., 1979, In Large Scale Characteristics of the Galaxy, IAU Symp. 84, 159, ed. Burton, W.B., Reidel, Dordrecht, Holland

Wouterloot,J.G.A., Brand,J., 1989, A&ASS, 80, 149

Zealey,W.J., Ninkov,Z., Rice,E., Hartley,M., Tritton,S.B., 1983, Astrophys. Letters, 23, 119

Zombeck M.V., 1980, in High Energy Astrophysics Handbook, SAO special report 386